

**Detecting and Learning Out-of-Distribution Data in the Open world:
Algorithm and Theory**

by

Yiyu Sun

A dissertation submitted in partial fulfillment of
the requirements for the degree of

Doctor of Philosophy

(Computer Sciences)

at the

UNIVERSITY OF WISCONSIN–MADISON

2023

Date of final oral examination: 07/19/2023

The dissertation is approved by the following members of the Oral Committee:

Jerry Xiaojin Zhu, Professor, Computer Sciences

Yong Jae Lee, Associate Professor, Computer Sciences

Yingyu Liang, Associate Professor, Computer Sciences

Yiqiao Zhong, Assistant Professor, Statistics

Sharon Yixuan Li (Advisor), Assistant Professor, Computer Sciences

© Copyright by Yiyou Sun 2023
All Rights Reserved

Acknowledgments

I would like to express my deepest gratitude to everyone who has contributed to the completion of this doctoral thesis. This research journey has been a transformative and enlightening experience, and I am fortunate to have received guidance, support, and encouragement from all individuals and institutions.

Firstly, I owe a huge thanks to my advisor, Professor Sharon Li. Her knowledge, guidance, and dedication to high standards have really shaped my work. She encouraged me to venture into the unknown, confront challenges, and dig deeper intellectually. When I faced significant setbacks, like when my papers were repeatedly rejected, she was there and continued to assure me that my work was valuable and helped me regain my confidence. Her support during these tough times was invaluable and helped me get back on track.

I'm also hugely grateful to my dissertation committee, Prof. Jerry Zhu, Prof. Yong Jae Lee, Prof. Yiqiao Zhong, and Prof. Yingyu Liang. Their expertise, constructive feedback, and insights have greatly improved my thesis. I'm also deeply grateful to my collaborators and labmates, Chuan Guo, Zhenmei Shi, Yifei Ming, Xuefeng Du, and Haoyue Bai, who have supported me tremendously. They enriched my thought process and created a supportive research environment.

Finally, my heartfelt appreciation goes to my family especially to my mom and my wife for their understanding and constant cheering. Their

patience, support, and unwavering belief in me have been the foundation of my achievements.

To everyone who helped with this thesis, whether I mentioned you or not, your support and encouragement have been invaluable. I am deeply grateful for all of you being part of my life.

Contents

Contents iii

List of Tables viii

List of Figures xi

Abstract xiii

1 Introduction 1

1.1 *Out-of-distribution (OOD) Detection* 3

1.2 *Open-world Representation Learning (ORL)* 5

1.3 *Contribution and Thesis Outline* 8

2 Background 12

2.1 *Problem Statement* 12

2.2 *Related Work* 15

2.3 *Notations* 18

I Out-of-distribution Detection

19

3 ReAct: OOD Detection With Rectified Activations 20

3.1 *Introduction* 21

3.2 *Methodology* 24

3.3	<i>Experiment</i>	25
3.3.1	Evaluation on Large-scale ImageNet Task	25
3.3.2	Evaluation on CIFAR Benchmarks	28
3.4	<i>Theoretical Insight</i>	30
3.5	<i>Discussion and Further Analysis</i>	35
3.5.1	Why do OOD samples trigger abnormal unit activation patterns?	35
3.5.2	What about networks trained with different normalization mechanisms?	37
3.6	<i>Additional Related Work</i>	38
3.7	<i>Summary</i>	39
4	DICE: Leverage Sparsification for OOD Detection	40
4.1	<i>Introduction</i>	41
4.2	<i>Method</i>	44
4.3	<i>Experiments</i>	47
4.3.1	Evaluation on CIFAR Benchmarks	48
4.3.2	Evaluation on Large-scale ImageNet Task	49
4.4	<i>Discussion and Ablations</i>	51
4.5	<i>Why does DICE improve OOD detection?</i>	54
4.6	<i>Additional Related Work</i>	57
4.7	<i>Summary</i>	58
5	OOD Detection with Deep Nearest Neighbors	59
5.1	<i>Introduction</i>	60
5.2	<i>Deep Nearest Neighbor for OOD detection</i>	63
5.3	<i>Experiments</i>	66
5.3.1	Evaluation on CIFAR Benchmarks	67
5.3.2	Evaluation on Large-scale ImageNet Task	71
5.4	<i>A Closer Look at KNN-based OOD Detection</i>	73
5.5	<i>Theoretical Justification</i>	77

5.6 *Additional Related Work* 79

5.7 *Summary* 79

II Open-world Representation Learning 80

6 When and How Does Known Class Help Discover Unknown Ones? A Spectral Analysis 81

6.1 *Introduction* 82

6.2 *Setup* 85

6.3 *Spectral Contrastive Learning for Novel Class Discovery* 86

6.3.1 *Graph-Theoretic Representation for NCD* 86

6.3.2 *NCD Spectral Contrastive Learning* 88

6.4 *Theoretical Analysis* 90

6.4.1 *Theoretical Setup* 90

6.4.2 *An Illustrative Example* 92

6.4.3 *Main Theory* 98

6.5 *Experiments on Common Benchmarks* 101

6.6 *Additional Related Work* 104

6.7 *Summary* 105

7 A Graph-Theoretic Framework for Understanding ORL 107

7.1 *Introduction* 108

7.2 *Problem Setup* 111

7.3 *A Spectral Approach for Open-world Representation Learning* 112

7.3.1 *A Graph-Theoretic Formulation* 113

7.3.2 *SORL: Spectral Open-World Representation Learning* 115

7.4 *Theoretical Analysis* 117

7.4.1 *An Illustrative Example* 117

7.4.2 *Main Theory* 119

7.5 *Empirical Validation of Theory* 124

7.6 *Broader Impact* 126

7.7	<i>Additional Related Work</i>	126
7.8	<i>Summary</i>	128
8	OpenCon: Open-world Contrastive Learning	129
8.1	<i>Introduction</i>	130
8.2	<i>Methodology</i>	133
8.2.1	Background: Generalized Contrastive Loss	133
8.2.2	Learning from Wild Unlabeled Data	134
8.2.3	Open-world Contrastive Loss	137
8.3	<i>Theoretical Understandings</i>	138
8.3.1	Analyzing the E-step	139
8.3.2	Analyzing the M-step	140
8.4	<i>Experimental Results</i>	141
8.5	<i>A Comprehensive Analysis of OpenCon</i>	146
8.6	<i>Additional Related Work</i>	150
8.7	<i>Summary</i>	152
9	Conclusion	154
9.1	<i>Future Work</i>	155
A	Appendix for Out-of-distribution Detection	157
A.1	<i>ReAct: OOD Detection With Rectified Activations</i>	157
A.1.1	Theoretical Details	157
A.1.2	Ablation Study on Different Layers	159
A.1.3	Using True BatchNorm Statistics on OOD Data	161
A.1.4	Unit Activation Patterns for Gaussian Noise	162
A.2	<i>DICE: Leverage Sparsification for OOD Detection</i>	164
A.2.1	Variance Reduction with Correlated Variables	164
A.2.2	Validation Strategy	165
A.2.3	More results on the effect of Sparsity Parameter	166
A.2.4	Detailed OOD Detection Performance for CIFAR	166

A.3	<i>OOD Detection with Deep Nearest Neighbors</i>	169
A.3.1	Theoretical Analysis	169
A.3.2	Configurations	171
A.3.3	Results on Different Architecture	172
B	Appendix for Open-world Representation Learning	173
B.1	<i>When and How Does Known Class Help Discover Unknown Ones? A Spectral Analysis</i>	173
B.1.1	Proof Details for Section 6.3	173
B.1.2	Proof for Eigenvalue in Toy Example	178
B.1.3	Additional Details for Section 6.4.3	184
B.1.4	Experimental Details	205
B.2	<i>A Graph-theoretic Framework for Understanding ORL</i>	207
B.2.1	Technical Details of Spectral Open-world Representation Learning	207
B.2.2	Technical Details for Toy Example	211
B.2.3	Technical Details for Main Theory	221
B.2.4	Analysis on Other Contrastive Losses	237
B.2.5	Additional Experiments Details	240
B.3	<i>OpenCon: Open-world Contrastive Learning</i>	242
B.3.1	Preliminaries of Contrastive Losses	242
B.3.2	Algorithm	244
B.3.3	Additional Theoretical Details	244
B.3.4	Additional Experiments	248
	References	255

List of Tables

2.1	Comparison of problem settings related to the open-world representation learning.	14
2.2	List of common math notations.	18
3.1	Comparison with ReAct and competitive post hoc out-of-distribution detection methods.	27
3.2	Effect of rectification threshold for inference.	28
3.3	Performance of different OOD scoring functions equipped with ReAct.	29
3.4	Comparison with oracle using OOD’s BN statistics.	35
3.5	Effectiveness of ReAct for different normalization methods.	37
4.1	Comparison with out-of-distribution detection method on CIFAR benchmarks.	49
4.2	Comparison with out-of-distribution detection methods on ImageNet.	50
4.3	Effect of different sparsification methods for OOD detection with ImageNet as ID dataset.	53
4.4	Ablation on different strategies of choosing a subset of units.	54
4.5	Difference between the mean of ID’s output and OOD’s output.	57
5.1	Comparison with OOD detection methods on CIFAR-10.	67
5.2	Comparison with other non-parametric methods.	70
5.3	Results on hard OOD detection tasks.	71

5.4	Comparison of OOD baseline methods on ImageNet.	72
5.5	Performance on ViT-B/16 model fine-tuned on ImageNet-1k. .	73
5.6	Comparison of KNN-based method with and w/o. activation truncation.	76
6.1	Comaprison of NCD baselines in clustering accuracy on the novel set.	102
6.2	Comparison of baselines' results with overall/novel/known ac- curacy.	103
7.1	Main Results of comparing baselines in open-world represen- tation learning.	125
8.1	Main Results of OpenCon and baseline methods' performance in open-world representation learning.	143
8.2	Comparison of accuracy on ViT-B/16 architecture. Results are reported on ImageNet-100.	146
8.3	Effect of OOD detection threshold p	147
8.4	Ablation study on loss component in OpenCon.	148
8.5	Performance with an unknown number of classes.	149
8.6	Performance varying different labeling ratios and different num- bers of known classes.	150
A.1	Ablation study of applying ReAct on different layers.	160
A.2	Detailed results on six common OOD benchmark datasets. . .	163
A.3	Effect of varying sparsity parameter p on CIFAR-10 and Ima- geNet.	166
A.4	Detailed results for sparsification baselines on six common OOD benchmark datasets.	167
A.5	Detailed results for OOD detection baselines on six common OOD benchmark datasets.	168
A.6	Results on CIFAR-10/100 with DenseNet-101.	172

B.1	Comparison with modified losses.	250
B.2	Results on CIFAR-10 dataset.	251
B.3	Hyperparameters used for OpenCon.	253
B.4	Comparison of OOD detection performance with popular methods in OpenCon.	254

List of Figures

1.1	Illustration of two sub-problems of open-world machine learning and their relationship.	2
1.2	The outline of the thesis.	8
3.1	Plot of the distribution of per-unit activations and uncertainty scores of ID and OOD before and after truncation.	22
3.2	Positively skewed distribution of μ_i (mean of each unit) in the penultimate layer for four OOD datasets.	32
3.3	Plot showing the relationship between the skewness parameter ϵ and the chaotic-ness parameter σ on activation reduction after applying ReAct.	33
3.4	The distribution of per-unit activations in the penultimate layer for OOD data by using true vs. mismatched BatchNorm statistics for OOD data.	36
3.5	The distribution of per-unit activations in the penultimate layer for ID and OOD on model trained with weight normalization.	38
4.1	Illustration of unit contribution to the class output.	42
4.2	Illustration of out-of-distribution detection using DICE.	45
4.3	Effect of varying sparsity parameter p during inference time.	52
4.4	Plot of the average unit contribution in the penultimate layer in a sorted manner.	55

5.1	Illustration of the framework using nearest neighbors for OOD detection.	63
5.2	Comparison with the effect of different k and sampling ratio α	74
5.3	Ablation results on different k , sampling ratio α , normalization, feature layer, etc.	75
5.4	Distribution plot of features' norm and k -NN distance with or w/o. normalization.	76
6.1	Illustration of scenarios where different known classes could result in different novel clusters.	83
6.2	An illustrative example for theoretical analysis.	91
6.3	UMAP visualization of the feature embedding.	98
7.1	Illustration of the research question in Open-world Representation Learning.	108
7.2	An illustrative example for theoretical analysis.	119
7.3	Visualization of representation space for toy example.	120
8.1	Illustration of our learning framework.	131
8.2	UMAP visualization of the feature embedding.	145
A.1	The distribution of per-unit activations in the penultimate layer for ImageNet and iNaturalist on different layers.	160
A.2	The distribution of per-unit activations in the penultimate layer for Gaussian Noise and ImageNet.	162
A.3	Covariance matrix of unit contribution estimated on the OOD dataset SVHN.	165
B.1	Sensitivity analysis of hyper-parameters.	205
B.2	An illustrative example for theoretical analysis (appendix).	212
B.3	Distribution of OOD score for unlabeled data.	249
B.4	UMAP visualization of the feature embedding from more classes.	252
B.5	Sensitivity analysis of hyper-parameters.	253

Abstract

This thesis makes considerable contributions to the realm of machine learning, specifically in the context of open-world scenarios where systems face previously unseen data and contexts. Traditional machine learning models are usually trained and tested within a fixed and known set of classes, a condition known as the closed-world setting. While this assumption works in controlled environments, it falls short in real-world applications where new classes or categories of data can emerge dynamically and unexpectedly.

To address this, our research investigates two intertwined steps essential for open-world machine learning: *Out-of-distribution (OOD) Detection* and *Open-world Representation Learning (ORL)*. OOD detection focuses on identifying instances from unknown classes that fall outside the model's training distribution. This process reduces the risk of making overly confident, erroneous predictions about unfamiliar inputs. Moving beyond OOD detection, ORL extends the capabilities of the model to not only detect unknown instances but also learn from and incorporate knowledge about these new classes.

In the realm of OOD detection, our work first introduces pioneering methodologies, namely ReACT and DICE, that can effectively differentiate samples from known and unknown classes. ReACT truncates abnormally high unit activations during test time to reduce the model's overconfidence in the output, while DICE leverages a model's most contribut-

ing weights by sparsification for OOD detection. Moreover, we present a distance-based OOD detection method with the introduction of a non-parametric approach using K-nearest neighbor (KNN) distance, with a paradigm shift in eschewing rigid distributional assumptions about the underlying feature space.

Moving beyond OOD detection, ORL involves deeper exploration into learning the unknown, answering crucial research questions about the interplay between known and unknown classes, and the role of label information in shaping representations. Through rigorous investigations, we aim to illuminate how knowledge about known classes can help uncover previously unseen classes and how label information impacts the learning and representation of both known and novel classes. This exploration inspires the development of a comprehensive algorithmic framework (OpenCon) for ORL, underpinned by a theoretical interpretation from the Expectation-maximization perspective.

By delving into these research problems of open-world learning, this thesis paves the way for building machine learning models that are not only performant but also reliable in the face of the evolving complexities of the real world.

Chapter 1

Introduction

Advances in machine learning have revolutionized numerous domains, including image classification (Deng et al., 2009; He et al., 2016a), object detection (Girshick, 2015; Sun et al., 2017), segmentation (Chen et al., 2017), video processing (Kahou et al., 2016), and audio recognition (Purwins et al., 2019), driving innovation and transforming the way we interact with technology. Noticeably, the vast majority of learning algorithms have been driven by the **closed-world** setting. For example, the face recognition systems of border control assume the inputs are all face images, in which case the traditional methods are sufficient to satisfy the industrial requirements (Boulkenafet et al., 2015; Li et al., 2016a). These applications assume that the classes are stationary and unchanged. This assumption, however, rarely holds for models deployed in the wild.

One important characteristic of the **open-world** is that the intelligent system will encounter new contexts and data that were not taught to the algorithms during training, therefore requiring safe handling and adaptation to the novel data. Traditional ML algorithms are typically unreliable to such out-of-distribution (OOD) data and can fail catastrophically (Nguyen et al., 2015) (e.g., blindly predicting an OOD sample from an unknown class into a known class with high confidence). Preventing disastrous and

overconfident outcomes for safe decision-making is thus a critical problem within trustworthy and open-world machine learning. This area already has numerous applications in autonomous driving, cloud computing, voice-assisted smartphones, smart logistics, healthcare, insurance, e-commerce systems, and many other industries. For example, a medical machine learning system may encounter a new disease it has never seen (Sun et al., 2021b); an e-commerce classifier may come across brand-new products in the market (Bigcommerce, 2023); an autonomous driving model can run into an unknown object on the road (Templeton, 2020). As the demand for intelligent systems grows, the need for machine learning algorithms to handle open-world scenarios becomes increasingly paramount. Open-world machine learning is an upcoming frontier and has gained increasing interest within the computer science community in the last few years.

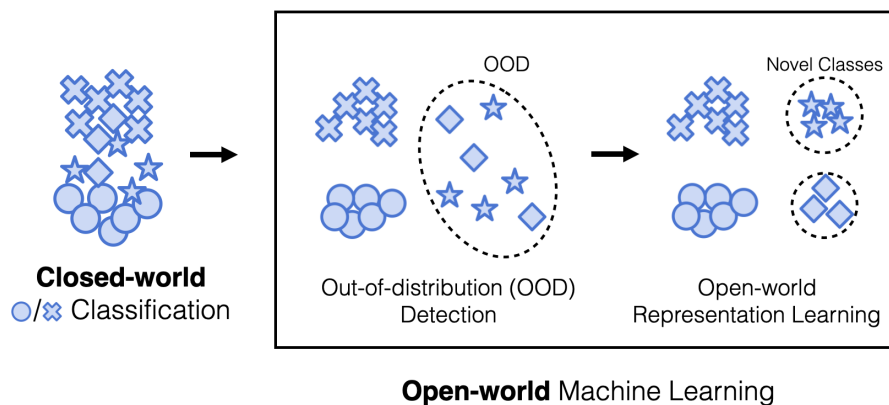


Figure 1.1: The thesis focuses on the open-world machine learning problem, composed of two sub-problems: *Out-of-distribution (OOD) Detection* and *Open-world Representation Learning (ORL)*. The figure uses a toy example with a binary classification problem of the circle and the cross. OOD detection aims to detect OOD samples (star and square) that are not in the training categories (circle and cross). ORL aims to learn distinguishable representations for all classes including known classes and OOD classes.

Within this field, two prominent research topics emerge as the central areas of investigation: *Out-of-distribution (OOD) Detection* and *Open-world Representation Learning (ORL)*. The relationship between these research topics is illustrated in Figure 1.1. At a high level, OOD detection can be seen as the initial step in extending the closed-world classification problem to the open world. A reliable machine learning model should not only accurately classify in-distribution (ID) samples but also possess the capability to identify samples that lie outside the known distribution. Moving beyond OOD detection, the ORL problem further requires models to learn the hidden classes within OOD samples, in addition to the known classes. We delve deeper into this discussion in the subsequent paragraphs.

1.1 Out-of-distribution (OOD) Detection

The research revolves around effectively identifying instances from unknown classes or categories. In traditional machine learning, algorithms assume a closed-world setting with a fixed and known set of classes during training and inference (He et al., 2016a; Huang et al., 2017). However, in open-world scenarios, where new classes can emerge dynamically, existing models often struggle to identify instances from previously unseen categories accurately (Nguyen et al., 2015). Developing robust techniques for Out-of-distribution Detection is crucial for reliably distinguishing between known and unknown classes, enabling more reliable machine learning systems.

A driving idea behind OOD detection is that the model should be much less confident about samples outside of its training distribution. However, modern neural networks can produce overconfident predictions on OOD inputs. This observation goes back to the early work by Nguyen et al. (2015). This phenomenon renders the separation of in-

distribution (ID) and OOD data a non-trivial task, which attracts growing research attention in several thriving directions:

(a) One line of work attempted to perform OOD detection by devising scoring functions, including OpenMax score (Bendale and Boulton, 2015), maximum softmax probability (Hendrycks and Gimpel, 2017), ODIN score (Liang et al., 2018), deep ensembles (Lakshminarayanan et al., 2017), Mahalanobis distance-based score (Lee et al., 2018), energy score (Liu et al., 2020; Lin et al., 2021; Wang et al., 2021; Morteza and Li, 2022), gradient-based score (Huang et al., 2021b) and ViM score (Wang et al., 2022b). On this line, this doctoral thesis includes two representative works (ReACT (Sun et al., 2021a) and DICE (Sun and Li, 2022)) which push the boundaries of novel methodologies in detecting OOD data.

Specifically, ReACT (Sun et al., 2021a) is proposed as a simple yet effective solution for reducing model overconfidence in OOD data. The key idea behind ReACT is to truncate the abnormally high unit activations during test-time OOD detection. Empirical and theoretical insights are provided to characterize and explain how ReACT improves OOD uncertainty estimation. By rectifying the activations, the outsized contribution of hidden units on OOD output can be attenuated, resulting in stronger separability from ID data.

The success of ReACT has led to a significant follow-up work called DICE (Sun and Li, 2022) which delves deeper into the detection of OOD data by investigating the influence of weights. DICE leverages the observation that a model’s prediction for an ID class depends on only a subset of important units and their corresponding weights. Building on this observation, DICE introduces a novel idea of ranking weights based on their measure of contribution and selectively using the most contributing weights to derive the output for OOD detection.

(b) Another avenue of exploration in OOD detection involves the adoption of distance-based approaches, which operate under the assumption

that the test OOD samples are relatively far away from the ID data. In particular, CSI (Tack et al., 2020) investigate the type of data augmentations that are particularly beneficial for OOD detection. Other works (Winkens et al., 2020; Schwag et al., 2021) verify the effectiveness of applying the off-the-shelf multi-view contrastive losses such as SimCLR (Chen et al., 2020a) and SupCon (Khosla et al., 2020) for OOD detection.

Prior works commonly make a strong distributional assumption, assuming the underlying feature space follows a class-conditional Gaussian distribution. Unlike previous methods, this thesis introduces a non-parametric approach, specifically utilizing K-nearest neighbor (KNN) distance (Sun et al., 2022) and not relying on any specific distributional assumption about the underlying feature space. This crucial paradigm shift provides greater flexibility and generality in detecting OOD samples, as it does not impose rigid distributional assumptions.

By advancing the understanding and techniques in OOD detection, this research contributes to the development of more reliable and robust machine learning models, paving the way for applications in open-world scenarios where the presence of unknown classes is a crucial challenge to overcome.

1.2 Open-world Representation Learning (ORL)

Beyond detecting the OOD data from unknown classes, an extended line of research lies in the ability to learn and incorporate knowledge in these unknown classes. Concretely, the model has access to the training dataset with both labeled and unlabeled data. The labeled dataset contains samples that belong to a set of known classes, while the unlabeled dataset has a mixture of samples from both the known and novel classes. In practice,

such unlabeled in-the-wild data can be collected almost for free upon deploying a model in the open world, and thus is available in abundance. This gives rise to the pressing demand for the advancement of ORL algorithms, enabling more robust and adaptable open-world machine learning systems.

The learning setting that considers both labeled and unlabeled data with a mixture of known and novel classes is first proposed in [Cao et al. \(2022\)](#) and inspires a proliferation of follow-up works ([Pu et al., 2023](#); [Zhang et al., 2022a](#); [Rizve et al., 2022](#); [Vaze et al., 2022](#)) advancing empirical success where most works put emphasis on learning high-quality representations ([Vaze et al., 2022](#); [Pu et al., 2023](#); [Zhang et al., 2022a](#)). The thesis further *advances theoretical understanding* by answering two unresolved research questions ([Sun et al., 2023b,a](#)) as well as providing effective empirical solutions ([Sun and Li, 2023](#); [Sun et al., 2023b,a](#)).

The first research question we aim to address is “*when and how does known class help discover unknown ones?*” Recognizing the potential interplay between known and unknown classes is essential for effective open-world representation learning. By investigating this question, we seek to uncover the unsolved mystery in Novel Class Discovery (NCD) ([Hsu et al., 2018](#); [Han et al., 2019](#); [Hsu et al., 2019](#); [Zhong et al., 2021b](#); [Han et al., 2020a](#); [Yang et al., 2022c](#); [Sun and Li, 2023](#)) by which knowledge about known classes can facilitate the discovery and recognition of previously unseen classes. Understanding these dynamics is crucial for designing algorithms that can leverage the relationships and similarities between known and unknown classes, leading to enhanced representation learning in open-world scenarios.

The second research question we explore is “*what is the role of label information in shaping representations for both known and novel classes?*” In open-world representation learning, label information plays a vital role in guiding the formation of effective representations. By examining this

question, we aim to shed light on how label information influences the learning process and the resulting representations for both known and novel classes. Investigating the impact of label information on the representation space can provide valuable insights into the change of the representations' discriminative power in known classes and how it generalizes to the novel class.

Finally, the thesis tackles the empirical challenges in ORL. Different from self-supervised representation learning (Van den Oord et al., 2018; Chen et al., 2020a; Caron et al., 2020; He et al., 2020), open-world representation learning is a distinct endeavor that goes beyond simply leveraging unlabeled data to uncover meaningful representations. It encompasses the challenging task of effectively capturing the underlying structures and characteristics of both known and unknown classes. In this monograph, we provide a unified and comprehensive algorithmic framework (Sun and Li, 2023) accompanied by a theoretical interpretation from the Expectation-maximization (EM) perspective, tackling unique challenges within open-world representation learning.

Through rigorous theoretical analysis and algorithmic development, this monograph strives to address these research questions, contributing to the advancement of open-world representation learning. By elucidating the relationships between known and unknown classes and understanding the role of label information, we aim to unlock new avenues for representation learning in open-world settings, empowering machine learning systems to effectively capture the complexities and nuances of diverse and evolving real-world environments.

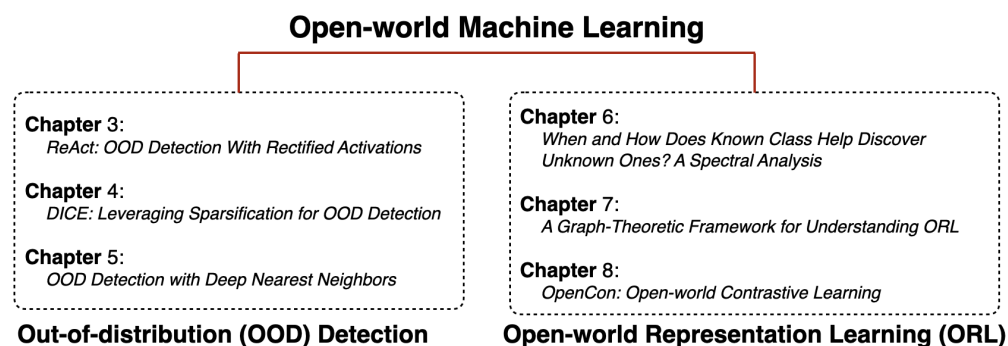


Figure 1.2: Thesis outline including *Out-of-Distribution detection* and *Open-world Representation Learning*.

1.3 Contribution and Thesis Outline

This doctoral thesis makes significant contributions to the field of open-world machine learning, with a specific focus on two key research topics: *Out-of-Distribution detection* and *Open-world Representation Learning*, with outline illustrated in Figure 1.2. The central contribution of this thesis lies in the development of novel methodologies and theoretical insights to address these challenges.

One of the primary contributions of this thesis lies in the development of several competitive algorithms for OOD detection, addressing the problem of model overconfidence in OOD inputs. This thesis unveils the mechanisms underlying overconfident predictions on OOD data, providing insights into why such phenomena occur. The introduction of the ReACT (Sun et al., 2021a), DICE (Sun and Li, 2022) and KNN (Sun et al., 2022) technique further offers practical post hoc solutions to reduce model overconfidence on OOD data. The empirical and theoretical insights gained from these algorithms shed light on the improvement of OOD detection performance and establish a solid ground for future work in this research topic.

Furthermore, this thesis highlights the importance of open-world rep-

resentation learning as a crucial second step beyond the OOD detection process. Open-world representation learning is required to effectively capture the underlying structures and characteristics of both known and unknown classes, enabling the development of robust and adaptable machine learning systems in open-world scenarios, where new classes can emerge dynamically. This thesis presents novel methodologies (Sun and Li, 2023; Sun et al., 2023a,b) for open-world representation learning, producing a compact representation space for both known and novel classes. The monograph also establishes the theoretical foundations of the ORL problem by elucidating the relationships between known and unknown classes and understanding the role of label information, empowering machine learning system developers to effectively capture the complexities and nuances of diverse and evolving real-world environments.

In terms of the thesis outline:

Chapter 2 offers a meticulous description of the problem setup, encompassing a comprehensive literature review that surveys the current body of research on out-of-distribution (OOD) detection and open-world representation learning.

Chapter 3, Chapter 4, and Chapter 5 investigate the out-of-distribution detection problem:

Chapter 3 presents the theoretical foundations and insights into the mechanisms of “why model gets overconfidence in OOD data”. This chapter also introduces the ReACT technique with the key idea that truncates the abnormally high unit activations for test-time OOD detection. The content of this chapter is primarily based on Sun et al. (2021a).

Chapter 4 introduces DICE, which extended the research scope beyond the unit activations and investigated the influence of weight in OOD detection. DICE leverages the observation that a model’s prediction for

an ID class depends on only a subset of important units (and corresponding weights). The idea is to rank weights based on the measure of contribution, and selectively use the most contributing weights to derive the output for OOD detection. The content of this chapter is primarily based on [Sun and Li \(2022\)](#).

Chapter 5 describes a distance-based OOD detection by using k -th nearest neighbor distances, which operates under the assumption that the test OOD samples are relatively far away from the ID data. Importantly, it brings a crucial paradigm shift from a parametric to a non-parametric distance-based approach for OOD detection. The content of this chapter is primarily based on [Sun et al. \(2022\)](#).

Chapter 6, Chapter 7, and Chapter 8 fall under the umbrella of open-world representation learning:

Chapter 6 aims to answer an underexplored research question “*when and how does known class help discover unknown ones?*” Tailored to the problem, we introduce a graph-theoretic representation that can be learned by a novel NCD Spectral Contrastive Loss (NSCL), which is appealing for practical usage while enjoying theoretical guarantees. The content of this chapter is primarily based on [Sun et al. \(2023b\)](#).

Chapter 7 investigates the second research question in open-world representation learning: “*what is the role of label information in shaping representations for both known and novel classes?*” Our graph-theoretic framework (SORL) illuminates practical algorithms and shed light on how label information influences the learning process and the resulting representations for both known and novel classes. The content of this chapter is primarily based on [Sun et al. \(2023a\)](#).

Chapter 8 introduces OpenCon, a pioneering training framework for open-world representation learning. It establishes a contrastive loss framework that tackles unique challenges in the ORL problem: (a) the lack of

clear separation between known vs. novel data in unlabeled data, and (b) the lack of supervision for data in novel classes. The content of this chapter is primarily based on [Sun and Li \(2023\)](#).

Finally, **Chapter 9** concludes the thesis by summarizing the contributions, discussing the implications of the research findings, and outlining potential directions for future work. Through these contributions and the systematic exploration of OOD detection and open-world representation learning, this thesis advances the understanding and state-of-the-art in the field, providing valuable insights and practical methodologies to enhance the reliability and adaptability of machine learning models in open-world scenarios.

Chapter 2

Background

2.1 Problem Statement

In this section, we introduce the problem setup of *Out-of-distribution Detection* and *Open-world Representation Learning*. We delve into the investigation of the OOD Detection problem in Chapter 3, Chapter 4, and Chapter 5. Furthermore, we explore the ORL problem in Chapter 6, Chapter 7, and Chapter 8. Note that Chapter 6 specifically focuses on a sub-problem of ORL known as *Novel Class Discovery* (NCD), which we will elaborate on in detail within Chapter 6.

2.1.1 Out-of-distribution Detection

In OOD detection, we consider supervised multi-class classification, where \mathcal{X} denotes the input space and $\mathcal{Y}_l = \{1, 2, \dots, C\}$ denotes the label space. The training set $\mathcal{D}_{in} = \{(\mathbf{x}_i, y_i)\}_{i=1}^n$ is drawn *i.i.d.* from the joint data distribution $\mathcal{P}_{\mathcal{X}\mathcal{Y}_l}$. Let \mathcal{P}_{in} denote the marginal distribution on \mathcal{X} . Let $f : \mathcal{X} \mapsto \mathbb{R}^C$ be a neural network trained on samples drawn from $\mathcal{P}_{\mathcal{X}\mathcal{Y}_l}$ to output a logit vector, which is used to predict the label of an input sample.

When deploying a machine model in the real world, a reliable classi-

fier should not only accurately classify known in-distribution (ID) samples, but also identify as “unknown” any OOD input. This can be achieved by having an OOD detector, in tandem with the classification model f . OOD detection can be formulated as a binary classification problem. At test time, the goal of OOD detection is to decide whether a sample $\mathbf{x} \in \mathcal{X}$ is from \mathcal{P}_{in} (ID) or not (OOD). The decision can be made via a level set estimation:

$$\mathcal{S}_\lambda(\mathbf{x}) = \begin{cases} \text{ID} & S(\mathbf{x}) \geq \lambda \\ \text{OOD} & S(\mathbf{x}) < \lambda \end{cases},$$

where samples with higher scores $S(\mathbf{x})$ are classified as ID and vice versa, and λ is the threshold. In practice, OOD is often defined by a distribution that simulates unknowns encountered during deployment time, such as samples from an irrelevant distribution whose label set has no intersection with \mathcal{Y} and therefore should not be predicted by the model.

2.1.2 Open-world Representation Learning

In addition to detecting out-of-distribution (OOD) samples, the open-world representation learning setting places significant emphasis on the objective of not only identifying new classes within OOD samples but also learning the existing classes in the wild. To formalize this, we provide a description of the data setup and the learning goal:

Data setup. We consider the training dataset $\mathcal{D} = \mathcal{D}_l \cup \mathcal{D}_u$ with two parts:

1. The labeled set $\mathcal{D}_l = \{\mathbf{x}_i, y_i\}_{i=1}^n$, with $y_i \in \mathcal{Y}_l$. The label set \mathcal{Y}_l is known.
2. The unlabeled set $\mathcal{D}_u = \{\mathbf{x}_i\}_{i=1}^m$, where each sample $\mathbf{x}_i \in \mathcal{X}$ can come from either known or novel classes¹. Note that we do not have

¹It generalizes the problem of Novel Class Discovery (NCD) (Han et al., 2019), which assumes the unlabeled set is purely from novel classes.

access to the labels in \mathcal{D}_u . For mathematical convenience, we denote the underlying label set as \mathcal{Y}_{all} , where $\mathcal{Y}_l \subset \mathcal{Y}_{\text{all}}$ implies category shift and expansion. Accordingly, the set of novel classes is $\mathcal{Y}_n = \mathcal{Y}_{\text{all}} \setminus \mathcal{Y}_l$, where the *subscript* n stands for “**n**ovel”. The model has no knowledge of the set \mathcal{Y}_n nor its size.

Goal. Under the setting, the goal is to learn distinguishable representations for *both known and novel classes* simultaneously.

Table 2.1: Comparison of problem settings related to the open-world representation learning.

Problem Setting	Labeled data	Unlabeled data	
		Known classes	Novel classes
Semi-supervised learning	Yes	Yes	No
Robust semi-supervised learning	Yes	Yes	Yes (Reject)
Supervised learning	Yes	No	No
Novel class discovery	Yes	No	Yes (Discover)
Open-world representation learning	Yes	Yes	Yes (Cluster)

Difference w.r.t. existing problem settings. The open-world representation learning is a practical and relatively novel problem, which differs from existing problem settings (see Table 2.1 for a summary). In particular, (a) we consider *both labeled data and unlabeled data* in training, and (b) we consider a mixture of *both known and novel classes* in unlabeled data. Note that our setting generalizes traditional representation learning. For example, Supervised Contrastive Learning (SupCon) (Khosla et al., 2020) only assumes the labeled set \mathcal{D}_l , without considering the unlabeled data \mathcal{D}_u . Weakly supervised contrastive learning (Zheng et al., 2021) assumes the same classes in labeled and unlabeled data, *i.e.*, $\mathcal{Y}_l = \mathcal{Y}_{\text{all}}$, and hence remains closed-world. Self-supervised learning (Chen et al., 2020a) relies completely on the unlabeled set \mathcal{D}_u and does not assume the availability of the labeled dataset. The setup is also known as open-world semi-supervised learning (OSSL) or generalized category discovery (GCD), which is introduced in Cao et al. (2022) and Vaze et al.

(2022) respectively. Despite the similar setup, the learning goal of ORL is different: Cao et al. (2022) and Vaze et al. (2022) focus on classification accuracy, while ORL aims to learn high-quality embeddings.

2.2 Related Work

This section includes an introduction to the related works in *Out-of-distribution Detection* and *Open-world Representation Learning*. Additionally, each chapter includes discussions on other research areas relevant to its specific topic.

2.2.1 Out-of-distribution Detection

The phenomenon of neural networks’ overconfidence in out-of-distribution data is first revealed in Nguyen et al. (2015) with the learning theory established in recent work (Fang et al., 2022). This research area attracts growing research attention in several thriving directions.

Training-based OOD Detection. One promising line of work addressed OOD detection by training-time regularization (Lee et al., 2017; Bevandić et al., 2018; Malinin and Gales, 2018; Hendrycks et al., 2018; Geifman and El-Yaniv, 2019; Hein et al., 2019; Meinke and Hein, 2020; Mohseni et al., 2020; Liu et al., 2020; Jeong and Kim, 2020; Van Amersfoort et al., 2020; Yang et al., 2021; Chen et al., 2021; Wei et al., 2022; Ming et al., 2022b; Katz-Samuels et al., 2022; Du et al., 2022a; Tao et al., 2023; Bai et al., 2023). For example, models are encouraged to give predictions with uniform distribution (Lee et al., 2017; Hendrycks et al., 2018) or higher energies (Liu et al., 2020; Ming et al., 2022b; Du et al., 2022b; Katz-Samuels et al., 2022) for outlier data. Most regularization methods require the availability of auxiliary OOD data. VOS (Du et al., 2022c) alleviates the need by automatically synthesizing virtual outliers that can meaningfully regularize the model’s decision boundary during training. Although these methods

have demonstrated empirical success, their practical application scope is limited due to the requirement of a re-training process. Moreover, in the case of large models such as CLIP (Radford et al., 2021), the re-training process can be prohibitively expensive. The thesis does not encompass a discussion on this particular research direction but instead places a greater emphasis on the inference-based method, which we will introduce in the subsequent paragraph.

Inference-based OOD Detection. This category of methods operates on a pre-trained network and detects OOD samples in a post hoc manner. They offer flexibility by allowing for plug-and-play functionality with most existing models. These methods can be broadly categorized into two branches: output-based and distance-based methods:

(a) *Output-based methods.* This line of work attempted to perform OOD detection by devising scoring functions based on the model’s output, including OpenMax score (Bendale and Boulton, 2015), maximum softmax probability (Hendrycks and Gimpel, 2017), ODIN score (Liang et al., 2018), deep ensembles (Lakshminarayanan et al., 2017), energy score (Liu et al., 2020; Lin et al., 2021; Wang et al., 2021; Morteza and Li, 2022), gradient-based score (Huang et al., 2021b), MOS score (Huang and Li, 2021) and ViM score (Wang et al., 2022b). On this line, this doctoral thesis includes two representative works – ReAct (Sun et al., 2021a) in Chapter 3 and DICE (Sun and Li, 2022) in Chapter 4 which push the boundaries of novel methodologies in detecting OOD data.

(b) *Distance-based methods.* Another avenue of exploration in OOD detection involves the adoption of distance-based approaches, which operate under the assumption that the test OOD samples are relatively far away from the ID data. CSI (Tack et al., 2020) investigate the type of data augmentations that are particularly beneficial for OOD detection. Other works (Winkens et al., 2020; Schwag et al., 2021) verify the effectiveness of applying the off-the-shelf multi-view contrastive losses such as Sim-

CLR (Chen et al., 2020a) and SupCon (Khosla et al., 2020) for OOD detection. Ming et al. (2023) propose a prototype-based contrastive learning framework for OOD detection, which promotes stronger ID-OOD separability than SupCon loss. Prior works commonly make a strong distributional assumption, assuming the underlying feature space follows a class-conditional Gaussian distribution. Unlike previous methods, this thesis introduces a non-parametric approach, specifically utilizing K-nearest neighbor (KNN) distance (Sun et al., 2022) in Chapter 5 and not relying on any specific distributional assumption about the underlying feature space. Performance-wise, this method outperforms 13 competitive rivals according to a recent survey study (Yang et al., 2022b).

2.2.2 Open-world Representation Learning

The learning setting that considers both labeled and unlabeled data with a mixture of known and novel classes is first proposed in Cao et al. (2022) and inspires a proliferation of follow-up works (Pu et al., 2023; Zhang et al., 2022a; Rizve et al., 2022; Vaze et al., 2022) advancing empirical success. Most works put emphasis on learning high-quality embeddings (Vaze et al., 2022; Pu et al., 2023; Zhang et al., 2022a). In particular, Vaze et al. (2022) employs contrastive learning with both supervised and self-supervised signals. Pu et al. (2023) improves clustering accuracy by learning conceptual representation and Zhang et al. (2022a) applies a two-stage approach that refines the embedding by an affinity graph after a pre-training stage. Different from prior works, the thesis further *advancing theoretical understanding* by answering two unresolved research questions (Sun et al., 2023b,a) in Chapter 6 and Chapter 7 as well as providing effective learning algorithms (Sun and Li, 2023) in Chapter 8.

2.3 Notations

In this section, we define common notation that is shared throughout the thesis. Specific additional notations are defined within each respective chapter. It is crucial to recognize that the notations utilized in one chapter do not carry over to others.

Table 2.2: List of common math notations.

$[n]$	the set $\{1, \dots, n\}$
$\ \cdot\ _1$	l_1 norm of a matrix or a vector
$\ \cdot\ _2$	l_2 norm of a matrix or a vector
$\ \cdot\ _F$	the Frobenius norm of a matrix
$\mathbf{1}_n$	n -dimensional vector with all 1
$\mathbf{0}_n$	n -dimensional vector with all 0
$\mathbf{1}_{m \times n}$	m -by- n matrix with all 1
$\mathbf{0}_{m \times n}$	m -by- n matrix with all 0
I_n	identity matrix with shape $n \times n$
$V_{(i,j)}/V_{ij}$	the value at i -th row and j -th column of a matrix V
$V_{k,(i,j)}$	the value at i -th row and j -th column of a matrix V_k
$\mathbf{v}_{(i)}/\mathbf{v}_i$	i -th value for a vector \mathbf{v}
$\mathbf{v}_{k,(i)}$	i -th value for a subscripted vector \mathbf{v}_k
$\langle \mathbf{u}, \mathbf{v} \rangle$	inner-production between \mathbf{u} and \mathbf{v}
V^\dagger	Moore-Penrose inverse of matrix V

Part I

Out-of-distribution Detection

Chapter 3

ReAct: OOD Detection With Rectified Activations

Publication Statement. This chapter is joint work with Chuan Guo and Yixuan Li. The paper version of this chapter appeared in NeurIPS21 ([Sun et al., 2021a](#)).

Out-of-distribution (OOD) detection has received much attention lately due to its practical importance in enhancing the safe deployment of neural networks. One of the primary challenges is that models often produce highly confident predictions on OOD data, which undermines the driving principle in OOD detection that the model should only be confident about in-distribution samples. In this chapter, we introduce **ReAct**—a simple and effective technique for reducing model overconfidence in OOD data. ReAct is motivated by a novel analysis of internal activations of neural networks, which displays highly distinctive signature patterns for OOD distributions. ReAct can generalize effectively to different network architectures and different OOD detection scores. We empirically demonstrate that ReAct achieves competitive detection performance on a comprehensive suite of benchmark datasets, and give theoretical explication.

3.1 Introduction

Neural networks deployed in real-world systems often encounter out-of-distribution (OOD) inputs—unknown samples that the network has not been exposed to during training. Identifying and handling these OOD inputs can be paramount in safety-critical applications such as autonomous driving (Filos et al., 2020) and health care. For example, an autonomous vehicle may fail to recognize objects on the road that do not appear in its object detection model’s training set, potentially leading to a crash. This can be prevented if the system identifies the unrecognized object as OOD and warns the driver in advance.

A driving idea behind OOD detection is that the model should be much more uncertain about samples outside of its training distribution. However, Nguyen et al. (2015) revealed that modern neural networks can produce overconfident predictions on OOD inputs. This phenomenon renders the separation of in-distribution (ID) and OOD data a non-trivial task. Indeed, much of the prior work on OOD detection focused on defining more suitable measures of OOD uncertainty (Hsu et al., 2020; Lakshminarayanan et al., 2017; Liang et al., 2018; Lee et al., 2018; Liu et al., 2020; Huang et al., 2021b). Despite the improvement, it is arguable that continued research progress in OOD detection requires insights into the fundamental cause and mitigation of model overconfidence on OOD data.

In this chapter, we start by revealing an important observation that OOD data can trigger unit activation patterns that are significantly different from ID data. Figure 3.1(b) shows the distribution of activations in the penultimate layer of ResNet-50 trained on ImageNet (Deng et al., 2009). Each point on the horizontal axis corresponds to a single unit. The mean and standard deviation are shown by the solid line and shaded area, respectively. The mean activation for ID data (blue) is well-behaved with a near-constant mean and standard deviation. In contrast, for OOD data (gray), the mean activation has significantly larger variations across

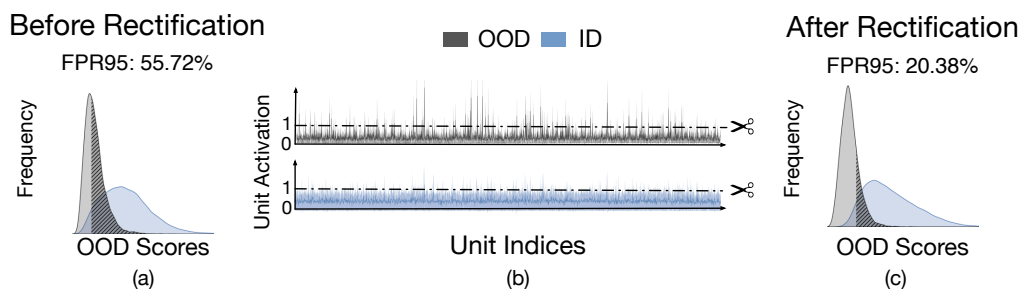


Figure 3.1: Plots showing (a) the distribution of ID (ImageNet (Deng et al., 2009)) and OOD (iNaturalist (Horn et al., 2018)) uncertainty scores before truncation, (b) the distribution of per-unit activations in the penultimate layer for ID and OOD data, and (c) the distribution of OOD uncertainty scores (Liu et al., 2020) after rectification. Applying ReAct drastically improves the separation of ID and OOD data. See text for details.

units and is biased towards having sharp positive values (*i.e.*, positively skewed). As a result, such high unit activation can undesirably manifest in model output, producing overconfident predictions on OOD data. A similar distributional property holds for other OOD datasets as well.

The above observation naturally inspires a simple yet surprisingly effective method—**Rectified Activations** (dubbed **ReAct**) for OOD detection. In particular, the outsized activation of a few selected hidden units can be attenuated by rectifying the activations at an upper limit $c > 0$. Conveniently, this can be done on a pre-trained model without any modification to training. The dashed horizontal line in Figure 3.1(b) shows the cutoff point c , and its effect on the OOD uncertainty score is shown in Figure 3.1(c). After rectification, the output distributions for ID and OOD data become much more well-separated and the false positive rate (FPR) is significantly reduced from 55.72% to 20.38%. Importantly, this truncation largely preserves the activation for in-distribution data, and therefore ensures the classification accuracy on the original task is largely comparable.

We provide both empirical and theoretical insights, characterizing and explaining the mechanism by which ReAct improves OOD detection. We perform extensive evaluations and establish competitive performance on a suite of common OOD detection benchmarks, including CIFAR-10 and CIFAR-100, as well as a large-scale ImageNet dataset (Deng et al., 2009). ReAct outperforms Energy score (Liu et al., 2020) by a large margin, reducing the average FPR95 by up to 25.05%. We further analyze our method theoretically and show that ReAct is more beneficial when OOD activations are more chaotic (*i.e.*, having a larger variance) and positively skewed compared to ID activations, a behavior that is typical of many OOD datasets (*cf.* Figure 3.1). In summary, the **key results and contributions** for this chapter are:

1. We introduce ReAct—a simple and effective *post hoc* OOD detection approach that utilizes activation truncation. We show that ReAct can generalize effectively to different network architectures and works with different OOD detection methods including MSP (Hendrycks and Gimpel, 2017), ODIN (Liang et al., 2018), and energy score (Liu et al., 2020).
2. We extensively evaluate ReAct on a suite of OOD detection tasks and establish a competitive performance among post hoc methods. Compared to the previous best method, ReAct achieves an FPR95 reduction of 25.05% on a large-scale ImageNet benchmark.
3. We provide both empirical ablation and theoretical analysis, revealing important insights that abnormally high activations on OOD data can harm their detection and how ReAct effectively mitigates this issue. Our insight inspires future research to further examine the internal mechanisms of neural networks for OOD detection.

3.2 Methodology

We introduce a simple and surprisingly effective technique, **Rectified Activations** (ReAct), for improving OOD detection performance. Our key idea is to perform *post hoc* modification to the unit activation, so to bring the overall activation pattern closer to the well-behaved case. Specifically, we consider a pre-trained neural network parameterized by θ , which encodes an input $\mathbf{x} \in \mathbb{R}^d$ to a feature space with dimension m . We denote by $h(\mathbf{x}) \in \mathbb{R}^m$ the feature vector from the penultimate layer of the network. A weight matrix $\mathbf{W} \in \mathbb{R}^{m \times C}$ connects the feature $h(\mathbf{x})$ to the output $f(\mathbf{x})$, where C is the total number of classes in $\mathcal{Y} = \{1, 2, \dots, C\}$.

ReAct: Rectified Activation. We propose the ReAct operation, which is applied on the penultimate layer of a network:

$$\bar{h}(\mathbf{x}) = \text{ReAct}(h(\mathbf{x}); c), \quad (3.1)$$

where $\text{ReAct}(x; c) = \min(x, c)$ and is applied element-wise to the feature vector $h(\mathbf{x})$. In effect, this operation truncates activations above c to limit the effect of noise. The model output after *rectified activation* is given by:

$$f^{\text{ReAct}}(\mathbf{x}; \theta) = \mathbf{W}^\top \bar{h}(\mathbf{x}) + \mathbf{b}, \quad (3.2)$$

where $\mathbf{b} \in \mathbb{R}^C$ is the bias vector. A higher c indicates a larger threshold of activation truncation. When $c = \infty$, the output becomes equivalent to the original output $f(\mathbf{x}; \theta)$ without rectification, where $f(\mathbf{x}; \theta) = \mathbf{W}^\top h(\mathbf{x}) + \mathbf{b}$. Ideally, the rectification parameter c should be chosen to sufficiently preserve the activations for ID data while rectifying that of OOD data. In practice, we set c based on the p -th percentile of activations estimated on the ID data. For example, when $p = 90$, it indicates that 90% percent of the ID activations are less than the threshold c . We discuss the effect of percentile in detail in Section 3.3.

OOD detection with rectified activation. During test time, ReAct can be leveraged by a variety of downstream OOD scoring functions relying on $f^{\text{ReAct}}(\mathbf{x}; \theta)$:

$$\mathcal{S}_\lambda(\mathbf{x}; f^{\text{ReAct}}) = \begin{cases} \text{in} & S(\mathbf{x}; f^{\text{ReAct}}) \geq \lambda \\ \text{out} & S(\mathbf{x}; f^{\text{ReAct}}) < \lambda \end{cases}, \quad (3.3)$$

where a thresholding mechanism is exercised to distinguish between ID and OOD during test time. To align with the convention, samples with higher scores $S(\mathbf{x}; f)$ are classified as ID and vice versa. The threshold λ is typically chosen so that a high fraction of ID data (*e.g.*, 95%) is correctly classified. ReAct can be compatible with several commonly used OOD scoring functions derived from the model output $f(\mathbf{x}; \theta)$, including the softmax confidence (Hendrycks and Gimpel, 2017), ODIN score (Liang et al., 2018), and the energy score (Liu et al., 2020). In Section 3.3, we default to using the energy score (since it is hyperparameter-free and does not require fine-tuning), but demonstrate the benefit of using ReAct with other OOD scoring functions too.

3.3 Experiment

In this section, we evaluate ReAct on a suite of OOD detection tasks. We first evaluate a on large-scale OOD detection benchmark based on ImageNet (Huang and Li, 2021) (Section 3.3.1), and then proceed in Section 3.3.2 with CIFAR benchmarks (Krizhevsky et al., 2009).

3.3.1 Evaluation on Large-scale ImageNet Task

We first evaluate ReAct on a large-scale OOD detection benchmark developed in Huang and Li (2021). Compared to the CIFAR benchmarks that are routinely used in literature, the ImageNet benchmark is more chal-

lenging due to a larger label space ($C = 1,000$). Moreover, such large-scale evaluation is more relevant to real-world applications, where the deployed models often operate on images that have high resolution and contain more classes than the CIFAR benchmarks.

Setup. We use a pre-trained ResNet-50 model (He et al., 2016b) for ImageNet-1k. At test time, all images are resized to 224×224 . We evaluate on four test OOD datasets from (subsets of) Places365 (Zhou et al., 2017), Textures (Cimpoi et al., 2014), iNaturalist (Horn et al., 2018), and SUN (Xiao et al., 2010) with non-overlapping categories w.r.t ImageNet. We use a validation set of Gaussian noise images, which are generated by sampling from $\mathcal{N}(0, 1)$ for each pixel location. To ensure validity, we further verify the activation pattern under Gaussian noise, which exhibits a similar distributional trend with positive skewness and chaoticness; see Figure A.2 in Appendix A.1.4 for details. We select p from $\{10, 65, 80, 85, 90, 95, 99\}$ based on the FPR95 performance. The optimal p is 90.

Comparison with competitive OOD detection methods. In Table 3.1, we compare ReAct with OOD detection methods that are competitive in the literature. For a fair comparison, all methods use the pre-trained networks *post hoc*. We report performance for each OOD test dataset, as well as the average of the four. ReAct outperforms all baselines considered, including Maximum Softmax Probability (Hendrycks and Gimpel, 2017), ODIN (Liang et al., 2018), Mahalanobis distance (Lee et al., 2018), and energy score (Liu et al., 2020). Noticeably, ReAct reduces the FPR95 by **25.05%** compared to Liang et al. (2018) on ResNet. Note that Mahalanobis requires training a separate binary classifier, and displays limiting performance since the increased size of label space makes the class-conditional Gaussian density estimation less viable. In contrast, ReAct is much easier to use in practice, and can be implemented through a simple *post hoc* activation rectification.

Effect of rectification threshold c . We now characterize the effect of the

Table 3.1: **Main results.** Comparison with competitive *post hoc* out-of-distribution detection methods. All methods are based on a model trained on **ID data only** (ImageNet-1k), without using any auxiliary outlier data. \uparrow indicates larger values are better and \downarrow indicates smaller values are better. The compared baselines include MSP (Hendrycks and Gimpel, 2017), ODIN (Liang et al., 2018), Mahalanobis (Lee et al., 2018), and Energy (Liu et al., 2020). All values are percentages.

Model	Methods	OOD Datasets								Average	
		iNaturalist		SUN		Places		Textures		FPR95	AUROC
		FPR95 \downarrow	AUROC \uparrow	FPR95 \downarrow	AUROC \uparrow	FPR95 \downarrow	AUROC \uparrow	FPR95 \downarrow	AUROC \uparrow	\downarrow	\uparrow
ResNet	MSP	54.99	87.74	70.83	80.86	73.99	79.76	68.00	79.61	66.95	81.99
	ODIN	47.66	89.66	60.15	84.59	67.89	81.78	50.23	85.62	56.48	85.41
	Mahalanobis	97.00	52.65	98.50	42.41	98.40	41.79	55.80	85.01	87.43	55.47
	Energy	55.72	89.95	59.26	85.89	64.92	82.86	53.72	85.99	58.41	86.17
	ReAct (Ours)	20.38	96.22	24.20	94.20	33.85	91.58	47.30	89.80	31.43	92.95
MobileNet	MSP	64.29	85.32	77.02	77.10	79.23	76.27	73.51	77.30	73.51	79.00
	ODIN	55.39	87.62	54.07	85.88	57.36	84.71	49.96	85.03	54.20	85.81
	Mahalanobis	62.11	81.00	47.82	86.33	52.09	83.63	92.38	33.06	63.60	71.01
	Energy	59.50	88.91	62.65	84.50	69.37	81.19	58.05	85.03	62.39	84.91
	ReAct (Ours)	42.40	91.53	47.69	88.16	51.56	86.64	38.42	91.53	45.02	89.47

rectification parameter c , which can be modulated by the percentile p described in Section 3.2. In Table 3.2, we summarize the OOD detection performance, where we vary $p = \{10, 65, 80, 85, 90, 95, 99\}$. This ablation confirms that over-activation does compromise the ability to detect OOD data, and ReAct can effectively alleviate this problem. Moreover, when p is sufficiently large, ReAct can improve OOD detection while maintaining a comparable ID classification accuracy. Alternatively, once a sample is detected to be ID, one can always use the original activation $h(\mathbf{x})$, which is guaranteed to give identical classification accuracy. When p is too small, OOD performance starts to degrade as expected.

Effect on other network architectures. We show that ReAct is effective on a different architecture in Table 3.1. In particular, we consider a lightweight model MobileNet-v2 (Sandler et al., 2018), which can be suitable for OOD detection in on-device mobile applications. Same as before, we apply ReAct on the output of the penultimate layer, with the rectification threshold

Table 3.2: Effect of rectification threshold for inference. Model is trained on ImageNet using ResNet-50 (He et al., 2016a). All numbers are percentages and are averaged over 4 OOD test datasets.

Rectification percentile	FPR95 ↓	AUROC ↑	AUPR ↑	ID ACC. ↑	Threshold c
No ReAct	58.41	86.17	96.88	75.08	∞
$p = 99$	44.57	90.45	97.96	75.12	2.25
$p = 95$	35.39	92.39	98.37	74.76	1.50
$p = 90$	31.43	92.95	98.50	73.75	1.00
$p = 85$	34.08	92.05	98.35	72.91	0.84
$p = 80$	41.51	89.54	97.91	71.93	0.72
$p = 65$	74.62	74.14	94.39	67.14	0.50
$p = 10$	74.70	57.55	86.06	1.22	0.06

chosen based on the 90-th percentile. Our method reduces the FPR95 by **9.18%** compared to the best baseline considered (Liang et al., 2018).

What about applying ReAct on other layers? Our results suggest that applying ReAct on the penultimate layer is the most effective, since the activation patterns are most distinctive. To see this, we provide the activation and performance study for intermediate layers in Appendix A.1.2 (see Figure A.1 and Table A.1). Interestingly, early layers display less distinctive signatures between ID and OOD data. This is expected because neural networks generally capture lower-level features in early layers (such as Gabor filters (Zeiler and Fergus, 2014) in layer 1), whose activations can be very similar between ID and OOD. The semantic-level features only emerge as with deeper layers, where ReAct is the most effective.

3.3.2 Evaluation on CIFAR Benchmarks

Datasets. We evaluate on CIFAR-10 and CIFAR-100 (Krizhevsky et al., 2009) datasets as in-distribution data, using the standard split with 50,000 training images and 10,000 test images. For OOD data, we consider six common benchmark datasets: Textures (Cimpoi et al., 2014), SVHN (Net-

zer et al., 2011), Places365 (Zhou et al., 2017), LSUN-Crop (Yu et al., 2015), LSUN-Resize (Yu et al., 2015), and iSUN (Xu et al., 2015).

Experimental details. We train a standard ResNet-18 (He et al., 2016a) model on in-distribution data. The feature dimension of the penultimate layer is 512. For both CIFAR-10 and CIFAR-100, the models are trained for 100 epochs. The start learning rate is 0.1 and decays by a factor of 10 at epochs 50, 75, and 90. For threshold c , we use the 90-th percentile of activations estimated on the ID data.

ReAct is compatible with various OOD scoring functions. We show in Table 3.3 that ReAct is a flexible method that is compatible with alternative scoring functions $S(\mathbf{x}; f^{\text{ReAct}})$. To see this, we consider commonly used scoring functions, and compare the performance both with and without using ReAct respectively. In particular, we consider softmax confidence (Hendrycks and Gimpel, 2017), ODIN score (Liang et al., 2018) as well as energy score (Liu et al., 2020)—all of which derive OOD scores directly from the output $f(\mathbf{x})$. In particular, using ReAct on energy score yields the best performance, which is desirable as energy is a

Table 3.3: **Ablation results.** ReAct is compatible with different OOD scoring functions. For each ID dataset, we use the same model and compare the performance with and without ReAct respectively. \uparrow indicates larger values are better and \downarrow indicates smaller values are better. All values are percentages and are averaged over multiple OOD test datasets. Detailed performance for each OOD test dataset is available in Table A.2.

Method	CIFAR-10			CIFAR-100			ImageNet		
	FPR95 \downarrow	AUROC \uparrow	AUPR \uparrow	FPR95 \downarrow	AUROC \uparrow	AUPR \uparrow	FPR95 \downarrow	AUROC \uparrow	AUPR \uparrow
MSP	56.71	91.17	79.11	80.72	76.83	78.41	66.95	81.99	95.76
MSP + ReAct	53.81	91.70	92.11	75.45	80.40	84.28	58.28	87.06	97.22
Energy	35.60	93.57	95.01	71.93	82.82	86.28	58.41	86.17	96.88
Energy+ReAct	32.91	94.27	95.53	59.61	87.48	89.63	31.43	92.95	98.50
ODIN	31.10	93.79	94.95	66.21	82.88	86.25	56.48	85.41	96.61
ODIN+ReAct	28.81	94.04	94.82	59.91	85.23	87.53	44.10	90.70	98.04

hyperparameter-free OOD score and is easy to compute in practice. Note that Mahalanobis (Lee et al., 2018) estimates OOD score using feature representations instead of the model output $f(\mathbf{x})$, hence is less compatible with ReAct. On all three in-distribution datasets, using ReAct consistently outperforms the counterpart without rectification. Results in Table 3.3 are based on the average across multiple OOD test datasets. Detailed performance for each OOD test dataset is provided in Table A.2.

3.4 Theoretical Insight

To better understand the effect of ReAct, we mathematically model the ID and OOD activations as rectified Gaussian distributions and derive their respective distributions after applying ReAct. These modeling assumptions are based on the activation statistics observed on ImageNet in Figure 3.1. In the following analysis, we show that ReAct reduces mean OOD activations more than ID activations since OOD activations are more positively skewed (see Section A.1.1 for derivations).

ID activations. Let $h(\mathbf{x}) = (z_1, \dots, z_m) =: \mathbf{z}$ be the activations for the penultimate layer. We assume each $z_i \sim \mathcal{N}^R(\mu, \sigma_{\text{in}}^2)$ for some $\sigma_{\text{in}} > 0$. Here $\mathcal{N}^R(\mu, \sigma_{\text{in}}^2) = \max(0, \mathcal{N}(\mu, \sigma_{\text{in}}^2))$ denotes the rectified Gaussian distribution, which reflects the fact that activations after ReLU have no negative components. Before truncation with ReAct, the expectation of z_i is given by:

$$\mathbb{E}_{\text{in}}[z_i] = \left[1 - \Phi\left(\frac{-\mu}{\sigma_{\text{in}}}\right)\right] \cdot \mu + \phi\left(\frac{-\mu}{\sigma_{\text{in}}}\right) \cdot \sigma_{\text{in}},$$

where Φ and ϕ denote the cdf and pdf of the standard normal distribution, respectively. After rectification with ReAct, the expectation of $\bar{z}_i = \min(z_i, c)$ is:

$$\mathbb{E}_{\text{in}}[\bar{z}_i] = \left[\Phi\left(\frac{c-\mu}{\sigma_{\text{in}}}\right) - \Phi\left(\frac{-\mu}{\sigma_{\text{in}}}\right)\right] \cdot \mu + \left[1 - \Phi\left(\frac{c-\mu}{\sigma_{\text{in}}}\right)\right] \cdot c + \left[\phi\left(\frac{-\mu}{\sigma_{\text{in}}}\right) - \phi\left(\frac{c-\mu}{\sigma_{\text{in}}}\right)\right] \cdot \sigma_{\text{in}},$$

The reduction in activation after ReAct is:

$$\mathbb{E}_{\text{in}}[z_i - \bar{z}_i] = \phi\left(\frac{c - \mu}{\sigma_{\text{in}}}\right) \cdot \sigma_{\text{in}} - \left[1 - \Phi\left(\frac{c - \mu}{\sigma_{\text{in}}}\right)\right] \cdot (c - \mu) \quad (3.4)$$

OOD activations. We model OOD activations as being generated by a two-stage process: Each OOD distribution defines a set of μ_i 's that represent the mode of the activation distribution for unit i , and the activations z_i given μ_i is represented by $z_i|\mu_i \sim \mathcal{N}^R(\mu_i, \tau^2)$ with $\tau > 0$. For instance, the dark gray line in Figure 3.1 shows the set μ_i 's on the iNaturalist dataset, and the light gray area depicts the distribution of $z_i|\mu_i$. One commonality across different OOD datasets is that the distribution of μ_i is *positively skewed*. The assumption of positive skewness is motivated by our observation on real OOD data. Indeed, Figure 3.2 shows the empirical distribution of μ_i on an ImageNet pre-trained model for four OOD datasets, all of which display strong positive-skewness, *i.e.*, the right tail has a much higher density than the left tail. This observation is surprisingly consistent across datasets and model architectures. Although a more in-depth understanding of the fundamental cause of positive skewness is important, for this work, we chose to rely on this empirically verifiable assumption and instead focus on analyzing our method ReAct.

Utilizing the positive-skewness property of μ_i , we analyze the distribution of z_i after marginalizing out μ_i , which corresponds to averaging across different μ_i 's induced by various OOD distributions. Let $x_i|\mu_i \sim \mathcal{N}(\mu_i, \tau^2)$ so that $z_i|\mu_i = \max(x_i|\mu_i, 0)$. Since $x_i|\mu_i$ is symmetric and μ_i is positively-skewed, the marginal distribution of x_i is also positively-skewed¹, which we model with the epsilon-skew-normal (ESN) distribution (Mudholkar and Hutson, 2000). Specifically, we assume that $x_i \sim$

¹This can be argued rigorously using Pearson's mode skewness coefficient if the distribution of μ_i is unimodal.

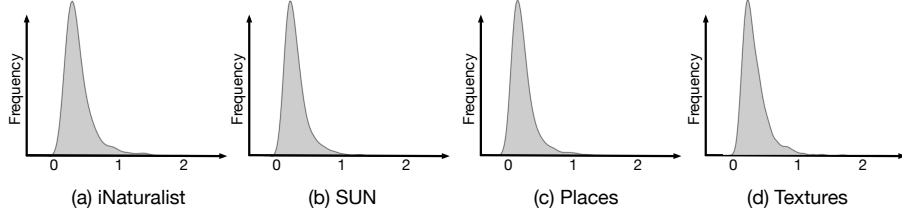


Figure 3.2: Positively skewed distribution of μ_i (mean of each unit) in the penultimate layer for four OOD datasets (iNaturalist (Horn et al., 2018), SUN (Xiao et al., 2010), Places (Zhou et al., 2017), Textures (Cimpoi et al., 2014)). Model is trained on ImageNet. Note that the right tail has a higher density than the left tail. By left and right tail we refer to the samples that are to the left and right of the *median*, which is close to the mode in the case of skewed distribution.

ESN($\mu, \sigma_{\text{out}}^2, \epsilon$), which has the following density function:

$$q(x) = \begin{cases} \phi((x - \mu)/\sigma_{\text{out}}(1 + \epsilon))/\sigma_{\text{out}} & \text{if } x < \mu, \\ \phi((x - \mu)/\sigma_{\text{out}}(1 - \epsilon))/\sigma_{\text{out}} & \text{if } x \geq \mu. \end{cases} \quad (3.5)$$

with $\epsilon \in [-1, 1]$ controlling the skewness. In particular, the ESN distribution is positively-skewed when $\epsilon < 0$. It follows that $z_i = \max(x_i, 0)$, with expectation:

$$\mathbb{E}_{\text{out}}[z_i] = \mu - (1 + \epsilon)\Phi\left(\frac{-\mu}{(1 + \epsilon)\sigma_{\text{out}}}\right) \cdot \mu + (1 + \epsilon)^2\phi\left(\frac{-\mu}{(1 + \epsilon)\sigma_{\text{out}}}\right) \cdot \sigma_{\text{out}} - \frac{4\epsilon}{\sqrt{2\pi}} \cdot \sigma_{\text{out}}. \quad (3.6)$$

Expectation after applying ReAct becomes:

$$\begin{aligned} \mathbb{E}_{\text{out}}[\bar{z}_i] &= \mu - (1 + \epsilon)\Phi\left(\frac{-\mu}{(1 + \epsilon)\sigma_{\text{out}}}\right) \cdot \mu + (1 - \epsilon) \left[1 - \Phi\left(\frac{c - \mu}{(1 - \epsilon)\sigma_{\text{out}}}\right) \right] \cdot (c - \mu) \\ &\quad + \left[(1 + \epsilon)^2\phi\left(\frac{-\mu}{(1 + \epsilon)\sigma_{\text{out}}}\right) - (1 - \epsilon)^2\phi\left(\frac{c - \mu}{(1 - \epsilon)\sigma_{\text{out}}}\right) - \frac{4\epsilon}{\sqrt{2\pi}} \right] \cdot \sigma_{\text{out}}, \end{aligned} \quad (3.7)$$

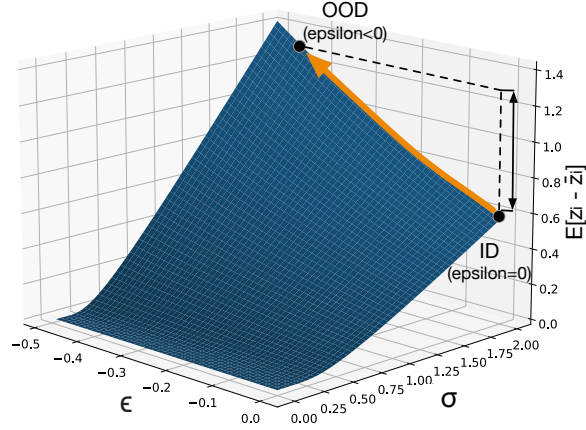


Figure 3.3: Plot showing the relationship between the skewness parameter ϵ and the chaotic-ness parameter σ on activation reduction after applying ReAct. The function $\mathbb{E}[z_i - \bar{z}_i]$ is increasing in both $-\epsilon$ and σ , which suggests that ReAct has a greater reduction effect for activation distributions with positive skewness ($\epsilon < 0$) and chaotic-ness—two signature characteristics of OOD activation.

Hence:

$$\mathbb{E}_{\text{out}}[z_i - \bar{z}_i] = (1-\epsilon)^2 \phi\left(\frac{c-\mu}{(1-\epsilon)\sigma_{\text{out}}}\right) \cdot \sigma_{\text{out}} - (1-\epsilon) \left[1 - \Phi\left(\frac{c-\mu}{(1-\epsilon)\sigma_{\text{out}}}\right)\right] \cdot (c-\mu), \quad (3.8)$$

which recovers Equation 3.4 when $\epsilon = 0$ and $\sigma_{\text{out}} = \sigma_{\text{in}}$.

Remark 1: Activation reduction on OOD is more than ID. Figure 3.3 shows a plot of $\mathbb{E}[z_i - \bar{z}_i]$ for $\mu = 0.5$ and $c = 1$. Observe that decreasing ϵ (more positive-skewness) or increasing σ (more chaotic-ness) leads to a larger reduction in the mean activation after applying ReAct. For example, under the same σ , a larger $\mathbb{E}_{\text{out}}[z_i - \bar{z}_i] - \mathbb{E}_{\text{in}}[z_i - \bar{z}_i]$ can be observed by the gap of z -axis value between $\epsilon = 0$ and $\epsilon < 0$ (e.g., $\epsilon = -0.4$). This suggests that rectification on average affects OOD activations more severely

compared to ID activations.

Remark 2: Output reduction on OOD is more than ID. To derive the effect on the distribution of model output, consider output logits $f(\mathbf{z}) = W\mathbf{z} + \mathbf{b}$ and assume without loss of generality that $W\mathbf{1} > 0$ element-wise. This can be achieved by adding a positive constant to W without changing the output probabilities or classification decision. Let $\delta = \mathbb{E}_{\text{out}}[\mathbf{z} - \bar{\mathbf{z}}] - \mathbb{E}_{\text{in}}[\mathbf{z} - \bar{\mathbf{z}}] > 0$. Then:

$$\begin{aligned} \mathbb{E}_{\text{out}}[f(\mathbf{z}) - f(\bar{\mathbf{z}})] &= \mathbb{E}_{\text{out}}[W(\mathbf{z} - \bar{\mathbf{z}})] = W\mathbb{E}_{\text{out}}[\mathbf{z} - \bar{\mathbf{z}}] = W(\mathbb{E}_{\text{in}}[\mathbf{z} - \bar{\mathbf{z}}] + \delta\mathbf{1}) \\ &= \mathbb{E}_{\text{in}}[W(\mathbf{z} - \bar{\mathbf{z}})] + \delta W\mathbf{1} \\ &> \mathbb{E}_{\text{in}}[f(\mathbf{z}) - f(\bar{\mathbf{z}})]. \end{aligned}$$

Hence the increased separation between OOD and ID activations transfers to the output space as well. Note that the condition of $W\mathbf{1} > 0$ is sufficient but not necessary for this result to hold. In fact, our experiments in Section 3.3 do not require this condition. However, we verified empirically that ensuring $W\mathbf{1} > 0$ by adding a positive constant to W and applying ReAct does confer benefits to OOD detection, which validates our theoretical analysis.

Why ReAct improves the OOD scoring functions? Our theoretical analysis above shows that ReAct suppresses logit output for OOD data more so than for ID data. This means that for detection scores depending on the logit output (*e.g.*, energy score (Liu et al., 2020)), the gap between OOD and ID score will be enlarged after applying ReAct, which makes thresholding more capable of separating OOD and ID inputs; see Figure 3.1(a) and (c) for a concrete example showing this effect.

3.5 Discussion and Further Analysis

3.5.1 Why do OOD samples trigger abnormal unit activation patterns?

So far we have shown that OOD data can trigger unit activation patterns that are significantly different from ID data, and that ReAct can effectively alleviate this issue (empirically in Section 3.3 and theoretically in Section 3.4). Yet a question left in mystery is *why* such a pattern occurs in modern neural networks? Answering this question requires carefully examining the internal mechanism by which the network is trained and evaluated. Here we provide one plausible explanation for the activation patterns observed in Figure 3.1, with the hope of shedding light for future research.

Table 3.4: Comparison with oracle using OOD’s BN statistics. The model is trained on ImageNet (see Section 3.3.1). Values are AUROC.

Method	iNaturalist	Places	SUN	Textures
Oracle (batch OOD for estimating BN statistics)	99.59	99.09	98.32	91.43
ReAct (single OOD)	96.22	94.20	91.58	89.80
No ReAct (Liu et al., 2020)	89.95	85.89	82.86	85.99

Intriguingly, our analysis reveals an important insight that batch normalization (BatchNorm) (Ioffe and Szegedy, 2015)—a common technique employed during model training—is in fact both a blessing (for ID classification) and a curse (for OOD detection). Specifically, for a unit activation denoted by z , the network estimates the running mean $\mathbb{E}_{\text{in}}(z)$ and variance $\text{Var}_{\text{in}}(z)$, over the entire ID training set during training. During inference time, the network applies BatchNorm statistics $\mathbb{E}_{\text{in}}(z)$ and $\text{Var}_{\text{in}}(z)$, which helps normalize the activations for the test data with the

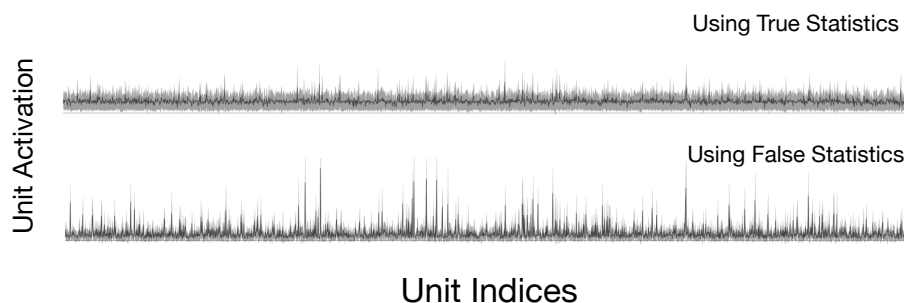


Figure 3.4: The distribution of per-unit activations in the penultimate layer for OOD data (iNaturalist) by using *true* (top) vs. *mismatched* (bottom) BatchNorm statistics for OOD data.

same distribution \mathcal{D}_{in} :

$$\text{BatchNorm}(z; \gamma, \beta, \epsilon) = \frac{z - \mathbb{E}_{\text{in}}[z]}{\sqrt{\text{Var}_{\text{in}}[z] + \epsilon}} \cdot \gamma + \beta \quad (3.9)$$

However, our key observation is that using *mismatched* BatchNorm statistics—that are estimated on \mathcal{D}_{in} yet blindly applied to the OOD \mathcal{D}_{out} —can trigger abnormally high unit activations. As a thought experiment, we instead apply the *true* BatchNorm statistics estimated on a batch of OOD images and we observe well-behaved activation patterns with near-constant mean and standard deviations—just like the ones observed on the ID data (see Figure 3.4, top). Our study therefore reveals one of the fundamental causes for neural networks to produce overconfident predictions for OOD data. After applying the true statistics (estimated on OOD), the output distributions between ID and OOD data become much more separable. While this thought experiment has shed some guiding light, the solution of estimating BatchNorm statistics on a batch of OOD data is not at all satisfactory and realistic. Arguably, it poses a strong and impractical assumption of having access to a batch of OOD data during test time. Despite its limitation, we view it as an oracle, which serves as an *upper*

bound on performance for ReAct.

In particular, results in Table 3.4 suggest that our method favorably matches the oracle performance using the ground truth BN statistics. This is encouraging as our method does not impose any batch assumption and can be feasible for *single-input* testing scenarios.

Table 3.5: **Effectiveness of ReAct for different normalization methods.** ReAct consistently improves OOD detection performance for the model trained with GroupNorm and WeightNorm. In-distribution is ImageNet-1k dataset. **Bold** numbers are superior results.

Methods	OOD Datasets								Average		
	iNaturalist		SUN		Places		Textures		FPR95	AUROC	
	FPR95	AUROC	FPR95	AUROC	FPR95	AUROC	FPR95	AUROC	FPR95	AUROC	
		↓	↑	↓	↑	↓	↑	↓	↑	↓	↑
GroupNorm	w.o. ReAct	65.38	88.45	65.11	85.52	65.46	84.34	69.17	83.22	66.28	85.38
	w/ ReAct	39.45	92.95	51.57	87.90	52.78	87.32	62.50	81.76	51.58	87.48
WeightNorm	w.o. ReAct	40.71	92.52	48.07	89.39	50.92	87.87	61.65	80.71	50.34	87.62
	w/ ReAct	19.73	95.91	31.39	93.21	42.34	88.94	13.74	96.98	26.80	93.76

3.5.2 What about networks trained with different normalization mechanisms?

Going beyond batch normalization (Ioffe and Szegedy, 2015), we further investigate (1) whether networks trained with alternative normalization approaches exhibit similar activation patterns, and (2) whether ReAct is helpful there. To answer this question, we additionally evaluate networks trained with WeightNorm (Salimans and Kingma, 2016) and GroupNorm (Wu and He, 2018)—two other well-known normalization methods. As shown in Figure 3.5, the unit activations also display highly distinctive signature patterns between ID and OOD data, with more chaos on OOD data. In all cases, the networks are trained to adapt to the ID data, resulting in abnormal activation signatures on OOD data in testing. Unlike BatchNorm, there is no easy oracle (*e.g.*, re-estimating the statistics on OOD data) to counteract the ill-fated normalizations.

We apply ReAct on models trained with WeightNorm and GroupNorm, and report results in Table 3.5. Our results suggest that ReAct is consistently effective under various normalization schemes. For example, ReAct reduces the average FPR95 by **23.54%** and **14.7%** respectively. Overall, ReAct has shown broad efficacy and compatibility with different OOD scoring functions (Section 3.3.2).

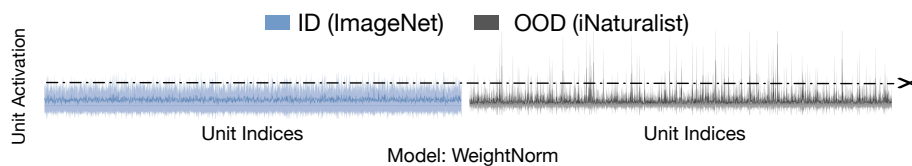


Figure 3.5: The distribution of per-unit activations in the penultimate layer for ID (ImageNet (Deng et al., 2009)) and OOD (iNaturalist (Horn et al., 2018)) on model trained with weight normalization (Salimans and Kingma, 2016).

3.6 Additional Related Work

Neural network activation analysis. Neural networks have been studied at the granularity of the activation of individual layers (Ioffe and Szegedy, 2015; Morcos et al., 2018; Yosinski et al., 2014; Zhou et al., 2018; Sun et al., 2019), or individual networks (Li et al., 2016b). In particular, Li et al. (2016b) studied the similarity of activation space between two independently trained neural networks. Previously, Hein et al. (2019) showed that neural networks with ReLU activation can lead to arbitrary high activation for inputs far away from the training data. We show that using ReAct could efficiently alleviate this undesirable phenomenon. ReAct does not rely on auxiliary data and can be conveniently used for pre-trained models. The idea of rectifying unit activation (Krizhevsky, 2010), which is known as Relu6, was used to facilitate the learning of sparse features. In this chapter, we show that rectifying activation can drastically alleviate the overconfidence issue for OOD data, and as a result, improve OOD detection.

Distributional shifts. Distributional shifts have attracted increasing research interests (Koh et al., 2021). It is important to recognize and differentiate various types of distributional shift problems. Literature in OOD detection is commonly concerned about model reliability and detection of label-space shifts, where the OOD inputs have disjoint labels *w.r.t.* ID data and therefore *should not be predicted by the model*. Meanwhile, some works considered label distribution shift (Saerens et al., 2002; Lipton et al., 2018; Shrikumar and Kundaje, 2019; Azizzadenesheli et al., 2019; Alexandari et al., 2020; Wu et al., 2021a), where the label space is common between ID and OOD but the marginal label distribution changes, as well as covariate shift in the input space (Hendrycks and Dietterich, 2019; Ovadia et al., 2019), where inputs can be corruption-shifted or domain-shifted (Sun et al., 2020b; Hsu et al., 2020). It is important to note that our work focuses on the detection of shifts where the label space \mathcal{Y} is different between ID and OOD data and hence the model should not make any prediction, instead of covariate shift where the model is expected to generalize.

3.7 Summary

This chapter provides a simple activation rectification strategy termed ReAct, which truncates the high activations during test time for OOD detection. We provide both empirical and theoretical insights characterizing and explaining the mechanism by which ReAct improves OOD uncertainty estimation. By rectifying the activations, the outsized contribution of hidden units on OOD output can be attenuated, resulting in a stronger separability from ID data. Extensive experiments show ReAct can significantly improve the performance of OOD detection on both common benchmarks and large-scale image classification models. Our insights have inspired future research to further examine the internal mechanisms of neural networks for OOD detection.

Chapter 4

DICE: Leverage Sparsification for OOD Detection

Publication Statement. This chapter is joint work with Yixuan Li. The paper version of this chapter appeared in ECCV22 (Sun and Li, 2022).

ReAct led to subsequent research in this chapter that delves beyond unit activations, focusing on exploring the impact of weight and unit jointly in out-of-distribution (OOD) detection. In particular, conventional approaches often rely on an OOD score derived from the overparameterized weight space, while largely neglecting the significance of *sparsification*. In this chapter, we reveal important insights that reliance on unimportant weights and units can directly attribute to the brittleness of OOD detection. To mitigate the issue, we propose a sparsification-based OOD detection framework termed **DICE**. Our key idea is to rank weights based on a measure of contribution, and selectively use the most salient weights to derive the output for OOD detection. We provide both empirical and theoretical insights, characterizing and explaining the mechanism by which DICE improves OOD detection. By pruning away noisy signals, DICE provably reduces the output variance for OOD data, resulting in a sharper

output distribution and stronger separability from ID data. We demonstrate the effectiveness of sparsification-based OOD detection on several benchmarks and establish competitive performance.

4.1 Introduction

Deep neural networks deployed in real-world systems often encounter out-of-distribution (OOD) inputs—samples from unknown classes that the network has not been exposed to during training, and therefore should not be predicted by the model in testing. Being able to estimate and mitigate OOD uncertainty is paramount for safety-critical applications such as medical diagnosis (Roy et al., 2021; Wang et al., 2017) and autonomous driving (Filos et al., 2020). For example, an autonomous vehicle may fail to recognize objects on the road that do not appear in its detection model’s training set, potentially leading to a crash. This gives rise to the importance of OOD detection, which allows the learner to express ignorance and take precautions in the presence of OOD data.

The main challenge in OOD detection stems from the fact that modern deep neural networks can easily produce overconfident predictions on OOD inputs, making the separation between in-distribution (ID) and OOD data a non-trivial task. The vulnerability of machine learning to OOD data can be hard-wired in high-capacity models used in practice. In particular, modern deep neural networks can overfit observed patterns in the training data (Zhang et al., 2016), and worse, activate features on unfamiliar inputs (Nguyen et al., 2015). To date, existing OOD detection methods commonly derive OOD scores using overparameterized weights, while largely overlooking the role of *sparsification*. This chapter aims to bridge the gap.

In this chapter, we start by revealing key insights that reliance on unimportant units and weights can directly attribute to the brittleness of OOD

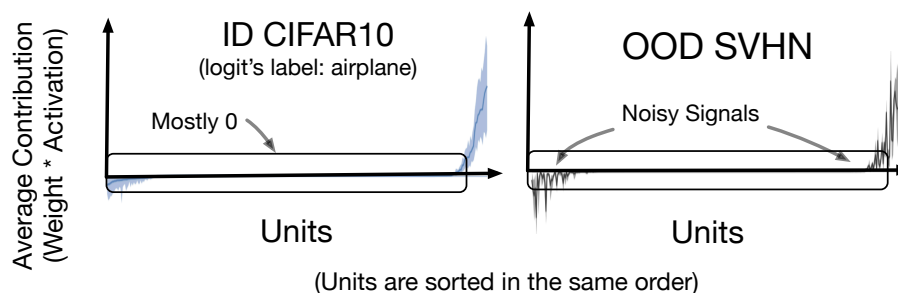


Figure 4.1: Illustration of unit contribution (*i.e.*, $\text{weight} \times \text{activation}$) to the class output. For class c , the output $f_c(\mathbf{x})$ is the summation of unit contribution from the penultimate feature layer of a neural network. *Units are sorted in the same order*, based on the expectation of ID data’s contribution (averaged over many CIFAR-10 samples) on the x -axis. **Shades indicate the variance for each unit.** **Left:** For in-distribution data (CIFAR-10, airplane), only a subset of units contributes to the model output. **Right:** In contrast, out-of-distribution (OOD) data can trigger a non-negligible fraction of units with noisy signals, as indicated by the variances.

detection. Empirically on a network trained with CIFAR-10, we show that an OOD image can activate a non-negligible fraction of units in the penultimate layer (see Figure 4.1, right). Each point on the horizontal axis corresponds to a single unit. The y-axis measures the unit contribution (*i.e.*, $\text{weight} \times \text{activation}$) to the output of class AIRPLANE, with the solid line and the shaded area indicating the mean and variance, respectively. Noticeably, for OOD data (gray), we observe a non-negligible fraction of “noisy” units that display high variances of contribution, which is then aggregated to the model’s output through summation. As a result, such noisy signals can undesirably manifest in model output—increasing the variance of output distribution and reducing the separability from ID data.

The above observation motivates a simple and effective method, *Directed Sparisification (DICE)*, for OOD detection. DICE leverages the observa-

tion that a model’s prediction for an ID class depends on only a subset of important units (and corresponding weights), as evidenced in Figure 4.1 (left). To exploit this, our novel idea is to rank weights based on the measure of contribution, and selectively use the most contributing weights to derive the output for OOD detection. As a result of the weight sparsification, we show that the model’s output becomes more separable between ID and OOD data. Importantly, DICE can be conveniently used by post hoc weight masking on a pre-trained network and therefore can preserve the ID classification accuracy. Orthogonal to existing works on sparsification for accelerating computation, our primary goal is to explore the sparsification approach for improved OOD detection performance.

We provide both empirical and theoretical insights characterizing and explaining the mechanism by which DICE improves OOD detection. We perform extensive evaluations and establish competitive performance on common OOD detection benchmarks, including CIFAR-10, CIFAR-100 (Krizhevsky et al., 2009), and a large-scale ImageNet benchmark (Huang and Li, 2021). Compared to the competitive post hoc method ReAct (Sun et al., 2021a), DICE reduces the FPR95 by up to 12.55%. Moreover, we perform ablation using various sparsification techniques and demonstrate the benefit of directed sparsification for OOD detection. Theoretically, by pruning away noisy signals from unimportant units and weights, DICE *provably reduces the output variance* and results in a sharper output distribution (see Section 4.5). The sharper distributions lead to a stronger separability between ID and OOD data and overall improved OOD detection performance (*c.f.* Figure 4.2). The key results and contributions for this chapter are:

1. (Methodology) We introduce DICE, a simple and effective approach for OOD detection utilizing post hoc weight sparsification. In the realm of OOD detection, DICE holds a significant place as it pioneered the exploration and exemplification of the efficacy of sparsi-

fication.

2. (Experiments) We extensively evaluate DICE on common benchmarks and establish competitive performance among post hoc OOD detection baselines. DICE outperforms the ReAct (Sun et al., 2021a) by reducing the FPR95 by up to 12.55%. We show DICE can effectively improve OOD detection while preserving the classification accuracy of ID data.
3. (Theory and ablations) We provide ablation and theoretical analysis that improves understanding of a sparsification-based method for OOD detection. Our analysis reveals an important variance reduction effect, which probably explains the effectiveness of DICE. The aforementioned insights serve as a catalyst for further investigation into weight sparsification techniques aimed at out-of-distribution (OOD) detection.

4.2 Method

Method overview. The key idea of DICE is to selectively use a subset of important weights to derive the output for OOD detection. By utilizing sparsification, the network prevents adding irrelevant information to the output. We illustrate our idea in Figure 4.2. Without DICE (*left*), the final output is a summation of weighted activations across all units, which can have a high variance for OOD data (colored in gray). In contrast, with DICE (*right*), the variance of output can be significantly reduced, which improves separability from ID data. We proceed with describing our method in detail, and provide the theoretical explanation later in Section 4.5.

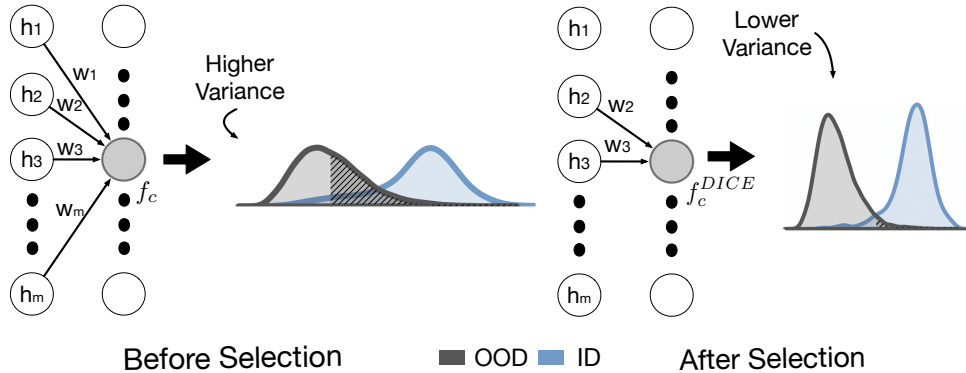


Figure 4.2: Illustration of out-of-distribution detection using *Directed Sparsification* (DICE). We consider a pre-trained neural network, which encodes an input \mathbf{x} to a feature vector $h(\mathbf{x}) \in \mathbb{R}^m$. **Left:** The logit output $f_c(\mathbf{x})$ of class c is a linear combination of activation from *all* units in the preceding layer, weighted by w_i . The full connection results in a high variance for OOD data’s output, as depicted in the gray. **Right:** Our proposed approach leverages a selective subset of weights, which effectively reduces the output variance for OOD data, resulting in a sharper score distribution and stronger separability from ID data. The output distributions are based on CIFAR-10 trained network, with ID class label “frog” and SVHN as OOD.

4.2.1 DICE: Directed Sparsification

We consider a deep neural network parameterized by θ , which encodes an input $\mathbf{x} \in \mathbb{R}^d$ to a feature space with dimension m . We denote by $h(\mathbf{x}) \in \mathbb{R}^m$ the feature vector from the penultimate layer of the network. A weight matrix $\mathbf{W} \in \mathbb{R}^{m \times C}$ connects the feature $h(\mathbf{x})$ to the output $f(\mathbf{x})$.

Contribution matrix. We perform a *directed sparsification* based on a measure of contribution, and preserve the most important weights in \mathbf{W} . To measure the contribution, we define a contribution matrix $\mathbf{V} \in \mathbb{R}^{m \times C}$, where each column $\mathbf{v}_c \in \mathbb{R}^m$ is given by:

$$\mathbf{v}_c = \mathbb{E}_{\mathbf{x} \in \mathcal{D}_{in}} [\mathbf{w}_c \odot h(\mathbf{x})], \quad (4.1)$$

where \odot indicates the element-wise multiplication, and \mathbf{w}_c indicates weight vector for class c . Each element in $\mathbf{v}_c \in \mathbb{R}^m$ intuitively measures the corresponding unit’s average contribution to class c , estimated empirically on in-distribution data \mathcal{D}_{in} . A larger value indicates a higher contribution to the output $f_c(\mathbf{x})$ of class c . The vector \mathbf{v}_c is derived for all classes $c \in \{1, 2, \dots, C\}$, forming the contribution matrix \mathbf{V} . Each element $v_c^i \in \mathbf{V}$ measures the average contribution (weight \times activation) from a unit i to the output class $c \in \{1, 2, \dots, C\}$.

We can now select the top- k weights based on the k -largest elements in \mathbf{V} . In particular, we define a masking matrix $\mathbf{M} \in \mathbb{R}^{m \times C}$, which returns a matrix by setting 1 for entries corresponding to the k largest elements in \mathbf{V} and setting other elements to 0. The model output under *contribution-directed sparsification* is given by

$$f^{\text{DICE}}(\mathbf{x}; \theta) = (\mathbf{M} \odot \mathbf{W})^\top h(\mathbf{x}) + \mathbf{b}, \quad (4.2)$$

where $\mathbf{b} \in \mathbb{R}^C$ is the bias vector. The procedure described above essentially accounts for information from the most relevant units in the penultimate layer. Importantly, the sparsification can be conveniently imposed by *post hoc* weight masking on the final layer of a pre-trained network, without changing any parameterizing of the neural network. Therefore one can improve OOD detection while preserving the ID classification accuracy.

Sparsity parameter p . To align with the convention in literature, we use the sparsity parameter $p = 1 - \frac{k}{m \cdot C}$ in the remainder of this chapter. A higher p indicates a larger fraction of weights dropped. When $p = 0$, the output becomes equivalent to the original output $f(\mathbf{x}; \theta)$ using dense transformation, where $f(\mathbf{x}; \theta) = \mathbf{W}^\top h(\mathbf{x}) + \mathbf{b}$. We provide ablations on the sparsity parameter later in Section 4.4.

4.2.2 OOD Detection with DICE

Our method DICE in Section 4.2 can be flexibly leveraged by the downstream OOD scoring function:

$$\mathcal{S}_\lambda(\mathbf{x}) = \begin{cases} \text{in} & S_\theta(\mathbf{x}) \geq \lambda \\ \text{out} & S_\theta(\mathbf{x}) < \lambda \end{cases}, \quad (4.3)$$

where a thresholding mechanism is exercised to distinguish between ID and OOD during test time. The threshold λ is typically chosen so that a high fraction of ID data (*e.g.*, 95%) is correctly classified. Following recent work by Liu *et. al* (Liu et al., 2020), we derive an energy score using the logit output $f^{\text{DICE}}(\mathbf{x}; \theta)$ with contribution-directed sparsification. The function maps the logit outputs $f^{\text{DICE}}(\mathbf{x}; \theta)$ to a scalar $E_\theta(\mathbf{x}) \in \mathbb{R}$, which is relatively lower for ID data:

$$S_\theta(\mathbf{x}) = -E_\theta(\mathbf{x}) = \log \sum_{c=1}^C \exp(f_c^{\text{DICE}}(\mathbf{x}; \theta)). \quad (4.4)$$

The energy score can be viewed as the log of the denominator in softmax function:

$$p(y|\mathbf{x}) = \frac{p(\mathbf{x}, y)}{p(\mathbf{x})} = \frac{\exp(f_y(\mathbf{x}; \theta))}{\sum_{c=1}^C \exp(f_c(\mathbf{x}; \theta))}, \quad (4.5)$$

and enjoys better theoretical interpretation than using posterior probability $p(y|\mathbf{x})$. Later in Section 4.5, we formally characterize and explain why DICE improves the separability of the scores between ID and OOD data.

4.3 Experiments

In this section, we evaluate our method on a suite of OOD detection tasks. We begin with the CIFAR benchmarks that are routinely used in literature (Section 4.3.1). In Section 4.3.2, we continue with a large-scale OOD de-

tection task based on ImageNet.

4.3.1 Evaluation on CIFAR Benchmarks

Experimental details. We use CIFAR-10 (Krizhevsky et al., 2009), and CIFAR-100 (Krizhevsky et al., 2009) datasets as in-distribution data. We use the standard split with 50,000 training images and 10,000 test images. We evaluate the model on six common OOD benchmark datasets: Textures (Cimpoi et al., 2014), SVHN (Netzer et al., 2011), Places365 (Zhou et al., 2017), LSUN-Crop (Yu et al., 2015), LSUN-Resize (Yu et al., 2015), and iSUN (Xu et al., 2015). We use DenseNet-101 architecture (Huang et al., 2017) and train on in-distribution datasets. The feature dimension of the penultimate layer is 342. For both CIFAR-10 and CIFAR-100, the model is trained for 100 epochs with batch size 64, weight decay 0.0001 and momentum 0.9. The start learning rate is 0.1 and decays by a factor of 10 at epochs 50, 75, and 90. We use the validation strategy in Appendix A.2.2 to select p .

DICE vs. competitive baselines. We show the results in Table 4.1, where DICE outperforms competitive baselines. In particular, we compare with Maximum Softmax Probability (Hendrycks and Gimpel, 2017), ODIN (Liang et al., 2018), Mahalanobis distance (Lee et al., 2018), Generalized ODIN (Hsu et al., 2020), Energy score (Liu et al., 2020), and ReAct (Sun et al., 2021a) (Chapter 3). For a fair comparison, all the methods derive the OOD score post hoc from the same pre-trained model, except for G-ODIN which requires model re-training.

On CIFAR-100, we show that DICE reduces the average FPR95 by **18.73%** compared to the vanilla energy score (Liu et al., 2020) without sparsification. Moreover, our method also outperforms ReAct (Sun et al., 2021a) (Chapter 3) by 12.55%. While ReAct only considers activation space, DICE examines *both the weights and activation* values together—the mul-

Table 4.1: Comparison with competitive *post hoc* out-of-distribution detection method on CIFAR benchmarks. All values are percentages and are averaged over 6 OOD test datasets. The full results for each evaluation dataset are provided in Appendix A.2.4. We report standard deviations estimated across 5 independent runs. [§] indicates an exception, where model retraining using a different loss function is required.

Method	CIFAR-10		CIFAR-100	
	FPR95 ↓	AUROC ↑	FPR95 ↓	AUROC ↑
MSP (Hendrycks and Gimpel, 2017)	48.73	92.46	80.13	74.36
ODIN (Liang et al., 2018)	24.57	93.71	58.14	84.49
GODIN [§] (Hsu et al., 2020)	34.25	90.61	52.87	85.24
Mahalanobis (Lee et al., 2018)	31.42	89.15	55.37	82.73
Energy (Liu et al., 2020)	26.55	94.57	68.45	81.19
ReAct (Sun et al., 2021a)	26.45	94.95	62.27	84.47
DICE	20.83\pm1.58	95.24\pm0.24	49.72\pm1.69	87.23\pm0.73

tiplication of which directly determines the network’s logit output. Overall our method is more generally applicable, and can be implemented through a simple post hoc weight masking.

ID classification accuracy. Given the *post hoc* nature of DICE, once the input image is marked as ID, one can always use the original fc layer, which is guaranteed to give identical classification accuracy. This incurs minimal overhead and results in optimal performance for both classification and OOD detection. We also measure the classification accuracy under different sparsification parameter p . Due to the space limit, the full results are available in Table A.3 in Appendix.

4.3.2 Evaluation on Large-scale ImageNet Task

Dataset. We then evaluate DICE on a large-scale ImageNet classification model. Following MOS (Huang and Li, 2021), we use four OOD test datasets from (subsets of) Places365 (Zhou et al., 2017), Textures (Cim-

Table 4.2: **Main results.** Comparison with competitive *post hoc* out-of-distribution detection methods. All methods are based on a discriminative model trained on ImageNet. \uparrow indicates larger values are better and \downarrow indicates smaller values are better. All values are percentages. **Bold** numbers are superior results.

Methods	OOD Datasets								Average	
	iNaturalist		SUN		Places		Textures		FPR95	AUROC
	\downarrow	\uparrow	\downarrow	\uparrow	\downarrow	\uparrow	\downarrow	\uparrow	\downarrow	\uparrow
MSP	54.99	87.74	70.83	80.86	73.99	79.76	68.00	79.61	66.95	81.99
ODIN	47.66	89.66	60.15	84.59	67.89	81.78	50.23	85.62	56.48	85.41
GODIN	61.91	85.40	60.83	85.60	63.70	83.81	77.85	73.27	66.07	82.02
Mahalanobis	97.00	52.65	98.50	42.41	98.40	41.79	55.80	85.01	87.43	55.47
Energy	55.72	89.95	59.26	85.89	64.92	82.86	53.72	85.99	58.41	86.17
ReAct	20.38	96.22	24.20	94.20	33.85	91.58	47.30	89.80	31.43	92.95
DICE	25.63	94.49	35.15	90.83	46.49	87.48	31.72	90.30	34.75	90.77
DICE + ReAct	18.64	96.24	25.45	93.94	36.86	90.67	28.07	92.74	27.25	93.40

poi et al., 2014), iNaturalist (Horn et al., 2018), and SUN (Xiao et al., 2010) with non-overlapping categories *w.r.t.* ImageNet. The evaluations span a diverse range of domains including fine-grained images, scene images, and textural images. OOD detection for the ImageNet model is more challenging due to both a larger feature space ($m = 2,048$) as well as a larger label space ($C = 1,000$). In particular, the large-scale evaluation can be relevant to real-world applications, where the deployed models often operate on images that have high resolution and contain many class labels. Moreover, as the number of feature dimensions increases, noisy signals may increase accordingly, which can make OOD detection more challenging.

Experimental details. We use a pre-trained ResNet-50 model (He et al., 2016b) for ImageNet-1k provided by Pytorch. At test time, all images are resized to 224×224 . We use the entire training dataset to estimate the contribution matrix and masking matrix M . We use the validation strategy in Appendix A.2.2 to select p .

Comparison with baselines. In Table 4.2, we compare DICE with com-

petitive post hoc OOD detection methods. We report performance for each OOD test dataset, as well as the average of the four. We first contrast DICE with energy score (Liu et al., 2020), which allows us to see the direct benefit of using sparsification under the same scoring function. DICE reduces the FPR95 drastically from 58.41% to 34.75%, a **23.66%** improvement using sparsification. Second, we contrast with ReAct, which demonstrates strong performance on this challenging task using activation truncation. With the truncated activation proposed in ReAct, we show that DICE can further reduce the FPR95 by 5.78% with weight sparsification. Since the comparison is conducted on the same scoring function and feature activation, the performance improvement from ReAct to DICE+ReAct precisely highlights the benefit of using weight sparsification as opposed to the full weights. Lastly, Mahalanobis displays limiting performance on ImageNet, while being computationally expensive due to estimating the inverse of the covariance matrix. In contrast, DICE is easy to use in practice, and can be implemented through simple post hoc weight masking.

4.4 Discussion and Ablations

Ablation on sparsity parameter p . We now characterize the effect of the sparsity parameter p . In Figure 4.3, we summarize the OOD detection performance for DenseNet trained on CIFAR-100, where we vary $p = \{0.1, 0.3, 0.5, 0.7, 0.9, 0.99\}$. Interestingly, we observe the performance improves with mild sparsity parameter p . A significant improvement can be observed from $p = 0$ (no sparsity) to $p = 0.1$. As we will theoretically later in Section 4.5, this is because the leftmost part of units being pruned has larger variances for OOD data (gray shade). Units in the middle part have small variances and contributions for both ID and OOD, therefore leading to similar performance as p increases mildly. This ablation con-

firmly that over-parameterization does compromise the OOD detection ability, and DICE can effectively alleviate the problem. In the extreme case when p is too large (*e.g.*, $p = 0.99$), the OOD performance starts to degrade as expected.

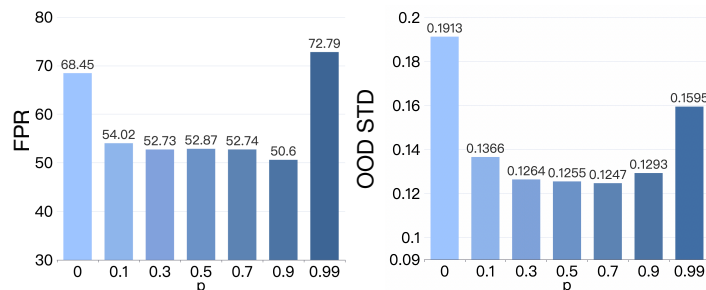


Figure 4.3: Effect of varying sparsity parameter p during inference time. Model is trained on CIFAR-100 using DenseNet101 (Huang et al., 2017).

Effect of variance reduction for output distribution. Figure 4.2 shows that DICE has an interesting variance reduction effect on the output distribution for OOD data, and at the same time preserves the information for the ID data (CIFAR-10, class “frog”). The output distribution without any sparsity ($p = 0$) appears to have a larger variance, resulting in less separability from ID data (see left of Figure 4.2). In contrast, sparsification with DICE results in a sharper distribution, which benefits OOD detection. In Figure 4.3, we also measure the standard deviation of energy score for OOD data (normalized by the mean of ID data’s OOD scores in each setting). By way of sparsification, DICE can reduce the output variance. In Section 4.5, we formally characterize this and provide a theoretical explanation.

Ablation on pruning methods. In this ablation, we evaluate OOD detection performance under the most common *post hoc* sparsification methods. Here we primarily consider post hoc sparsification strategy which operates conveniently on a *pre-trained* network, instead of training with sparse regularization or architecture modification. The property is es-

Table 4.3: **Ablation results.** Effect of different *post hoc* sparsification methods for OOD detection with ImageNet as ID dataset. All sparsification methods are based on the same OOD scoring function (Liu et al., 2020), with sparsity parameter $p = 0.7$. All values are percentages and are averaged over multiple OOD test datasets.

Method	FPR95 ↓	AUROC ↑
Weight-Dropout	76.28	76.55
Unit-Dropout	83.91	64.98
Weight-Pruning	52.81	87.08
Unit-Pruning	90.80	49.15
DICE (Ours)	34.75	90.77

pecially desirable for the adoption of OOD detection methods in real-world production environments, where the overhead cost of retraining can be sometimes prohibitive. Orthogonal to existing works on sparsification, our primary goal is to explore the role of sparsification for improved OOD detection performance, rather than establishing a generic sparsification algorithm. We consider the most common strategies, covering both unit-based and weight-based sparsification methods: (1) unit dropout (Srivastava et al., 2014) which randomly drops a fraction of units, (2) unit pruning (Li et al., 2017) which drops units with the smallest l_2 norm of the corresponding weight vectors, (3) weight dropout (Wan et al., 2013) which randomly drops weights in the fully connected layer, and (4) weight pruning (Han et al., 2015) drops weights with the smallest entries under the l_1 norm. For consistency, we use the same OOD scoring function and the same sparsity parameter for all.

Our ablation reveals several important insights shown in Table 4.3. First, in contrasting weight dropout vs. DICE, a salient performance gap of 41.53% (FPR95) is observed under the same sparsity. This suggests the importance of dropping weights *directedly* rather than *randomly*. Second, DICE outperforms a popular l_1 -norm-based pruning method (Han et al.,

Table 4.4: Ablation on different strategies of choosing a subset of units. Values are FPR95 (averaged over multiple test datasets).

Method	CIFAR-10↓	CIFAR-100 ↓
Bottom- k	91.87	99.70
(Top+Bottom)- k	24.25	59.93
Random- k	62.12	77.48
Top- k (DICE)	20.83 \pm 1.58	49.72 \pm 1.69

2015) by up to 18.06% (FPR95). While it prunes weights with low magnitude, negative weights with large l_1 -norm can be kept. The negative weights can undesirably corrupt the output with noisy signals (as shown in Figure 4.1). The performance gain of DICE over (Han et al., 2015) attributes to our contribution-directed sparsification, which is better suited for OOD detection.

Ablation on unit selection. We have shown that choosing a subset of weights (with $top-k$ unit contribution) significantly improves the OOD detection performance. In this ablation, we also analyze those “lower contribution units” for OOD detection. Specifically, we consider: (1) *Bottom- k* which only includes k unit contribution with least contribution values, (2) *top+bottom- k* which includes k unit contribution with largest and smallest contribution values, (3) *random- k* which randomly includes k unit contribution and (4) *top- k* which is equivalent to DICE method. In Table 4.4, we show that DICE outperforms these variants.

4.5 Why does DICE improve OOD detection?

In this section, we formally explain the mechanism by which reliance on irrelevant units hurts OOD detection and how DICE effectively mitigates the issue. Our analysis highlights that DICE reduces the output variance for both ID and OOD data. Below we provide details.

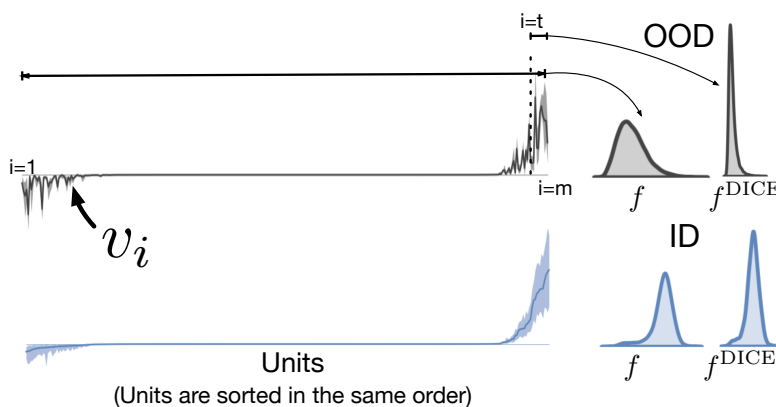


Figure 4.4: Units in the penultimate layer are sorted based on the average contribution to a CIFAR-10 class (“airplane”). OOD data (SVHN) can trigger a non-negligible fraction of units with noisy signals on the CIFAR-10 trained model.

Setup. For a class c , we consider the unit contribution vector \mathbf{v} , the element-wise multiplication between the feature vector $h(\mathbf{x})$ and corresponding weight vector \mathbf{w} . We contrast the two outputs with and without sparsity:

$$f_c = \sum_{i=1}^m v_i \quad (\text{w.o sparsity}),$$

$$f_c^{\text{DICE}} = \sum_{i \in \text{top units}} v_i \quad (\text{w. sparsity}),$$

where f_c is the output using the summation of all units’ contribution, and f_c^{DICE} takes the input from the top units (ranked based on the average contribution on ID data, see bottom of Figure 4.4).

DICE reduces the output variance. We consider the unit contribution vector for OOD data $\mathbf{v} \in \mathbb{R}^m$, where each element is a *random variable* v_i with mean $\mathbb{E}[v_i] = \mu_i$ and variance $\text{Var}[v_i] = \sigma_i^2$. For simplicity, we assume each component is independent, but our theory can be extended to correlated variables (see Remark 1). Importantly, indices in \mathbf{v} are sorted based on *the same order* of unit contribution on ID data. By using units

on the rightmost side, we now show the key result that DICE reduces the output variance.

Proposition 4.1. *Let v_i and v_j be two independent random variables. Denote the summation $r = v_i + v_j$, we have $\mathbb{E}[r] = \mathbb{E}[v_i] + \mathbb{E}[v_j]$ and $\text{Var}[r] = \text{Var}[v_i] + \text{Var}[v_j]$.*

Lemma 4.2. *When taking the top $m - t$ units, the output variable f_c^{DICE} under sparsification has reduced variance:*

$$\text{Var}[f_c] - \text{Var}[f_c^{DICE}] = \sum_{i=1}^t \sigma_i^2$$

Proof. The proof directly follows Proposition 1.

Remark 1 (Extension to correlated variables). We can show in a more general case with correlated variables, the variance reduction is:

$$\sum_{i=1}^t \sigma_i^2 + 2 \sum_{1 \leq i < j \leq m} \text{Cov}(v_i, v_j) - 2 \sum_{t < i < j \leq m} \text{Cov}(v_i, v_j),$$

where $\text{Cov}(\cdot, \cdot)$ is the covariance. Our analysis shows that the covariance matrix primarily consists of 0, which indicates the independence of variables. Moreover, the summation of non-zero entries in the full matrix (i.e., the second term) is greater than that of the submatrix with top units (i.e., the third term), resulting in a larger variance reduction than in Lemma 4.2. See complete proof in Appendix A.2.1.

Remark 2. Energy score is compatible with DICE since it directly operates in the logit space. Our theoretical analysis above shows that DICE reduces the variance of each logit $f_c(\mathbf{x})$. This means that for detection scores such as energy score, the gap between OOD and ID score will be enlarged after applying DICE, which makes thresholding more capable of separating OOD and ID inputs and benefit OOD detection.

Table 4.5: Difference between the mean of ID’s output and OOD’s output. Here we use CIFAR-100 as ID data and $\Delta = \mathbb{E}_{\text{in}}[\max_c f_c^{\text{DICE}}] - \mathbb{E}_{\text{out}}[\max_c f_c^{\text{DICE}}]$ is averaged over six common OOD benchmark datasets described in Section 4.3.

Sparsity	$p = 0.9$	$p = 0.7$	$p = 0.5$	$p = 0.3$	$p = 0.1$	$p = 0$
Δ	7.92	7.28	7.99	8.04	7.36	6.67

Remark 3 (Mean of output). Beyond variance, we further show in Table 4.5 the effect of sparsity on the mean of output: $\mathbb{E}_{\text{in}}[\max_c f_c^{\text{DICE}}]$ and $\mathbb{E}_{\text{out}}[\max_c f_c^{\text{DICE}}]$. The gap between the two directly translates into the OOD score separability. We show that DICE maintains similar (or even enlarges) differences in terms of mean as sparsity p increases. Therefore, DICE overall benefits OOD detection due to both *reduced output variances* and *increased differences of mean*—the combination of both effects leads to stronger separability between ID and OOD.

Remark 4 (Variance reduction on ID data). Note that we can also show the effect of variance reduction for ID data in a similar way. Importantly, DICE effectively preserves the most important information akin to the ID data, while reducing noisy signals that are harmful to OOD detection. Overall the variance reduction effect on both ID and OOD data leads to stronger separability.

4.6 Additional Related Work

Pruning and sparsification. A great number of effort has been put into improving *post hoc* pruning and training time regularization for deep neural networks (Ba and Frey, 2013; Babaeizadeh et al., 2016; Gomez et al., 2019; Han et al., 2016, 2015; Li et al., 2017; Louizos et al., 2018). Many works obtain a sparse model by training with sparse regularization (Ba and Frey, 2013; Babaeizadeh et al., 2016; Han et al., 2016; Louizos et al., 2018; Sun et al., 2019) or architecture modification (Gomez et al., 2019;

Li et al., 2017), while our work primarily considers *post hoc* sparsification strategy which operates conveniently on a pre-trained network. On this line, two popular Bernoulli dropout techniques include unit dropout and weight dropout (Srivastava et al., 2014). *Post hoc* pruning strategies truncate weights with low magnitude (Han et al., 2015), or drop units with low weight norms (Li et al., 2017). In (Wong et al., 2021), they use a sparse linear layer to help identify spurious correlations and explain misclassifications. Orthogonal to existing works, our goal is to improve the OOD detection performance rather than accelerate computation and network debugging. In this chapter, we first demonstrate that sparsification can be useful for OOD detection. An in-depth discussion and comparison of these methods are presented in Section 4.4.

4.7 Summary

This chapter provides a simple sparsification strategy termed DICE, which ranks weights based on a contribution measure and then uses the most significant weights to derive the output for OOD detection. We provide both empirical and theoretical insights characterizing and explaining the mechanism by which DICE improves OOD detection. By exploiting the most important weights, DICE provably reduces the output variance for OOD data, resulting in a sharper output distribution and stronger separability from ID data. Extensive experiments show DICE can significantly improve the performance of OOD detection for over-parameterized networks. We hope our research can raise more attention to the importance of weight sparsification for OOD detection.

Chapter 5

OOD Detection with Deep Nearest Neighbors

Publication Statement. This chapter is joint work with Yifei Ming, Xiaojin Zhu, and Yixuan Li. The paper version of this chapter appeared in ICML22 ([Sun et al., 2022](#)).

In this chapter, we delve into an alternate pathway for Out-of-Distribution (OOD) detection, focusing on the utilization of distance-based methodologies. These techniques have shown significant potential, identifying test samples as OOD if their distance from in-distribution (ID) data considerably exceeds a set threshold. However, it is essential to note that previous approaches tend to carry a potent assumption about the distribution of the underlying feature space, an assumption that may not consistently hold true. Therefore, we examine the efficacy of a non-parametric approach using nearest-neighbor distance for OOD detection - an aspect that has hitherto received scant attention in the existing literature. Unlike prior works, our method does not impose any distributional assumption, hence providing stronger flexibility and generality. We demonstrate the effectiveness of nearest-neighbor-based OOD detection on several bench-

marks and establish superior performance. Under the same model trained on ImageNet-1k, our method substantially reduces the false positive rate (FPR95) by 24.77% compared to a strong baseline SSD+, which uses a parametric approach Mahalanobis distance in detection.

5.1 Introduction

Modern machine learning models deployed in the open world often struggle with out-of-distribution (OOD) inputs—samples from a different distribution that the network has not been exposed to during training, and therefore should not be predicted at test time. A reliable classifier should not only accurately classify known in-distribution (ID) samples, but also identify as “unknown” any OOD input. This gives rise to the importance of OOD detection, which determines whether an input is ID or OOD and enables the model to take precautions.

A rich line of OOD detection algorithms has been developed recently, among which distance-based methods demonstrated promise (Lee et al., 2018; Tack et al., 2020; Schwag et al., 2021). Distance-based methods leverage feature embeddings extracted from a model, and operate under the assumption that the test OOD samples are relatively far away from the ID data. For example, Lee et al. (2018) modeled the feature embedding space as a mixture of multivariate Gaussian distributions, and used the maximum Mahalanobis distance (Mahalanobis, 1936) to all class centroids for OOD detection. However, all these approaches make a strong distributional assumption of the underlying feature space being class-conditional Gaussian. As we verify, the learned embeddings can fail the Henze-Zirkler multivariate normality test (Henze and Zirkler, 1990). This limitation leads to the open question:

Can we leverage the non-parametric nearest neighbor approach for OOD detection?

Unlike prior works, the non-parametric approach does not impose any distributional assumption about the underlying feature space, hence providing stronger *flexibility and generality*. Despite its simplicity, the nearest neighbor approach has received scant attention. Looking at the literature on OOD detection in the past several years, there has not been any work that demonstrated the efficacy of a non-parametric nearest neighbor approach for this problem. This suggests that making the seemingly simple idea work is non-trivial. Indeed, we found that simply using the nearest neighbor distance derived from the feature embedding of a standard classification model is not performant.

In this chapter, we challenge the status quo by presenting the first study exploring and demonstrating the efficacy of the non-parametric nearest-neighbor distance for OOD detection. To detect OOD samples, we compute the k -th nearest neighbor (KNN) distance between the embedding of test input and the embeddings of the training set and use a threshold-based criterion to determine if the input is OOD or not. In a nutshell, we perform non-parametric level set estimation, partitioning the data into two sets (ID vs. OOD) based on the deep k -nearest neighbor distance. KNN offers compelling advantages of being: (1) **distributional assumption free**, (2) **OOD-agnostic** (*i.e.*, the distance threshold is estimated on the ID data only, and does not rely on information of unknown data), (3) **easy-to-use** (*i.e.*, no need to calculate the inverse of the covariance matrix which can be numerically unstable), and (4) **model-agnostic** (*i.e.*, the testing procedure is applicable to different model architectures and training losses).

Our exploration leads to both empirical effectiveness (Section 5.3 & 5.4) and theoretical justification (Section 5.5). By studying the role of representation space, we show that a compact and normalized feature space is the key to the success of the nearest neighbor approach for OOD detection. Extensive experiments show that KNN outperforms the paramet-

ric approach, and scales well to the large-scale dataset. Computationally, modern implementations of approximate nearest neighbor search allow us to do this in milliseconds even when the database contains billions of images (Johnson et al., 2019). On a challenging ImageNet OOD detection benchmark (Huang and Li, 2021), our KNN-based approach achieves superior performance under a similar inference speed as the baseline methods. The overall simplicity and effectiveness of KNN make it appealing for real-world applications. We summarize our contributions below:

1. We present the first study exploring and demonstrating the efficacy of non-parametric density estimation with nearest neighbors for OOD detection—a simple, flexible yet overlooked approach in literature. It draws attention to the strong promise of the non-parametric approach, which obviates data assumption on the feature space.
2. We demonstrate the superior performance of the KNN-based method on several OOD detection benchmarks, different model architectures (including CNNs and ViTs), and different training losses. Under the same model trained on ImageNet-1k, our method substantially reduces the false positive rate (FPR95) by **24.77%** compared to a strong baseline SSD+ (Sehwag et al., 2021), which uses a parametric approach (*i.e.*, Mahalanobis distance (Lee et al., 2018)) for detection.
3. We offer new insights on the key components to make KNN effective in practice, including feature normalization and a compact representation space. Our findings are supported by extensive ablations and experiments. These insights are valuable to the community in carrying out future research.
4. We provide theoretical analysis, showing that KNN-based OOD detection can reject inputs equivalent to the Bayes optimal estimator.

By modeling the nearest neighbor distance in the feature space, our theory (1) directly connects to our method which also operates in the feature space, and (2) complements our experiments by considering the universality of OOD data.

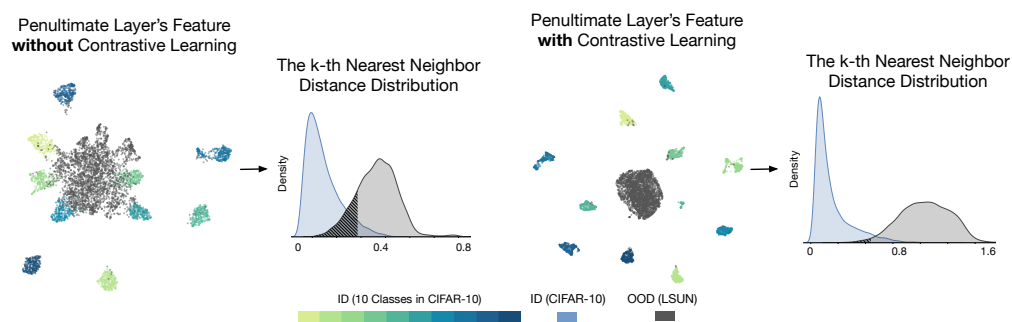


Figure 5.1: Illustration of our framework using nearest neighbors for OOD detection. KNN performs non-parametric level set estimation, partitioning the data into two sets (ID vs. OOD) based on the k -th nearest neighbor distance. The distances are estimated from the penultimate feature embeddings, visualized via UMAP (McInnes et al., 2018). Models are trained on ResNet-18 (He et al., 2016b) using cross-entropy loss (left) v.s. contrastive loss (right). The in-distribution data is CIFAR-10 (colored in non-gray colors) and OOD data is LSUN (colored in gray). The shaded grey area in the density distribution plot indicates OOD samples that are misidentified as ID data.

5.2 Deep Nearest Neighbor for OOD detection

In this section, we describe our approach using the deep k -Nearest Neighbor (KNN) for OOD detection. We illustrate our approach in Figure 5.1, which at a high level, can be categorized as a distance-based method. Distance-based methods leverage feature embeddings extracted from a model and operate under the assumption that the test OOD samples are relatively far away from the ID data. Previous distance-based OOD detection methods employed parametric density estimation and modeled

the feature embedding space as a mixture of multivariate Gaussian distributions (Lee et al., 2018). However, such an approach makes a strong distributional assumption of the learned feature space, which may not necessarily hold¹.

In this chapter, we instead explore the efficacy of *non-parametric density estimation using nearest neighbors* for OOD detection. Despite the simplicity, KNN approach is not systematically explored or compared in most current OOD detection papers. Specifically, we compute the k -th nearest neighbor distance between the embedding of each test image and the training set, and use a simple threshold-based criterion to determine if an input is OOD or not. Importantly, we use the normalized penultimate feature $\mathbf{z} = \phi(\mathbf{x})/\|\phi(\mathbf{x})\|_2$ for OOD detection, where $\phi : \mathcal{X} \mapsto \mathbb{R}^m$ is a feature encoder. Denote the embedding set of training data as $\mathcal{Z}_n = (\mathbf{z}_1, \mathbf{z}_2, \dots, \mathbf{z}_n)$. During testing, we derive the normalized feature vector \mathbf{z}^* for a test sample \mathbf{x}^* , and calculate the Euclidean distances $\|\mathbf{z}_i - \mathbf{z}^*\|_2$ with respect to embedding vectors $\mathbf{z}_i \in \mathcal{Z}_n$. We reorder \mathcal{Z}_n according to the increasing distance $\|\mathbf{z}_i - \mathbf{z}^*\|_2$. Denote the reordered data sequence as $\mathcal{Z}'_n = (\mathbf{z}_{(1)}, \mathbf{z}_{(2)}, \dots, \mathbf{z}_{(n)})$. The decision function for OOD detection is given by:

$$\mathcal{S}_\lambda(\mathbf{z}^*; k) = \mathbf{1}\{-r_k(\mathbf{z}^*) \geq \lambda\},$$

where $r_k(\mathbf{z}^*) = \|\mathbf{z}^* - \mathbf{z}_{(k)}\|_2$ is the distance to the k -th nearest neighbor (k -NN) and $\mathbf{1}\{\cdot\}$ is the indicator function. The threshold λ is typically chosen so that a high fraction of ID data (e.g., 95%) is correctly classified. The threshold does not depend on OOD data.

We summarize our approach in Algorithm 1. Noticeably, KNN-based OOD detection offers several compelling advantages:

1. **Distributional assumption free:** Non-parametric nearest neighbor

¹We verified this by performing the Henze-Zirkler multivariate normality test (Henze and Zirkler, 1990) on the embeddings. The testing results show that the feature vectors for each class are not normally distributed at the significance level of 0.05.

Algorithm 1 OOD Detection with Deep Nearest Neighbors

Input: Training dataset \mathcal{D}_{in} , pre-trained neural network encoder ϕ , test sample \mathbf{x}^* , threshold λ

For \mathbf{x}_i in the training data \mathcal{D}_{in} , collect feature vectors $\mathcal{Z}_n = (\mathbf{z}_1, \mathbf{z}_2, \dots, \mathbf{z}_n)$

Testing Stage:

Given a test sample, we calculate feature vector $\mathbf{z}^* = \phi(\mathbf{x}^*) / \|\phi(\mathbf{x}^*)\|_2$

Reorder \mathcal{Z}_n according to the increasing value of $\|\mathbf{z}_i - \mathbf{z}^*\|_2$ as $\mathcal{Z}'_n = (\mathbf{z}_{(1)}, \mathbf{z}_{(2)}, \dots, \mathbf{z}_{(n)})$

Output: OOD detection decision $\mathbf{1}\{-\|\mathbf{z}^* - \mathbf{z}_{(k)}\|_2 \geq \lambda\}$

approach does not impose distributional assumptions about the underlying feature space. KNN therefore provides stronger flexibility and generality, and is applicable even when the feature space does not conform to the mixture of Gaussians.

2. **OOD-agnostic:** The testing procedure does not rely on the information of unknown data. The distance threshold is estimated on the ID data only.
3. **Easy-to-use:** Modern implementations of approximate nearest neighbor search allow us to do this in milliseconds even when the database contains billions of images (Johnson et al., 2019). In contrast, Mahalanobis distance requires calculating the inverse of the covariance matrix, which can be numerically unstable.
4. **Model-agnostic:** The testing procedure applies to a variety of model architectures, including CNNs and more recent Transformer-based ViT models (Dosovitskiy et al., 2021). Moreover, we will show that KNN is agnostic to the training procedure as well, and is compatible with models trained under different loss functions (e.g., cross-entropy loss and contrastive loss).

We proceed to show the efficacy of the KNN-based OOD detection approach in Section 5.3.

5.3 Experiments

The goal of our experimental evaluation is to answer the following questions: (1) How does KNN fare against the parametric counterpart such as Mahalanobis distance for OOD detection? (2) Can KNN scale to a more challenging task when the training data is large-scale (*e.g.*, ImageNet)? (3) Is KNN-based OOD detection effective under different model architectures and training objectives? (4) How do various design choices affect the performance?

Evaluation metrics. We report the following metrics: (1) the false positive rate (FPR95) of OOD samples when the true positive rate of ID samples is at 95%, (2) the area under the receiver operating characteristic curve (AUROC), (3) ID classification accuracy (ID ACC), and (4) per-image inference time (in milliseconds, averaged across test images).

Training losses. In our experiments, we aim to show that KNN-based OOD detection is agnostic to the training procedure, and is compatible with models trained under different losses. We consider two types of loss functions, with and without contrastive learning respectively. We employ (1) cross-entropy loss which is the most commonly used training objective in classification, and (2) supervised contrastive learning (Sup-Con) (Khosla et al., 2020)—the latest development for representation learning, which leverages the label information by aligning samples belonging to the same class in the embedding space.

Remark on the implementation. All of the experiments are based on PyTorch (Paszke et al., 2019). Code is made publicly available online. We use Faiss (Johnson et al., 2019), a library for efficient nearest neighbor search. Specifically, we use `faiss.IndexFlatL2` as the indexing method with Euclidean distance. In practice, we pre-compute the embeddings for all images and store them in a key-value map to make KNN search efficient. The embedding vectors for ID data only need to be extracted

once after the training is completed.

5.3.1 Evaluation on CIFAR Benchmarks

Table 5.1: **Results on CIFAR-10.** Comparison with competitive OOD detection methods. All methods are based on a discriminative model trained on ID data only, without using outlier data. \uparrow indicates larger values are better and vice versa.

Method	SVHN		LSUN		OOD Dataset				Places365		Average		ID ACC
	FPR \downarrow	AUROC \uparrow	FPR \downarrow	AUROC \uparrow	iSUN		Texture		FPR \downarrow	AUROC \uparrow	FPR \downarrow	AUROC \uparrow	
Without Contrastive Learning													
MSP	59.66	91.25	45.21	93.80	54.57	92.12	66.45	88.50	62.46	88.64	57.67	90.86	94.21
ODIN	53.78	91.30	10.93	97.93	28.44	95.51	55.59	89.47	43.40	90.98	38.43	93.04	94.21
Energy	54.41	91.22	10.19	98.05	27.52	95.59	55.23	89.37	42.77	91.02	38.02	93.05	94.21
GODIN	18.72	96.10	11.52	97.12	30.02	94.02	33.58	92.20	55.25	85.50	29.82	92.97	93.64
Maha.	9.24	97.80	67.73	73.61	6.02	98.63	23.21	92.91	83.50	69.56	37.94	86.50	94.21
KNN (Ours)	27.97	95.48	18.50	96.84	24.68	95.52	26.74	94.96	47.84	89.93	29.15	94.55	94.21
With Contrastive Learning													
CSI	37.38	94.69	5.88	98.86	10.36	98.01	28.85	94.87	38.31	93.04	24.16	95.89	94.38
SSD+	1.51	99.68	6.09	98.48	33.60	95.16	12.98	97.70	28.41	94.72	16.52	97.15	95.07
KNN+	2.42	99.52	1.78	99.48	20.06	96.74	8.09	98.56	23.02	95.36	11.07	97.93	95.07

Datasets. We begin with the CIFAR benchmarks that are routinely used in literature. We use the standard split with 50,000 training images and 10,000 test images. We evaluate the methods on common OOD datasets: Textures (Cimpoi et al., 2014), SVHN (Netzer et al., 2011), Places365 (Zhou et al., 2017), LSUN-C (Yu et al., 2015), and iSUN (Xu et al., 2015). All images are of size 32×32 .

Experiment details. We use ResNet-18 as the backbone for CIFAR-10. Following the original settings in Khosla et al. (2020), models with Sup-Con loss are trained for 500 epochs, with the batch size of 1024. The temperature τ is 0.1. The dimension of the penultimate feature where we perform the nearest neighbor search is 512. The dimension of the projection head is 128. We use the cosine annealing learning rate (Loshchilov and Hutter, 2017) starting at 0.5. We use $k = 50$ for CIFAR-10 and $k = 200$ for CIFAR-100, which is selected from $k = \{1, 10, 20, 50, 100, 200, 500, 1000, 3000, 5000\}$

using the validation method in (Hendrycks et al., 2018). We train the models using stochastic gradient descent with momentum 0.9, and weight decay 10^{-4} . The model without contrastive learning is trained for 100 epochs. The start learning rate is 0.1 and decays by a factor of 10 at epochs 50, 75, and 90 respectively.

Nearest neighbor distance achieves superior performance. We present results in Table 5.1, where non-parametric KNN approach shows favorable performance. Our comparison covers an extensive collection of competitive methods in the literature. For clarity, we divide the baseline methods into two categories: trained with and without contrastive losses. Several baselines derive OOD scores from a model trained with common softmax cross-entropy (CE) loss, including MSP (Hendrycks and Gimpel, 2017), ODIN (Liang et al., 2018), Mahalanobis (Lee et al., 2018), and Energy (Liu et al., 2020). GODIN (Hsu et al., 2020) is trained using a DeConf-C loss, which does not involve contrastive loss either. For methods involving contrastive losses, we use the same network backbone architecture and embedding dimension, while only varying the training objective. These methods include CSI (Tack et al., 2020) and SSD+ (Sehwag et al., 2021). For terminology clarity, KNN refers to our method trained with CE loss, and KNN+ refers to the variant trained with SupCon loss. We highlight two groups of comparisons:

- **KNN vs. Mahalanobis** (without contrastive learning): Under the *same* model trained with cross-entropy (CE) loss, our method achieves an average FPR95 of 29.15%, compared to that of Mahalanobis distance 37.94%. The performance gain precisely demonstrates the advantage of KNN over the parametric method Mahalanobis distance.
- **KNN+ vs. SSD+** (with contrastive loss): KNN+ and SSD+ are fundamentally different in OOD detection mechanisms, despite both benefit from the contrastively learned representations. SSD+ mod-

eled the feature embedding space as a multivariate Gaussian distribution for each class, and use Mahalanobis distance (Lee et al., 2018) for OOD detection. Under the *same* model trained with Supervised Contrastive Learning (SupCon) loss, our method with the nearest neighbor distance reduces the average FPR95 by 5.45%, which is a relatively 32.99% reduction in error. It further suggests the advantage of using nearest neighbors without making any distributional assumptions on the feature embedding space.

The above comparison suggests that the nearest neighbor approach is compatible with models trained both with and without contrastive learning. In addition, KNN is also simpler to use and implement than CSI, which relies on sophisticated data augmentations and ensembling in testing. Lastly, as a result of the improved embedding quality, the ID accuracy of the model trained with SupCon loss is improved by 0.86% on CIFAR-10 and 2.45% on ImageNet compared to training with the CE loss. Due to space constraints, we provide results on DenseNet (Huang et al., 2017) in Appendix A.3.3.

Contrastively learned representation helps. While contrastive learning has been extensively studied in recent literature, its role remains untapped when coupled with a non-parametric approach (such as nearest neighbors) for OOD detection. We examine the effect of using supervised contrastive loss for KNN-based OOD detection. We provide both qualitative and quantitative evidence, highlighting advantages over the standard softmax cross-entropy (CE) loss. (1) We visualize the learned feature embeddings in Figure 5.1 using UMAP (McInnes et al., 2018), where the colors encode different class labels. A salient observation is that the representation with SupCon is more distinguishable and compact than the representation obtained from the CE loss. The high-quality embedding space indeed confers benefits for KNN-based OOD detection. (2) Beyond visualization, we also quantitatively compare the performance of KNN-

based OOD detection using embeddings trained with SupCon vs CE. As shown in Table 5.1, KNN+ with contrastively learned representations reduces the FPR95 on all test OOD datasets compared to using embeddings from the model trained with CE loss.

Comparison with other non-parametric methods. In Table 5.2, we compare the nearest neighbor approach with other non-parametric methods. For a fair comparison, we use the same embeddings trained with SupCon loss. Our comparison covers an extensive collection of outlier detection methods in literature including: IForest (Liu et al., 2008), OCSVM (Schölkopf et al., 2001), LODA (Pevny, 2016), PCA (Shyu et al., 2003), and LOF (Breunig et al., 2000). The parameter setting for these methods is available in Appendix A.3.2. We show that KNN+ outperforms alternative non-parametric methods by a large margin.

Table 5.2: Comparison with other non-parametric methods. Results are averaged across all test OOD datasets. Model is trained on CIFAR-10.

	FPR95↓	AUROC↑
IForest (Liu et al., 2008)	65.49	76.98
OCSVM (Schölkopf et al., 2001)	52.27	65.16
LODA (Pevny, 2016)	76.38	62.59
PCA (Shyu et al., 2003)	37.26	83.13
LOF (Breunig et al., 2000)	40.06	93.47
KNN+ (ours)	11.07	97.93

Evaluations on hard OOD tasks. Hard OOD samples are particularly challenging to detect. To test the limit of the non-parametric KNN approach, we follow CSI (Tack et al., 2020) and evaluate on several hard OOD datasets: LSUN-FIX, ImageNet-FIX, ImageNet-R, and CIFAR-100. The results are summarized in Table 5.3. Under the same model, KNN+ consistently outperforms SSD+.

Table 5.3: Evaluation (FPR95) on hard OOD detection tasks. The model is trained on CIFAR-10 with SupCon loss.

	LSUN-FIX	ImageNet-FIX	ImageNet-R	C-100
SSD+	29.86	32.26	45.62	45.50
KNN+ (Ours)	21.52	25.92	29.92	38.83

5.3.2 Evaluation on Large-scale ImageNet Task

We evaluate on a large-scale OOD detection task based on ImageNet (Deng et al., 2009). Compared to the CIFAR benchmarks above, the ImageNet task is more challenging due to a large amount of training data. Our goal is to verify KNN’s performance benefits and whether it scales computationally with millions of samples.

Setup. We use a ResNet-50 backbone (He et al., 2016b) and train on ImageNet-1k (Deng et al., 2009) with resolution 224×224 . Following the experiments in Khosla et al. (2020), models with SupCon loss are trained for 700 epochs, with a batch size of 1024. The temperature τ is 0.1. The dimension of the penultimate feature where we perform the nearest neighbor search is 2048. The dimension of the project head is 128. We use the cosine learning rate (Loshchilov and Hutter, 2017) starting at 0.5. We train the models using stochastic gradient descent with momentum 0.9, and weight decay 10^{-4} . We use $k = 1000$ which follows the same validation procedure as before. When randomly sampling $\alpha\%$ training data for nearest neighbor search, k is scaled accordingly to $1000 \cdot \alpha\%$.

Following the ImageNet-based OOD detection benchmark in MOS (Huang and Li, 2021), we evaluate on four test OOD datasets that are subsets of: Places365 (Zhou et al., 2017), Textures (Cimpoi et al., 2014), iNaturalist (Horn et al., 2018), and SUN (Xiao et al., 2010) with non-overlapping categories *w.r.t.* ImageNet. The evaluations span a diverse range of domains including fine-grained images, scene images, and textural images.

Table 5.4: **Results on ImageNet.** All methods are based on a model trained on ID data only (ImageNet-1k (Deng et al., 2009)). We report the OOD detection performance, along with the per-image inference time.

Methods	Inference time (ms)	OOD Datasets								ID ACC		
		iNaturalist		SUN		Places		Textures			Average	
		FPR95 ↓	AUROC ↑	FPR95 ↓	AUROC ↑	FPR95 ↓	AUROC ↑	FPR95 ↓	AUROC ↑		FPR95 ↓	AUROC ↑
Without Contrastive Learning												
MSP	7.04	54.99	87.74	70.83	80.86	73.99	79.76	68.00	79.61	66.95	81.99	75.08
ODIN	7.05	47.66	89.66	60.15	84.59	67.89	81.78	50.23	85.62	56.48	85.41	75.08
Energy	7.04	55.72	89.95	59.26	85.89	64.92	82.86	53.72	85.99	58.41	86.17	75.08
GODIN	7.04	61.91	85.40	60.83	85.60	63.70	83.81	77.85	73.27	66.07	82.02	70.43
Mahalanobis	35.83	97.00	52.65	98.50	42.41	98.40	41.79	55.80	85.01	87.43	55.47	75.08
KNN ($\alpha = 100\%$)	10.31	59.77	85.89	68.88	80.08	78.15	74.10	10.90	97.42	54.68	84.37	75.08
KNN ($\alpha = 1\%$)	7.04	59.08	86.20	69.53	80.10	77.09	74.87	11.56	97.18	54.32	84.59	75.08
With Contrastive Learning												
SSD+	28.31	57.16	87.77	78.23	73.10	81.19	70.97	36.37	88.52	63.24	80.09	79.10
KNN+ ($\alpha = 100\%$)	10.47	30.18	94.89	48.99	88.63	59.15	84.71	15.55	95.40	38.47	90.91	79.10
KNN+ ($\alpha = 1\%$)	7.04	30.83	94.72	48.91	88.40	60.02	84.62	16.97	94.45	39.18	90.55	79.10

Nearest neighbor approach achieves superior performance without compromising the inference speed. In Table 5.4, we compare our approach with OOD detection methods that are competitive in the literature. The baselines are the same as what we described in Section 5.3.1 except for CSI². We report both OOD detection performance and the inference time (measured by milliseconds). We highlight three trends: (1) KNN+ outperforms the best baseline by **18.01%** in FPR95. (2) Compared to SSD+, KNN+ substantially reduces the FPR95 by **24.77%** averaged across all test sets. The limiting performance of SSD+ is due to the increased size of label space and data complexity, which makes the class-conditional Gaussian assumption less viable. In contrast, our non-parametric method does not suffer from this issue, and can better estimate the density of the complex distribution for OOD detection. (3) KNN+ achieves strong performance with a comparable inference speed as the baselines. In particular, we show that performing nearest neighbor distance estimation with only 1% randomly sampled training data can yield a similar performance as

²The training procedure of CSI is computationally prohibitive on ImageNet, which takes three months on 8 Nvidia 2080Tis.

using the full dataset.

Nearest neighbor approach is competitive on ViT. Going beyond convolutional neural networks, we show in Table 5.5 that the nearest neighbor approach is effective for transformer-based ViT model (Dosovitskiy et al., 2021). We adopt the ViT-B/16 architecture fine-tuned on the ImageNet-1k dataset using cross-entropy loss. Under the same ViT model, our non-parametric KNN method consistently outperforms Mahalanobis.

Table 5.5: Performance comparison (FPR95) on ViT-B/16 model fine-tuned on ImageNet-1k.

	iNaturalist	SUN	Places	Textures
Mahalanobis (parametric)	17.56	80.51	84.12	70.51
KNN (non-parametric)	7.30	48.40	56.46	39.91

5.4 A Closer Look at KNN-based OOD Detection

We provide further analysis and ablations to understand the behavior of KNN-based OOD detection. All the ablations are based on the ImageNet model trained with SupCon loss (same as in Section 5.3.2).

Effect of k and sampling ratio. In Figure 5.2 and Figure 5.3 (a), we systematically analyze the effect of k and the dataset sampling ratios α . We vary the number of neighbors $k = \{1, 10, 20, 50, 100, 200, 500, 1000, 3000, 5000\}$ and random sampling ratio $\alpha = \{1\%, 10\%, 50\%, 100\%\}$. We note several interesting observations: (1) The optimal OOD detection (measured by FPR95) remains *similar* under different random sampling ratios α . (2) The optimal k is consistent with the one chosen by our validation strategy. For example, the optimal k is 1,000 when $\alpha = 100\%$; and the optimal k becomes 10 when $\alpha = 1\%$. (3) Varying k does not significantly affect

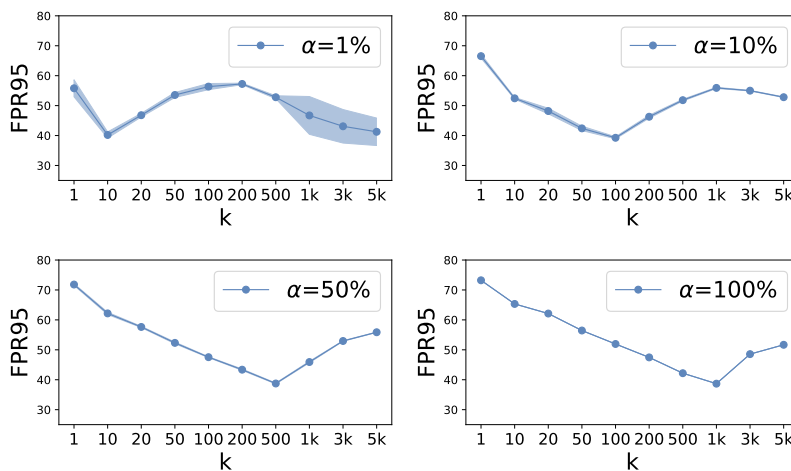


Figure 5.2: Comparison with the effect of different k and sampling ratio α . We report an average FPR95 score over four test OOD datasets. The variances are estimated across 5 different random seeds. The solid blue line represents the averaged value across all runs and the shaded blue area represents the standard deviation. Note that the full ImageNet dataset ($\alpha = 100\%$) has 1000 images per class.

the inference speed when k is relatively small (e.g., $k < 1000$) as shown in Figure 5.3 (a).

Feature normalization is critical. In this ablation, we contrast the performance of KNN-based OOD detection with and without feature normalization. The k -th NN distance can be derived by $r_k(\frac{\phi(\mathbf{x})}{\|\phi(\mathbf{x})\|})$ and $r_k(\phi(\mathbf{x}))$, respectively. As shown in Figure 5.3 (b), using feature normalization improved the FPR95 drastically by **61.05%**, compared to the counterpart without normalization. To better understand this, we look into the Euclidean distance $r = \|u - v\|_2$ between two vectors u and v . The norm of the feature vector u and v could notably affect the value of the Euclidean distance. Interestingly, recent studies share the observation in Figure 5.4 (a) that the ID data has a larger L_2 feature norm than OOD data (Tack et al., 2020; Huang et al., 2021b). Therefore, the Euclidean distance be-

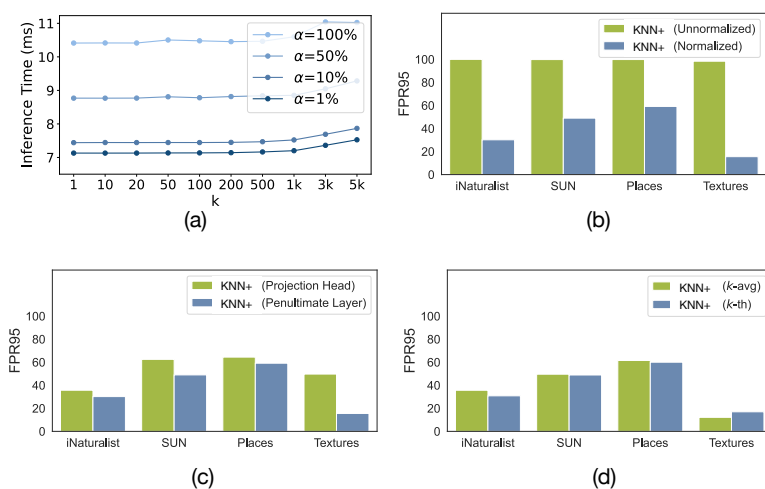


Figure 5.3: **Ablation results.** In (a), we compare the inference speed (per-image) using different k and sampling ratio α . For (b) (c) (d), the FPR95 value is reported over all test OOD datasets. Specifically, (b) compares the effect of using normalization in the penultimate layer feature vs. without normalization, (c) compares using features in the penultimate layer feature vs the projection head, and (d) compares the OOD detection performance using k -th and averaged k (k -avg) nearest neighbor distance.

tween ID features can be large (Figure 5.4 (b)). This contradicts the hope that ID data has a smaller k -NN distance than OOD data. Indeed, the normalization effectively mitigated this problem, as evidenced in Figure 5.4 (c). Empirically, the normalization plays a key role in the nearest neighbor approach to be successful in OOD detection as shown in Figure 5.3 (b).

Using the penultimate layer’s feature is better than using the projection head. In this chapter, we follow the convention in SSD+, which uses features from the penultimate layer instead of the projection head. We also verify in Figure 5.3 (c) that using the penultimate layer’s feature is better than using the projection head on all test OOD datasets. This is likely due to the penultimate layer preserving more information than the

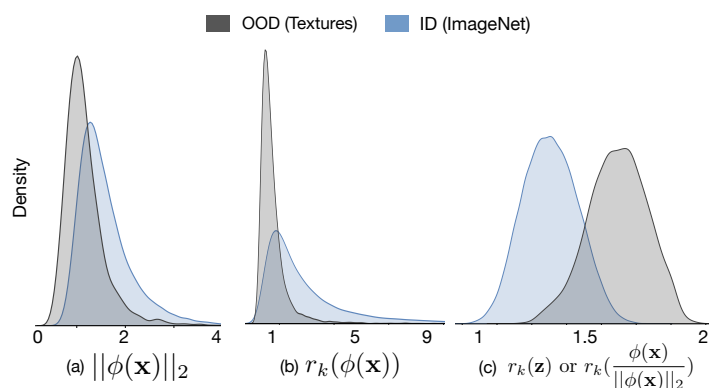


Figure 5.4: Distribution of (a) the L_2 -norm of feature embeddings, (b) the k -NN distance with the *unnormalized* feature embeddings, and (c) the k -NN distance with the *normalized* features.

projection head, which has much smaller dimensions.

KNN can be further boosted by activation rectification. We show that KNN+ can be made stronger with a ReAct (Sun et al., 2021a) (Chapter 3). It was shown that the OOD data can have overly high activations on some feature dimensions, and this rectification is effective in suppressing the values. Empirically, we compare the results in Table 5.6 by using the activation rectification and achieve improved OOD detection performance.

Table 5.6: Comparison of KNN-based method with and without activation truncation. The ID data is ImageNet-1k. The value is averaged over all test OOD datasets.

Method	FPR95↓	AUROC↑
KNN+	38.47	90.91
KNN+ (w. ReAct (Sun et al., 2021a))	26.45	93.76

Using k -th and averaged k nearest neighbors’ distance has similar performance. We compare two variants for OOD detection: k -th nearest neighbor distance vs. averaged k (k -avg) nearest neighbor distance. The comparison is shown in Figure 5.3 (d), where the average performance

(on four datasets) is on par. The reported results are based on the full ID dataset ($\alpha = 100\%$) with the optimal k chosen for k -th NN and k -avg NN respectively. Despite the similar performance, using k -th NN distance has a stronger theoretical interpretation, as we show in the next section.

5.5 Theoretical Justification

In this section, we provide a theoretical analysis of using KNN for OOD detection. By modeling the KNN in the feature space, our theory (1) directly connects to our method which also operates in the feature space, and (2) complements our experiments by considering the universality of OOD data. Our goal here is to analyze the average performance of our algorithm while being OOD-agnostic and training-agnostic.

Setup. We consider OOD detection task as a special binary classification task, where the negative samples (OOD) are only available in the testing stage. We assume the input is from feature embeddings space \mathcal{Z} and the labeling set $\mathcal{G} = \{0(\text{OOD}), 1(\text{ID})\}$. In the inference stage, the testing set $\{(\mathbf{z}_i, g_i)\}$ is drawn *i.i.d.* from $P_{\mathcal{Z}\mathcal{G}}$.

Denote the marginal distribution on \mathcal{Z} as \mathcal{P} . We adopt the Huber contamination model (Huber, 1964) to model the fact that we may encounter both ID and OOD data in test time:

$$\mathcal{P} = \varepsilon\mathcal{P}_{out} + (1 - \varepsilon)\mathcal{P}_{in},$$

where \mathcal{P}_{in} and \mathcal{P}_{out} are the underlying distributions of feature embeddings for ID and OOD data, respectively, and ε is a constant controlling the fraction of OOD samples in testing. We use lower case $p_{in}(\mathbf{z}_i)$ and $p_{out}(\mathbf{z}_i)$ to denote the probability density function, where $p_{in}(\mathbf{z}_i) = p(\mathbf{z}_i|g_i = 1)$ and $p_{out}(\mathbf{z}_i) = p(\mathbf{z}_i|g_i = 0)$.

A key challenge in OOD detection (and theoretical analysis) is the

lack of knowledge on OOD distribution, which can arise universally outside ID data. We thus try to keep our analysis general and reflect the fact that we do not have any strong prior information about OOD. For this reason, we model OOD data with an equal chance to appear outside of the high-density region of ID data, $p_{out}(\mathbf{z}) = c_0 \mathbf{1}\{p_{in}(\mathbf{z}) < c_1\}$ ³. The Bayesian classifier is known as the optimal binary classifier defined by $h_{Bay}(\mathbf{z}_i) = \mathbf{1}\{p(g_i = 1|\mathbf{z}_i) \geq \beta\}$ ⁴, assuming the underlying density function is given.

Without such oracle information, our method applies k -NN as the distance measure which acts as a probability density estimation, and thus provides the decision boundary based on it. Specifically, KNN's hypothesis class \mathcal{H} is given by $\{h : h_{\lambda,k,\mathbf{z}_n}(\mathbf{z}_i) = \mathbf{1}\{-r_k(\mathbf{z}_i) \geq \lambda\}\}$, where $r_k(\mathbf{z}_i)$ is the distance to the k -th nearest neighbor (*c.f.* Section 5.2).

Main result. We show that our KNN-based OOD detector can reject inputs equivalent to the estimated Bayesian binary decision function. A small KNN distance $r_k(\mathbf{z}_i)$ directly translates into a high probability of being ID, and vice versa. We depict this in the following Theorem.

Theorem 5.1. *With the setup specified above, if $\hat{p}_{out}(\mathbf{z}_i) = \hat{c}_0 \mathbf{1}\{\hat{p}_{in}(\mathbf{z}_i; k, n) < \frac{\beta \epsilon \hat{c}_0}{(1-\beta)(1-\epsilon)}\}$, and $\lambda = -m^{-1} \sqrt{\frac{(1-\beta)(1-\epsilon)k}{\beta \epsilon c_b n \hat{c}_0}}$, we have*

$$\mathbf{1}\{-r_k(\mathbf{z}_i) \geq \lambda\} = \mathbf{1}\{\hat{p}(g_i = 1|\mathbf{z}_i) \geq \beta\},$$

where $\hat{p}(\cdot)$ denotes the empirical estimation. The proof is in Appendix A.3.1.

³In experiments, as it is difficult to simulate the universal OOD, we approximate it by using a diverse yet finite collection of datasets. Our theory is thus complementary to our experiments and captures the universality of OOD data.

⁴Note that β does not have to be $\frac{1}{2}$ for the Bayesian classifier to be optimal. β can be any value larger than $\frac{(1-\epsilon)c_1}{(1-\epsilon)c_1 + \epsilon c_0}$ when $\epsilon c_0 \geq (1-\epsilon)c_1$.

5.6 Additional Related Work

KNN for anomaly detection. KNN has been explored for anomaly detection (Jing et al., 2014; Zhao and Lai, 2020; Bergman et al., 2020), which aims to detect abnormal input samples from one class. We focus on OOD detection, which requires additionally performing multi-class classification for ID data. Some other recent works (Dang et al., 2015; Gu et al., 2019; Pires et al., 2020) explore the effectiveness of KNN-based anomaly detection for the tabular data. The potential of using KNN for OOD detection in deep neural networks is currently underexplored. Our work provides both new empirical insights and theoretical analysis of using the KNN-based approach for OOD detection.

5.7 Summary

this chapter presents the first study exploring and demonstrating the efficacy of the non-parametric nearest-neighbor distance for OOD detection. Unlike prior works, the non-parametric approach does not impose any distributional assumption about the underlying feature space, hence providing stronger flexibility and generality. We provide important insights that a high-quality feature embedding and a suitable distance measure are two indispensable components for the OOD detection task. Extensive experiments show KNN-based method can notably improve the performance on several OOD detection benchmarks, establishing superior results. We hope our work inspires future research on using the non-parametric approach to OOD detection.

Part II

**Open-world Representation
Learning**

Chapter 6

When and How Does Known Class Help Discover Unknown Ones? A Spectral Analysis

Publication Statement. This chapter is joint work with Zhenmei Shi, Yingyu Liang, and Yixuan Li. The paper version of this chapter appeared in ICML23 ([Sun et al., 2023b](#)).

The pivotal progression beyond recognizing OOD samples involves discovering latent classes within these samples. This unique task, known as Novel Class Discovery (NCD), is dedicated to the identification of new classes within an unlabeled dataset by leveraging pre-established knowledge from a labeled set of familiar classes. In the context of open-world representation learning, which accommodates unlabeled samples from both known and novel classes, NCD emerges as a distinct and significant sub-problem, specifically focusing on unveiling these novel classes.

Despite its importance, there is a lack of theoretical foundations for NCD. This chapter bridges the gap by providing an analytical framework to formalize and investigate *when and how known classes can help discover*

novel classes. Tailored to the NCD problem, we introduce a graph-theoretic representation that can be learned by a novel NCD Spectral Contrastive Loss (NSCL). Minimizing this objective is equivalent to factorizing the graph’s adjacency matrix, which allows us to derive a provable error bound and provide the sufficient and necessary condition for NCD. Empirically, NSCL can match or outperform several strong baselines on common benchmark datasets, which is appealing for practical usage while enjoying theoretical guarantees.

6.1 Introduction

Though modern machine learning methods have achieved remarkable success (He et al., 2016a; Chen et al., 2020a; Song et al., 2020; Wang et al., 2022a), the vast majority of learning algorithms have been driven by the closed-world setting, where the classes are assumed stationary and unchanged between training and testing. However, machine learning models in the open world will inevitably encounter novel classes that are outside the existing known categories (Sun et al., 2021a, 2022; Ming et al., 2022a, 2023). Novel Class Discovery (NCD) (Han et al., 2019) has emerged as an important problem, which aims to cluster similar samples in an unlabeled dataset (of novel classes) by way of utilizing knowledge from the labeled data (of known classes). Key to NCD is harnessing the power of labeled data for possible knowledge sharing and transfer to the unlabeled data (Hsu et al., 2018; Han et al., 2019; Hsu et al., 2019; Zhong et al., 2021b; Han et al., 2020a; Yang et al., 2022c; Sun and Li, 2023).

One promising approach for NCD is to learn feature representation jointly from both labeled and unlabeled data, so that meaningful cluster structures emerge as novel classes. We argue that interesting intricacies can arise in this learning process—the resulting novel clusters may be very different, depending on the type of known class provided. We

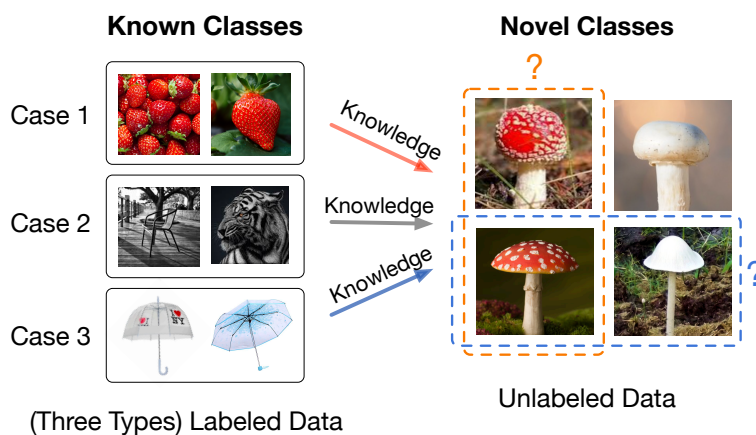


Figure 6.1: **Novel Class Discovery (NCD)** aims to cluster similar samples in unlabeled data (right), by way of utilizing knowledge from the labeled data (left). We illustrate scenarios where different known classes could result in different novel clusters (e.g., red mushrooms or mushrooms with umbrella shapes). This chapter aims to provide a formal understanding.

exemplify the nuances in Figure 6.1. In one scenario, the novel class “red mushroom” can be discovered, provided with the known class “strawberry” of a shared color feature. Alternatively, a different novel class can also emerge by grouping the bottom two images together (as “mushroom with umbrella shape” class), if the umbrella-shape images are given as a known class to the learner. We argue—perhaps obviously—that a formalized understanding of the intricate phenomenon is needed. This motivates our research:

When and how does the known class help discover novel classes?

Despite the empirical successes in recent years, there is a limited theoretical understanding and formalization for novel class discovery. To the best of our knowledge, there is no prior work that investigated this research question from a rigorous theoretical standpoint or provided prov-

able error bound. Our work thus complements the existing works by filling in the critical blank.

In this chapter, we start by formalizing a new learning algorithm that facilitates the understanding of NCD from a spectral analysis perspective. Our theoretical framework first introduces a graph-theoretic representation tailored for NCD, where the vertices are all the labeled and unlabeled data points, and classes form connected sub-graphs (Section 6.3.1). Based on this graph representation, we then introduce a new loss called NCD Spectral Contrastive Loss (NSCL) and show that minimizing our loss is equivalent to performing spectral decomposition on the graph (Section 6.3.2). Such equivalence allows us to derive the formal error bound for NCD based on the properties of the graph, which directly encodes the relations between known and novel classes.

We analyze the NCD quality by the linear probing performance on novel data, which is the least error of all possible linear classifiers with the learned representation. Our main result (Theorem 6.6) suggests that the linear probing error can be significantly reduced (even to 0) when the linear span of known samples’ feature covers the “ignorance space” of unlabeled data in discovering novel classes. Lastly, we verify that our theoretical guarantees can translate into empirical effectiveness. In particular, NSCL establishes competitive performance on common NCD benchmarks, outperforming the best baseline by **10.6%** on the CIFAR-100-50 dataset (with 50 novel classes).

Our **main contributions** are:

1. We provide the first provable framework for the NCD problem, formalizing it by spectral decomposition of the graph containing both known and novel data. Our framework allows the research community to gain insights from a graph-theoretic perspective.
2. We propose a new loss called NCD Spectral Contrastive Loss (NSCL) and show that minimizing our loss is equivalent to performing sin-

gular decomposition on the graph. The loss leads to strong empirical performance while enjoying theoretical guarantees.

3. We provide theoretical insight by formally defining the semantic relationship between known and novel classes. Based on that, we derive an error bound of novel class discovery and investigate the sufficient and necessary conditions for the perfect discovery results.

6.2 Setup

In Section 2.1, we delineated the problem setup for Open-World Representation Learning, taking into account unlabeled samples from both known and novel classes. In this chapter, we shift our focus to a more specific subset of the problem—Novel Class Discovery—which exclusively examines unlabeled samples from unidentified classes. Formally, we describe the data setup and learning goal for novel class discovery (NCD).

Data setup. We consider the empirical training set $\mathcal{D}_l \cup \mathcal{D}_u$ as a union of labeled and unlabeled data. The labeled dataset is given by $\mathcal{D}_l = \{(\bar{x}_1, y_1), \dots, (\bar{x}_i, y_i), \dots\}$, where y_i belongs to known class space \mathcal{Y}_l ; and the unlabeled dataset is $\mathcal{D}_u = \{\bar{x}_1, \dots, \bar{x}_j, \dots\}$. We assume that each unlabeled sample $\bar{x} \in \mathcal{D}_u$ belongs to one of the **novel** classes, *which do not overlap with the known classes* \mathcal{Y}_l . We use \mathcal{P}_l and \mathcal{P}_u to denote the marginal distributions of labeled and unlabeled data in the input space. Further, we let \mathcal{P}_{l_i} denote the distribution of labeled samples with class label $i \in \mathcal{Y}_l$.

Learning goal. We assume that there exists an underlying class space $\mathcal{Y}_u = \{1, \dots, |\mathcal{Y}_u|\}$ for unlabeled data \mathcal{X}_u , which is not revealed to the learner. The goal of novel class discovery is to learn a clustering for the novel data, which can be mapped to \mathcal{Y}_u with low error.

6.3 Spectral Contrastive Learning for Novel Class Discovery

In this section, we introduce a new learning algorithm for NCD, from a graph-theoretic perspective. NCD is inherently a clustering problem—grouping similar points in unlabeled data \mathcal{D}_u into the same cluster, by way of possibly utilizing helpful information from the labeled data \mathcal{D}_l . This clustering process can be fundamentally modeled by a graph, where the vertices are all the data points and classes form connected sub-graphs. Our novel framework first introduces a graph-theoretic representation for NCD, where edges connect similar data points (Section 6.3.1). We then propose a new loss that performs spectral decomposition on the similarity graph and can be written as a contrastive learning objective on neural net representations (Section 6.3.2).

6.3.1 Graph-Theoretic Representation for NCD

We start by formally defining the augmentation graph and adjacency matrix. For notation clarity, we use \bar{x} to indicate the natural sample (raw inputs without augmentation). Given an \bar{x} , we use $\mathcal{T}(x|\bar{x})$ to denote the probability of x being augmented from \bar{x} . For instance, when \bar{x} represents an image, $\mathcal{T}(\cdot|\bar{x})$ can be the distribution of common augmentations such as Gaussian blur, color distortion, and random cropping. The augmentation allows us to define a general population space \mathcal{X} , which contains all the original images along with their augmentations. In our case, \mathcal{X} ($|\mathcal{X}| = N$) is composed of two parts \mathcal{X}_l ($|\mathcal{X}_l| = N_l$), \mathcal{X}_u ($|\mathcal{X}_u| = N_u$) which represents the division into labeled data with known classes and unlabeled data with novel classes respectively. Unlike unsupervised learning (Chen et al., 2020a), NCD has access to both labeled and unlabeled data. This leads to two cases where two samples x and x^+ form a **positive pair** if:

- (a) x and x^+ are augmented from the same unlabeled image $\bar{x}_u \sim \mathcal{P}_u$.
- (b) x and x^+ are augmented from two labeled samples \bar{x}_l and \bar{x}'_l with the same known class i . In other words, both \bar{x}_l and \bar{x}'_l are drawn independently from \mathcal{P}_i .

We define the graph $G(\mathcal{X}, w)$ with vertex set \mathcal{X} and edge weights w . For any two augmented data $x, x' \in \mathcal{X}$, $w_{xx'}$ is the marginal probability of generating the pair (x, x') :

$$w_{xx'} \triangleq \alpha \sum_{i \in \mathcal{Y}_l} \mathbb{E}_{\bar{x}_l \sim \mathcal{P}_i} \mathbb{E}_{\bar{x}'_l \sim \mathcal{P}_i} \mathcal{T}(x|\bar{x}_l) \mathcal{T}(x'|\bar{x}'_l) + \beta \mathbb{E}_{\bar{x}_u \sim \mathcal{P}_u} \mathcal{T}(x|\bar{x}_u) \mathcal{T}(x'|\bar{x}_u), \quad (6.1)$$

↑ case (b)
↑ case (a)

where α, β modulates the importance between unlabeled and labeled data. The magnitude of $w_{xx'}$ indicates the “positiveness” or similarity between x and x' . We then use $w_x = \sum_{x' \in \mathcal{X}} w_{xx'}$ to denote the total edge weights connected to vertex x .

As a standard technique in graph theory (Chung, 1997), we use the *normalized adjacency matrix*:

$$\dot{A} \triangleq D^{-1/2} A D^{-1/2}, \quad (6.2)$$

where $A \in \mathbb{R}^{N \times N}$ is adjacency matrix with entries $A_{xx'} = w_{xx'}$ and $D \in \mathbb{R}^{N \times N}$ is a diagonal matrix with $D_{xx} = w_x$. The normalization balances the degree of each node, reducing the influence of vertices with very large degrees. The adjacency matrix defines the probability of x and x' being considered as the positive pair from the perspective of augmentation, which helps derive the NCD Spectral Contrastive Loss as we show next.

6.3.2 NCD Spectral Contrastive Learning

In this subsection, we propose a formal definition of NCD Spectral Contrastive Loss, which can be derived from a spectral decomposition of \dot{A} . The derivation of the loss is inspired by (HaoChen et al., 2021), and allows us to theoretically show the equivalence between learning feature embeddings and the projection on the top- k SVD components of \dot{A} . Importantly, such equivalence facilitates the theoretical understanding based on the semantic relation between known and novel classes encoded in \dot{A} .

Specifically, we consider low-rank matrix approximation:

$$\min_{F \in \mathbb{R}^{N \times k}} \mathcal{L}_{\text{mf}}(F, A) \triangleq \|\dot{A} - FF^\top\|_F^2 \quad (6.3)$$

According to the Eckart–Young–Mirsky theorem (Eckart and Young, 1936), the minimizer of this loss function is $F^* \in \mathbb{R}^{N \times k}$ such that $F^*F^{*\top}$ contains the top- k components of \dot{A} 's SVD decomposition.

Now, if we view each row \mathbf{f}_x^\top of F as a learned feature embedding $f : \mathcal{X} \mapsto \mathbb{R}^k$, the $\mathcal{L}_{\text{mf}}(F, A)$ can be written as a form of the contrastive learning objective. We formalize this connection in Theorem 6.1 below.

Theorem 6.1. *We define $\mathbf{f}_x = \sqrt{w_x}f(x)$ for some function f . Recall α, β are hyper-parameters defined in Eq. (6.1). Then minimizing the loss function $\mathcal{L}_{\text{mf}}(F, A)$ is equivalent to minimizing the following loss function for f , which we term **NCD Spectral Contrastive Loss (NSCL)**:*

$$\begin{aligned} \mathcal{L}_{\text{nscl}}(f) \triangleq & -2\alpha\mathcal{L}_1(f) - 2\beta\mathcal{L}_2(f) \\ & + \alpha^2\mathcal{L}_3(f) + 2\alpha\beta\mathcal{L}_4(f) + \beta^2\mathcal{L}_5(f), \end{aligned} \quad (6.4)$$

where

$$\begin{aligned}
\mathcal{L}_1(f) &= \sum_{i \in \mathcal{Y}_l} \mathbb{E}_{\substack{\bar{x}_l \sim \mathcal{P}_l, \bar{x}'_l \sim \mathcal{P}_l, \\ x \sim \mathcal{T}(\cdot | \bar{x}_l), x^+ \sim \mathcal{T}(\cdot | \bar{x}'_l)}} \left[f(x)^\top f(x^+) \right], \\
\mathcal{L}_2(f) &= \mathbb{E}_{\substack{\bar{x}_u \sim \mathcal{P}_u, \\ x \sim \mathcal{T}(\cdot | \bar{x}_u), x^+ \sim \mathcal{T}(\cdot | \bar{x}_u)}} \left[f(x)^\top f(x^+) \right], \\
\mathcal{L}_3(f) &= \sum_{i \in \mathcal{Y}_l} \sum_{j \in \mathcal{Y}_l} \mathbb{E}_{\substack{\bar{x}_l \sim \mathcal{P}_l, \bar{x}'_l \sim \mathcal{P}_l, \\ x \sim \mathcal{T}(\cdot | \bar{x}_l), x^- \sim \mathcal{T}(\cdot | \bar{x}'_l)}} \left[\left(f(x)^\top f(x^-) \right)^2 \right], \\
\mathcal{L}_4(f) &= \sum_{i \in \mathcal{Y}_l} \mathbb{E}_{\substack{\bar{x}_l \sim \mathcal{P}_l, \bar{x}_u \sim \mathcal{P}_u, \\ x \sim \mathcal{T}(\cdot | \bar{x}_l), x^- \sim \mathcal{T}(\cdot | \bar{x}_u)}} \left[\left(f(x)^\top f(x^-) \right)^2 \right], \\
\mathcal{L}_5(f) &= \mathbb{E}_{\substack{\bar{x}_u \sim \mathcal{P}_u, \bar{x}'_u \sim \mathcal{P}_u, \\ x \sim \mathcal{T}(\cdot | \bar{x}_u), x^- \sim \mathcal{T}(\cdot | \bar{x}'_u)}} \left[\left(f(x)^\top f(x^-) \right)^2 \right].
\end{aligned}$$

Proof. (sketch) We can expand $\mathcal{L}_{\text{mf}}(F, A)$ and obtain

$$\begin{aligned}
\mathcal{L}_{\text{mf}}(F, A) &= \sum_{x, x' \in \mathcal{X}} \left(\frac{w_{xx'}}{\sqrt{w_x w_{x'}}} - \mathbf{f}_x^\top \mathbf{f}_{x'} \right)^2 = \text{const} + \\
&\sum_{x, x' \in \mathcal{X}} \left(-2w_{xx'} f(x)^\top f(x') + w_x w_{x'} \left(f(x)^\top f(x') \right)^2 \right)
\end{aligned}$$

The form of $\mathcal{L}_{\text{nscl}}(f)$ is derived from plugging $w_{xx'}$ (defined in Eq. (6.1)) and w_x . We include the details in Appendix B.1.1.2. \square

Interpretation of $\mathcal{L}_{\text{nscl}}(f)$. At a high level, \mathcal{L}_1 and \mathcal{L}_2 push the embeddings of **positive pairs** to be closer while \mathcal{L}_3 , \mathcal{L}_4 and \mathcal{L}_5 pull away the embeddings of **negative pairs**. In particular, \mathcal{L}_1 samples two random augmentation views of two images from labeled data with the **same** class label, and \mathcal{L}_2 samples two views from the same image in \mathcal{X}_u . For negative pairs, \mathcal{L}_3 uses two augmentation views from two samples in \mathcal{X}_l with **any** class label. \mathcal{L}_4 uses two views of one sample in \mathcal{X}_l and another one in \mathcal{X}_u . \mathcal{L}_5 uses two views from two random samples in \mathcal{X}_u .

6.4 Theoretical Analysis

So far we have presented a spectral approach for NCD based on the augmentation graph. Under this formulation, we now formally investigate and analyze: *when and how does the known class help discover novel class?* We start by showing that analyzing the linear probing performance is equivalent to analyzing the regression residual using singular vectors of \dot{A} in Sec. 6.2. We then construct a toy example to illustrate and verify the key insight in Sec. 6.4.2. We finally provide a formal theory for the general case in Sec. 6.4.3.

6.4.1 Theoretical Setup

Representation for unlabeled data. We apply NCD spectral learning objective $\mathcal{L}_{nscf}(f)$ in Equation 6.4 and assume the optimizer is capable to obtain the representation that minimizes the loss. We can then obtain the F^* s.t. $F^*F^{*\top}$ are the top- k components of \dot{A} 's SVD decomposition. To ease the analysis, we will focus on the top- k singular vectors $V^* \in \mathbb{R}^{N \times k}$ of \dot{A} such that $F^* = V^* \sqrt{\Sigma_k}$, where Σ_k is the diagonal matrix with top- k singular values $(\sigma_1, \dots, \sigma_k)$.

Since we are primarily interested in the unlabeled data, we split V^* into two parts: $U^* \in \mathbb{R}^{N_u \times k}$ for unlabeled data and $L^* \in \mathbb{R}^{N_l \times k}$ for labeled data, respectively. Assuming the first N_l rows/columns in \dot{A} corresponds to the labeled data, we can conveniently rewrite V^* as:

$$V^* = \begin{bmatrix} L^*(\text{labeled part}) \\ U^*(\text{unlabeled part}) \end{bmatrix} \quad (6.5)$$

Linear probing evaluation. With the learned representation for the unlabeled data, we can evaluate NCD quality by the linear probing performance. The strategy is commonly used in self-supervised learning (Chen

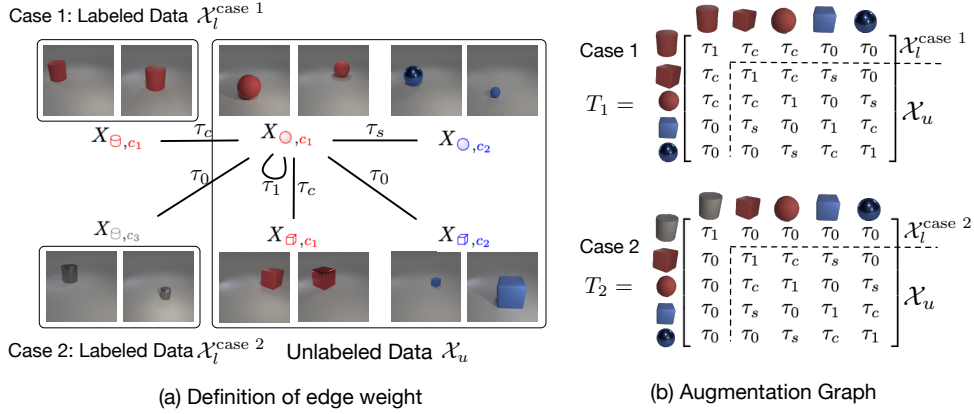


Figure 6.2: An illustrative example for theoretical analysis. (a) The unlabeled data \mathcal{X}_u consists of 3D objects of sphere/cube with red/blue colors. We consider two cases of labeled data: (1) Case 1 uses red cylinders that are correlated with the target novel class (red). (2) Case 2 uses gray cylinders which have no correlation with \mathcal{X}_u . (b) The augmentation matrices for case 1 and case 2 respectively. See definition in Eq. (6.7). Best viewed in color.

et al., 2020a). Specifically, the weight of a linear classifier is denoted as $\mathbf{M} \in \mathbb{R}^{k \times |\mathcal{Y}_u|}$. The class prediction is given by $h(x; f, \mathbf{M}) = \operatorname{argmax}_{i \in \mathcal{Y}_u} (f(x)^\top \mathbf{M})_i$. The linear probing performance is given by the least error of all possible linear classifiers:

$$\mathcal{E}(f) \triangleq \min_{\mathbf{M} \in \mathbb{R}^{k \times |\mathcal{Y}_u|}} \sum_{x \in \mathcal{X}_u} \mathbb{1}[y(x) \neq h(x; f, \mathbf{M})], \quad (6.6)$$

where $y(x)$ indicates the ground-truth class of x .

Residual analysis. With defined U^* , we can bound the linear probing error $\mathcal{E}(f)$ by the residual of the regression error $\mathcal{R}(U^*)$ as we show in Lemma 6.2 with proof in Appendix B.1.1.1.

Lemma 6.2. Denote the $\mathbf{y}(x) \in \mathbb{R}^{|\mathcal{Y}_u|}$ as a one-hot vector whose $y(x)$ -th position is 1 and 0 elsewhere. Let $\mathbf{Y} \in \mathbb{R}^{N_u \times |\mathcal{Y}_u|}$ as a binary mask whose rows are stacked

by $\mathbf{y}(x)$. We have:

$$\mathcal{R}(U^*) \triangleq \min_{\mathbf{M} \in \mathbb{R}^{k \times |\mathcal{Y}_u|}} \|\mathbf{Y} - U^* \mathbf{M}\|_F^2 \geq \frac{1}{2} \mathcal{E}(f).$$

Note that we can rewrite $\mathcal{R}(U^*)$ as the summation of individual residual terms $\mathcal{R}(U^*, \vec{y}_i)$: $\mathcal{R}(U^*) = \sum_{i \in \mathcal{Y}_u} \mathcal{R}(U^*, \vec{y}_i)$, where

$$\mathcal{R}(U^*, \vec{y}_i) \triangleq \min_{\vec{\mu}_i \in \mathbb{R}^k} \|\vec{y}_i - U^* \vec{\mu}_i\|_2^2,$$

and $\vec{y}_i \in \mathbb{R}^{N_u}$ is the i -th column of \mathbf{Y} and $\vec{\mu}_i \in \mathbb{R}^k$ is the i -th column of \mathbf{M} . Without losing the generality, our analysis will revolve around the residual term $\mathcal{R}(U^*, \vec{y}_i)$ for specific class i . It is clear that if learned representation U^* encodes more information of the label vector \vec{y}_i , the residual $\mathcal{R}(U^*, \vec{y}_i)$ becomes smaller¹. Such insight can be used to investigate which type of known class is more helpful for learning the representation of novel classes.

6.4.2 An Illustrative Example

We consider a toy example that helps illustrate the core idea of our theoretical findings. Specifically, the example aims to cluster 3D objects of different colors and shapes, as shown in Figure 6.2 (a). These images are generated by a 3D rendering software (Johnson et al., 2017) with user-defined properties including colors, shape, size, position, etc.

In what follows, we define two data configurations and corresponding graphs, where the labeled data is correlated with the attribute of unlabeled data (**case 1**) vs. not (**case 2**). We are interested in contrasting the representations (in form of singular vectors) and residuals derived from

¹In an extreme case, if the first column of U^* is exactly the same as \vec{y}_i , one can set $\vec{\mu}_i = [1, 0, 0, \dots]^T$ to make residual zero.

both scenarios. The proof of all theorems in this section is provided in Appendix B.1.2.

Motivation and data design. For simplicity, we focus on two main properties: color and shape. Formally, the images with shape s and color c are sampled from a generation procedure \mathcal{G} :

$$X_{s,c} \sim \mathcal{G}(s, c),$$

where $s \in \{\boxplus (\text{cube}), \circ (\text{sphere}), \ominus (\text{cylinder})\}$, $c \in \{c_1 (\text{red}), c_2 (\text{blue}), c_3 (\text{gray})\}$.

We then construct our unlabeled dataset containing red/blue cubes/spheres as:

$$\mathcal{X}_u \triangleq \{X_{\boxplus, c_1}, X_{\circ, c_1}, X_{\boxplus, c_2}, X_{\circ, c_2}\}.$$

For simplicity, we assume each element in \mathcal{X}_u is a single example. W.o.l.g, we also assume the red cube and red sphere form the target novel class. Then the corresponding labeling vector on \mathcal{X}_u is defined by:

$$\vec{y} \triangleq \{1, 1, 0, 0\}.$$

To answer “*when and how does the known class help discover novel class?*”, we construct two separate scenarios: one helps and the other one does not. Specifically, in the first case, we let the labeled data $\mathcal{X}_l^{\text{case 1}}$ be strongly correlated with the target class (red color) in unlabeled data:

$$\mathcal{X}_l^{\text{case 1}} \triangleq \{X_{\ominus, c_1}\} (\text{red cylinder}).$$

In the second case, we construct the labeled data that has no correlation with any novel classes. We use gray cylinders which have no overlap in either shape and color:

$$\mathcal{X}_l^{\text{case 2}} \triangleq \{X_{\ominus, c_3}\} (\text{gray cylinder}).$$

Putting it together, our entire training dataset is $\mathcal{X}^{\text{case } 1} = \mathcal{X}_l^{\text{case } 1} \cup \mathcal{X}_u$ or $\mathcal{X}^{\text{case } 2} = \mathcal{X}_l^{\text{case } 2} \cup \mathcal{X}_u$. We aim to verify the hypothesis that: *the representation learned by $\mathcal{X}^{\text{case } 1}$ provides a much smaller regression residual to \vec{y} than $\mathcal{X}^{\text{case } 2}$ for color class.*

Augmentation graph. Based on the data, we now define the probability of augmenting an image $X_{s,c}$ to another $X'_{s',c'}$:

$$\mathcal{T}(X'_{s',c'} | X_{s,c}) = \begin{cases} \tau_1 & \text{if } s = s', c = c', \\ \tau_s & \text{if } s = s', c \neq c', \\ \tau_c & \text{if } s \neq s', c = c', \\ \tau_0 & \text{if } s \neq s', c \neq c', \end{cases} \quad (6.7)$$

It is natural to assume the magnitude order that follows $\tau_1 \gg \max(\tau_s, \tau_c)$ and $\min(\tau_s, \tau_c) \gg \tau_0$. In two data settings $\mathcal{X}^{\text{case } 1}$ and $\mathcal{X}^{\text{case } 2}$, the corresponding augmentation matrices T_1, T_2 formed by $\mathcal{T}(\cdot|\cdot)$ are presented in Fig. 6.2 (b). According to Eq. (6.1), it can be verified that the adjacency matrices are $A_1 = T_1^2$ and $A_2 = T_2^2$ respectively.

Main analysis. We are primarily interested in analyzing the difference of the representation space derived from A_1 vs. A_2 . Since $\tau_1 \gg \max(\tau_s, \tau_c)$, one can show that A_1 and A_2 are positive-definite. The singular vector is thus equivalent to the eigenvector. Also note that A_1 and their square root T_1 have the same eigenvectors and order. It is thus equivalent to analyzing the eigenvectors of T_1 . Same with A_2 and T_2 . In this toy example, we consider the eigenvalue problem of the unnormalized adjacency matrix² for simplicity.

We put analysis on the top-2 eigenvectors $V_1^*, V_2^* \in \mathbb{R}^{5 \times 2}$ for A_1/A_2 — as we will see later, the top-1 eigenvector of T_1/T_2 usually functions at distinguishing known vs novel data, while the 2nd eigenvector functions

²The normalized/unnormalized adjacency matrix corresponds to the NCut/RatioCut problem respectively (Von Luxburg, 2007).

at distinguishing color or shape.

We let $U_1^* \in \mathbb{R}^{4 \times 2}$ contains the last 4 rows of V_1^* , and corresponds to the “representation” for the unlabeled data only. U_2^* is defined in the same way *w.r.t.* A_2 . We have the following theorem:

Theorem 6.3. *Assume $\tau_1 = 1, \tau_0 = 0, \tau_s < 1.5\tau_c$. We have*

$$U_1^* = \begin{bmatrix} a_1 & a_1 & b_1 & b_1 \\ a_2 & a_2 & b_2 & b_2 \end{bmatrix}^\top,$$

where a_1, b_1 are some positive real numbers, and a_2, b_2 has different signs.

$$U_2^* = \begin{cases} \frac{1}{2} \begin{bmatrix} 1 & 1 & 1 & 1 \\ 1 & 1 & -1 & -1 \end{bmatrix}^\top, & \text{if } \tau_s < \tau_c, \\ \frac{1}{2} \begin{bmatrix} 1 & 1 & 1 & 1 \\ -1 & 1 & -1 & 1 \end{bmatrix}^\top, & \text{if } \tau_s > \tau_c, \end{cases}$$

With label vector $\vec{y} = \{1, 1, 0, 0\}$, we have

$$\mathcal{R}(U_1^*, \vec{y}) = 0, \mathcal{R}(U_2^*, \vec{y}) = \begin{cases} 0, & \text{if } \tau_s < \tau_c \\ 1, & \text{if } \tau_s > \tau_c. \end{cases} \quad (6.8)$$

Interpretation of Theorem 6.3: The discussion can be divided into two cases: (1) $\tau_s < \tau_c$. (2) $\tau_s > \tau_c$. In the **first case** $\tau_s < \tau_c$, the connection between the same-color data pair is already stronger than the same-shape data pair. Thus the eigenvector corresponding to color information ($\frac{1}{2}[1, 1, -1, -1]^\top$) will be more prominent (and ranked higher in U_2^*) than “shape eigenvector” ($\frac{1}{2}[-1, 1, -1, 1]^\top$). Since the feature U_2^* already encodes sufficient information (color) of the labeling vector \vec{y} , fitting \vec{y} becomes easy and the residual $\mathcal{R}(U_2^*, \vec{y})$ becomes 0.

In NCD, we are more interested in the second case ($\tau_s > \tau_c$), where unlabeled data indeed need some help from labeled data for better clustering. Such help comes from the semantic connection between labeled data and unlabeled data. In our toy example, the semantic connection comes from the first row/column of T_1 and T_2 . However, the first row/column of T_2 is $[1, 0, 0, 0, 0]$, which means there is no extra information offered from $\mathcal{X}_l^{\text{case 2}}$. It is because $\mathcal{X}_l^{\text{case 2}}$ contains gray cylinders which have neither colors nor shapes connection to unlabeled data \mathcal{X}_u . Contrarily, $\mathcal{X}_l^{\text{case 1}}$ with red cylinder provides strong color prior. This allows the “color eigenvector” ($[a_2, a_2, -b_2, -b_2]$) to become a main component in U_1^* , making the residual $\mathcal{R}(U_1^*, \vec{y}) = 0$ even when $\tau_s > \tau_c$.

Main takeaway. In Theorem 6.3, we have verified the hypothesis that incorporating labeled data $\mathcal{X}_l^{\text{case 1}}$ (red cylinder) can reduce the residual $\mathcal{R}(U_1^*, \vec{y})$ more than using $\mathcal{X}_l^{\text{case 2}}$, especially when color is a weaker signal than shape in unlabeled data.

Extension: A more general result. Note that T_1 and T_2 are special cases of the following $T(t)$ with $t \in [\tau_0, \tau_c]$:

$$T(t) = \begin{bmatrix} \tau_1 & t & t & \tau_0 & \tau_0 \\ t & \tau_1 & \tau_c & \tau_s & \tau_0 \\ t & \tau_c & \tau_1 & \tau_0 & \tau_s \\ \tau_0 & \tau_s & \tau_0 & \tau_1 & \tau_c \\ \tau_0 & \tau_0 & \tau_s & \tau_c & \tau_1 \end{bmatrix},$$

where t indicates the strength of the connection between labeled data and a novel class in unlabeled data. Let U_t^* be the representation for unlabeled data derived from $T(t)$. The following theorem indicates that the residual decreases when t increases and the residual becomes 0 when t is larger than a threshold \bar{t} depending on the gap between τ_s and τ_c .

Theorem 6.4. Assume $\tau_1 = 1, \tau_0 = 0, 1.5\tau_c > \tau_s > \tau_c$. Let $\bar{t} = \sqrt{\frac{2(\tau_s - \tau_c)^2 \tau_c}{2\tau_c - \tau_s}}$,

$r : \mathbb{R} \mapsto (0, 1)$ be a real value function, we have

$$\mathcal{R}(U_t^*, \vec{y}) = \begin{cases} 0, & \text{if } t \in (\bar{t}, \tau_s), \\ r(t), & \text{if } t \in (0, \bar{t}), \\ 1, & \text{if } t = 0. \end{cases} \quad (6.9)$$

Can adding labeled data be harmful? We exemplify the scenario in Figure 6.1, where the umbrella images are given as a known class, undesirably causing the “mushroom with umbrella shape” to be grouped together. To formally analyze this case, we construct **case 3**:

$$\mathcal{X}_t^{\text{case 3}} \triangleq \{X_{\square, c_3}\}(\text{gray cube}).$$

In this case, we have the following Lemma 6.5.

Lemma 6.5. *If $\frac{\tau_c}{\tau_s} \in (1, 1.5)$, $\mathcal{R}(U_3^*, \vec{y}) - \mathcal{R}(U_2^*, \vec{y}) = 1$.*

The residual in case 3 is now larger than in case 2, since the shape is treated as a more important feature than the color feature (which relates to the target class). The main takeaway of this lemma is that the labeled data can be harmful when its connection with unlabeled data is undesirably stronger in the spurious feature dimension.

Qualitative results. The theoretical results can be verified in our empirical results by visualization in Fig. 6.3. Due to the space limitation, we include experimental details in Appendix B.1.4.2. As seen in Fig. 6.3 (a), the features of unlabeled data \mathcal{X}_u jointly learned with red cylinder $\mathcal{X}_t^{\text{case 1}}$ are more distinguishable by color attribute, as opposed to Fig. 6.3 (b).

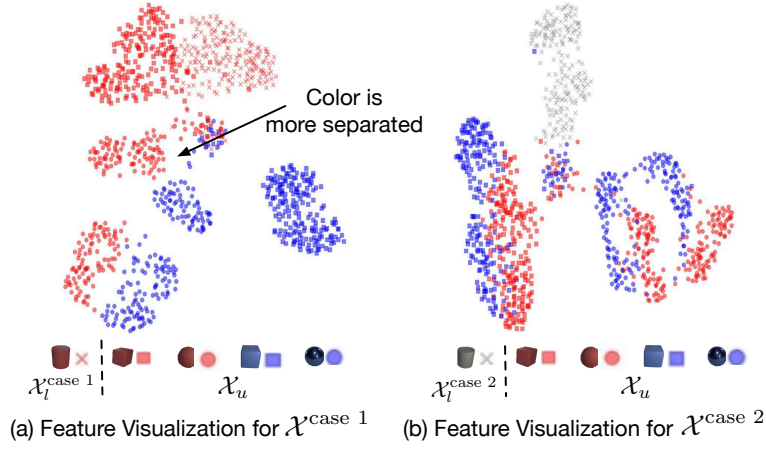


Figure 6.3: UMAP (McInnes et al., 2018) visualization of the feature embedding learned from $\mathcal{X}^{\text{case 1}}$ and $\mathcal{X}^{\text{case 2}}$ respectively. The model is trained with NCD Spectral Contrastive Loss.

6.4.3 Main Theory

The toy example offers an important insight that using the labeled data help reduce the residual when it provides the missing information of unlabeled data. In this section, we will formalize this insight by extending the toy example to a more general setting with N samples. We start with the definition of notations.

Notations. Recall that $V^* \in \mathbb{R}^{N \times k}$ is defined as the top- k singular vectors of \dot{A} , which is further split into two parts $L^* = [l_1, l_2, \dots, l_k] \in \mathbb{R}^{N_l \times k}$, $U^* = [u_1, u_2, \dots, u_k] \in \mathbb{R}^{N_u \times k}$, for labeled and unlabeled samples respectively. Then we let $V^b \in \mathbb{R}^{N \times (N-k)}$ be the remaining singular vectors of \dot{A} except top- k . Similarly, we split V^b into two parts ($L^b = [l_{k+1}, l_{k+2}, \dots, l_N] \in \mathbb{R}^{N_l \times (N-k)}$, $U^b = [u_{k+1}, u_{k+2}, \dots, u_N] \in \mathbb{R}^{N_u \times (N-k)}$).

We now present our first main result in Theorem 6.6.

Theorem 6.6. Denote the projection matrix $P_{L^b} = L^{b\top}(L^b L^{b\top})^\dagger L^b$, where † denotes the Moore-Penrose inverse. For any labeling vector $\vec{y} \in \{0, 1\}^{N_u}$, we

have

$$\mathcal{R}(U^*, \vec{y}) \leq \|(I - P_{L^b})U^{b^\top} \vec{y}\|_2^2. \quad (6.10)$$

Interpretation of Theorem 6.6. The bound of residual in Ineq. (6.10) is composed of two projections: U^{b^\top} and $(I - P_{L^b})$. We first consider the ignorance space formed by the first projection:

$$\text{ignorance space} \triangleq U^{b^\top} \vec{y},$$

which contains the information of the labeling vector \vec{y} that is not encoded in the learned representation U^* of the unlabeled data. Intuitively, when $\mathcal{R}(U^*, \vec{y}) > 0$, the labeling vector \vec{y} does not lie in the span of the existing representation U^* . On the other hand, $\mathcal{R}([U^* \ U^b], \vec{y}) = 0$ since U^* together with U^b forms a full rank space. We also define a measure of the ignorance degree of the current feature space: **ignorance degree** $\triangleq \mathfrak{I}(\vec{y}) = \frac{\|U^{b^\top} \vec{y}\|_2}{\|\vec{y}\|_2}$.

The second projection matrix $(I - P_{L^b})$ is composed of L^b , which we deem as the extra knowledge from known classes:

$$\text{extra knowledge} \triangleq L^b.$$

Multiplying the second projection matrix $(I - P_{L^b})$ further reduces the norm of the ignorance space by considering the extra knowledge from labeled data, since P_{L^b} is a projection matrix that projects a vector to the linear span of L^b . In the extreme case, when $U^{b^\top} \vec{y}$ fully lies in the linear span of L^b , the residual $\mathcal{R}(U^*, \vec{y})$ goes 0.

Next, we present another main theorem that bounds the linear probing error $\mathcal{E}(f)$ based on the relations between the known and novel classes. See Appendix B.1.3.4 for a detailed discussion and assumption.

Theorem 6.7. Let $[A_{ul} \in \mathbb{R}^{N_u \times N_l}, A_{uu} \in \mathbb{R}^{N_u \times N_u}]$ be the sub-matrix of the last N_u rows of \dot{A} , and q_i be the i -th eigenvector of A_{uu} . The linear probing error can be bounded as follows:

$$\mathcal{E}(f) \lesssim \frac{2N_u}{|\mathcal{Y}_u|} \left(\sum_i^{|\mathcal{Y}_u|} \underbrace{\mathfrak{I}(\vec{y}_i)}_{\text{ignorance degree}} (1 - \underbrace{\kappa(\vec{y}_i)^2}_{\text{knowledge coverage}}) + \frac{\|\dot{A} - \bar{A}\|_2}{\sigma_k - \sigma_{k+1}} \right),$$

where

$$\kappa(\vec{y}) = \cos(\bar{U}^{b\top} \vec{y}, \bar{\mathbf{p}}) \gtrsim \min_{i>k, j>k} \frac{2\sqrt{\frac{\vec{y}^\top q_i}{\bar{\eta}_u^i q_i} \frac{\vec{y}^\top q_j}{\bar{\eta}_u^j q_j}}}{\frac{\vec{y}^\top q_i}{\bar{\eta}_u^i q_i} + \frac{\vec{y}^\top q_j}{\bar{\eta}_u^j q_j}},$$

and \bar{A} is the approximation of \dot{A} by taking the expectation in the rows/-columns of labeled samples (Appendix B.1.3.2) with a similar motivation as the SBM model (Holland et al., 1983). In such condition, $\bar{U}^{b\top}$, $\bar{\mathbf{p}}$ and η_u is the approximation to $U^{b\top}$, L^b and A_{ul} accordingly.

Interpretation of $\kappa(\vec{y})$. We provide the detailed derivation of $\kappa(\vec{y})$ in Lemma B.16. Intuitively, $\kappa(\vec{y})$ measures the usefulness and relevance of knowledge from known classes for NCD. We formally call it coverage, which measures the cosine distance between the ignorance space and the extra knowledge:

$$\text{coverage} \triangleq \kappa(\vec{y}) = \cos(\underbrace{\bar{U}^{b\top} \vec{y}}_{\text{ignorance space}}, \underbrace{\bar{\mathbf{p}}}_{\text{extra knowledge}}).$$

Our Theorem 6.7 thus meaningfully shows that the linear probing error can be bounded more tightly as $\kappa(\vec{y})$ increases (i.e., when labeled data provides more useful information for the unlabeled data).

Implication of Theorem 6.7. Our theorem allows us to formalize answers to the “When and How” question. Firstly, the Theorem answers “how the labeled data helps”—because the knowledge from the known classes

changes the representation of unlabeled data and reduces the ignorance space for novel class discovery. Secondly, the Theorem answers “*when the labeled data helps*”. Specifically, labeled data helps when the coverage between ignorance space and extra knowledge is nonzero. In the extreme case, if the extra knowledge fully covers the ignorance space, we get the perfect performance (0 linear probing error).

6.5 Experiments on Common Benchmarks

Beyond theoretical insights, we show empirically that our proposed NCD spectral loss is effective on common benchmark datasets CIFAR-10 and CIFAR-100 (Krizhevsky et al., 2009). Following the well-established NCD benchmarks (Han et al., 2019, 2020b; Fini et al., 2021), each dataset is divided into two subsets, the labeled set that contains labeled images belonging to a set of known classes, and an unlabeled set with novel classes. Our comparison is on three benchmarks: C10-5 means CIFAR-10 datasets split with 5 known classes and 5 novel classes and C100-80 means CIFAR-100 datasets split with 80 known classes while C100-50 has 50 known classes. The division is consistent with Fini et al. (2021). We train the model by the proposed NSCL algorithm with details in Appendix B.1.4.1 and measure performance on the features in the penultimate layer of ResNet-18.

NSCL is competitive in discovering novel classes. Our proposed loss NSCL is amenable to the theoretical understanding of NCD, which is our primary goal of this work. Beyond theory, we show that NSCL is equally desirable in empirical performance. In particular, NSCL outperforms its rivals by a significant margin, as evidenced in Table 6.1. Our comparison covers an extensive collection of common NCD algorithms and baselines. In particular, on C100-50, we improve upon the best baseline ComEx by **10.6%**. This finding further validates that putting analysis on NSCL is

appealing for both theoretical and empirical reasons.

Table 6.1: Main Results. Results are reported in clustering accuracy (%) on the *training* split of the novel set. With the learned feature, we perform a K-Means clustering with the default setting in Python’s `sklearn` package. The accuracy of the novel classes is measured by solving an optimal assignment problem using the Hungarian algorithm (Kuhn, 1955). “C” is short for CIFAR. SCL denotes training with Spectral Contrastive Loss purely on \mathcal{D}_u while SCL[‡] is trained on $\mathcal{D}_u \cup \mathcal{D}_l$ unsupervisedly.

Method	C10-5	C100-80	C100-50
KCL (Hsu et al., 2018)	72.3	42.1	-
MCL (Hsu et al., 2019)	70.9	21.5	-
DTC (Han et al., 2019)	88.7	67.3	35.9
RS+ (Han et al., 2020a)	91.7	75.2	44.1
DualRank (Zhao and Han, 2021)	91.6	75.3	-
Joint (Jia et al., 2021)	93.4	76.4	-
UNO (Fini et al., 2021)	92.6	85.0	52.9
ComEx (Yang et al., 2022c)	93.6	85.7	53.4
SCL (HaoChen et al., 2021)	92.4	72.7	51.8
SCL [‡] (HaoChen et al., 2021)	93.7	68.9	53.3
NSCL (Ours)	97.5	85.9	64.0

Ablation study on the unsupervised counterpart. To verify whether the known classes indeed help discover new classes, we compare NSCL with the unsupervised counterpart (dubbed SCL) that is purely trained on the unlabeled data \mathcal{D}_u . Results show that the labeled data offers tremendous help and improves **13.2%** in novel class accuracy.

Supervision signals are important in the labeled data. We also analyze how much the supervision signals in labeled data help. To investigate it, we compare our method NSCL with SCL trained on $\mathcal{D}_u \cup \mathcal{D}_l$ in a purely unsupervised manner. The difference is that SCL does not utilize the label information in \mathcal{D}_l . We denote this setting as SCL[‡] in Table 6.1. Results show that NSCL provides stronger performance than SCL[‡]. The abla-

Table 6.2: Comparison of results reported in overall/novel/known accuracy (%) on the *test* split of CIFAR. The three metrics are calculated as follows. (1) **Known accuracy**: For the features from the labeled data, we train an additional linear head by linear probing and then measure classification accuracy based on the prediction \vec{h}_l ; (2) **Novel accuracy**: For features from the unlabeled data, we perform a K-Means clustering with the default setting in Python’s `sklearn` package, which produces the clustering prediction \vec{h}_u . The clustering accuracy is further measured by solving an optimal assignment problem using the Hungarian algorithm (Kuhn, 1955); (3) **Overall accuracy**. The overall accuracy is measured by concatenating the prediction \vec{h}_l and \vec{h}_u and then solving the assignment problem.

Method	C10-5			C100-50		
	All	Novel	Known	All	Novel	Known
DTC (Han et al., 2019)	68.7	78.6	58.7	32.5	34.7	30.2
RankStats (Han et al., 2020a)	89.7	88.8	90.6	55.3	40.9	69.7
UNO (Fini et al., 2021)	95.8	95.1	96.6	65.4	52.0	78.8
ComEx (Yang et al., 2022c)	95.0	93.2	96.7	67.2	54.5	80.1
NSCL (Ours)	95.5	96.7	94.2	67.4	57.1	77.4

tion suggests that relevant knowledge of known classes indeed provides meaningful help in novel class discovery.

NSCL is competitive in the inductive setting. We report performance comparison in Table 6.2, comprehensively measuring three accuracy metrics for all/novel/known classes respectively. Different from Table 6.1 which reports clustering results in a transductive manner, the performance in Table 6.2 is reported on the test split. For evaluation, we first collect the feature representations and then report overall/novel/known accuracy with inference details provided in the caption of Table 6.2. We see that NSCL establishes comparable performance with baselines on the labeled data from known classes and superior performance on novel class discovery. Notably, NSCL outperforms UNO (Fini et al., 2021) on C10-5 by 1.6% and outperforms ComEx (Yang et al., 2022c) by 2.6% on C100-50

in terms of novel accuracy.

6.6 Additional Related Work

Novel class discovery. Early works tackled novel category discovery (NCD) as a transfer learning problem, such as DTC (Han et al., 2019), KCL (Hsu et al., 2018), MCL (Hsu et al., 2019). Many subsequent works incorporate representation learning for NCD, including RankStats (Han et al., 2020a), NCL (Zhong et al., 2021a) and UNO (Fini et al., 2021). CompEx (Yang et al., 2022c) further uses a novelty detection module to better separate novel and known. However, none of the previous works theoretically analyzed the key question: *when and how do known classes help?* Li et al. (2022c) try to answer this question from an empirical perspective by comparing labeled datasets from different levels of semantic similarity. Chi et al. (2021) directly define a solvable condition for the NCD problem but do not investigate the semantic relationship between known and novel classes. This chapter introduces the first work that systematically investigates the “when and how” questions by modeling the sample relevance from a graph-theoretic perspective and providing a provable error bound for the NCD problem.

Spectral graph theory. Spectral graph theory is a classic research problem (Chung, 1997; Cheeger, 2015; Kannan et al., 2004; Lee et al., 2014; McSherry, 2001), which aims to partition the graph by studying the eigenspace of the adjacency matrix. The spectral graph theory is also widely applied in machine learning (Ng et al., 2001; Shi and Malik, 2000; Blum, 2001; Zhu et al., 2003; Argyriou et al., 2005; Shaham et al., 2018). Recently, HaoChen et al. (2021) derive a spectral contrastive loss from the factorization of the graph’s adjacency matrix which facilitates theoretical study in unsupervised domain adaptation (Shen et al., 2022; HaoChen et al., 2022). The graph definition in existing works is purely formed by the unlabeled data,

whereas our graph and adjacency matrix is uniquely tailored for the NCD problem setting and consists of both labeled data from known classes and unlabeled data from novel classes. We offer new theoretical guarantees and insights based on the relations between known and novel classes, which has not been explored in the previous literature.

Theoretical analysis on contrastive learning. Recent works have advanced contrastive learning with empirical success (Chen et al., 2020a; Khosla et al., 2020; Zhang et al., 2021; Wang et al., 2022a), which necessitates a theoretical foundation. Arora et al. (2019); Lee et al. (2021); Tosh et al. (2021a,b); Balestriero and LeCun (2022); Shi et al. (2023) provided provable guarantees on the representations learned by contrastive learning for linear probing. Shen et al. (2022); HaoChen et al. (2021, 2022) further modeled the pairwise relation from the graphic view and provided error analysis of the downstream tasks. However, the existing body of work has mostly focused on *unsupervised learning*. There is no prior theoretical work considering the NCD problem where both labeled and unlabeled data are presented. In this chapter, we systematically investigate how the label information can change the representation manifold and affect the downstream novel class discovery task.

6.7 Summary

In this chapter, we present a theoretical framework of novel class discovery and provide new insight on the research question: “*when and how does the known class help discover novel classes?*”. Specifically, we propose a graph-theoretic representation that can be learned through a new NCD Spectral Contrastive Loss (NSCL). Minimizing this objective is equivalent to factoring the graph’s adjacency matrix, which allows us to analyze the NCD quality by measuring the linear probing error on novel samples’ features. Our main result (Theorem 6.6) suggests such error can

be significantly reduced (even to 0) when the linear span of known samples' feature covers the "ignorance space" of unlabeled data in discovering novel classes. Our framework is also empirically appealing to use since it can achieve similar or better performance than existing methods on benchmark datasets. In summary, NSCL establishes a robust foundation for open-world representation learning by deciphering the influence of known classes in discovering new classes. This contributes profound theoretical and empirical impacts that stretch beyond conventional boundaries.

Chapter 7

A Graph-Theoretic Framework for Understanding ORL

Publication Statement. This chapter is joint work with Zhenmei Shi, and Yixuan Li. The paper version of this chapter appeared in NeurIPS23 ([Sun et al., 2023a](#)).

The preceding chapter delved into the analysis of the Novel Class Discovery (NCD) problem, which operates under the presumption that all training samples from known classes are labeled, thereby focusing its intent on discovering new classes within the unlabeled data. Open-world representation learning, on the other hand, pursues a more general objective, which endeavors to infer both known and novel classes in unlabeled data by leveraging prior knowledge from a labeled set. However, despite its significance, the theoretical underpinnings for this complex problem remain notably deficient, indicating a pressing need for further research and exploration in this domain.

This chapter bridges the gap by formalizing a graph-theoretic framework tailored for the open-world setting, where the clustering can be theoretically characterized by graph factorization. Our graph-theoretic

framework illuminates practical algorithms and provides guarantees. Specifically, utilizing our graph formulation, we present the algorithm — Spectral Open-world Representation Learning (SORL). This technique, though bearing similarities to NSCL as discussed in Chapter 6, operates within a distinct problem domain. The process of minimizing the corresponding loss is fundamentally analogous to executing a spectral decomposition on the graph. Such equivalence allows us to derive a provable error bound on the clustering performance for both known and novel classes, and analyze rigorously when labeled data helps. Empirically, SORL can match or outperform several strong baselines on common benchmark datasets, which is appealing for practical usage while enjoying theoretical guarantees.

7.1 Introduction

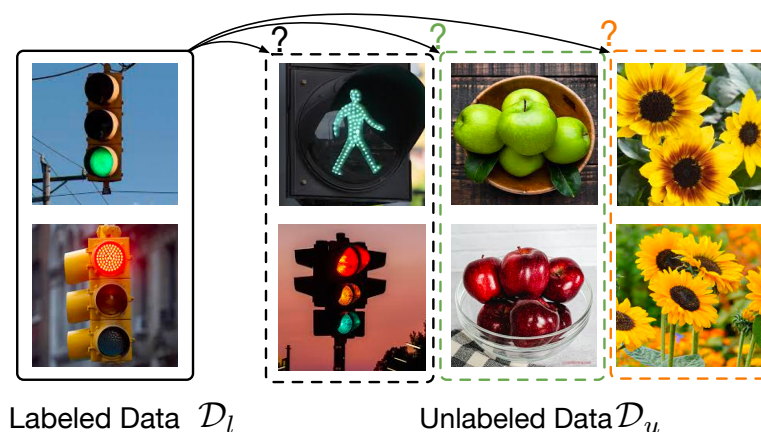


Figure 7.1: Open-world Representation Learning aims to learn representations that can correctly cluster samples in the novel class and classify samples in the known classes by utilizing knowledge from the labeled data. An open question is “*what is the role of the label information in shaping representations for both known and novel classes?*” This chapter aims to provide a formal understanding.

Machine learning models in the open world inevitably encounter data from both known and novel classes. Traditional supervised machine learning models are trained on a closed set of labels, and thus can struggle to effectively cluster new semantic concepts. On the other hand, open-world representation learning approaches, such as those discussed in studies (Cao et al., 2022; Vaze et al., 2022; Sun and Li, 2023), enable models to distinguish *both known and novel classes*, making them highly desirable for real-world scenarios. As shown in Figure 7.1, the learner has access to a labeled training dataset \mathcal{D}_l (from known classes) as well as a large unlabeled dataset \mathcal{D}_u (from both known and novel classes). By optimizing feature representations jointly from both labeled and unlabeled data, the learner aims to create meaningful cluster structures that correspond to either known or novel classes. With the explosive growth of data generated in various domains, open-world representation learning has emerged as a crucial problem in the field of machine learning.

Motivation. Different from self-supervised learning (Van den Oord et al., 2018; Chen et al., 2020a; Caron et al., 2020; He et al., 2020; Zbontar et al., 2021; Bardes et al., 2022; Chen and He, 2021; HaoChen et al., 2021), open-world representation learning allows harnessing the power of the labeled data for possible knowledge sharing and transfer to unlabeled data, and from known classes to novel classes. In this joint learning process, we argue that interesting intricacies can arise—the labeled data provided may be beneficial or unhelpful to the resulting clusters. We exemplify the nuances in Figure 7.1. In one scenario, when the model learns the labeled known classes (e.g., traffic light) by pushing red and green lights closer, such a relationship might transfer to help cluster green and red apples into a coherent cluster. Alternatively, when the connection between the labeled data and the novel class (e.g., flower) is weak, the benefits might be negligible. We argue—perhaps obviously—that a formalized understanding of the intricate phenomenon is needed.

Theoretical significance. To date, theoretical understanding of open-world representation learning is still in its infancy. In this chapter, we aim to fill the critical blank by analyzing this important learning problem from a rigorous theoretical standpoint. Our exposition gravitates around the open question: *what is the role of labeled data in shaping representations for both known and novel classes?* To answer this question, we formalize a graph-theoretic framework tailored for the open-world setting, where the vertices are all the data points and connected sub-graphs form classes (either known or novel). The edges are defined by a combination of supervised and self-supervised signals, which reflects the availability of both labeled and unlabeled data. Importantly, this graph facilitates the understanding of open-world representation learning from a spectral analysis perspective, where the clustering can be theoretically characterized by graph factorization. Based on the graph-theoretic formulation, we derive a formal error bound by contrasting the clustering performance for all classes, before and after adding the labeling information. Our Theorem 7.2 reveals the sufficient condition for the improved clustering performance for a class. Under the K-means measurement, the unlabeled samples in one class can be better clustered, if their overall connection to the labeled data is stronger than their self-clusterability.

Practical significance. Our graph-theoretic framework also illuminates practical algorithms with provided guarantees. In particular, based on our graph formulation, we present the algorithm called Spectral Open-world Representation Learning (SORL) adapted from Sun et al. (2023b). Minimizing this loss is equivalent to performing spectral decomposition on the graph (Section 7.3.2), which brings two key benefits: (1) it allows us to analyze the representation space and resulting clustering performance in closed-form; (2) practically, it enables end-to-end training in the context of deep networks. We show that our learning algorithm leads to strong empirical performance while enjoying theoretical guarantees. The

learning objective can be effectively optimized using stochastic gradient descent on modern neural network architecture, making it desirable for real-world applications.

7.2 Problem Setup

While Chapter 2.1 previously addressed the context of open-world representation learning, the subtle disparities in the notation for the purpose of theoretical analysis necessitate a re-visitation of the problem setup and notations. Formally, this section reiterates the data setup and learning objectives inherent in open-world representation learning.

Data setup. We consider the empirical training set $\mathcal{D}_l \cup \mathcal{D}_u$ as a union of labeled and unlabeled data.

1. The labeled set $\mathcal{D}_l = \{\bar{x}_i, y_i\}_{i=1}^n$, with $y_i \in \mathcal{Y}_l$. The label set \mathcal{Y}_l is known.
2. The unlabeled set $\mathcal{D}_u = \{\bar{x}_i\}_{i=1}^m$, where each sample \bar{x}_i can come from either known or novel classes¹. Note that we do not have access to the labels in \mathcal{D}_u . For mathematical convenience, we denote the underlying label set as \mathcal{Y}_{all} , where $\mathcal{Y}_l \subset \mathcal{Y}_{\text{all}}$. We denote $C = |\mathcal{Y}_{\text{all}}|$ the total number of classes.

We use \mathcal{P}_l and \mathcal{P} to denote the marginal distributions of labeled data and all data in the input space, respectively. Further, we let \mathcal{P}_{l_i} denote the distribution of labeled samples with class label $i \in \mathcal{Y}_l$.

Learning goal. Under the setting, the goal is to learn distinguishable representations *for both known and novel classes* simultaneously. The representation quality will be measured using classic metrics, such as K-

¹This generalizes the problem of Novel Class Discovery (Han et al., 2019; Hsu et al., 2018, 2019; Zhao and Han, 2021; Zhong et al., 2021a; Fini et al., 2021), which assumes the unlabeled set is *purely* from novel classes.

means clustering accuracy, which we will define mathematically in Section 7.4.2.2.

Theoretical analysis goal. We aim to comprehend the role of label information in shaping representations for both known and novel classes. It’s important to note that our theoretical approach aims to understand the perturbation in the clustering performance by labeling existing, previously unlabeled data points within the dataset. By contrasting the clustering performance before and after labeling these instances, we uncover the underlying structure and relations that the labels may reveal. This analysis provides invaluable insights into how labeling information can be effectively leveraged to enhance the representations of both known and novel classes.

7.3 A Spectral Approach for Open-world Representation Learning

In this section, we formalize and tackle the open-world representation learning (ORL) problem from a graph-theoretic view. Our fundamental idea is to formulate ORL as a clustering problem—where similar data points are grouped into the same cluster, by way of possibly utilizing helpful information from the labeled data \mathcal{D}_l . This clustering process can be modeled by a graph, where the vertices are all the data points and classes form connected sub-graphs. Specifically, utilizing our graph formulation, we present the algorithm — Spectral Open-world Representation Learning (SORL) in Section 7.3.2. The process of minimizing the corresponding loss is fundamentally analogous to executing a spectral decomposition on the graph.

7.3.1 A Graph-Theoretic Formulation

We start by formally defining the augmentation graph and adjacency matrix. For clarity, we use \bar{x} to indicate the natural sample (raw inputs without augmentation). Given an \bar{x} , we use $\mathcal{T}(x|\bar{x})$ to denote the probability of x being augmented from \bar{x} . For instance, when \bar{x} represents an image, $\mathcal{T}(\cdot|\bar{x})$ can be the distribution of common augmentations (Chen et al., 2020a) such as Gaussian blur, color distortion, and random cropping. The augmentation allows us to define a general population space \mathcal{X} , which contains all the original images along with their augmentations. In our case, \mathcal{X} is composed of augmented samples from both labeled and unlabeled data, with cardinality $|\mathcal{X}| = N$. We further denote \mathcal{X}_l as the set of samples (along with augmentations) from the labeled data part.

We define the graph $G(\mathcal{X}, w)$ with vertex set \mathcal{X} and edge weights w . To define edge weights w , we decompose the graph connectivity into two components: (1) self-supervised connectivity $w^{(u)}$ by treating all points in \mathcal{X} as entirely unlabeled, and (2) supervised connectivity $w^{(l)}$ by adding labeled information from \mathcal{P}_l to the graph. We proceed to define these two cases separately.

First, by assuming all points as unlabeled, two samples (x, x^+) are considered a **positive pair** if:

Unlabeled Case (u): x and x^+ are augmented from the same image $\bar{x} \sim \mathcal{P}$.

For any two augmented data $x, x' \in \mathcal{X}$, $w_{xx'}^{(u)}$ denotes the marginal probability of generating the pair:

$$w_{xx'}^{(u)} \triangleq \mathbb{E}_{\bar{x} \sim \mathcal{P}} \mathcal{T}(x|\bar{x}) \mathcal{T}(x'|\bar{x}), \quad (7.1)$$

which can be viewed as self-supervised connectivity (Chen et al., 2020a; HaoChen et al., 2021). However, different from self-supervised learning, ORL has access to the labeled information for a subset of nodes, which

allows adding additional connectivity to the graph. Accordingly, the positive pair can be defined as:

Labeled Case (1): x and x^+ are augmented from two labeled samples \bar{x}_l and \bar{x}'_l with the same known class i . In other words, both \bar{x}_l and \bar{x}'_l are drawn independently from \mathcal{P}_i .

Considering both case (u) and case (1), the overall edge weight for any pair of data (x, x') is given by:

$$w_{xx'} = \eta_u w_{xx'}^{(u)} + \eta_l w_{xx'}^{(l)}, \text{ where } w_{xx'}^{(l)} \triangleq \sum_{i \in \mathcal{Y}_i} \mathbb{E}_{\bar{x}_l \sim \mathcal{P}_i} \mathbb{E}_{\bar{x}'_l \sim \mathcal{P}_i} \mathcal{T}(x|\bar{x}_l) \mathcal{T}(x'|\bar{x}'_l), \quad (7.2)$$

and η_u, η_l modulates the importance between the two cases. The magnitude of $w_{xx'}$ indicates the “positiveness” or similarity between x and x' . We then use $w_x = \sum_{x' \in \mathcal{X}} w_{xx'}$ to denote the total edge weights connected to a vertex x .

Remark: A graph perturbation view. With the graph connectivity defined above, we can now define the adjacency matrix $A \in \mathbb{R}^{N \times N}$ with entries $A_{xx'} = w_{xx'}$. Importantly, the adjacency matrix can be decomposed into two parts:

$$A = \eta_u A^{(u)} + \eta_l A^{(l)}, \quad (7.3)$$

↓ *Perturbation by adding labels*

which can be regarded as the self-supervised adjacency matrix $A^{(u)}$ perturbed by additional labeling information encoded in $A^{(l)}$. This graph perturbation view serves as a critical foundation for our theoretical analysis of the clustering performance in Section 7.4. As a standard technique in graph theory (Chung, 1997), we use the *normalized adjacency matrix* of $G(\mathcal{X}, w)$:

$$\dot{A} \triangleq D^{-\frac{1}{2}} A D^{-\frac{1}{2}}, \quad (7.4)$$

where $D \in \mathbb{R}^{N \times N}$ is a diagonal matrix with $D_{xx} = w_x$. The normalization

balances the degree of each node, reducing the influence of vertices with very large degrees. The normalized adjacency matrix defines the probability of x and x' being considered as the positive pair from the perspective of augmentation, which helps derive the new representation learning loss as we show next.

7.3.2 SORL: Spectral Open-World Representation Learning

We introduce the algorithm called Spectral Open-world Representation Learning (SORL), which can be derived from a spectral decomposition of \dot{A} . This technique, though bearing similarities to NSCL as discussed in Chapter 6, operates within a different problem domain. The algorithm has both practical and theoretical values. First, it enables efficient end-to-end training in the context of modern neural networks. More importantly, it allows drawing a theoretical equivalence between learned representations and the top- k singular vectors of \dot{A} . Such equivalence facilitates theoretical understanding of the clustering structure encoded in \dot{A} . Specifically, we consider low-rank matrix approximation:

$$\min_{F \in \mathbb{R}^{N \times k}} \mathcal{L}_{\text{mf}}(F, A) \triangleq \left\| \dot{A} - FF^\top \right\|_F^2 \quad (7.5)$$

According to the Eckart–Young–Mirsky theorem (Eckart and Young, 1936), the minimizer of this loss function is $F_k \in \mathbb{R}^{N \times k}$ such that $F_k F_k^\top$ contains the top- k components of \dot{A} 's SVD decomposition.

Now, if we view each row \mathbf{f}_x^\top of F as a scaled version of learned feature embedding $f : \mathcal{X} \mapsto \mathbb{R}^k$, the $\mathcal{L}_{\text{mf}}(F, A)$ can be written as a form of the contrastive learning objective. We formalize it in Theorem 7.1 below².

²Theorem 7.1 is primarily adapted from Theorem 6.1 with a distinction in the data setting, as Chapter 6 does not consider known class samples within the unlabeled dataset.

Theorem 7.1. We define $\mathbf{f}_x = \sqrt{w_x}f(x)$ for some function f . Recall η_u, η_l are coefficients defined in Eq. (7.1). Then minimizing the loss function $\mathcal{L}_{\text{mf}}(F, A)$ is equivalent to minimizing the following loss function for f , which we term **Spectral Open-world Representation Learning (SORL)**:

$$\mathcal{L}_{\text{SORL}}(f) \triangleq -2\eta_u\mathcal{L}_1(f) - 2\eta_l\mathcal{L}_2(f) + \eta_u^2\mathcal{L}_3(f) + 2\eta_u\eta_l\mathcal{L}_4(f) + \eta_l^2\mathcal{L}_5(f), \quad (7.6)$$

where

$$\begin{aligned} \mathcal{L}_1(f) &= \sum_{i \in \mathcal{Y}_l} \mathbb{E}_{\substack{\bar{x}_l \sim \mathcal{P}_l, \bar{x}'_l \sim \mathcal{P}_l, \\ x \sim \mathcal{T}(\cdot | \bar{x}_l), x^+ \sim \mathcal{T}(\cdot | \bar{x}'_l)}} [f(x)^\top f(x^+)], \\ \mathcal{L}_2(f) &= \mathbb{E}_{\substack{\bar{x}_u \sim \mathcal{P}, \\ x \sim \mathcal{T}(\cdot | \bar{x}_u), x^+ \sim \mathcal{T}(\cdot | \bar{x}_u)}} [f(x)^\top f(x^+)], \\ \mathcal{L}_3(f) &= \sum_{i, j \in \mathcal{Y}_l} \mathbb{E}_{\substack{\bar{x}_l \sim \mathcal{P}_l, \bar{x}'_l \sim \mathcal{P}_j, \\ x \sim \mathcal{T}(\cdot | \bar{x}_l), x^- \sim \mathcal{T}(\cdot | \bar{x}'_l)}} \left[(f(x)^\top f(x^-))^2 \right], \\ \mathcal{L}_4(f) &= \sum_{i \in \mathcal{Y}_l} \mathbb{E}_{\substack{\bar{x}_l \sim \mathcal{P}_l, \bar{x}_u \sim \mathcal{P}, \\ x \sim \mathcal{T}(\cdot | \bar{x}_l), x^- \sim \mathcal{T}(\cdot | \bar{x}_u)}} \left[(f(x)^\top f(x^-))^2 \right], \\ \mathcal{L}_5(f) &= \mathbb{E}_{\substack{\bar{x}_u \sim \mathcal{P}, \bar{x}'_u \sim \mathcal{P}, \\ x \sim \mathcal{T}(\cdot | \bar{x}_u), x^- \sim \mathcal{T}(\cdot | \bar{x}'_u)}} \left[(f(x)^\top f(x^-))^2 \right]. \end{aligned}$$

Proof. (sketch) We can expand $\mathcal{L}_{\text{mf}}(F, A)$ and obtain

$$\begin{aligned} \mathcal{L}_{\text{mf}}(F, A) &= \sum_{x, x' \in \mathcal{X}} \left(\frac{w_{xx'}}{\sqrt{w_x w_{x'}}} - \mathbf{f}_x^\top \mathbf{f}_{x'} \right)^2 \\ &= \text{const} + \sum_{x, x' \in \mathcal{X}} \left(-2w_{xx'} f(x)^\top f(x') + w_x w_{x'} (f(x)^\top f(x'))^2 \right) \end{aligned}$$

The form of $\mathcal{L}_{\text{SORL}}(f)$ is derived from plugging $w_{xx'}$ (defined in Eq. (7.1)) and w_x . Full proof is in Appendix B.2.1. \square

Interpretation of $\mathcal{L}_{\text{SORL}}(f)$. At a high level, \mathcal{L}_1 and \mathcal{L}_2 push the em-

beddings of **positive pairs** to be closer while \mathcal{L}_3 , \mathcal{L}_4 and \mathcal{L}_5 pull away the embeddings of **negative pairs**. In particular, \mathcal{L}_1 samples two random augmentation views of two images from labeled data with the **same** class label, and \mathcal{L}_2 samples two views from the same image in \mathcal{X} . For negative pairs, \mathcal{L}_3 uses two augmentation views from two samples in \mathcal{X}_l with **any** class label. \mathcal{L}_4 uses two views of one sample in \mathcal{X}_l and another one in \mathcal{X} . \mathcal{L}_5 uses two views from two random samples in \mathcal{X} .

7.4 Theoretical Analysis

So far we have presented a spectral approach for open-world representation learning based on graph factorization. Under this framework, we now formally analyze: *how does the labeling information shape the representations for known and novel classes?*

7.4.1 An Illustrative Example

We consider a toy example that helps illustrate the core idea of our theoretical findings. Specifically, the example aims to distinguish 3D objects with different shapes, as shown in Figure 7.2. These images are generated by a 3D rendering software (Johnson et al., 2017) with user-defined properties including colors, shape, size, position, etc. We are interested in contrasting the representations (in the form of singular vectors), when the label information is either incorporated in training or not.

Data design. Suppose the training samples come from three types, \mathcal{X}_{\square} , \mathcal{X}_{\circ} , \mathcal{X}_{\ominus} . Let \mathcal{X}_{\square} be the sample space with **known** class, and \mathcal{X}_{\circ} , \mathcal{X}_{\ominus} be the sample space with **novel** classes. Further, the two novel classes are constructed to have different relationships with the known class. Specifically, \mathcal{X}_{\circ} shares some similarity with \mathcal{X}_{\square} in color (red and blue); whereas another novel class \mathcal{X}_{\ominus} has no obvious similarity with the known class.

Without any labeling information, it can be difficult to distinguish \mathcal{X}_\circ from \mathcal{X}_{\square} since samples share common colors. We aim to verify the hypothesis that: *adding labeling information to \mathcal{X}_{\square} (i.e., connecting \square and \square) has a larger (beneficial) impact to cluster \mathcal{X}_\circ than \mathcal{X}_{\square} .*

Augmentation graph. Based on the data design, we formally define the augmentation graph, which encodes the probability of augmenting a source image \bar{x} to the augmented view x :

$$\mathcal{T}(x | \bar{x}) = \begin{cases} \tau_1 & \text{if } \text{color}(x) = \text{color}(\bar{x}), \text{shape}(x) = \text{shape}(\bar{x}); \\ \tau_c & \text{if } \text{color}(x) = \text{color}(\bar{x}), \text{shape}(x) \neq \text{shape}(\bar{x}); \\ \tau_s & \text{if } \text{color}(x) \neq \text{color}(\bar{x}), \text{shape}(x) = \text{shape}(\bar{x}); \\ \tau_0 & \text{if } \text{color}(x) \neq \text{color}(\bar{x}), \text{shape}(x) \neq \text{shape}(\bar{x}). \end{cases} \quad (7.7)$$

With Eq. (7.7) and the definition of the adjacency matrix in Section 7.3.1, we can derive the analytic form of $A^{(u)}$ and A , as shown in Figure 7.2(b). We refer readers to Appendix B.2.2 for the detailed derivation. The two matrices allow us to contrast the connectivity changes in the graph, before and after the labeling information is added.

Insights. We are primarily interested in analyzing the difference of the representation space derived from $A^{(u)}$ and A . We visualize the top-3 eigenvectors³ of the normalized adjacency matrix $\dot{A}^{(u)}$ and \dot{A} in Figure 7.3(a), where the results are based on the magnitude order $\tau_1 \gg \tau_c > \tau_s > 0$. Our key takeaway is: *adding labeling information to known class \mathcal{X}_{\square} helps better distinguish the known class itself and the novel class \mathcal{X}_\circ , which has a stronger connection/similarity with \mathcal{X}_{\square} .*

Qualitative analysis. Our theoretical insight can also be verified empirically, by learning representations on over 10,000 samples using the loss defined in Section 7.3.2. Due to the space limitation, we include ex-

³When $\tau_1 \gg \tau_c > \tau_s > 0$, the top-3 eigenvectors are almost equivalent to the feature embedding.

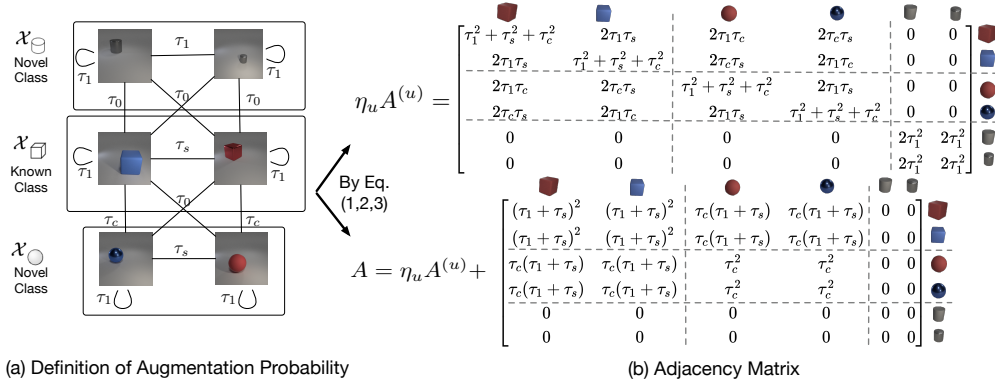


Figure 7.2: An illustrative example for theoretical analysis. We consider a 6-node graph with one known class (cube) and two novel classes (sphere, cylinder). (a) The augmentation probabilities between nodes are defined by their color and shape in Eq. (7.7). (b) The adjacency matrix can then be calculated by Equations in Sec. 7.3.1 where we let $\tau_0 = 0, \eta_u = 6, \eta_l = 4$. The calculation details are in Appendix B.2.2. The magnitude order follows $\tau_1 \gg \tau_c > \tau_s > 0$.

perimental details in Appendix B.2.5.1. In Figure 7.3(b), we visualize the learned features through UMAP (McInnes et al., 2018). Indeed, we observe that samples become more concentrated around different shape classes after adding labeling information to the cube class.

7.4.2 Main Theory

The toy example offers an important insight that the added labeled information is more helpful for the class with a stronger connection to the known class. In this section, we formalize this insight by extending the toy example to a more general setting. As a roadmap, we derive the result through three steps: (1) derive the closed-form solution of the learned representations; (2) define the clustering performance by the K-means measure; (3) contrast the resulting clustering performance before and after adding labels. We start by deriving the representations.

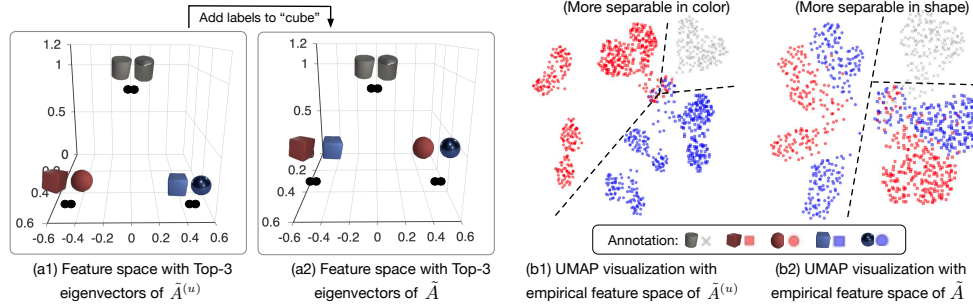


Figure 7.3: Visualization of representation space for toy example. (a) Theoretically contrasting the feature formed by top-3 eigenvectors of $\hat{A}^{(u)}$ and \hat{A} respectively. (b) UMAP visualization of the features learned without (left) and with labeled information (right). Details are in Appendix B.2.2 (eigenvector calculation) and Appendix B.2.5.1 (visualization setting).

7.4.2.1 Learned Representations in Analytic Form

Representation without labels. To obtain the representations, one can train the neural network $f : \mathcal{X} \mapsto \mathbb{R}^k$ using the spectral loss defined in Equation 7.6. We assume that the optimizer is capable to obtain the representation $Z^{(u)} \in \mathbb{R}^{N \times k}$ that minimizes the loss, where each row vector $\mathbf{z}_i = f(x_i)^\top$. Recall that Theorem 7.1 allows us to derive a closed-form solution for the learned feature space by the spectral decomposition of the adjacency matrix, which is $\hat{A}^{(u)}$ in the case without labeling information. Specifically, we have $F_k^{(u)} = \sqrt{D^{(u)}} Z^{(u)}$, where $F_k^{(u)} F_k^{(u)\top}$ contains the top- k components of $\hat{A}^{(u)}$'s SVD decomposition and $D^{(u)}$ is the diagonal matrix defined based on the row sum of $A^{(u)}$. We further define the top- k singular vectors of $A^{(u)}$ as $V_k^{(u)} \in \mathbb{R}^{N \times k}$, so we have $F_k^{(u)} = V_k^{(u)} \sqrt{\Sigma_k^{(u)}}$, where $\Sigma_k^{(u)}$ is a diagonal matrix of the top- k singular values of $A^{(u)}$. By equalizing the two forms of $F_k^{(u)}$, the closed-form solution of the learned feature space is given by $Z^{(u)} = [D^{(u)}]^{-\frac{1}{2}} V_k^{(u)} \sqrt{\Sigma_k^{(u)}}$.

Representation perturbation by adding labels. We now analyze how the representation is “perturbed” as a result of adding label information. We

consider $|\mathcal{Y}_l| = 1^4$ to facilitate a better understanding of our key insight. We can rewrite A in Eq. 7.3 as:

$$A(\delta) \triangleq \eta_u A^{(u)} + \delta \mathbb{I}^\top,$$

where we replace η_l to δ to be more apparent in representing the perturbation and define $\mathbb{I} \in \mathbb{R}^N$, $(\mathbb{I})_x = \mathbb{E}_{\bar{x}_l \sim \mathcal{P}_{l_1}} \mathcal{T}(x|\bar{x}_l)$. Note that \mathbb{I} can be interpreted as the vector of “the semantic connection for sample x to the labeled data”. One can easily extend to r classes by letting $\mathbb{I} \in \mathbb{R}^{N \times r}$.

Here we treat the adjacency matrix as a function of the perturbation. In a similar manner as above, we can derive the normalized adjacency matrix $\tilde{A}(\delta)$ and the feature representation $Z(\delta)$ in closed-form. The details are included in Appendix B.2.3.3.

7.4.2.2 Evaluation Target

With the learned representations, we can evaluate their quality by the clustering performance. Our theoretical analysis of the clustering performance can well connect to empirical evaluation strategy in the literature (Yang et al., 2022c) using K -means clustering accuracy/error. Formally, we define the ground-truth partition of clusters by $\Pi = \{\pi_1, \pi_2, \dots, \pi_C\}$, where π_i is the set of samples’ indices with underlying label y_i and C is the total number of classes (including both known and novel). We further let $\boldsymbol{\mu}_\pi = \mathbb{E}_{i \in \pi} \mathbf{z}_i$ be the center of features in π , and the average of all feature vectors be $\boldsymbol{\mu}_\Pi = \mathbb{E}_{j \in [N]} \mathbf{z}_j$.

The clustering performance of K-means depends on two measurements: **Intra-class** measure and **Inter-class** measure. Specifically, we let the intra-class measure be the average Euclidean distance from the samples’ feature to the corresponding cluster center and we measure the inter-class sepa-

⁴To understand the perturbation by adding labels from more than one class, one can take the summation of the perturbation by each class.

ration as the distances between cluster centers:

$$\mathcal{M}_{\text{intra-class}}(\Pi, Z) \triangleq \sum_{\pi \in \Pi} \sum_{i \in \pi} \|\mathbf{z}_i - \boldsymbol{\mu}_\pi\|^2, \mathcal{M}_{\text{inter-class}}(\Pi, Z) \triangleq \sum_{\pi \in \Pi} |\pi| \|\boldsymbol{\mu}_\pi - \boldsymbol{\mu}_\Pi\|^2. \quad (7.8)$$

Strong clustering results translate into low $\mathcal{M}_{\text{intra-class}}$ and high $\mathcal{M}_{\text{inter-class}}$. Thus we define the **K-means measure** as:

$$\mathcal{M}_{kms}(\Pi, Z) \triangleq \mathcal{M}_{\text{intra-class}}(\Pi, Z) / \mathcal{M}_{\text{inter-class}}(\Pi, Z). \quad (7.9)$$

We also formally show in Theorem B.20 (Appendix) that the K-means clustering error⁵ is asymptotically equivalent to the K-means measure we defined above.

7.4.2.3 Perturbation in Clustering Performance

With the evaluation target defined above, our main analysis will revolve around analyzing “*how the extra label information help reduces $\mathcal{M}_{kms}(\Pi, Z)$* ”. Formally, we investigate the following error difference, as a result of added label information:

$$\Delta_{kms}(\delta) = \mathcal{M}_{kms}(\Pi, Z) - \mathcal{M}_{kms}(\Pi, Z(\delta)),$$

where the closed-form solution is given by the following theorem. Positive $\Delta_{kms}(\delta)$ means improved clustering, as a result of adding labeling information.

⁵It is theoretically inconvenient to directly analyze the clustering error since it is a non-differentiable target.

Theorem 7.2. (Main result.) Denote $V_{\emptyset}^{(u)} \in \mathbb{R}^{N \times (N-k)}$ as the null space of $V_k^{(u)}$ and $\tilde{A}_k^{(u)} = V_k^{(u)} \Sigma_k^{(u)} V_k^{(u)\top}$ as the rank- k approximation for $\tilde{A}^{(u)}$. Given $\delta, \eta_1 > 0$ and let \mathcal{G}_k as the spectral gap between k -th and $k+1$ -th singular values of $\tilde{A}^{(u)}$, we have:

$$\Delta_{kms}(\delta) = \delta \eta_1 \operatorname{Tr} \left(\Upsilon \left(V_k^{(u)} V_k^{(u)\top} \mathfrak{U}^\top (I + V_{\emptyset}^{(u)} V_{\emptyset}^{(u)\top}) - 2\tilde{A}_k^{(u)} \operatorname{diag}(\mathfrak{l}) \right) \right) + O\left(\frac{1}{\mathcal{G}_k} + \delta^2\right),$$

where $\operatorname{diag}(\cdot)$ converts the vector to the corresponding diagonal matrix and $\Upsilon \in \mathbb{R}^{N \times N}$ is a matrix encoding the **ground-truth clustering structure** in the way that $\Upsilon_{xx'} > 0$ if x and x' has the same label and $\Upsilon_{xx'} < 0$ otherwise. The concrete form and the proof are in Appendix B.2.3.3.

Theorem 7.2 is more general but less intuitive to understand. To gain a better insight, we introduce Theorem 7.3 which provides more direct implications. We provide the justification of the assumptions and the formal proof in Appendix B.2.3.4.

Theorem 7.3. (Intuitive result.) Assuming the spectral gap \mathcal{G}_k is sufficiently large and \mathfrak{l} lies in the linear span of $V_k^{(u)}$. We also assume $\forall \pi_c \in \Pi, \forall i \in \pi_c, \mathfrak{l}_{(i)} =: \mathfrak{l}_{\pi_c}$ which represents the connection between class c to the labeled data. Given $\delta, \eta_1, \eta_2 > 0$, we have:

$$\Delta_{kms}(\delta) \geq \delta \eta_1 \eta_2 \sum_{\pi_c \in \Pi} |\pi_c| \mathfrak{l}_{\pi_c} \Delta_{\pi_c}(\delta),$$

where

$$\Delta_{\pi_c}(\delta) = \left(\mathfrak{l}_{\pi_c} - \frac{1}{N} \right) - \left(\frac{2N - 2|\pi_c|}{N} \right) \left(\mathbb{E}_{i \in \pi_c} \mathbb{E}_{j \in \pi_c} \mathbf{z}_i^\top \mathbf{z}_j - \mathbb{E}_{i \in \pi_c} \mathbb{E}_{j \notin \pi_c} \mathbf{z}_i^\top \mathbf{z}_j \right).$$

Connection from class c to the labeled data.
Intra-class similarity
Inter-class similarity

Implications. In Theorem 7.3, we define the **class-wise perturbation** of the K-means measure as $\Delta_{\pi_c}(\delta)$. This way, we can interpret the effect of adding labels for a specific class c . If we desire $\Delta_{\pi_c}(\delta)$ to be large, the sufficient condition is that

connection of class c to the labeled data > intra-class similarity - inter-class similarity.

We use examples in Figure 7.1 to epitomize the core idea. Specifically, our unlabeled samples consist of three underlying classes: traffic lights (known), apples (novel), and flowers (novel). **(a)** For unlabeled traffic lights from *known classes* which are strongly connected to the labeled data, adding labels to traffic lights can largely improve the clustering performance; **(b)** For *novel classes* like apples, it may also help when they have a strong connection to the traffic light, and their intra-class similarity is not as strong (due to different colors); **(c)** However, labeled data may offer little improvement in clustering the flower class, due to the minimal connection to the labeled data and that flowers’ self-clusterability is already strong.

7.5 Empirical Validation of Theory

Beyond theoretical insights, we show empirically that SORL is effective on standard benchmark image classification datasets CIFAR-10/100 (Krizhevsky et al., 2009). Following the seminal work ORCA (Cao et al., 2022), classes are divided into 50% known and 50% novel classes. We then use 50% of samples from the known classes as the labeled dataset, and the rest as the unlabeled set. We follow the evaluation strategy in (Cao et al., 2022) and report the following metrics: (1) classification accuracy on known classes, (2) clustering accuracy on the novel data, and (3) overall accuracy on all classes. More experiment details are in Appendix B.2.5.2.

Table 7.1: Main Results. Mean and std are estimated on five different runs. Baseline numbers are from (Sun and Li, 2023; Cao et al., 2022).

Method	CIFAR-10			CIFAR-100		
	All	Novel	Known	All	Novel	Known
FixMatch (Kurakin et al., 2020)	49.5	50.4	71.5	20.3	23.5	39.6
DS³L (Guo et al., 2020)	40.2	45.3	77.6	24.0	23.7	55.1
CGDL (Sun et al., 2020a)	39.7	44.6	72.3	23.6	22.5	49.3
DTC (Han et al., 2019)	38.3	39.5	53.9	18.3	22.9	31.3
RankStats (Zhao and Han, 2021)	82.9	81.0	86.6	23.1	28.4	36.4
SimCLR (Chen et al., 2020a)	51.7	63.4	58.3	22.3	21.2	28.6
ORCA (Cao et al., 2022)	88.3 \pm 0.3	87.5 \pm 0.2	89.9 \pm 0.4	47.2 \pm 0.7	41.0 \pm 1.0	66.7 \pm 0.2
GCD (Vaze et al., 2022)	87.5 \pm 0.5	86.7 \pm 0.4	90.1 \pm 0.3	46.8 \pm 0.5	43.4 \pm 0.7	69.7\pm0.4
SORL (Ours)	93.5 \pm 1.0	92.5 \pm 0.1	94.0 \pm 0.2	56.1 \pm 0.3	52.0 \pm 0.2	68.2 \pm 0.1

SORL achieves competitive performance. Our proposed loss SORL is amenable to the theoretical understanding, which is our primary goal of this work. Beyond theory, we show that SORL is equally desirable in empirical performance. In particular, SORL displays competitive performance compared to existing methods, as evidenced in Table 7.1. Our comparison covers an extensive collection of very recent algorithms developed for this problem, including ORCA (Cao et al., 2022), GCD (Vaze et al., 2022). We also compare methods in related problem domains: (1) Semi-Supervised Learning (Kurakin et al., 2020; Guo et al., 2020; Sun et al., 2020a), (2) Novel Class Discovery (Han et al., 2019; Zhao and Han, 2021), (3) common representation learning method SimCLR (Chen et al., 2020a). In particular, on CIFAR-100, we improve upon the best baseline ORCA by **8.9%** in terms of overall accuracy. Our result further validates that putting analysis on SORL is appealing for both theoretical and empirical reasons.

7.6 Broader Impact

From a theoretical perspective, our graph-theoretic framework can facilitate and deepen the understanding of other representation learning methods that commonly involve the notion of positive/negative pairs. In Appendix B.2.4, we exemplify how our framework can be potentially generalized to other common contrastive loss functions (Van den Oord et al., 2018; Khosla et al., 2020; Chen et al., 2020a), and baseline methods that are tailored for the open-world representation learning problem (e.g., GCD (Vaze et al., 2022)). Hence, we believe our theoretical framework has a broader utility and significance.

From a practical perspective, our work can directly impact and benefit many real-world applications, where unlabeled data are produced at an incredible rate today. Major companies exhibit a strong need for making their machine learning systems and services amendable for the open-world setting but lack fundamental and systematic knowledge. Hence, our research advances the understanding of open-world machine learning and helps the industry improve ML systems by discovering insights and structures from unlabeled data.

7.7 Additional Related Work

Semi-supervised learning. Semi-supervised learning (SSL) is a classic problem in machine learning. SSL typically assumes the same class space between labeled and unlabeled data, and hence remains closed-world. A rich line of empirical works (Chapelle et al., 2006; Lee et al., 2013; Sajjadi et al., 2016; Laine and Aila, 2017; Zhai et al., 2019; Rebuffi et al., 2020; Kurakin et al., 2020; Guo et al., 2020; Chen et al., 2020c; Yu et al., 2020; Park et al., 2023; Saito et al., 2021; Huang et al., 2021a; Yang et al., 2022a; Liu et al., 2010) and theoretical efforts (Oymak and Gulcu, 2021;

Sokolovska et al., 2008; Singh et al., 2008; Balcan and Blum, 2005; Rigollet, 2007; Wasserman and Lafferty, 2007; Niyogi, 2013) have been made to address this problem. An important class of SSL methods is to represent data as graphs and predict labels by aggregating proximal nodes' labels (Zhu, 2002; Zhang et al., 2009; Wang and Zhang, 2006; Fergus et al., 2009; Jebara et al., 2009; Zhou et al., 2004; Argyriou et al., 2005). Different from classic SSL, we allow its semantic space to cover both known and novel classes. Accordingly, we contribute a new graph-theoretic framework tailored to the open-world setting, and reveal new insights on how the labeled data can benefit the clustering performance on both known and novel classes.

Spectral graph theory. Spectral graph theory is a classic research problem Von Luxburg (2007); Chung (1997); Cheeger (2015); Kannan et al. (2004); Lee et al. (2014); McSherry (2001), which aims to partition the graph by studying the eigenspace of the adjacency matrix. The spectral graph theory is also widely applied in machine learning Ng et al. (2001); Shi and Malik (2000); Blum (2001); Zhu et al. (2003); Argyriou et al. (2005); Shaham et al. (2018); Sun et al. (2023b). Recently, HaoChen et al. (2021) derive a spectral contrastive loss from the factorization of the graph's adjacency matrix which facilitates theoretical study in unsupervised domain adaptation Shen et al. (2022); HaoChen et al. (2022). In these works, the graph's formulation is exclusively based on unlabeled data. Sun et al. Sun et al. (2023b) later expanded this spectral contrastive loss approach to cater to learning environments that encompass both labeled data from known classes and unlabeled data from novel ones. In this chapter, our adaptation of the loss function from Sun et al. (2023b) is tailored to address the open-world representation learning challenge, considering known class samples within unlabeled data.

Theory for self-supervised learning. A proliferation of works in self-supervised representation learning demonstrates the empirical success (Van den

Oord et al., 2018; Chen et al., 2020a; Caron et al., 2020; He et al., 2020; Zbontar et al., 2021; Bardes et al., 2022; Chen and He, 2021; HaoChen et al., 2021) with the theoretical foundation by providing provable guarantees on the representations learned by contrastive learning for linear probing (Arora et al., 2019; Lee et al., 2021; Tosh et al., 2021a,b; Balestriero and LeCun, 2022; Shi et al., 2023). From the graphic view, Shen et al. (2022); HaoChen et al. (2021, 2022) model the pairwise relation by the augmentation probability and provided error analysis of the downstream tasks. The existing body of work has mostly focused on *unsupervised learning*. In this chapter, we systematically investigate how the label information can change the representation manifold and affect the downstream clustering performance on both known and novel classes.

7.8 Summary

In this chapter, we present a graph-theoretic framework for open-world representation learning. The framework facilitates the understanding of how representations change as a result of adding labeling information to the graph. Specifically, we learn representation through Spectral Open-world Representation Learning (SORL). Minimizing this objective is equivalent to factorizing the graph's adjacency matrix, which allows us to analyze the clustering error difference between having vs. excluding labeled data. Our main results suggest that the clustering error can be significantly reduced if the connectivity to the labeled data is stronger than their self-clusterability. Our framework is also empirically appealing to use since it achieves competitive performance on par with existing baselines. We also hope our framework and insights can inspire the broader representation learning community to understand the role of labeling prior.

Chapter 8

OpenCon: Open-world Contrastive Learning

Publication Statement. This chapter is a joint work with Yixuan Li. The paper version of this chapter appeared in TMLR23 ([Sun and Li, 2023](#)).

In the preceding chapters, we have established a solid theoretical foundation for open-world representation learning. As we delve deeper into this thesis, we unveil a pioneering learning framework, dubbed Open-World Contrastive Learning (OpenCon). This cutting-edge approach provides solutions to the empirical challenges stemming from the theoretical concepts previously discussed. OpenCon adeptly grapples with the complexities of constructing compact representations for both known and novel classes, while also facilitating novelty discovery along the way. The efficacy of OpenCon is demonstrated through rigorous testing on challenging benchmark datasets, where it exhibits superior performance. On the ImageNet dataset, OpenCon significantly outperforms the current best method by 11.9% and 7.4% on the novel and overall classification accuracy, respectively. Theoretically, OpenCon can be rigorously interpreted from an EM algorithm perspective—minimizing our contrastive loss par-

tially maximizes the likelihood by clustering similar samples in the embedding space.

8.1 Introduction

Modern machine learning methods have achieved remarkable success (Sun et al., 2017; Van den Oord et al., 2018; Chen et al., 2020a; Caron et al., 2020; He et al., 2020; Zheng et al., 2021; Wu et al., 2021b; Cha et al., 2021; Cui et al., 2021; Jiang et al., 2021; Gao et al., 2021; Zhong et al., 2021a; Zhao and Han, 2021; Fini et al., 2021; Tsai et al., 2022; Zhang et al., 2022c; Wang et al., 2022a). Noticeably, the vast majority of learning algorithms have been driven by the closed-world setting, where the classes are assumed stationary and unchanged. This assumption, however, rarely holds for models deployed in the wild. One important characteristic of open world is that the model will naturally encounter novel classes. Considering a realistic scenario, where a machine learning model for recognizing products in e-commerce may encounter brand-new products together with old products. Similarly, an autonomous driving model can run into novel objects on the road, in addition to known ones. Under the setting, the model should ideally learn to distinguish not only the known classes, but also the novel categories. This problem is proposed as open-world semi-supervised learning (Cao et al., 2022) or generalized category discovery (Vaze et al., 2022). Research efforts have only started very recently to address this important and realistic problem.

Formally, we are given a labeled training dataset \mathcal{D}_l as well as an unlabeled dataset \mathcal{D}_u . The labeled dataset contains samples that belong to a set of known classes, while the unlabeled dataset has a mixture of samples from *both the known and novel classes*. In practice, such unlabeled in-the-wild data can be collected almost for free upon deploying a model in the open world, and thus is available in abundance. Under the setting,

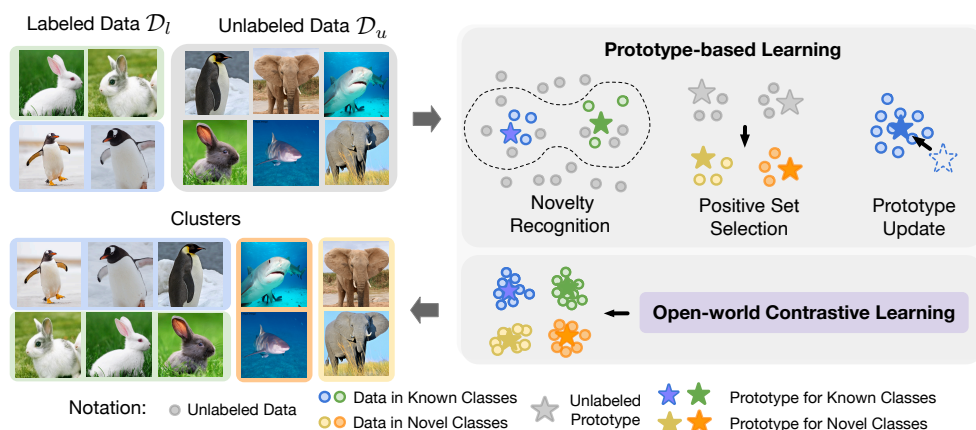


Figure 8.1: Illustration of our learning framework *Open-world Contrastive Learning* (OpenCon). The model is trained on a labeled dataset \mathcal{D}_l of known classes, and an unlabeled dataset \mathcal{D}_u (with samples from both known and novel classes). OpenCon aims to learn distinguishable representations for both known (blue and green) and novel (yellow and orange) classes simultaneously. See Section 8.2 for details.

our goal is to learn distinguishable representations for both known and novel classes simultaneously. While this setting naturally suits many real-world applications, it also poses unique challenges due to: (a) the lack of clear separation between known vs. novel data in \mathcal{D}_u , and (b) the lack of supervision for data in novel classes. Traditional representation learning methods are not designed for this new setting. For example, supervised contrastive learning (SupCon) (Khosla et al., 2020) only assumes the labeled set \mathcal{D}_l , without considering the unlabeled data \mathcal{D}_u . Weakly supervised contrastive learning (Zheng et al., 2021) assumes the same classes in labeled and unlabeled data, hence remaining closed-world and less generalizable to novel samples. Self-supervised learning (Chen et al., 2020a) relies completely on the unlabeled set \mathcal{D}_u and does not utilize the availability of the labeled dataset \mathcal{D}_l .

Targeting these challenges, we formally introduce a new learning frame-

work, *open-world contrastive learning* (dubbed **OpenCon**). OpenCon is designed to produce a compact representation space for both known and novel classes, and facilitates novelty discovery along the way. Key to our framework, we propose a novel prototype-based learning strategy, which encapsulates two components. First, we leverage the prototype vectors to separate known vs. novel classes in unlabeled data \mathcal{D}_u . The prototypes can be viewed as a set of representative embeddings, one for each class, and are updated by the evolving representations. Second, to mitigate the challenge of lack of supervision, we generate pseudo-positive pairs for contrastive comparison. We define the positive set to be those examples carrying the same approximated label, which is predicted based on the closest class prototype. In effect, the loss encourages closely aligned representations to all samples from the same predicted class, rendering a compact clustering of the representation.

Our framework offers several compelling advantages. (1) Empirically, OpenCon establishes strong performance on challenging benchmark datasets, outperforming existing baselines by a significant margin (Section 8.4). OpenCon is also competitive without knowing the number of novel classes in advance—achieving similar or even slightly better performance compared to the oracle (in which the number of classes is given). (2) Theoretically, we demonstrate that our prototype-based learning can be rigorously interpreted from an Expectation-Maximization (EM) algorithm perspective. (3) Our framework is end-to-end trainable, and is compatible with both CNN-based and Transformer-based architectures. The **main contributions** are:

1. We propose a novel framework, open-world contrastive learning (OpenCon), tackling a largely unexplored problem in representation learning. As an integral part of our framework, we also introduce a prototype-based learning algorithm, which facilitates novelty discovery and learning distinguishable representations.

2. Empirically, OpenCon establishes competitive performance on challenging tasks. For example, on the ImageNet dataset, OpenCon substantially outperforms the current best method ORCA (Cao et al., 2022) by **11.9%** and **7.4%** in terms of novel and overall accuracy.
3. We provide insights through extensive ablations, showing the effectiveness of components in our framework. Theoretically, we show a formal connection with the EM algorithm—minimizing our contrastive loss partially maximizes the likelihood by clustering similar samples in the embedding space.

8.2 Methodology

We formally introduce a new learning framework, *open-world contrastive learning* (dubbed OpenCon), which is designed to produce compact representation space for both known and novel classes. The open-world setting posits unique challenges for learning effective representations, namely due to (1) the lack of the separation between known vs. novel data in \mathcal{D}_u , (2) the lack of supervision for data in novel classes. Our learning framework targets these challenges.

8.2.1 Background: Generalized Contrastive Loss

We start by defining a generalized contrastive loss that can characterize the family of contrastive losses. We will later instantiate the formula to define our open-world contrastive loss (Section 8.2.2 and Section 8.2.3). Specifically, we consider a deep neural network encoder $\phi : \mathcal{X} \mapsto \mathbb{R}^d$ that maps the input \mathbf{x} to a L_2 -normalized feature embedding $\phi(\mathbf{x})$. Contrastive losses operate on the normalized feature $\mathbf{z} = \phi(\mathbf{x})$. In other words, the features have unit norm and lie on the unit hypersphere. For a given anchor

point \mathbf{x} , we define the per-sample contrastive loss:

$$\mathcal{L}_\phi(\mathbf{x}; \tau, \mathcal{P}(\mathbf{x}), \mathcal{N}(\mathbf{x})) = -\frac{1}{|\mathcal{P}(\mathbf{x})|} \sum_{\mathbf{z}^+ \in \mathcal{P}(\mathbf{x})} \log \frac{\exp(\mathbf{z}^+ \cdot \mathbf{z}^+ / \tau)}{\sum_{\mathbf{z}^- \in \mathcal{N}(\mathbf{x})} \exp(\mathbf{z}^+ \cdot \mathbf{z}^- / \tau)}, \quad (8.1)$$

where τ is the temperature parameter, \mathbf{z} is the L_2 -normalized embedding vector of \mathbf{x} , $\mathcal{P}(\mathbf{x})$ is the positive set of embeddings *w.r.t.* \mathbf{z} , and $\mathcal{N}(\mathbf{x})$ is the negative set of embeddings.

In open-world contrastive learning, the crucial challenge is how to construct $\mathcal{P}(\mathbf{x})$ and $\mathcal{N}(\mathbf{x})$ for *different types of samples*. Recall that we have two broad categories of training data: (1) labeled data \mathcal{D}_l with known class, and (2) unlabeled data \mathcal{D}_u with both known and novel classes. In conventional supervised CL frameworks with \mathcal{D}_l only, the positive sample pairs can be easily drawn according to the ground-truth labels (Khosla et al., 2020). That is, $\mathcal{P}(\mathbf{x})$ consists of embeddings of samples that carry the same label as the anchor point \mathbf{x} , and $\mathcal{N}(\mathbf{x})$ contains all the embeddings in the multi-viewed mini-batch excluding itself. However, this is not straightforward in the open-world setting with novel classes.

8.2.2 Learning from Wild Unlabeled Data

We now dive into the most challenging part of the data, \mathcal{D}_u , which contains both known and novel classes. We propose a novel prototype-based learning strategy that tackles the challenges of: (1) the separation between known and novel classes in \mathcal{D}_u , and (2) pseudo label assignment that can be used for positive set construction for novel classes. Both components facilitate the goal of learning compact representations, and enable end-to-end training.

Key to our framework, we keep a prototype embedding vector μ_c for each class $c \in \mathcal{Y}_{\text{all}}$. Here \mathcal{Y}_{all} contains both known classes \mathcal{Y}_l and novel classes $\mathcal{Y}_n = \mathcal{Y}_{\text{all}} \setminus \mathcal{Y}_l$, and $\mathcal{Y}_l \cap \mathcal{Y}_n = \emptyset$. The prototypes can be viewed

as a set of representative embedding vectors. All the prototype vectors $\mathbf{M} = [\boldsymbol{\mu}_1 | \dots | \boldsymbol{\mu}_c | \dots]_{c \in \mathcal{Y}_{\text{all}}}$ are randomly initiated at the beginning of training, and will be updated along with learned embeddings. We will also discuss determining the cardinality $|\mathcal{Y}_{\text{all}}|$ (*i.e.*, number of prototypes) in Section 8.5.

Prototype-based OOD detection. We leverage the prototype vectors to perform out-of-distribution (OOD) detection, *i.e.*, separate known vs. novel data in \mathcal{D}_u . For any given sample $\mathbf{x}_i \in \mathcal{D}_u$, we measure the cosine similarity between its embedding $\phi(\mathbf{x}_i)$ and prototype vectors of known classes \mathcal{Y}_l . If the sample embedding is far away from all the known class prototypes, it is more likely to be a novel sample, and vice versa. Formally, we propose the level set estimation:

$$\mathcal{D}_n = \{\mathbf{x}_i | \max_{j \in \mathcal{Y}_l} \boldsymbol{\mu}_j^\top \cdot \phi(\mathbf{x}_i) < \lambda\}, \quad (8.2)$$

where a thresholding mechanism is exercised to distinguish between known and novel samples during training time. The threshold λ can be chosen based on the labeled data \mathcal{D}_l . Specifically, one can calculate the scores $\max_{j \in \mathcal{Y}_l} \boldsymbol{\mu}_j^\top \cdot \phi(\mathbf{x}_i)$ for all the samples in \mathcal{D}_l , and use the score at the p -percentile as the threshold. For example, when $p = 90$, that means 90% of labeled data is above the threshold. We provide ablation on the effect of p later in Section 8.5 and theoretical insights into why OOD detection helps open-world representation learning in Appendix B.3.3.1.

Positive and negative set selection. Now that we have identified novel samples from the unlabeled sample, we would like to facilitate learning compact representations for \mathcal{D}_n , where samples belonging to the same class are close to each other. As mentioned earlier, the crucial challenge is how to construct the positive set, denoted as $\mathcal{P}_n(\mathbf{x})$. In particular, we do not have any supervision signal for unlabeled data in the novel classes. We propose utilizing the predicted label $\hat{y} = \operatorname{argmax}_{j \in \mathcal{Y}_{\text{all}}} \boldsymbol{\mu}_j^\top \cdot \phi(\mathbf{x})$ for

positive set selection.

For a mini-batch \mathcal{B}_n with samples drawn from \mathcal{D}_n , we apply two random augmentations for each sample and generate a multi-viewed batch $\tilde{\mathcal{B}}_n$. We denote the embeddings of the multi-viewed batch as \mathcal{A}_n , where the cardinality $|\mathcal{A}_n| = 2|\mathcal{B}_n|$. For any sample \mathbf{x} in the mini-batch $\tilde{\mathcal{B}}_n$, we propose selecting the positive and negative set of embeddings as follows:

$$\mathcal{P}_n(\mathbf{x}) = \{\mathbf{z}' | \mathbf{z}' \in \{\mathcal{A}_n \setminus \mathbf{z}\}, \hat{y}' = \hat{y}\}, \quad (8.3)$$

$$\mathcal{N}_n(\mathbf{x}) = \mathcal{A}_n \setminus \mathbf{z}, \quad (8.4)$$

where \mathbf{z} is the L_2 -normalized embedding of \mathbf{x} , and \hat{y}' is the predicted label for the corresponding training example of \mathbf{z}' . In other words, we define the positive set of \mathbf{x} to be those examples carrying the same *approximated* label prediction \hat{y} .

With the positive and negative sets defined, we are now ready to introduce our new contrastive loss for open-world data. We desire embeddings where samples assigned with the same pseudo-label can form a compact cluster. Following the general template in Equation 8.1, we define a novel loss function:

$$\mathcal{L}_n = \sum_{\mathbf{x} \in \tilde{\mathcal{B}}_n} \mathcal{L}_\phi(\mathbf{x}; \tau_n, \mathcal{P}_n(\mathbf{x}), \mathcal{N}_n(\mathbf{x})). \quad (8.5)$$

For each anchor, the loss encourages the network to align embeddings of its positive pairs while repelling the negatives. *All* positives in a multi-viewed batch (*i.e.*, the augmentation-based sample as well as any of the remaining samples with the same label) contribute to the numerator. The loss encourages the encoder to give closely aligned representations to *all* entries from the same *predicted* class, resulting in a compact representation space. We provide visualization in Figure 8.2 (right).

Prototype update. The most canonical way to update the prototype em-

beddings is to compute it in every iteration of training. However, this would extract a heavy computational toll and in turn cause unbearable training latency. Instead, we update the class-conditional prototype vector in a moving-average style (Li et al., 2020; Wang et al., 2022a):

$$\boldsymbol{\mu}_c := \text{Normalize}(\gamma\boldsymbol{\mu}_c + (1 - \gamma)\mathbf{z}), \text{ for } c = \begin{cases} y \text{ (ground truth label)}, & \text{if } \mathbf{z} \in \mathcal{D}_l \\ \operatorname{argmax}_{j \in \mathcal{Y}_n} \boldsymbol{\mu}_j^\top \cdot \mathbf{z}, & \text{if } \mathbf{z} \in \mathcal{D}_n \end{cases} \quad (8.6)$$

Here, the prototype $\boldsymbol{\mu}_c$ of class c is defined by the moving average of the normalized embeddings \mathbf{z} , whose predicted class conforms to c . \mathbf{z} are embeddings of samples from $\mathcal{D}_l \cup \mathcal{D}_n$. γ is a tunable hyperparameter.

Remark: We exclude samples in $\mathcal{D}_u \setminus \mathcal{D}_n$ because they may contain non-distinguishable data from known and unknown classes, which undesirably introduce noise to the prototype estimation. We verify this phenomenon by comparing the performance of mixing $\mathcal{D}_u \setminus \mathcal{D}_n$ with labeled data \mathcal{D}_l for training the known classes. The results verify our hypothesis that the non-distinguishable data would be harmful to the overall accuracy. We provide more discussion on this in Appendix B.3.4.1.

8.2.3 Open-world Contrastive Loss

Putting it all together, we define the open-world contrastive loss (dubbed **OpenCon**) as the following:

$$\mathcal{L}_{\text{OpenCon}} = \lambda_n \mathcal{L}_n + \lambda_l \mathcal{L}_l + \lambda_u \mathcal{L}_u, \quad (8.7)$$

where \mathcal{L}_n is the newly devised contrastive loss for the novel data, \mathcal{L}_l is the supervised contrastive loss (Khosla et al., 2020) employed on the labeled data \mathcal{D}_l , and \mathcal{L}_u is the self-supervised contrastive loss (Chen et al., 2020a) employed on the unlabeled data \mathcal{D}_u . λ are the coefficients of loss

terms. Details of \mathcal{L}_l and \mathcal{L}_u are in Appendix B.3.1, along with the complete pseudo-code in Algorithm 2 (Appendix).

Remark. Our loss components work collaboratively to enhance the embedding quality in an open-world setting. The overall objective well suits the complex nature of our training data, which blends both labeled and unlabeled data. As we will show later in Section 8.5, a simple solution by combining supervised contrastive loss (on labeled data) and self-supervised loss (on unlabeled data) is suboptimal. Instead, having \mathcal{L}_n is critical to encourage closely aligned representations to *all* entries from the same predicted class, resulting in an overall more compact representation for novel classes.

8.3 Theoretical Understandings

Overview. Our learning objective using wild data (*c.f.* Section 8.2.2) can be rigorously interpreted from an Expectation-Maximization (EM) algorithm perspective. We start by introducing the high-level ideas of how our method can be decomposed into E-step and M-step respectively. At the **E-step**, we assign each data example $\mathbf{x} \in \mathcal{D}_n$ to one specific cluster. In OpenCon, it is estimated by using the prototypes: $\hat{y}_i = \operatorname{argmax}_{j \in \mathcal{Y}_{\text{all}}} \boldsymbol{\mu}_j^\top \cdot \phi(\mathbf{x}_i)$. At the **M-step**, the EM algorithm aims to maximize the likelihood under the posterior class probability from the previous E-step. Theoretically, we show that minimizing our contrastive loss \mathcal{L}_n (Equation 8.5) partially maximizes the likelihood by clustering similar examples. In effect, our loss concentrates similar data to the corresponding prototypes, encouraging the compactness of features.

8.3.1 Analyzing the E-step

In **E-step**, the goal of the EM algorithm is to maximize the likelihood with learnable feature encoder ϕ and prototype matrix $\mathbf{M} = [\boldsymbol{\mu}_1 | \dots | \boldsymbol{\mu}_c | \dots]$, which can be lower bounded:

$$\sum_i^{|\mathcal{D}_n|} \log p(\mathbf{x}_i | \phi, \mathbf{M}) \geq \sum_i^{|\mathcal{D}_n|} q_i(c) \log \sum_{c \in \mathcal{Y}_{\text{all}}} \frac{p(\mathbf{x}_i, c | \phi, \mathbf{M})}{q_i(c)},$$

where $q_i(c)$ is denoted as the density function of a possible distribution over c for sample \mathbf{x}_i . By using the fact that $\log(\cdot)$ function is concave, the inequality holds with equality when $\frac{p(\mathbf{x}_i, c | \phi, \mathbf{M})}{q_i(c)}$ is a constant value, therefore we set:

$$q_i(c) = \frac{p(\mathbf{x}_i, c | \phi, \mathbf{M})}{\sum_{c \in \mathcal{Y}_{\text{all}}} p(\mathbf{x}_i, c | \phi, \mathbf{M})} = \frac{p(\mathbf{x}_i, c | \phi, \mathbf{M})}{p(\mathbf{x}_i | \phi, \mathbf{M})} = p(c | \mathbf{x}_i, \phi, \mathbf{M}),$$

which is the posterior class probability. To estimate $p(c | \mathbf{x}_i, \phi, \mathbf{M})$, we model the data using the von Mises-Fisher (vMF) (Fisher, 1953) distribution since the normalized embedding locates in a high-dimensional hyper-spherical space.

Assumption 8.1. *The density function is given by $f(\mathbf{x} | \boldsymbol{\mu}, \kappa) = c_d(\kappa) e^{\kappa \boldsymbol{\mu}^\top \phi(\mathbf{x})}$, where κ is the concentration parameter and $c_d(\kappa)$ is a coefficient.*

With the vMF distribution assumption in 8.1, we have $p(c | \mathbf{x}_i, \phi, \mathbf{M}) = \sigma_c(\mathbf{M}^\top \cdot \phi(\mathbf{x}_i))$, where σ denotes the softmax function and σ_c is the c -th element. Empirically we take a one-hot prediction with $\hat{y}_i = \operatorname{argmax}_{j \in \mathcal{Y}_{\text{all}}} \boldsymbol{\mu}_j^\top \cdot \phi(\mathbf{x}_i)$ since each example inherently belongs to exactly one prototype, so we let $q_i(c) = \mathbf{1}\{c = \hat{y}_i\}$.

8.3.2 Analyzing the M-step

In **M-step**, using the label distribution prediction $q_i(c)$ in the E-step, the optimization for the network ϕ and the prototype matrix \mathbf{M} is given by:

$$\operatorname{argmax}_{\phi, \mathbf{M}} \sum_{i=1}^{|\mathcal{D}_n|} \sum_{c \in \mathcal{Y}_{\text{all}}} q_i(c) \log \frac{p(\mathbf{x}_i, c | \phi, \mathbf{M})}{q_i(c)} \quad (8.8)$$

The joint optimization target in Equation 8.8 is then achieved by rewriting the Equation 8.8 according to the following Lemma 8.2 with proof in Appendix B.3.3.2:

Lemma 8.2. (*Zha et al., 2001*) *We define the set of samples with the same prediction $\mathcal{S}(c) = \{\mathbf{x}_i \in \mathcal{D}_n | \hat{y}_i = c\}$. The maximization step is equivalent to aligning the feature vector $\phi(\mathbf{x})$ to the corresponding prototype $\boldsymbol{\mu}_c$:*

$$\operatorname{argmax}_{\phi, \mathbf{M}} \sum_{i=1}^{|\mathcal{D}_n|} \sum_{c \in \mathcal{Y}_{\text{all}}} q_i(c) \log \frac{p(\mathbf{x}_i, c | \phi, \mathbf{M})}{q_i(c)} = \operatorname{argmax}_{\phi, \mathbf{M}} \sum_{c \in \mathcal{Y}_{\text{all}}} \sum_{\mathbf{x} \in \mathcal{S}(c)} \phi(\mathbf{x})^\top \cdot \boldsymbol{\mu}_c$$

In our algorithm, the maximization step is achieved by optimizing \mathbf{M} and ϕ separately.

(a) **Optimizing \mathbf{M} :**

For fixed ϕ , the optimal prototype is given by $\boldsymbol{\mu}_c^* = \text{Normalize}(\mathbb{E}_{\mathbf{x} \in \mathcal{S}(c)}[\phi(\mathbf{x})])$.

This optimal form empirically corresponds to our prototype estimation in Equation 8.6. Empirically, it is expensive to collect all features in $\mathcal{S}(c)$. We use the estimation of $\boldsymbol{\mu}_c$ by moving average:

$$\boldsymbol{\mu}_c := \text{Normalize}(\gamma \boldsymbol{\mu}_c + (1 - \gamma)\phi(\mathbf{x})), \forall \mathbf{x} \in \mathcal{S}(c).$$

(b) **Optimizing ϕ :**

We then show that the contrastive loss \mathcal{L}_n composed with the alignment loss part \mathcal{L}_a encourages the closeness of features from positive pairs.

By minimizing \mathcal{L}_a , it is approximately maximizing the target in Equation 8.8 with the optimal prototypes μ_c^* . We can decompose the loss as follows:

$$\begin{aligned} \mathcal{L}_n &= -\frac{1}{|\mathcal{P}(\mathbf{x})|} \sum_{\mathbf{z}^+ \in \mathcal{P}(\mathbf{x})} \log \frac{\exp(\mathbf{z}^\top \cdot \mathbf{z}^+ / \tau)}{\sum_{\mathbf{z}^- \in \mathcal{N}(\mathbf{x})} \exp(\mathbf{z} \cdot \mathbf{z}^- / \tau)} \\ &= \underbrace{-\frac{1}{|\mathcal{P}(\mathbf{x})|} \sum_{\mathbf{z}^+ \in \mathcal{P}(\mathbf{x})} (\mathbf{z}^\top \cdot \mathbf{z}^+ / \tau)}_{\mathcal{L}_a(\mathbf{x})} + \underbrace{\frac{1}{|\mathcal{P}(\mathbf{x})|} \sum_{\mathbf{z}^+ \in \mathcal{P}(\mathbf{x})} \log \sum_{\mathbf{z}^- \in \mathcal{N}(\mathbf{x})} \exp(\mathbf{z}^\top \cdot \mathbf{z}^- / \tau)}_{\mathcal{L}_b(\mathbf{x})}. \end{aligned}$$

In particular, the first term $\mathcal{L}_a(\mathbf{x})$ is referred to as the alignment term (Wang and Isola, 2020), which encourages the compactness of features from positive pairs. To see this, we have the following lemma 8.3 with proof in Appendix B.3.3.2.

Lemma 8.3. *Minimizing $\mathcal{L}_a(\mathbf{x})$ is equivalent to the maximization step w.r.t. parameter ϕ .*

$$\operatorname{argmin}_{\phi} \sum_{\mathbf{x} \in \mathcal{D}_n} \mathcal{L}_a(\mathbf{x}) = \operatorname{argmax}_{\phi} \sum_{c \in \mathcal{Y}_{\text{all}}} \sum_{\mathbf{x} \in \mathcal{S}(c)} \phi(\mathbf{x})^\top \cdot \mu_c^*,$$

Summary. These observations validate that our framework learns representation for novel classes in an EM fashion. Importantly, we extend EM from a traditional learning setting to an open-world setting with the capability to handle real-world data arising in the wild. We proceed by introducing the empirical verification of our algorithm.

8.4 Experimental Results

Datasets. We evaluate on standard benchmark image classification datasets CIFAR-100 (Krizhevsky et al., 2009) and ImageNet (Deng et al., 2009).

For the ImageNet, we sub-sample 100 classes, following the same setting as ORCA (Cao et al., 2022) for fair comparison. Note that we focus on these tasks, as they are much more challenging than toy datasets with fewer classes. The additional comparison on CIFAR-10 is in Appendix B.3.4.2. By default, classes are divided into 50% seen and 50% novel classes. We then select 50% of known classes as the labeled dataset, and the rest as the unlabeled set. The division is consistent with Cao et al. (2022), which allows us to compare the performance in a fair setting. Additionally, we explore different ratios of unlabeled data and novel classes (see Section 8.5).

Evaluation metrics. We follow the evaluation strategy in Cao et al. (2022) and report the following metrics: (1) classification accuracy on known classes, (2) classification accuracy on the novel data, and (3) overall accuracy on all classes. The accuracy of the novel classes is measured by solving an optimal assignment problem using the Hungarian algorithm (Kuhn and Yaw, 1955). When reporting accuracy on all classes, we solve optimal assignments using both known and novel classes.

Experimental details. We use ResNet-18 as the backbone for CIFAR-100 and ResNet-50 as the backbone for ImageNet-100. The pre-trained backbones (no final FC layer) are identical to the ones in Cao et al. (2022). To ensure a fair comparison, we follow the same practice in Cao et al. (2022) and only update the parameters of the last block of ResNet. In addition, we add a trainable two-layer MLP projection head that projects the feature from the penultimate layer to a lower-dimensional space \mathbb{R}^d ($d = 128$), which is shown to be effective for contrastive loss (Chen et al., 2020a). We use the same data augmentation strategies as SimCLR (Chen et al., 2020a). Same as in Cao et al. (2022), we regularize the KL-divergence between the predicted label distribution $p(\hat{y})$ and the class prior to prevent the network degenerating into a trivial solution in which all instances are assigned to a few classes. We provide extensive details on the training

Table 8.1: Main Results. Asterisk (*) denotes that the original method can not recognize seen classes. Dagger (†) denotes the original method can not detect novel classes (and we had to extend it). Results on ORCA, GCD and OpenCon (mean and standard deviation) are averaged over five different runs. The ORCA results are reported based on the official repo (Cao, 2022).

Method	CIFAR-100			ImagNet-100		
	All	Novel	Seen	All	Novel	Seen
†FixMatch (Kurakin et al., 2020)	20.3	23.5	39.6	34.9	36.7	65.8
†DS ³ L (Guo et al., 2020)	24.0	23.7	55.1	30.8	32.5	71.2
†CGDL (Sun et al., 2020a)	23.6	22.5	49.3	31.9	33.8	67.3
*DTC (Han et al., 2019)	18.3	22.9	31.3	21.3	20.8	25.6
*RankStats (Zhao and Han, 2021)	23.1	28.4	36.4	40.3	28.7	47.3
*SimCLR (Chen et al., 2020a)	22.3	21.2	28.6	36.9	35.7	39.5
ORCA (Cao et al., 2022)	47.2 \pm 0.7	41.0 \pm 1.0	66.7 \pm 0.2	76.4 \pm 1.3	68.9 \pm 0.8	89.1 \pm 0.1
GCD (Vaze et al., 2022)	46.8 \pm 0.5	43.4 \pm 0.7	69.7 \pm 0.4	75.5 \pm 1.4	72.8 \pm 1.2	90.9 \pm 0.2
OpenCon (Ours)	52.7 \pm 0.6	47.8 \pm 0.6	69.1 \pm 0.3	83.8 \pm 0.3	80.8 \pm 0.3	90.6 \pm 0.1

configurations and all hyper-parameters in Appendix B.3.4.4.

OpenCon achieves SOTA performance. As shown in Table 1, OpenCon outperforms the rivals by a significant margin on both CIFAR and ImageNet datasets. Our comparison covers an extensive collection of algorithms, including the best-performed methods to date. In particular, on ImageNet-100, we improve upon the best baseline by 7.4% in terms of overall accuracy. It is also worth noting that OpenCon improves the accuracy of novel classes by 11.9%. Note that the open-world representation learning is a relatively new setting. Closest to our setting is the open-world semi-supervised learning (SSL) algorithms, namely ORCA (Cao et al., 2022) and GCD (Vaze et al., 2022)—that directly optimize the classification performance. While our framework emphasizes representation learning, we demonstrate the quality of learned embeddings by also measuring the classification accuracy. This can be easily done by leveraging our learned prototypes on a converged model: $\hat{y} = \operatorname{argmax}_{j \in \mathcal{Y}_{\text{all}}} \boldsymbol{\mu}_j^\top \cdot \phi(\mathbf{x})$.

We discuss the significance *w.r.t.* existing works in detail:

- **OpenCon vs. ORCA** Our framework bears significant differences *w.r.t.* ORCA in terms of learning goal and approach. (1) Our framework focuses on the representation learning problem, whereas ORCA optimizes for the classification performance using cross-entropy loss. Unlike ours, ORCA does not necessarily learn compact representations, as evidenced in Figure 8.2 (left). (2) We propose a novel open-world contrastive learning framework, whereas ORCA does not employ contrastive learning. ORCA uses a pairwise loss to predict similarities between pairs of instances, and does not consider negative samples. In contrast, our approach constructs both positive and negative sample sets, which encourage aligning representations to *all* entries from the same ground-truth label or predicted pseudo label (for novel classes). (3) Our framework explicitly considers OOD detection, which allows separating known vs. novel data in \mathcal{D}_u . ORCA does not consider this and can suffer from noise in the pairwise loss (*e.g.*, the loss may maximize the similarity between samples from known vs. novel classes).
- **OpenCon vs. GCD** There are two key differences to highlight: (1) GCD (Vaze et al., 2022) requires a two-stage training procedure, whereas our learning framework proposes an end-to-end training strategy. Specifically, GCD applies the SupCon loss (Khosla et al., 2020) on the labeled data \mathcal{D}_l and SimCLR loss (Chen et al., 2020a) on the unlabeled data \mathcal{D}_u . The feature is then clustered separately by a semi-supervised K-means method. However, the two-stage method hinders the useful pseudo-labels to be incorporated into the training stage, which results in suboptimal performance. In contrast, our prototype-based learning strategy alleviates the need for a separate clustering process (*c.f.* Section 8.2.2), which is therefore easy to use in practice and provides meaningful supervision for the un-

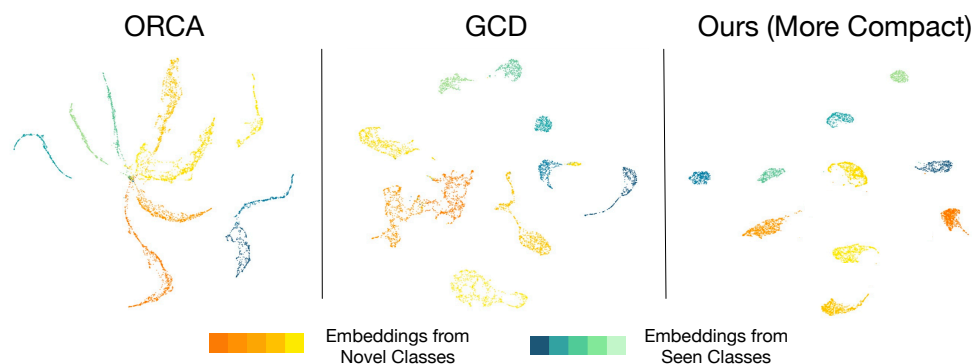


Figure 8.2: UMAP (McInnes et al., 2018) visualization of the feature embedding from 10 classes (5 for seen, 5 for novel) when the model is trained on ImageNet-100 with ORCA (Cao et al., 2022), GCD (Vaze et al., 2022) and OpenCon (ours).

labeled data. (2) We propose a contrastive loss \mathcal{L}_n better utilizing the pseudo-labels during training, which facilitates learning a more compact representation space for the novel data. From Table 8.1, we observe that OpenCon outperforms GCD by 8.3% (overall accuracy) on ImageNet-100, showcasing the benefits of our framework.

Lastly, for completeness, we compare methods in related problem domains: (1) *novel class detection*: DTC (Han et al., 2019), RANKSTATS (Zhao and Han, 2021), (2) *semi-supervised learning*: FIXMATCH (Kurakin et al., 2020), DS³L (Guo et al., 2020) and CGDL (Sun et al., 2020a). We also compare it with the common representation method SIMCLR (Chen et al., 2020a). These methods are not designed for the Open-SSL task, therefore the performance is less competitive.

OpenCon is competitive on ViT Going beyond convolutional neural networks, we show in Table 8.2 that the OpenCon is competitive for transformer-based ViT model (Dosovitskiy et al., 2020). We adopt the ViT-B/16 architecture with DINO pre-trained weights (Caron et al., 2021), following the pipeline used in Vaze et al. (2022). In Table 8.2, we compare

Table 8.2: Comparison of accuracy on ViT-B/16 architecture. Results are reported on ImageNet-100.

Methods	All	Novel	Seen
ORCA (Cao et al., 2022)	73.5	64.6	89.3
GCD (Vaze et al., 2022)	74.1	66.3	89.8
k -Means (MacQueen, 1967)	72.7	71.3	75.5
RankStats+ (Zhao and Han, 2021)	37.1	24.8	61.6
UNO+ (Fini et al., 2021)	70.3	57.9	95.0
OpenCon (Ours)	84.0	81.2	93.8

OpenCon’s performance with ORCA (Cao et al., 2022), GCD (Vaze et al., 2022), k -Means (MacQueen, 1967), RankStats+ (Zhao and Han, 2021) and UNO+ (Fini et al., 2021) on ViT-B-16 architecture. On ImageNet-100, we improve upon the best baseline by 9.9 in terms of overall accuracy.

OpenCon learns more distinguishable representations We visualize feature embeddings using UMAP (McInnes et al., 2018) in Figure 8.2. Different colors represent different ground-truth class labels. For clarity, we use the ImageNet-100 dataset and visualize a subset of 10 classes. We can observe that OpenCon produces a better embedding space than GCD and ORCA. In particular, ORCA does not produce distinguishable representations for novel classes, especially when the number of classes increases. The features of GCD are improved, yet with some class overlapping (*e.g.*, two orange classes). For reader’s reference, we also include the version with a subset of 20 classes in Appendix B.3.4.3, where OpenCon displays more distinguishable representations.

8.5 A Comprehensive Analysis of OpenCon

Prototype-based OOD detection is important. In Figure 8.3, we ablate the contribution of a key component in OpenCon: prototype-based OOD

detection (*c.f.* Section 8.2.2). To systematically analyze the effect, we report the performance under varying percentile $p \in \{0, 10, 30, 50, 70, 90\}$. Each p corresponds to a different threshold λ for separating known vs. novel data in \mathcal{D}_u . In the extreme case with $p = 0$, \mathcal{D}_n becomes equivalent to \mathcal{D}_u , and hence the contrastive loss \mathcal{L}_n is applied to the entire unlabeled data. We highlight two findings: (1) Without OOD detection ($p = 0$), the unseen accuracy reduces by 2.4%, compared to the best setting ($p = 70\%$). This affirms the importance of OOD detection for better representation learning. (2) A higher percentile p , in general, leads to better performance. We also provide theoretical insights in Appendix B.3.3.1 showing OOD detection helps contrastive learning of novel classes by having fewer candidate classes.

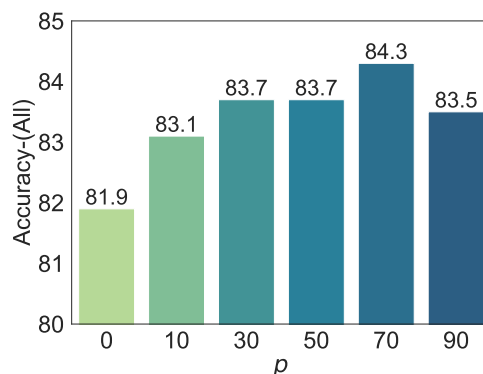


Table 8.3: Effect of p on ImageNet-100 and CIFAR-100, measured by the overall accuracy. $p = 0$ means no OOD detection.

Ablation study on the loss components. Recall that our overall objective function in Equation 8.7 consists of three parts. We ablate the contributions of each component in Table 8.4. Specifically, we modify OpenCon by removing: (i) supervised objective (*i.e.*, w/o \mathcal{D}_l), (ii) unsupervised objective on the entire unlabeled data (*i.e.*, w/o \mathcal{D}_u), and (iii) prototype-based contrastive learning on novel data \mathcal{D}_n . We have the following key

observations: (1) Both supervised objective \mathcal{L}_l and unsupervised loss \mathcal{L}_u are indispensable parts of open-world representation learning. This suits the complex nature of our training data, which requires learning on both labeled and unlabeled data, across both known and novel classes. (2) Purely combining SupCon (Khosla et al., 2020) and SimCLR (Chen et al., 2020a)—as used in GCD (Vaze et al., 2022)—does not give competitive results. For example, the overall accuracy is 9.3% lower than our method on the ImageNet-100 dataset. In contrast, having \mathcal{L}_n encourages closely aligned representations to *all* entries from the same *predicted* class, resulting in a more compact representation space for novel data. Overall, the ablation suggests that all losses in our framework work together synergistically to enhance the representation quality.

Table 8.4: Ablation study on loss component.

Loss Components	CIFAR-100			ImageNet-100		
	All	Novel	Seen	All	Novel	Seen
w/o \mathcal{L}_l	43.3	47.1	38.8	68.6	73.4	59.1
w/o \mathcal{L}_u	36.9	28.3	63.4	55.9	39.3	89.2
w/o \mathcal{L}_n	46.6	42.2	70.3	74.5	70.7	91.0
OpenCon (ours)	52.7\pm0.6	47.8\pm0.6	69.1 \pm 0.3	83.8\pm0.3	80.8\pm0.3	90.6 \pm 0.1

Handling an unknown number of novel classes. In practice, we often do not know the number of classes $|\mathcal{Y}_{\text{all}}|$ in advance. This is the dilemma faced by OpenCon and other baselines as well. In such cases, one can apply OpenCon by first estimating the number of classes. For a fair comparison, we use the same estimation technique¹ as in Han et al. (2019); Cao et al. (2022). On CIFAR-100, the estimated total number of classes is 124. At the beginning of training, we initialize the same number of prototypes accordingly. Results in Table 8.5 show that OpenCon outper-

¹A clustering algorithm is performed on the combination of labeled data and unlabeled data. The optimal number of classes is chosen by validating clustering accuracy on the labeled data.

forms the best baseline ORCA (Cao et al., 2022) by 7.3%. Interestingly, despite the initial number of classes, the training process will converge to solutions that closely match the ground truth number of classes. For example, at convergence, we observe a total number of 109 actual clusters. The remaining ones have no samples assigned, hence can be discarded. Overall, with the estimated number of classes, OpenCon can achieve similar performance compared to the setting in which the number of classes is known.

Table 8.5: Accuracy on CIFAR-100 dataset with an unknown number of classes.

Methods	All	Novel	Seen
ORCA (Cao et al., 2022)	46.4	40.0	66.3
GCD (Vaze et al., 2022)	47.2	41.9	69.8
OpenCon (Known $ \mathcal{Y}_{\text{all}} $)	53.7	48.7	69.0
OpenCon (Unknown $ \mathcal{Y}_{\text{all}} $)	53.7	48.2	68.8

OpenCon is robust under a smaller number of labeled examples, and a larger number of novel classes. We show that OpenCon’s strong performance holds under more challenging settings with: (1) reduced fractions of labeled examples, and (2) different ratios of known vs. novel classes. The results are summarized in Table 8.6. First, we reduce the labeling ratio from 50% (default) to 25% and 10%, while keeping the number of known classes to be the same (*i.e.*, 50). With fewer labeled samples in the known classes, the unlabeled sample set size will expand accordingly. It posits more challenges for novelty discovery and representation learning. On ImageNet-100, OpenCon substantially improves the novel class accuracy by **10%** compared to ORCA and GCD, when only 10% samples are labeled. Secondly, we further increase the number of novel classes, from 50 (default) to 75 and 90 respectively. On ImageNet-100 with 75 novel classes ($|\mathcal{Y}_l| = 25$), OpenCon improves the novel class accuracy by **16.7%**

Table 8.6: Accuracy on CIFAR-100 under varying different labeling ratios (for labeled data) and different numbers of known classes ($|\mathcal{Y}_l|$). The number of novel classes is $100 - |\mathcal{Y}_l|$.

Labeling Ratio	$ \mathcal{Y}_l $	Method	CIFAR-100			ImageNet-100		
			All	Novel	Seen	All	Novel	Seen
0.5	50	ORCA	47.0	41.3	66.2	76.6	69.0	88.9
		GCD	47.2	43.6	69.4	75.1	73.2	90.9
		OpenCon	53.7	48.7	69.0	84.3	81.1	90.7
0.25	50	ORCA	47.6	42.5	61.8	72.2	64.2	87.3
		GCD	41.4	39.3	66.0	76.7	69.1	89.1
		OpenCon	51.3	44.6	65.5	82.0	77.1	90.6
0.1	50	ORCA	41.2	37.7	54.6	68.7	56.8	83.4
		GCD	37.0	38.6	62.2	69.4	56.6	85.8
		OpenCon	48.2	44.4	62.5	75.4	66.8	85.2
0.5	25	ORCA	40.4	38.8	66.0	57.8	54.0	89.4
		GCD	41.6	39.2	70.0	65.3	63.2	90.8
		OpenCon	43.9	41.9	70.2	74.5	72.7	91.2
0.5	10	ORCA	34.3	33.8	67.4	45.1	43.6	93.0
		GCD	38.4	36.8	61.3	53.3	52.9	94.2
		OpenCon	40.9	40.5	69.9	59.0	58.2	94.3

over ORCA (Cao et al., 2022). Overall our experiments confirm the robustness of OpenCon under various settings.

8.6 Additional Related Work

Contrastive learning. A great number of works have explored the effectiveness of contrastive loss in unsupervised representation learning: InfoNCE (Van den Oord et al., 2018), SimCLR (Chen et al., 2020a), SWaV (Caron et al., 2020), MoCo (He et al., 2020), SEER (Goyal et al., 2021) and (Li et al., 2020, 2021b; Zhang et al., 2021). It motivates follow-up works to

on weakly supervised learning tasks (Zheng et al., 2021; Tsai et al., 2022), semi-supervised learning (Chen et al., 2020b; Li et al., 2021a; Zhang et al., 2022c; Yang et al., 2022a), supervised learning with noise (Wu et al., 2021b; Karim et al., 2022; Li et al., 2022a), continual learning (Cha et al., 2021), long-tailed recognition (Cui et al., 2021; Tian et al., 2021; Jiang et al., 2021; Li et al., 2022b), few-shot learning (Gao et al., 2021), partial label learning (Wang et al., 2022a), novel class discovery (Zhong et al., 2021a; Zhao and Han, 2021; Fini et al., 2021), hierarchical multi-label learning (Zhang et al., 2022b). Under different circumstances, all works adopt different choices of the positive set, which is not limited to the self-augmented view in SimCLR (Chen et al., 2020a). Specifically, with label information available, SupCon (Khosla et al., 2020) improved representation quality by aligning features within the same class. Without supervision for the unlabeled data, Dwibedi et al. (2021) used the nearest neighbor as positive pair to learn a compact embedding space. Different from prior works, we focus on the open-world representation learning problem, which is largely unexplored.

Novel category discovery. At an earlier stage, the problem of novel category discovery (NCD) is targeted as a transfer learning problem in DTC (Han et al., 2019), KCL (Hsu et al., 2018), MCL (Hsu et al., 2019). The learning is generally in a two-stage manner: the model is firstly trained with the labeled data and then transfers knowledge to learn the unlabeled data. OpenMix (Zhong et al., 2021b) further proposes an end-to-end framework by mixing the seen and novel classes in a joint space. In recent studies, many researchers incorporate representation learning for NCD like RankStats (Zhao and Han, 2021), NCL (Zhong et al., 2021a) and UNO (Fini et al., 2021). In the ORL setting, the unlabeled test set consists of novel classes but also classes are previously seen in the labeled data that need to be separated.

Semi-supervised learning. A great number of early works (Chapelle

et al., 2006; Lee et al., 2013; Sajjadi et al., 2016; Laine and Aila, 2017; Zhai et al., 2019; Rebuffi et al., 2020; Kurakin et al., 2020) have been proposed to tackle the problem of semi-supervised learning (SSL). Typically, a standard cross-entropy loss is applied to the labeled data, and a consistency loss (Laine and Aila, 2017; Kurakin et al., 2020) or self-supervised loss (Sajjadi et al., 2016; Zhai et al., 2019; Rebuffi et al., 2020) is applied to the unlabeled data. Under the closed-world assumption, SSL methods achieve competitive performance which is close to the supervised methods. Later works (Oliver et al., 2018; Chen et al., 2020c) point out that including novel classes in the unlabeled set can downgrade the performance. In Guo et al. (2020); Chen et al. (2020c); Yu et al. (2020); Park et al. (2023); Saito et al. (2021); Huang et al. (2021a); Yang et al. (2022a), OOD detection techniques are wielded to separate the OOD samples in the unlabeled data. Recent works (Vaze et al., 2022; Cao et al., 2022; Rizve et al., 2022) further require the model to group samples from novel classes into semantically meaningful clusters. In our framework, we unify the novelty class detection and the representation learning and achieve competitive performance.

8.7 Summary

This chapter provides a new learning framework, *open-world contrastive learning* (OpenCon) that learns highly distinguishable representations for both known and novel classes in an open-world setting. Our open-world setting can generalize traditional representation learning and offers stronger flexibility. We provide important insights that the separation between known vs. novel data in the unlabeled data and the pseudo supervision for data in novel classes is critical. Extensive experiments show that OpenCon can notably improve the accuracy on both known and novel classes compared to the current best method ORCA. As a shared chal-

lenge by all methods, one limitation is that the prototype number in our end-to-end training framework needs to be pre-specified. An interesting future work may include the mechanism to dynamically estimate and adjust the class number during the training stage.

Chapter 9

Conclusion

In conclusion, this thesis has provided significant contributions to the advancement of machine learning within open-world scenarios. Open-world learning, in contrast to traditional closed-world machine learning models, is confronted with novel, unseen data and contexts. This presents an unprecedented set of challenges that demand robust, innovative solutions. The thesis tackled these challenges in two interconnected stages: Out-of-distribution (OOD) Detection and Open-world Representation Learning (ORL).

The first stage, OOD detection, provides the foundation for identifying instances from previously unseen classes, thus reducing the risk of overconfident and potentially misleading predictions. We have developed pioneering methodologies, including ReACT (Chapter 3) and DICE (Chapter 4), and introduced a non-parametric approach using K-nearest neighbor (KNN) distance (Chapter 5), all of which enhance the effectiveness of OOD detection.

Building upon the OOD detection, the second stage, ORL, extends our capacity to learn from and incorporate knowledge about new classes. NSCL in Chapter 6 and SORL in Chapter 7 deepen our understanding of the complex interplay between known and unknown classes and the crit-

ical role of label information in shaping representations. This thesis answers these challenging questions, providing invaluable insights for the development of advanced ORL algorithms. Moreover, we provided an empirical solution in the form of a comprehensive contrastive learning framework in Chapter 8 for ORL, buttressed by theoretical interpretation from the Expectation-maximization perspective. This work is anticipated to significantly enhance machine learning’s adaptability and reliability in open-world scenarios.

By navigating the complexities of open-world learning, this thesis contributes to shaping a new paradigm in machine learning, one that is responsive and adaptable to ever-evolving open-world contexts. The insights, methodologies, and theoretical developments presented here pave the way for future research in open-world machine learning, making strides toward unknown-aware and unknown-adaptable AI systems.

9.1 Future Work

As we chart the future of open-world machine learning, there are several promising areas for further research. While this thesis has made significant strides in OOD detection and ORL, these areas of study are still in their nascent stages, and there are numerous unexplored avenues to investigate.

1. **Fine-tuning of Models with Growing Data:** Future studies could consider more sophisticated techniques for fine-tuning machine learning models in the face of new data. This might involve developing dynamic models capable of evolving their parameters as they encounter new classes without forgetting existing knowledge, thereby boosting their adaptability and effectiveness in open-world scenarios.

2. **Expanding the Scope of Open-world Learning:** Presently, open-world learning is most often associated with visual classification tasks. Future work can aim to extend this concept to other domains such as natural language processing, speech recognition, and recommendation systems.
3. **Ethical and Legal Considerations:** As machine learning models become increasingly ubiquitous in society, future research must consider the ethical and legal aspects of open-world learning. This could involve developing frameworks to ensure fairness, transparency, and accountability in open-world learning models.
4. **Real-world Testing and Implementation:** Lastly, while the results presented in this thesis exhibit considerable promise on benchmark datasets, the significant value lies in deploying and evaluating these models on real-world datasets. These datasets differ from benchmark collections in several ways; they may not have a balanced distribution of training samples across different classes and might not provide a clear separation between class sets. Implementing models in such environments helps identify practical challenges and areas for refinement that are not typically apparent in benchmark datasets. Conducting tests within this context, therefore, stands as a crucial step for future work, enabling us to fine-tune and validate our models under actual operating conditions and further improve their reliability and adaptability.

Overall, the future of open-world machine learning holds vast potential. As this field of research progresses, we are likely to see even more innovative solutions and methodologies, moving us closer to truly intelligent, adaptive, and reliable AI systems.

Appendix A

Appendix for Out-of-distribution Detection

A.1 ReAct: OOD Detection With Rectified Activations

A.1.1 Theoretical Details

Here we derive [Equation 3.8](#) for $\epsilon \geq 0$ and $\sigma_{\text{out}} = \sigma > 0$. Since $\text{ESN}(\mu, \sigma^2, 0) = \mathcal{N}^R(\mu, \sigma)$, we can obtain [Equation 3.4](#) for ID activation by specializing the result to $\epsilon = 0$. We begin with a useful lemma.

Lemma A.1. *Let $X \sim \text{ESN}(0, \sigma^2, \epsilon)$ and let $a \leq b \leq 0, 0 \leq c \leq d$. Then $\mathbb{P}(a \leq X \leq b) = (1 + \epsilon) \left[\Phi\left(\frac{b}{(1+\epsilon)\sigma}\right) - \Phi\left(\frac{a}{(1+\epsilon)\sigma}\right) \right]$ and $\mathbb{P}(c \leq X \leq d) = (1 - \epsilon) \left[\Phi\left(\frac{d}{(1-\epsilon)\sigma}\right) - \Phi\left(\frac{c}{(1-\epsilon)\sigma}\right) \right]$.*

Proof.

$$\begin{aligned}\mathbb{P}(a \leq X \leq b) &= (1 + \epsilon) \int_{x=a}^b \frac{1}{(1 + \epsilon)\sigma} \phi\left(\frac{x}{(1 + \epsilon)\sigma}\right) dx \\ &= (1 + \epsilon) \left[\Phi\left(\frac{b}{(1 + \epsilon)\sigma}\right) - \Phi\left(\frac{a}{(1 + \epsilon)\sigma}\right) \right]\end{aligned}$$

since the integral that of a $\mathcal{N}(0, (1 + \epsilon)^2\sigma^2)$ distribution between a and b . The result for $\mathbb{P}(c \leq X \leq d)$ follows analogously. \square

Suppose that $X_\mu \sim \text{ESN}(\mu, \sigma^2, \epsilon)$ with $\mu > 0$ and let $Z_\mu = \max(X_\mu, 0)$. Define $X = X_\mu - \mu$ so that $Z_\mu = \max(X + \mu, 0) = \max(X, -\mu) + \mu$. We can derive the expectation of $Z := \max(X, -\mu)$:

$$\mathbb{E}[Z] = \underbrace{-\mu \cdot \mathbb{P}(X < -\mu)}_{\text{(I)}} + \underbrace{\int_{x=-\mu}^0 \frac{x}{\sigma} \phi\left(\frac{x}{(1 + \epsilon)\sigma}\right) dx}_{\text{(II)}} + \underbrace{\int_{x=0}^{\infty} \frac{x}{\sigma} \phi\left(\frac{x}{(1 - \epsilon)\sigma}\right) dx}_{\text{(III)}}.$$

$$\text{(I)} = -\mu(1 + \epsilon)\Phi\left(\frac{-\mu}{(1 + \epsilon)\sigma}\right) \quad \text{by Lemma A.1;}$$

$$\text{(II)} = (1 + \epsilon) \int_{x=-\mu}^0 \frac{x}{(1 + \epsilon)\sigma} \phi\left(\frac{x}{(1 + \epsilon)\sigma}\right) dx = (1 + \epsilon)^2 \left[\phi\left(\frac{-\mu}{(1 + \epsilon)\sigma}\right) - \phi(0) \right] \sigma$$

since the integral is the expectation of an un-normalized truncated Gaussian between $-\mu$ and 0. Similarly, (III) is $(1 - \epsilon)$ times the expectation of an un-normalized Gaussian between 0 and ∞ , thus (III) = $(1 - \epsilon)^2\phi(0)\sigma$.

Combining (I)-(III) gives:

$$\begin{aligned}
\mathbb{E}[Z] &= -\mu(1 + \epsilon)\Phi\left(\frac{-\mu}{(1 + \epsilon)\sigma}\right) + (1 + \epsilon)^2 \left[\phi\left(\frac{-\mu}{(1 + \epsilon)\sigma}\right) - \phi(0) \right] \sigma + (1 - \epsilon)^2 \phi(0)\sigma \\
&= -\mu(1 + \epsilon)\Phi\left(\frac{-\mu}{(1 + \epsilon)\sigma}\right) + (1 + \epsilon)^2 \phi\left(\frac{-\mu}{(1 + \epsilon)\sigma}\right) \sigma + \phi(0)\sigma[(1 - \epsilon)^2 - (1 + \epsilon)^2] \\
&= -\mu(1 + \epsilon)\Phi\left(\frac{-\mu}{(1 + \epsilon)\sigma}\right) + (1 + \epsilon)^2 \phi\left(\frac{-\mu}{(1 + \epsilon)\sigma}\right) \sigma - 4\epsilon\phi(0)\sigma \\
&= -\mu(1 + \epsilon)\Phi\left(\frac{-\mu}{(1 + \epsilon)\sigma}\right) + (1 + \epsilon)^2 \phi\left(\frac{-\mu}{(1 + \epsilon)\sigma}\right) \sigma - \frac{4\epsilon}{\sqrt{2\pi}}\sigma.
\end{aligned}$$

Equation 3.6 follows since $\mathbb{E}[Z_\mu] = \mathbb{E}[Z] + \mu$. To derive Equation 3.7, note that the expectation of $\bar{Z} := \min(Z, c - \mu)$ is given by:

$$\mathbb{E}[\bar{Z}] = \text{(I)} + \text{(II)} + \underbrace{\int_{x=0}^{c-\mu} \frac{x}{\sigma} \phi\left(\frac{x}{(1 - \epsilon)\sigma}\right) dx}_{\text{(IV)}} + \underbrace{(c - \mu) \cdot \mathbb{P}(X > c - \mu)}_{\text{(V)}}.$$

(IV) = $(1 - \epsilon)^2 \left[\phi(0) - \phi\left(\frac{c-\mu}{(1-\epsilon)\sigma}\right) \right] \sigma$ follows from a similar argument as above, and

$$\text{(V)} = (c - \mu)(1 - \epsilon) \left[1 - \Phi\left(\frac{c - \mu}{(1 + \epsilon)\sigma}\right) \right]$$

can be derived using Lemma A.1. Combining (I),(II),(IV),(V) and observing that $\mathbb{E}[\min(Z_\mu, c)] = \mathbb{E}[\bar{Z}] + \mu$ gives Equation 3.7.

A.1.2 Ablation Study on Different Layers

We provide the activation patterns for intermediate layers in Figure A.1 and the OOD detection performance of applying ReAct to these layers in Table A.1. In particular, there are four residual blocks in the original ResNet-50 network (He et al., 2016b). The four layers (denoted by layer 1 - layer 4) are taken from the output of each residual block. Interestingly, early layers display less distinctive signatures between ID and

OOD data and ReAct performs worse than the baseline (Liu et al., 2020) when it is applied on layer 1 - layer 3. This is expected because neural networks generally capture lower-level features in early layers (such as Gabor filters (Zeiler and Fergus, 2014)), whose activations can be very similar between ID and OOD. The semantic-level features only emerge as with deeper layers, where ReAct is the most effective.

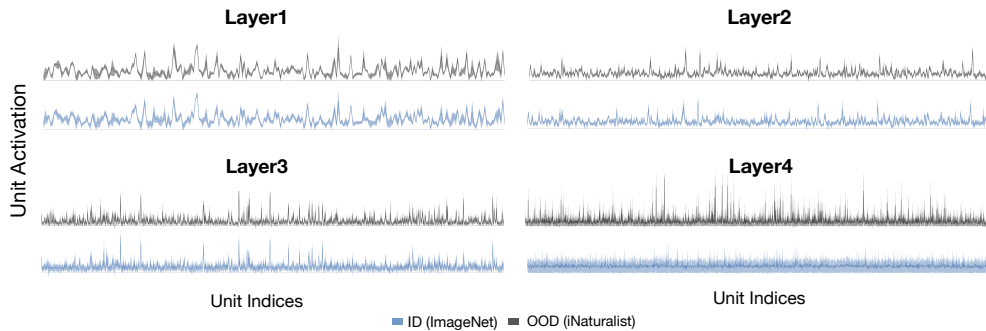


Figure A.1: The distribution of per-unit activations in the penultimate layer for ID (ImageNet, blue) and OOD (iNaturalist, gray) on different layers. Each layer (denoted by layer 1 - layer 4) corresponds to the output of each residual block in ResNet-50 (He et al., 2016b).

Table A.1: Ablation study of applying ReAct on different layers. We used ResNet-18 (He et al., 2016a) pre-trained on CIFAR-100 and ResNet-50 pre-trained on ImageNet. \uparrow indicates larger values are better and \downarrow indicates smaller values are better. All values are percentaged over multiple OOD test datasets described in Section 3.3.2 and Section 3.3.1.

Layers of applying ReAct	ID: CIFAR-100		ID: ImageNet	
	FPR95 \downarrow	AUROC \uparrow	FPR95 \downarrow	AUROC \uparrow
Layer1	90.86	68.17	84.83	74.88
Layer2	84.12	75.32	76.25	79.37
Layer3	73.4	80.91	63.87	86.46
Layer4 (ReAct)	59.61	87.48	31.43	92.95
No ReAct (Liu et al., 2020)	71.93	82.82	58.41	86.17

A.1.3 Using True BatchNorm Statistics on OOD Data

Typically, for a unit activation denoted by z , the network estimates the running mean $\mathbb{E}_{\text{in}}(z)$ and variance $\text{Var}_{\text{in}}(z)$, over the entire ID training set during training. During inference time, the network applies BatchNorm statistics (Ioffe and Szegedy, 2015) $\mathbb{E}_{\text{in}}(z)$ and $\text{Var}_{\text{in}}(z)$, which helps normalize the activations for the test data with the same distribution \mathcal{D}_{in} :

$$\text{BatchNorm}(z; \gamma, \beta, \epsilon) = \frac{z - \mathbb{E}_{\text{in}}[z]}{\sqrt{\text{Var}_{\text{in}}[z] + \epsilon}} \cdot \gamma + \beta \quad (\text{A.1})$$

However, our key observation is that using *mismatched* BatchNorm statistics—that are estimated on \mathcal{D}_{in} yet blindly applied to the OOD \mathcal{D}_{out} —can trigger abnormally high unit activations (see bottom of Figure 3.4). As a thought experiment, for OOD data, we instead apply the *true* BatchNorm statistics estimated on a batch of OOD images:

$$\text{BatchNorm}(z; \gamma, \beta, \epsilon) = \frac{z - \mathbb{E}_{\text{out}}[z]}{\sqrt{\text{Var}_{\text{out}}[z] + \epsilon}} \cdot \gamma + \beta. \quad (\text{A.2})$$

As a result, we observe well-behaved activation patterns with near-constant mean and standard deviations (see the top of Figure 3.4). Our study therefore reveals one of the fundamental causes for neural networks to produce overconfident predictions for OOD data. Despite the interesting observation, we note that estimating the true BN statistics for OOD poses a strong and impractical assumption of having access to a batch of OOD data during test time. In contrast, using ReAct does not operate under such an assumption and can be applied on any single OOD instance, as well as for neural networks trained with alternative normalization mechanisms (as we show in Section 3.5).

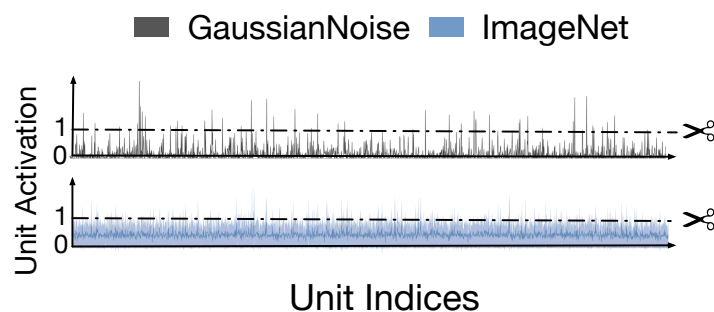


Figure A.2: The distribution of per-unit activations in the penultimate layer for OOD data (Gaussian Noise) and ID data (ImageNet) on ResNet50.

A.1.4 Unit Activation Patterns for Gaussian Noise

We provide the activation patterns for Gaussian noise input (our validation data) in Figure A.2. The experiment is based on ResNet-50 architecture (He et al., 2016b). We show that using Gaussian noise as input can lead to overly high unit activations, which is consistent with the observation in Figure 3.1 and Figure 3.5.

Table A.2: Detailed results on six common OOD benchmark datasets: Textures (Cimpoi et al., 2014), SVHN (Netzer et al., 2011), Places365 (Zhou et al., 2017), LSUN-Crop (Yu et al., 2015), LSUN-Resize (Yu et al., 2015), and iSUN (Xu et al., 2015). For each ID dataset, we use the same ResNet-18 architecture (He et al., 2016a) and compare the performance with and without ReAct respectively. \uparrow indicates larger values are better and \downarrow indicates smaller values are better.

ID Dataset	Methods	SVHN	LSUN-Crop	LSUN-Resize	iSUN	Textures	Places365	Average	FPR95 \downarrow / AUROC \uparrow / AUPR \uparrow	
CIFAR-10	MSP	59.66/91.25/78.84	45.21/93.80/80.81	51.93/92.73/80.04	54.57/92.12/80.01	66.45/88.5/79.47	62.46/88.64/75.48	56.71/91.17/79.11		
	MSP + ReAct	57.15/91.69/91.77	46.37/93.33/93.00	46.32/93.61/93.37	50.02/92.96/93.26	62.85/89.31/92.59	60.15/89.28/88.65	53.81/91.70/92.11		
	ODIN	60.37/88.27/89.82	7.81/98.58/98.73	9.24/98.25/98.51	11.62/97.91/98.38	52.09/89.17/93.72	45.49/90.58/90.55	31.10/93.79/94.95		
	ODIN+ReAct	51.77/88.87/89.09	14.99/97.29/97.42	6.84/98.65/98.81	9.55/98.28/98.62	43.81/90.41/94.16	45.87/90.73/90.82	28.81/94.04/94.82		
	Energy	54.41/91.22/93.05	10.19/98.05/98.33	23.45/96.14/96.92	27.52/95.59/96.78	55.23/89.37/94.01	42.77/91.02/90.98	35.60/93.57/95.01		
	Energy+ReAct	49.77/92.18/93.67	16.99/97.11/97.48	17.94/96.98/97.56	20.84/96.46/97.38	47.96/91.55/95.40	43.97/91.33/91.66	32.91/94.27/95.53		
CIFAR-100	MSP	81.32/77.74/78.78	70.11/83.51/83.02	82.46/75.73/76.32	82.26/76.16/78.26	85.11/73.36/80.79	83.06/74.47/73.27	80.72/76.83/78.41		
	MSP + ReAct	74.17/82.3/85.58	73.1/82.47/85.25	74.73/80.81/83.77	73.49/81.45/85.60	74.82/80.37/89.03	82.37/74.99/76.43	75.45/80.4/84.28		
	ODIN	40.94/93.29/94.49	28.72/94.51/94.93	79.61/82.13/85.09	76.66/83.51/87.35	83.63/72.37/82.80	87.71/71.46/72.85	66.21/82.88/86.25		
	ODIN+ReAct	22.87/95.63/96.13	36.61/91.45/91.20	75.02/85.53/88.42	70.21/86.51/89.89	66.79/82.69/89.52	87.94/69.57/70.01	59.91/85.23/87.53		
	Energy	81.74/84.56/88.39	34.78/93.93/94.77	73.57/82.99/85.57	73.36/83.80/87.40	85.87/74.94/84.12	82.23/76.68/77.40	71.93/82.82/86.28		
	Energy+ReAct	70.81/88.24/91.07	39.99/92.51/93.38	54.47/89.56/91.07	51.89/90.12/92.29	59.15/87.96/93.31	81.33/76.49/76.63	59.61/87.48/89.63		

A.2 DICE: Leverage Sparsification for OOD Detection

A.2.1 Variance Reduction with Correlated Variables

Extension of Lemma 2. We can show variance reduction in a more general case with correlated variables. The variance of output f_c without sparsification is:

$$\text{Var}[f_c] = \sum_{i=1}^m \sigma_i^2 + 2 \sum_{1 \leq i < j \leq m} \text{Cov}(v_i, v_j),$$

where $\text{Cov}(\cdot, \cdot)$ is the covariance. The expression states that the variance is the sum of the diagonal of the covariance matrix plus two times the sum of its upper triangular elements.

Similarly, the variance of output *with* directed sparsification (by taking the top units) is:

$$\text{Var}[f_c^{\text{DICE}}] = \sum_{i=t+1}^m \sigma_i^2 + 2 \sum_{t < i < j \leq m} \text{Cov}(v_i, v_j).$$

Therefore, the variance reduction is given by:

$$\sum_{i=1}^t \sigma_i^2 + 2 \sum_{1 \leq i < j \leq m} \text{Cov}(v_i, v_j) - 2 \sum_{t < i < j \leq m} \text{Cov}(v_i, v_j),$$

We show in Fig. A.3 that the covariance matrix of unit contribution v primarily consists of elements of 0, which indicates the independence of variables by large. The covariance matrix is estimated on the CIFAR-10 model with DenseNet-101, which is consistent with our main results in Table 4.2.

Moreover, the summation of non-zero entries in the full matrix (i.e., the second term) is greater than that of the submatrix with top units (i.e.,

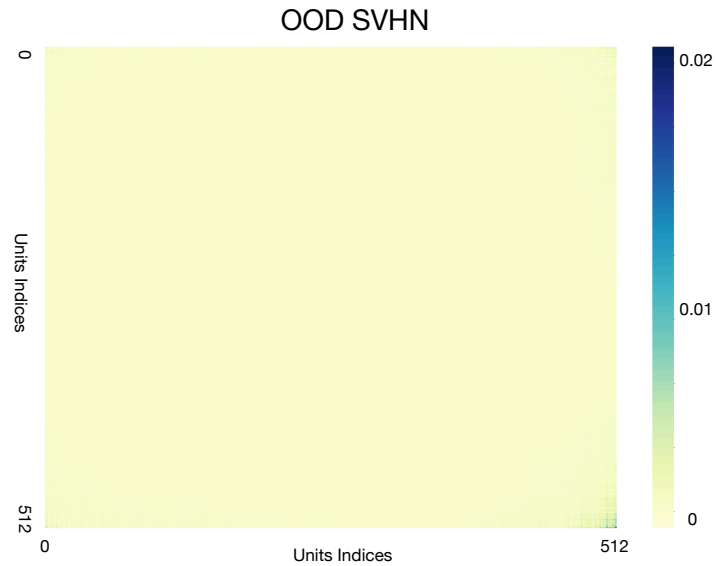


Figure A.3: Covariance matrix of unit contribution estimated on the OOD dataset SVHN. Model is trained on ID dataset CIFAR-10. The unit indices are sorted from low to high, based on the expectation value of ID’s unit contribution (airplane class, same as in Figure 4.1). The matrix primarily consists of elements with 0 value.

the third term), resulting in a larger variance reduction than in Lemma 4.2. In the case of OOD data (SVHN), we empirically measure the variance reduction, where $\sum_{i=1}^t \sigma_i^2 + 2 \sum_{1 \leq i < j \leq m} \text{Cov}(v_i, v_j)$ equals to **6.8** and $2 \sum_{t < i < j \leq m} \text{Cov}(v_i, v_j)$ equals to **2.2**. Therefore, DICE leads to a significant variance reduction effect.

A.2.2 Validation Strategy

We use a validation set of Gaussian noise images, which are generated by sampling from $\mathcal{N}(0, 1)$ for each pixel location. The optimal p is selected from $\{0.1, 0.3, 0.5, 0.7, 0.9, 0.99\}$, which is 0.9 for CIFAR-10/100 and 0.7 for ImageNet. We also show in Figure 4.3 using Gaussian can already find

the near-optimal one averaged over all OOD test datasets considered.

A.2.3 More results on the effect of Sparsity Parameter

We characterize the effect of sparsity parameter p on other ID datasets. In Table A.3, we summarize the OOD detection performance and classification performance for DenseNet trained on CIFAR-10 and ImageNet, where we vary $p = \{0.1, 0.3, 0.5, 0.7, 0.9, 0.99\}$. A similar trend is observed on CIFAR-100 as discussed in the main paper.

Table A.3: Effect of varying sparsity parameter p . Results are averaged on the test datasets described in Section 4.3.

Sparsity	CIFAR-10			ImageNet		
	FPR95 ↓	AUROC ↑	Acc. ↑	FPR95 ↓	AUROC ↑	Acc. ↑
$p = 0.99$	57.57	84.29	60.81	75.79	66.07	63.28
$p = 0.9$	21.76	94.91	94.38	40.10	89.09	73.36
$p = 0.7$	21.76	94.91	94.35	34.75	90.77	73.82
$p = 0.5$	21.76	94.91	94.35	34.58	90.80	73.80
$p = 0.3$	21.75	94.91	94.35	34.70	90.69	73.57
$p = 0.1$	21.92	94.90	94.33	40.25	89.44	73.38
$p = 0$	26.55	94.57	94.50	58.41	86.17	75.20

A.2.4 Detailed OOD Detection Performance for CIFAR

We report the detailed performance for all six test OOD datasets for models trained on CIFAR10 and CIFAR-100 respectively in Table A.4 and Table A.5.

Table A.4: Detailed results on six common OOD benchmark datasets: Textures (Cimpoi et al., 2014), SVHN (Netzer et al., 2011), Places365 (Zhou et al., 2017), LSUN-Crop (Yu et al., 2015), LSUN-Resize (Yu et al., 2015), and iSUN (Xu et al., 2015). For each ID dataset, we use the same DenseNet pretrained on CIFAR-10. \uparrow indicates larger values are better and \downarrow indicates smaller values are better.

Method Type	Method	SVHN		LSUN-c		LSUN-r		iSUN		Textures		Places365		Average	
		FPR95	AUROC	FPR95	AUROC	FPR95	AUROC	FPR95	AUROC	FPR95	AUROC	FPR95	AUROC	FPR95	AUROC
Non-Sparse	MSP	47.24	93.48	33.57	95.54	42.10	94.51	42.31	94.52	64.15	88.15	63.02	88.57	48.73	92.46
	ODIN	25.29	94.57	4.70	98.86	3.09	99.02	3.98	98.90	57.50	82.38	52.85	88.55	24.57	93.71
	GODIN	6.68	98.32	17.58	95.09	36.56	92.09	36.44	91.75	35.18	89.24	73.06	77.18	34.25	90.61
	Mahalanobis	6.42	98.31	56.55	86.96	9.14	97.09	9.78	97.25	21.51	92.15	85.14	63.15	31.42	89.15
	Energy	40.61	93.99	3.81	99.15	9.28	98.12	10.07	98.07	56.12	86.43	39.40	91.64	26.55	94.57
	ReAct	41.64	93.87	5.96	98.84	11.46	97.87	12.72	97.72	43.58	92.47	43.31	91.03	26.45	94.67
Sparse	Unit-Dropout	89.16	60.96	72.97	81.33	87.03	68.78	87.29	68.07	88.53	60.10	94.82	59.18	86.63	66.40
	Weight-Dropout	81.34	80.03	21.06	96.15	54.70	90.33	58.88	89.80	83.34	73.31	73.42	81.10	62.12	85.12
	Unit-Pruning	40.56	93.99	3.81	99.15	9.28	98.12	10.07	98.07	56.1	86.43	39.47	91.64	26.55	94.57
	Weight-Pruning	28.61	95.40	3.01	99.30	8.58	98.19	9.08	98.16	49.45	88.20	46.78	89.77	24.25	94.84
	DICE (ours)	25.99 ± 5.10	95.90 ± 1.08	0.26 ± 0.11	99.92 ± 0.02	3.91 ± 0.56	99.20 ± 0.15	4.36 ± 0.71	99.14 ± 0.15	41.90 ± 4.41	88.18 ± 1.80	48.59 ± 1.53	89.13 ± 0.31	20.83 ± 1.58	95.24 ± 0.24

Table A.5: Detailed results on six common OOD benchmark datasets: Textures (Cimpoi et al., 2014), SVHN (Netzer et al., 2011), Places365 (Zhou et al., 2017), LSUN-Crop (Yu et al., 2015), LSUN-Resize (Yu et al., 2015), and iSUN (Xu et al., 2015). For each ID dataset, we use the same DenseNet pretrained on CIFAR-100. \uparrow indicates larger values are better and \downarrow indicates smaller values are better.

Method Type	Method	SVHN		LSUN-c		LSUN-r		iSUN		Textures		Places365		Average	
		FPR95	AUROC	FPR95	AUROC	FPR95	AUROC	FPR95	AUROC	FPR95	AUROC	FPR95	AUROC	FPR95	AUROC
Non-Sparse	MSP	\downarrow 81.70	\uparrow 75.40	\downarrow 60.49	\uparrow 85.60	\downarrow 85.24	\uparrow 69.18	\downarrow 85.99	\uparrow 70.17	\downarrow 84.79	\uparrow 71.48	\downarrow 82.55	\uparrow 74.31	\downarrow 80.13	\uparrow 74.36
	ODIN	41.35	92.65	10.54	97.93	65.22	84.22	67.05	83.84	82.34	71.48	82.32	76.84	58.14	84.49
	GODIN	36.74	93.51	43.15	89.55	40.31	92.61	37.41	93.05	64.26	76.72	95.33	65.97	52.87	85.24
	Mahalanobis	22.44	95.67	68.90	86.30	23.07	94.20	31.38	93.21	62.39	79.39	92.66	61.39	55.37	82.73
	Energy	87.46	81.85	14.72	97.43	70.65	80.14	74.54	78.95	84.15	71.03	79.20	77.72	68.45	81.19
	ReAct	83.81	81.41	25.55	94.92	60.08	87.88	65.27	86.55	77.78	78.95	82.65	74.04	62.27	84.47
Sparse	Unit-Dropout	91.43	54.71	56.24	85.25	91.06	57.79	90.88	57.90	89.59	54.57	94.15	56.15	85.56	61.06
	Weight-Dropout	92.97	64.39	18.96	95.62	88.67	65.48	87.12	67.82	88.45	64.38	88.69	71.87	77.48	71.59
	Unit-Pruning	87.52	81.83	14.73	97.43	70.62	80.18	74.46	79.00	84.20	71.02	79.32	77.70	68.48	81.19
	Weight-Pruning	77.99	84.14	5.17	99.05	59.42	87.13	61.80	86.09	72.68	73.85	82.53	75.06	59.93	84.22
	DICE (ours)	54.65 $^{+4.94}$	88.84 $^{+0.39}$	0.93 $^{+0.07}$	99.74 $^{+0.01}$	49.40 $^{+1.99}$	91.04 $^{+1.49}$	48.72 $^{+1.55}$	90.08 $^{+1.36}$	65.04 $^{+0.66}$	76.42 $^{+0.35}$	79.58 $^{+2.34}$	77.26 $^{+1.08}$	49.72 $^{+1.69}$	87.23 $^{+0.73}$

A.3 OOD Detection with Deep Nearest Neighbors

A.3.1 Theoretical Analysis

Proof of Theorem 5.1. We now provide the proof sketch for readers to understand the key idea, which revolves around performing the empirical estimation of the probability $\hat{p}(g_i = 1|\mathbf{z}_i)$. By the Bayesian rule, the probability of \mathbf{z} being ID data is:

$$\begin{aligned} p(g_i = 1|\mathbf{z}_i) &= \frac{p(\mathbf{z}_i|g_i = 1) \cdot p(g_i = 1)}{p(\mathbf{z}_i)} \\ &= \frac{p_{in}(\mathbf{z}_i) \cdot p(g_i = 1)}{p_{in}(\mathbf{z}_i) \cdot p(g_i = 1) + p_{out}(\mathbf{z}_i) \cdot p(g_i = 0)} \\ \hat{p}(g_i = 1|\mathbf{z}_i) &= \frac{(1 - \varepsilon)\hat{p}_{in}(\mathbf{z}_i)}{(1 - \varepsilon)\hat{p}_{in}(\mathbf{z}_i) + \varepsilon\hat{p}_{out}(\mathbf{z}_i)}. \end{aligned}$$

Hence, estimating $\hat{p}(g_i = 1|\mathbf{z}_i)$ boils down to deriving the empirical estimation of $\hat{p}_{in}(\mathbf{z}_i)$ and $\hat{p}_{out}(\mathbf{z}_i)$, which we show below respectively.

Estimation for $\hat{p}_{in}(\mathbf{z}_i)$. Recall that \mathbf{z} is a normalized feature vector in \mathbb{R}^m . Therefore \mathbf{z} locates on the surface of a m -dimensional unit sphere. We denote $B(\mathbf{z}, r) = \{\mathbf{z}' : \|\mathbf{z}' - \mathbf{z}\|_2 \leq r\} \cap \{\|\mathbf{z}'\|_2 = 1\}$, which is a set of data points on the unit hyper-sphere and are at most r Euclidean distance away from the center \mathbf{z} . Note that the local dimension of $B(\mathbf{z}, r)$ is $m - 1$.

Assuming the density satisfies Lebesgue's differentiation theorem, the probability density function can be attained by:

$$p_{in}(\mathbf{z}_i) = \lim_{r \rightarrow 0} \frac{p(\mathbf{z} \in B(\mathbf{z}_i, r)|g_i = 1)}{|B(\mathbf{z}_i, r)|}.$$

In training time, we empirically observe n in-distribution samples $\mathcal{Z}_n = \{\mathbf{z}'_1, \mathbf{z}'_2, \dots, \mathbf{z}'_n\}$. We assume each sample \mathbf{z}'_j is *i.i.d* with a probability mass

$\frac{1}{n}$. The empirical point-density for the ID data can be estimated by k -NN distance:

$$\begin{aligned}\hat{p}_{in}(\mathbf{z}_i; k, n) &= \frac{p(\mathbf{z}'_j \in B(\mathbf{z}_i, r_k(\mathbf{z}_i)) | \mathbf{z}'_j \in \mathcal{Z}_n)}{|B(\mathbf{z}_i, r_k(\mathbf{z}_i))|} \\ &= \frac{k}{c_b n (r_k(\mathbf{z}_i))^{m-1}},\end{aligned}$$

where c_b is a constant. The following Lemma A.2 establishes the convergence rate of the estimator.

Lemma A.2.

$$\lim_{\frac{k}{n} \rightarrow 0} \hat{p}_{in}(\mathbf{z}_i; k, n) = p_{in}(\mathbf{z}_i).$$

Specifically,

$$\mathbb{E}[|\hat{p}_{in}(\mathbf{z}_i; k, n) - p_{in}(\mathbf{z}_i)|] = o\left(\sqrt{\frac{k}{n}} + \sqrt{\frac{1}{k}}\right).$$

The proof is given in Zhao and Lai (2020).

Estimation for $\hat{p}_{out}(\mathbf{z}_i)$. A key challenge in OOD detection is the lack of knowledge on OOD distribution, which can arise universally outside ID data. We thus try to keep our analysis general and reflect the fact that we do not have any strong prior information about OOD. For this reason, we model OOD data with an equal chance to appear outside of the high-density region of ID data. Our theory is thus complementary to our experiments and captures the universality of OOD data. Specifically, we denote

$$\hat{p}_{out}(\mathbf{z}_i) = \hat{c}_0 \mathbf{1}\left\{\hat{p}_{in}(\mathbf{z}_i; k, n) < \frac{\beta \varepsilon \hat{c}_0}{(1 - \beta)(1 - \varepsilon)}\right\}$$

where the threshold is chosen to satisfy the theorem.

Lastly, our theorem holds by plugging in the empirical estimation of $\hat{p}_{in}(\mathbf{z}_i)$ and $\hat{p}_{out}(\mathbf{z}_i)$.

Proof.

$$\begin{aligned}
& \mathbf{1}\{-r_k(\mathbf{z}_i) \geq \lambda\} \\
&= \mathbf{1}\{\varepsilon c_b n \hat{c}_0 (r_k(\mathbf{z}_i))^{m-1} \leq \frac{1-\beta}{\beta} (1-\varepsilon)k\} \\
&= \mathbf{1}\{\varepsilon c_b n \hat{c}_0 \mathbf{1}\{\varepsilon c_b n \hat{c}_0 (r_k(\mathbf{z}_i))^{m-1} > \frac{1-\beta}{\beta} (1-\varepsilon)k\} (r_k(\mathbf{z}_i))^{m-1} \leq \frac{1-\beta}{\beta} (1-\varepsilon)k\} \\
&= \mathbf{1}\{\varepsilon c_b n \hat{c}_0 \mathbf{1}\{\hat{p}_{in}(\mathbf{z}_i; k, n) < \frac{\beta \varepsilon \hat{c}_0}{(1-\beta)(1-\varepsilon)}\} (r_k(\mathbf{z}_i))^{m-1} \leq \frac{1-\beta}{\beta} (1-\varepsilon)k\} \\
&= \mathbf{1}\{\varepsilon c_b n \hat{p}_{out}(\mathbf{z}_i) (r_k(\mathbf{z}_i))^{m-1} \leq \frac{1-\beta}{\beta} (1-\varepsilon)k\} \\
&= \mathbf{1}\left\{\frac{k(1-\varepsilon)}{k(1-\varepsilon) + \varepsilon c_b n \hat{p}_{out}(\mathbf{z}_i) (r_k(\mathbf{z}_i))^{m-1}} \geq \beta\right\} \\
&= \mathbf{1}\{\hat{p}(g_i = 1 | \mathbf{z}_i) \geq \beta\}
\end{aligned}$$

□

A.3.2 Configurations

Non-parametric methods for anomaly detection. We provide implementation details of the non-parametric methods in this section. Specifically,

IForest (Liu et al., 2008) generates a random forest assuming the test anomaly can be isolated in fewer steps. We use 100 base estimators in the ensemble and each estimator draws 256 samples randomly for training. The number of features to train each base estimator is set to 512.

LOF (Breunig et al., 2000) defines an outlier score based on the sample's k -NN distances. We set $k = 50$.

LODA (Pevny, 2016) is an ensemble solution combining multiple weaker binary classifiers. The number of bins for the histogram is set to 10.

PCA (Shyu et al., 2003) detects anomaly samples with large values when mapping to the directions with small eigenvalues. We use 50 components for calculating the outlier scores.

OCSVM (Schölkopf et al., 2001) learns a decision boundary that corresponds to the desired density level set of with the kernel function. We use the RBF kernel with $\gamma = \frac{1}{512}$. The upper bound on the fraction of training error is set to 0.5.

Some of these methods (Schölkopf et al., 2001; Shyu et al., 2003) are specifically designed for anomaly detection scenarios that assume ID data is from one class. We show that k -NN distance with the class-aware embeddings can achieve both OOD detection and multi-class classification tasks.

A.3.3 Results on Different Architecture

In the main paper, we have shown that the nearest neighbor approach is competitive on ResNet. In this section, we show in Table A.6 that KNN’s strong performance holds on different network architectures DenseNet-101 (Huang et al., 2017). All the numbers reported are averaged over OOD test datasets described in Section 5.3.1.

Table A.6: **Comparison results with DenseNet-101.** Comparison with competitive out-of-distribution detection methods. All methods are based on a model trained on ID data only. All values are percentages and are averaged over all OOD test datasets.

Method	CIFAR-10			CIFAR-100		
	FPR95 ↓	AUROC ↑	ID ACC ↑	FPR95 ↓	AUROC ↑	ID ACC ↑
MSP	49.95	92.05	94.38	79.10	75.39	75.08
Energy	30.16	92.44	94.38	68.03	81.40	75.08
ODIN	30.02	93.86	94.38	55.96	85.16	75.08
Mahalanobis	35.88	87.56	94.38	74.57	66.03	75.08
GODIN	28.98	92.48	94.22	55.38	83.76	74.50
CSI	70.97	78.42	93.49	79.13	60.41	68.48
SSD+	16.21	96.96	94.45	43.44	88.97	75.21
KNN+	12.16	97.58	94.45	37.27	89.63	75.21

Appendix B

Appendix for Open-world Representation Learning

B.1 When and How Does Known Class Help Discover Unknown Ones? A Spectral Analysis

B.1.1 Proof Details for Section 6.3

B.1.1.1 Bound Linear Probing Error by Regression Residual

Lemma B.1. (Recap of Lemma 6.2) Denote by $\mathbf{y}(x) \in \mathbb{R}^{|\mathcal{Y}_u|}$ a one-hot vector, whose $y(x)$ -th position is 1 and 0 elsewhere. Let $\mathbf{Y} \in \mathbb{R}^{N_u \times |\mathcal{Y}_u|}$ be a matrix whose rows are stacked by $\mathbf{y}(x)$. We have:

$$\mathcal{R}(U^*) \triangleq \min_{\mathbf{M} \in \mathbb{R}^{k \times |\mathcal{Y}_u|}} \|\mathbf{Y} - U^* \mathbf{M}\|_F^2 \geq \frac{1}{2} \mathcal{E}(f)$$

Proof. Suppose $\tilde{f}(x) = \sqrt{w_x}f(x)$, we first show that

$$\|\mathbf{y}(x) - \tilde{f}(x)^\top \mathbf{M}\|^2 \geq \frac{1}{2} \mathbb{1} [y(x) \neq h(x; \tilde{f}, M)]$$

If $y(x) = h(x; \tilde{f}, M)$, it is clear that $\|\mathbf{y}(x) - \tilde{f}(x)^\top \mathbf{M}\|^2 \geq 0$. If $y(x) \neq h(x; \tilde{f}, M)$, then there exists another index $y' \neq y(x)$ so that $\tilde{f}(x)^\top \vec{\mu}_{y'} \geq \tilde{f}(x)^\top \vec{\mu}_{y(x)}$. Then,

$$\begin{aligned} \|\mathbf{y}(x) - \tilde{f}(x)^\top \mathbf{M}\|_2^2 &\geq (1 - \tilde{f}(x)^\top \vec{\mu}_{y(x)})^2 + (\tilde{f}(x)^\top \vec{\mu}_{y'})^2 \\ &\geq \frac{1}{2} (1 - \tilde{f}(x)^\top \vec{\mu}_{y(x)} + \tilde{f}(x)^\top \vec{\mu}_{y'})^2 \\ &\geq \frac{1}{2}, \end{aligned}$$

where the first inequality is by only keeping y' -th and $y(x)$ -th terms in the l_2 norm. We can then prove the lemma by:

$$\begin{aligned} \mathcal{R}(U^*) &= \min_{\mathbf{M} \in \mathbb{R}^{k \times |\mathcal{Y}_u|}} \|\mathbf{Y} - U^* \mathbf{M}\|_F^2 \\ &= \min_{\mathbf{M} \in \mathbb{R}^{k \times |\mathcal{Y}_u|}} \sum_{x \in \mathcal{X}_u} \|\mathbf{y}(x) - \sqrt{w_x} f(x)^\top \Sigma_k^{-\frac{1}{2}} \mathbf{M}\|^2 \\ &= \min_{\mathbf{M} \in \mathbb{R}^{k \times |\mathcal{Y}_u|}} \sum_{x \in \mathcal{X}_u} \|\mathbf{y}(x) - \sqrt{w_x} f(x)^\top \mathbf{M}\|^2 \\ &\geq \frac{1}{2} \min_{\mathbf{M} \in \mathbb{R}^{k \times |\mathcal{Y}_u|}} \sum_{x \in \mathcal{X}_u} \mathbb{1} [y(x) \neq h(x; \tilde{f}, M)] \\ &= \frac{1}{2} \mathcal{E}(f), \end{aligned}$$

where the second equation is given by $F^* \Sigma_k^{-\frac{1}{2}} = V_k$, and U^* is the last N_u rows of V_k , and the last equation is based on the fact that multiplying a scalar value on the output does not change the prediction result ($h(x; f, \mathbf{M}) = h(x; \tilde{f}, \mathbf{M})$). \square

B.1.1.2 Spectral Contrastive Loss

Theorem B.2. (Recap of Theorem 6.1) We define $\mathbf{f}_x = \sqrt{w_x}f(x)$ for some function f . Recall α, β is a hyper-parameter defined in Eq. (6.1). Then minimizing the loss function $\mathcal{L}_{\text{mf}}(F, A)$ is equivalent to minimizing the following loss function for f , which we term **NCD Spectral Contrastive Loss (NSCL)**:

$$\begin{aligned} \mathcal{L}_{\text{nscl}}(f) \triangleq & -2\alpha\mathcal{L}_1(f) - 2\beta\mathcal{L}_2(f) \\ & + \alpha^2\mathcal{L}_3(f) + 2\alpha\beta\mathcal{L}_4(f) + \beta^2\mathcal{L}_5(f), \end{aligned} \quad (\text{B.1})$$

where

$$\begin{aligned} \mathcal{L}_1(f) &= \sum_{i \in \mathcal{Y}_l} \mathbb{E}_{\substack{\bar{x}_l \sim \mathcal{P}_{l_i}, \bar{x}'_l \sim \mathcal{P}_{l_i}, \\ x \sim \mathcal{T}(\cdot | \bar{x}_l), x^+ \sim \mathcal{T}(\cdot | \bar{x}'_l)}} \left[f(x)^\top f(x^+) \right], \\ \mathcal{L}_2(f) &= \mathbb{E}_{\substack{\bar{x}_u \sim \mathcal{P}_u, \\ x \sim \mathcal{T}(\cdot | \bar{x}_u), x^+ \sim \mathcal{T}(\cdot | \bar{x}_u)}} \left[f(x)^\top f(x^+) \right], \\ \mathcal{L}_3(f) &= \sum_{i \in \mathcal{Y}_l} \sum_{j \in \mathcal{Y}_l} \mathbb{E}_{\substack{\bar{x}_l \sim \mathcal{P}_{l_i}, \bar{x}'_l \sim \mathcal{P}_{l_j}, \\ x \sim \mathcal{T}(\cdot | \bar{x}_l), x^- \sim \mathcal{T}(\cdot | \bar{x}'_l)}} \left[\left(f(x)^\top f(x^-) \right)^2 \right], \\ \mathcal{L}_4(f) &= \sum_{i \in \mathcal{Y}_l} \mathbb{E}_{\substack{\bar{x}_l \sim \mathcal{P}_{l_i}, \bar{x}_u \sim \mathcal{P}_u, \\ x \sim \mathcal{T}(\cdot | \bar{x}_l), x^- \sim \mathcal{T}(\cdot | \bar{x}_u)}} \left[\left(f(x)^\top f(x^-) \right)^2 \right], \\ \mathcal{L}_5(f) &= \mathbb{E}_{\substack{\bar{x}_u \sim \mathcal{P}_u, \bar{x}'_u \sim \mathcal{P}_u, \\ x \sim \mathcal{T}(\cdot | \bar{x}_u), x^- \sim \mathcal{T}(\cdot | \bar{x}'_u)}} \left[\left(f(x)^\top f(x^-) \right)^2 \right]. \end{aligned}$$

Proof. We can expand $\mathcal{L}_{\text{mf}}(F, A)$ and obtain

$$\begin{aligned} \mathcal{L}_{\text{mf}}(F, A) &= \sum_{x, x' \in \mathcal{X}} \left(\frac{w_{xx'}}{\sqrt{w_x w_{x'}}} - \mathbf{f}_x^\top \mathbf{f}_{x'} \right)^2 \\ &= \text{const} + \sum_{x, x' \in \mathcal{X}} \left(-2w_{xx'} f(x)^\top f(x') + w_x w_{x'} \left(f(x)^\top f(x') \right)^2 \right), \end{aligned}$$

where $\mathbf{f}_x = \sqrt{w_x}f(x)$ is a re-scaled version of $f(x)$. At a high level we follow the proof in (HaoChen et al., 2021), while the specific form of loss

varies with the different definitions of positive/negative pairs. The form of $\mathcal{L}_{nscI}(f)$ is derived from plugging $w_{xx'}$ and w_x .

Recall that $w_{xx'}$ is defined by

$$w_{xx'} = \alpha \sum_{i \in \mathcal{Y}_l} \mathbb{E}_{\bar{x}_l \sim \mathcal{P}_{l_i}} \mathbb{E}_{\bar{x}'_l \sim \mathcal{P}_{l_i}} \mathcal{T}(x|\bar{x}_l) \mathcal{T}(x'|\bar{x}'_l) + \beta \mathbb{E}_{\bar{x}_u \sim \mathcal{P}_u} \mathcal{T}(x|\bar{x}_u) \mathcal{T}(x'|\bar{x}_u),$$

and w_x is given by

$$\begin{aligned} w_x &= \sum_{x'} w_{xx'} \\ &= \alpha \sum_{i \in \mathcal{Y}_l} \mathbb{E}_{\bar{x}_l \sim \mathcal{P}_{l_i}} \mathbb{E}_{\bar{x}'_l \sim \mathcal{P}_{l_i}} \mathcal{T}(x|\bar{x}_l) \sum_{x'} \mathcal{T}(x'|\bar{x}'_l) + \beta \mathbb{E}_{\bar{x}_u \sim \mathcal{P}_u} \mathcal{T}(x|\bar{x}_u) \sum_{x'} \mathcal{T}(x'|\bar{x}_u) \\ &= \alpha \sum_{i \in \mathcal{Y}_l} \mathbb{E}_{\bar{x}_l \sim \mathcal{P}_{l_i}} \mathcal{T}(x|\bar{x}_l) + \beta \mathbb{E}_{\bar{x}_u \sim \mathcal{P}_u} \mathcal{T}(x|\bar{x}_u). \end{aligned}$$

Plugging $w_{xx'}$ we have,

$$\begin{aligned} -2 \sum_{x, x' \in \mathcal{X}} w_{xx'} f(x)^\top f(x') &= -2 \sum_{x, x^+ \in \mathcal{X}} w_{xx^+} f(x)^\top f(x^+) \\ &= -2\alpha \sum_{i \in \mathcal{Y}_l} \mathbb{E}_{\bar{x}_l \sim \mathcal{P}_{l_i}} \mathbb{E}_{\bar{x}'_l \sim \mathcal{P}_{l_i}} \sum_{x, x' \in \mathcal{X}} \mathcal{T}(x|\bar{x}_l) \mathcal{T}(x'|\bar{x}'_l) f(x)^\top f(x') \\ &\quad - 2\beta \mathbb{E}_{\bar{x}_u \sim \mathcal{P}_u} \sum_{x, x'} \mathcal{T}(x|\bar{x}_u) \mathcal{T}(x'|\bar{x}_u) f(x)^\top f(x') \\ &= -2\alpha \sum_{i \in \mathcal{Y}_l} \mathbb{E}_{\substack{\bar{x}_l \sim \mathcal{P}_{l_i}, \bar{x}'_l \sim \mathcal{P}_{l_i}, \\ x \sim \mathcal{T}(\cdot|\bar{x}_l), x^+ \sim \mathcal{T}(\cdot|\bar{x}'_l)}} [f(x)^\top f(x^+)] \\ &\quad - 2\beta \mathbb{E}_{\substack{\bar{x}_u \sim \mathcal{P}_u, \\ x \sim \mathcal{T}(\cdot|\bar{x}_u), x^+ \sim \mathcal{T}(\cdot|\bar{x}_u)}} [f(x)^\top f(x^+)] \\ &= -2\alpha \mathcal{L}_1(f) - 2\beta \mathcal{L}_2(f) \end{aligned}$$

Plugging w_x and $w_{x'}$ we have,

$$\begin{aligned}
& \sum_{x, x' \in \mathcal{X}} w_x w_{x'} \left(f(x)^\top f(x') \right)^2 = \sum_{x, x^- \in \mathcal{X}} w_x w_{x^-} \left(f(x)^\top f(x^-) \right)^2 \\
&= \sum_{x, x' \in \mathcal{X}} \left(\alpha \sum_{i \in \mathcal{Y}_l} \mathbb{E}_{\bar{x}_l \sim \mathcal{P}_{l_i}} \mathcal{T}(x | \bar{x}_l) + \beta \mathbb{E}_{\bar{x}_u \sim \mathcal{P}_u} \mathcal{T}(x | \bar{x}_u) \right) \\
&\quad \left(\alpha \sum_{j \in \mathcal{Y}_l} \mathbb{E}_{\bar{x}'_l \sim \mathcal{P}_{l_j}} \mathcal{T}(x^- | \bar{x}'_l) + \beta \mathbb{E}_{\bar{x}'_u \sim \mathcal{P}_u} \mathcal{T}(x^- | \bar{x}'_u) \right) \left(f(x)^\top f(x^-) \right)^2 \\
&= \alpha^2 \sum_{x, x^- \in \mathcal{X}} \sum_{i \in \mathcal{Y}_l} \mathbb{E}_{\bar{x}_l \sim \mathcal{P}_{l_i}} \mathcal{T}(x | \bar{x}_l) \sum_{j \in \mathcal{Y}_l} \mathbb{E}_{\bar{x}'_l \sim \mathcal{P}_{l_j}} \mathcal{T}(x^- | \bar{x}'_l) \left(f(x)^\top f(x^-) \right)^2 \\
&\quad + 2\alpha\beta \sum_{x, x^- \in \mathcal{X}} \sum_{i \in \mathcal{Y}_l} \mathbb{E}_{\bar{x}_l \sim \mathcal{P}_{l_i}} \mathcal{T}(x | \bar{x}_l) \mathbb{E}_{\bar{x}_u \sim \mathcal{P}_u} \mathcal{T}(x^- | \bar{x}_u) \left(f(x)^\top f(x^-) \right)^2 \\
&\quad + \beta^2 \sum_{x, x^- \in \mathcal{X}} \mathbb{E}_{\bar{x}_u \sim \mathcal{P}_u} \mathcal{T}(x | \bar{x}_u) \mathbb{E}_{\bar{x}'_u \sim \mathcal{P}_u} \mathcal{T}(x^- | \bar{x}'_u) \left(f(x)^\top f(x^-) \right)^2 \\
&= \alpha^2 \sum_{i \in \mathcal{Y}_l} \sum_{j \in \mathcal{Y}_l} \mathbb{E}_{\substack{\bar{x}_l \sim \mathcal{P}_{l_i}, \bar{x}'_l \sim \mathcal{P}_{l_j}, \\ x \sim \mathcal{T}(\cdot | \bar{x}_l), x^- \sim \mathcal{T}(\cdot | \bar{x}'_l)}} \left[\left(f(x)^\top f(x^-) \right)^2 \right] \\
&\quad + 2\alpha\beta \sum_{i \in \mathcal{Y}_l} \mathbb{E}_{\substack{\bar{x}_l \sim \mathcal{P}_{l_i}, \bar{x}_u \sim \mathcal{P}_u, \\ x \sim \mathcal{T}(\cdot | \bar{x}_l), x^- \sim \mathcal{T}(\cdot | \bar{x}_u)}} \left[\left(f(x)^\top f(x^-) \right)^2 \right] \\
&\quad + \beta^2 \sum_{\substack{\bar{x}_u \sim \mathcal{P}_u, \bar{x}'_u \sim \mathcal{P}_u, \\ x \sim \mathcal{T}(\cdot | \bar{x}_u), x^- \sim \mathcal{T}(\cdot | \bar{x}'_u)}} \left[\left(f(x)^\top f(x^-) \right)^2 \right] \\
&= \alpha^2 \mathcal{L}_3(f) + 2\alpha\beta \mathcal{L}_4(f) + \beta^2 \mathcal{L}_5(f).
\end{aligned}$$

□

B.1.2 Proof for Eigenvalue in Toy Example

Before we present the proof of Theorem 6.3, Theorem 6.4 and Lemma 6.5, we first present the following lemma B.3 which extensively explore the order and the form of eigenvectors of the general form $T(t)$. Note that T_1 and T_2 are special cases of the following $T(t)$ with $t \in [\tau_0, \tau_c]$:

$$T(t) = \begin{bmatrix} \tau_1 & t & t & \tau_0 & \tau_0 \\ t & \tau_1 & \tau_c & \tau_s & \tau_0 \\ t & \tau_c & \tau_1 & \tau_0 & \tau_s \\ \tau_0 & \tau_s & \tau_0 & \tau_1 & \tau_c \\ \tau_0 & \tau_0 & \tau_s & \tau_c & \tau_1 \end{bmatrix},$$

where t indicates the strength of the connection between labeled data and a novel class in unlabeled data.

Lemma B.3. *Assume $\tau_1 = 1$, $\tau_0 = 0$, $\tau_c < \tau_s < 1.5\tau_c$, $\bar{t} = \sqrt{\frac{2(\tau_s - \tau_c)^2 \tau_c}{2\tau_c - \tau_s}}$, let $a(\lambda) = \frac{\lambda - 1}{2t}$ and $b(\lambda) = \frac{\tau_s(\lambda - 1)}{2(\lambda - 1 - \tau_c)t}$ are real value functions, the matrix $T(t)$'s eigenvectors (not necessarily l_2 -normalized) and its eigenvalues are the following:*

(Case 1): If $t \in (\bar{t}, \tau_c]$,

$$\begin{aligned} v_1 &= [1, a(\lambda_1), a(\lambda_1), b(\lambda_1), b(\lambda_1)]^\top, & \lambda_1 &> 1 + \tau_s + \tau_c, \\ v_2 &= [1, a(\lambda_2), a(\lambda_2), b(\lambda_2), b(\lambda_2)]^\top, & \lambda_2 &\in [1 + \tau_s - \tau_c, 1 + \tau_c) \\ v_3 &= [0, -1, 1, -1, 1]^\top, & \lambda_3 &= 1 + \tau_s - \tau_c, \\ v_4 &= [1, a(\lambda_4), a(\lambda_4), b(\lambda_4), b(\lambda_4)]^\top, & \lambda_4 &\in (1 - \tau_s - \tau_c, 1) \\ v_5 &= [0, 1, -1, -1, 1]^\top, & \lambda_5 &= 1 - \tau_s - \tau_c, \end{aligned}$$

(Case 2): If $t \in (0, \bar{t})$,

$$\begin{aligned} v_1 &= [1, a(\lambda_1), a(\lambda_1), b(\lambda_1), b(\lambda_1)]^\top, & \lambda_1 &> 1 + \tau_s + \tau_c, \\ v_2 &= [0, -1, 1, -1, 1]^\top, & \lambda_2 &= 1 + \tau_s - \tau_c, \\ v_3 &= [1, a(\lambda_3), a(\lambda_3), b(\lambda_3), b(\lambda_3)]^\top, & \lambda_3 &\in [1, 1 + \tau_s - \tau_c) \\ v_4 &= [1, a(\lambda_4), a(\lambda_4), b(\lambda_4), b(\lambda_4)]^\top, & \lambda_4 &\in (1 - \tau_s - \tau_c, 1) \\ v_5 &= [0, 1, -1, -1, 1]^\top, & \lambda_5 &= 1 - \tau_s - \tau_c, \end{aligned}$$

(Case 3): If $t = 0$,

$$\begin{aligned} v_1 &= [0, 1, 1, 1, 1]^\top, & \lambda_1 &= 1 + \tau_s + \tau_c, \\ v_2 &= [0, -1, 1, -1, 1]^\top, & \lambda_2 &= 1 + \tau_s - \tau_c, \\ v_3 &= [1, 0, 0, 0, 0]^\top, & \lambda_3 &= 1 \\ v_4 &= [0, 1, 1, -1, -1]^\top, & \lambda_4 &= 1 - \tau_s + \tau_c \\ v_5 &= [0, 1, -1, -1, 1]^\top, & \lambda_5 &= 1 - \tau_s - \tau_c, \end{aligned}$$

Proof. For $t = 0$, Case 3, we can verify by direct calculation.

Now for Case 1 and Case 2, we consider $t \in (0, \tau_c)$. For any $i \in [5]$, denote $\hat{\lambda}_i$ as unordered eigenvalue and \hat{v}_i is its corresponding eigenvector. We can direct verify that

$$\hat{\lambda}_1 = 1 + \tau_s - \tau_c \tag{B.2}$$

$$\hat{\lambda}_2 = 1 - \tau_s - \tau_c, \tag{B.3}$$

are two eigenvalues of \tilde{A}_t and

$$\hat{v}_1 = [0, -1, 1, -1, 1]^\top \tag{B.4}$$

$$\hat{v}_2 = [0, 1, -1, -1, 1]^\top, \tag{B.5}$$

are two corresponding eigenvectors. Now, we prove for $i \in \{3, 4, 5\}$, $\hat{v}_i = [1, a(\hat{\lambda}_i), a(\hat{\lambda}_i), b(\hat{\lambda}_i), b(\hat{\lambda}_i)]^\top$ are eigenvector for $\hat{\lambda}_i$. For $i \in \{3, 4, 5\}$ we only need to show

$$\begin{cases} 1 + 2ta(\hat{\lambda}_i) & = \hat{\lambda}_i \\ t + (1 + \tau_c)a(\hat{\lambda}_i) + \tau_s b(\hat{\lambda}_i) & = \hat{\lambda}_i a(\hat{\lambda}_i) \\ \tau_s a(\hat{\lambda}_i) + (1 + \tau_c)b(\hat{\lambda}_i) & = \hat{\lambda}_i b(\hat{\lambda}_i). \end{cases} \quad (\text{B.6})$$

Equivalently to

$$\begin{cases} 1 + 2ta(\hat{\lambda}_i) - \hat{\lambda}_i & = 0 \\ t + (1 + \tau_c + \tau_s - \hat{\lambda}_i)(a(\hat{\lambda}_i)d + b(\hat{\lambda}_i)) & = 0 \\ t + (1 + \tau_c - \tau_s - \hat{\lambda}_i)(a(\hat{\lambda}_i) - b(\hat{\lambda}_i)) & = 0. \end{cases} \quad (\text{B.7})$$

Let $z_i = \hat{\lambda}_i - 1$. Equivalently to

$$\begin{cases} 1 + 2ta(\hat{\lambda}_i) - \hat{\lambda}_i & = 0 \\ (\hat{\lambda}_i - 1 - \tau_c)b(\hat{\lambda}_i) - \tau_s a(\hat{\lambda}_i) & = 0 \\ z_i^3 - 2\tau_c z_i^2 + (\tau_c^2 - \tau_s^2 - 2t^2)z_i + 2\tau_c t^2 & = 0. \end{cases} \quad (\text{B.8})$$

Let $g(z) = z^3 - 2\tau_c z^2 + (\tau_c^2 - \tau_s^2 - 2t^2)z + 2\tau_c t^2$, we can verify that $g(-\infty) < 0$, $g(-\tau_c - \tau_s) = -4\tau_c(\tau_c + \tau_s)^2 + 4t^2\tau_c + 2t^2\tau_s < 0$, $g(0) = 2\tau_c t^2 > 0$, $g(\tau_c) = -\tau_s^2\tau_c < 0$, $g(\tau_c + \tau_s) = -2\tau_s t^2 < 0$, $g(+\infty) > 0$. Thus, we have three solutions and satisfying $1 - \tau_c - \tau_s < \hat{\lambda}_5 < 1 < \hat{\lambda}_4 < 1 + \tau_c < 1 + \tau_c + \tau_s < \hat{\lambda}_3$.

As $\hat{\lambda}_i \neq 1 + \tau_c$ for $i \in \{3, 4, 5\}$, thus, equivalently to

$$\begin{cases} a(\hat{\lambda}_i) & = \frac{\hat{\lambda}_i - 1}{2t} \\ b(\hat{\lambda}_i) & = \frac{\tau_s(\hat{\lambda}_i - 1)}{2(\hat{\lambda}_i - 1 - \tau_c)t} \\ (\hat{\lambda}_i - 1)^3 - 2\tau_c(\hat{\lambda}_i - 1)^2 + (\tau_c^2 - \tau_s^2 - 2t^2)(\hat{\lambda}_i - 1) + 2\tau_c t^2 & = 0. \end{cases} \quad (\text{B.9})$$

When $t > \bar{t}$, we have $g(\tau_s - \tau_c) > 0$. Thus, we have $1 - \tau_c - \tau_s < \hat{\lambda}_5 < 1 + \tau_s - \tau_c < \hat{\lambda}_4 < 1 + \tau_c + \tau_s < \hat{\lambda}_3$. By reorder, we finish Case 1.

When $t < \bar{t}$, we have $g(\tau_s - \tau_c) < 0$. Thus, we have $1 - \tau_c - \tau_s < \hat{\lambda}_5 < 1 < \hat{\lambda}_4 < 1 + \tau_s - \tau_c < 1 + \tau_c + \tau_s < \hat{\lambda}_3$. By reorder the eigenvectors w.r.t the size of eigenvalues, we finish Case 2. \square

Theorem B.4. (Recap of Theorem 6.3) Assume $\tau_1 = 1, \tau_0 = 0, \tau_s < 1.5\tau_c$. We have

$$U_1^* = \begin{bmatrix} a_1 & a_1 & b_1 & b_1 \\ a_2 & a_2 & b_2 & b_2 \end{bmatrix}^\top,$$

where a_1, b_1 are some positive real numbers, and a_2, b_2 has different signs.

$$U_2^* = \begin{cases} \frac{1}{2} \begin{bmatrix} 1 & 1 & 1 & 1 \\ 1 & 1 & -1 & -1 \end{bmatrix}^\top, & \text{if } \tau_s < \tau_c, \\ \frac{1}{2} \begin{bmatrix} 1 & 1 & 1 & 1 \\ -1 & 1 & -1 & 1 \end{bmatrix}^\top, & \text{if } \tau_s > \tau_c, \end{cases}$$

With label vector $\vec{y} = \{1, 1, 0, 0\}$, we have

$$\mathcal{R}(U_1^*, \vec{y}) = 0, \mathcal{R}(U_2^*, \vec{y}) = \begin{cases} 0, & \text{if } \tau_s < \tau_c \\ 1, & \text{if } \tau_s > \tau_c. \end{cases} \quad (\text{B.10})$$

Proof. In the Case 1 and Case 3 of Lemma B.3, we have shown the U_1^* and U_2^* case when $\tau_s > \tau_c$ respectively. In this proof, we just need to show the case when $\tau_s < \tau_c$. For U_2^* and $\tau_s < \tau_c$, since $t = 0$, we can directly prove by giving the eigenvectors with order:

$$\begin{aligned} v_1 &= [0, 1, 1, 1, 1]^\top, & \lambda_1 &= 1 + \tau_s + \tau_c, \\ v_2 &= [0, 1, 1, -1, -1]^\top, & \lambda_2 &= 1 - \tau_s + \tau_c \\ v_3 &= [1, 0, 0, 0, 0]^\top, & \lambda_3 &= 1 \\ v_4 &= [0, -1, 1, -1, 1]^\top, & \lambda_4 &= 1 + \tau_s - \tau_c, \\ v_5 &= [0, 1, -1, -1, 1]^\top, & \lambda_5 &= 1 - \tau_s - \tau_c, \end{aligned}$$

For U_1^* , one can see that in the Case 1 of Lemma B.3, we still have $\lambda_2 > \lambda_3$ since $\tau_s < 1.5\tau_c < 2\tau_c$ holds. Therefore the order of v_2 and v_3 does not change. Then U_1^* is the concatenation of the last four dimensions of v_2 and v_1 .

Now we would like to show that a_1, b_1 are positive and a_2, b_2 have different signs. We have shown in Lemma B.3 that $a(\lambda) = \frac{\lambda-1}{2t}$ and $b(\lambda) = \frac{\tau_s(\lambda-1)}{2(\lambda-1-\tau_c)t}$. Since $a_1 = a(\lambda_1)$ and $b_1 = b(\lambda_1)$, one can show that $a_1 > 0, b_1 > 0$ since $\lambda_1 > 1 + \tau_s + \tau_c$. For $\lambda_2 \in [1 + \tau_s - \tau_c, 1 + \tau_c)$, it is clear that $a_2 = a(\lambda_2) > 0 > b(\lambda_2) = b_2$ when $\tau_s > \tau_c$, and conversely we have $a_2 = a(\lambda_2) < 0 < b(\lambda_2) = b_2$ when $\tau_s < \tau_c$. So a_2 and b_2 have different signs in both cases.

Recall $\mathcal{R}(U^*, \vec{y})$ is defined as:

$$\mathcal{R}(U^*, \vec{y}) = \min_{\vec{\mu} \in \mathbb{R}^k} \|\vec{y} - U^* \vec{\mu}\|_2^2,$$

Let $\vec{\mu} = [\frac{b_2}{a_1 b_2 - a_2 b_1}, \frac{-b_1}{a_1 b_2 - a_2 b_1}]^\top$, $\mathcal{R}(U_1^*, \vec{y}) = 0$. If $\tau_s < \tau_c$, let $\vec{\mu} = [1, 1]^\top$, then $\mathcal{R}(U_2^*, \vec{y}) = 0$. If $\tau_s > \tau_c$, $\vec{\mu}^* = U_2^{*\top} \vec{y} = [1, 0]^\top$ is the minimizer and we have $\mathcal{R}(U_2^*, \vec{y}) = 1$.

□

Theorem B.5. (Recap of Theorem 6.4) Assume $\tau_1 = 1, \tau_0 = 0, 1.5\tau_c > \tau_s > \tau_c$.

Let $\bar{t} = \sqrt{\frac{2(\tau_s - \tau_c)^2 \tau_c}{2\tau_c - \tau_s}}, r : \mathbb{R} \mapsto (0, 1)$ as a real value function, we have

$$\mathcal{R}(U_t^*, \vec{y}) = \begin{cases} 0, & \text{if } t \in (\bar{t}, \tau_s), \\ r(t), & \text{if } t \in (0, \bar{t}) \\ 1, & \text{if } t = 0. \end{cases} \quad (\text{B.11})$$

Proof. According to Lemma B.3, if $t \in (\bar{t}, \tau_s)$,

$$U_t^* = \begin{bmatrix} a_1 & a_1 & b_1 & b_1 \\ a_2 & a_2 & b_2 & b_2 \end{bmatrix}^\top,$$

where a_1, b_1 are some positive real numbers, and a_2, b_2 has different signs.

Let $\vec{\mu} = [\frac{b_2}{a_1 b_2 - a_2 b_1}, \frac{-b_1}{a_1 b_2 - a_2 b_1}]^\top, \mathcal{R}(U_t^*, \vec{y}) = 0$. If $t = 0, \mathcal{R}(U_t^*, \vec{y}) = 0$, which is proved in Theorem B.4 when $\tau_s > \tau_c$. If $t \in (0, \bar{t})$, as shown in Lemma B.3, we have

$$U_t^* = \begin{bmatrix} \frac{\lambda_1 - 1}{2t} & \frac{\lambda_1 - 1}{2t} & \frac{\tau_s(\lambda_1 - 1)}{2(\lambda_1 - 1 - \tau_c)t} & \frac{\tau_s(\lambda_1 - 1)}{2(\lambda_1 - 1 - \tau_c)t} \\ -1 & 1 & -1 & 1 \end{bmatrix}^\top,$$

where $\lambda_1 > 0$. $\vec{\mu}_* = (U_t^{*\top} U_t^*)^\dagger U_t^{*\top} \vec{y} = [\frac{\frac{\lambda_1 - 1}{2t}}{(\frac{\lambda_1 - 1}{2t})^2 + (\frac{\tau_s(\lambda_1 - 1)}{2(\lambda_1 - 1 - \tau_c)t})^2}, 0]^\top$, then:

$$\mathcal{R}(U_t^*, \vec{y}) = \frac{2\tau_s^2}{(\lambda_1 - 1 - \tau_c)^2 + \tau_s^2} = r(\lambda_1) \in (0, 1).$$

Note that λ_1 is a value dependent on t , therefore $r(\lambda_1)$ can be represented as $r(t)$.

□

Lemma B.6. (Recap of Lemma 6.5) If $\tau_s < \tau_c < 1.5\tau_s, \mathcal{R}(U_3^*, \vec{y}) = 1, \mathcal{R}(U_2^*, \vec{y}) = 0$.

Proof. When $\mathcal{X}_l^{\text{case } 3} \triangleq \{X_{\boxplus, c_3}\}$ (gray cube), we have

$$T_3 = \begin{bmatrix} \tau_1 & \tau_s & \tau_0 & \tau_s & \tau_0 \\ \tau_s & \tau_1 & \tau_c & \tau_s & \tau_0 \\ \tau_0 & \tau_c & \tau_1 & \tau_0 & \tau_s \\ \tau_s & \tau_s & \tau_0 & \tau_1 & \tau_c \\ \tau_0 & \tau_0 & \tau_s & \tau_c & \tau_1 \end{bmatrix},$$

Follow the same proof in Lemma B.3, one can show that

$$U_3^* = \begin{bmatrix} a_1 & b_1 & a_1 & b_1 \\ a_2 & b_2 & a_2 & b_2 \end{bmatrix}^\top,$$

where a_1, b_1 are some positive real numbers, and a_2, b_2 has different signs. Note that U_3^* forms the same linear span as

$$\frac{1}{2} \begin{bmatrix} 1 & 1 & 1 & 1 \\ -1 & 1 & -1 & 1 \end{bmatrix}^\top.$$

Therefore, we have $\mathcal{R}(U_3^*, \vec{y}) = 1$ as proved in Theorem B.4. \square

B.1.3 Additional Details for Section 6.4.3

This section acts as an expanded version of Section 6.4.3. We will first show in Section B.1.3.1 with the background and proof for Theorem 6.6 with the original adjacency matrix A . Then we present the analysis based on the approximation matrix \bar{A} in Section B.1.3.2. Finally, we show the formal proof of our main Theorem 6.7 in Section B.1.3.4. The proof of Theorem 6.7 requires two important ingredients (Lemma B.12 and Lemma B.16) with proof deferred in Section B.1.3.5 and Section B.1.3.6 respectively.

B.1.3.1 Sufficient and Necessary Condition for Perfect Residual

We first present the formal analysis in Theorem B.7 which is an extended version of Theorem 6.6 without approximation and we start with the recap of definitions.

Notations. Recall that $V^* \in \mathbb{R}^{N \times k}$ is defined as the top- k singular vectors of \dot{A} and we split the eigen-matrix into two parts for labeled and unlabeled samples respectively:

$$V^* = \begin{bmatrix} L^* \in \mathbb{R}^{N_l \times k} \\ U^* \in \mathbb{R}^{N_u \times k} \end{bmatrix} = \begin{bmatrix} l_1 & l_2 & \cdots & l_k \\ u_1 & u_2 & \cdots & u_k \end{bmatrix}$$

for labeled and unlabeled samples respectively. Then we let $V^b \in \mathbb{R}^{N \times (N-k)}$ be the remaining singular vectors of \dot{A} except top- k . Similarly, we split V^b into two parts:

$$V^b = \begin{bmatrix} L^b \in \mathbb{R}^{N_l \times (N-k)} \\ U^b \in \mathbb{R}^{N_u \times (N-k)} \end{bmatrix} = \begin{bmatrix} l_{k+1} & l_{k+2} & \cdots & l_N \\ u_{k+1} & u_{k+2} & \cdots & u_N \end{bmatrix}.$$

We can also split the matrix \dot{A} at the N_l -th row and the N_l -th column and we obtain $A_{ll} \in \mathbb{R}^{N_l \times N_l}$, $A_{ul} \in \mathbb{R}^{N_u \times N_l}$, $A_{uu} \in \mathbb{R}^{N_u \times N_u}$ with

$$\dot{A} = \begin{bmatrix} A_{ll} & A_{ul}^\top \\ A_{ul} & A_{uu} \end{bmatrix}.$$

Theorem B.7. (No approximation) Denote the projection matrix $\mathbf{P}_{L^b} = L^b \mathbf{P} (L^b L^b \mathbf{P})^\dagger L^b$, where \dagger denotes the Moore-Penrose inverse. For any labeling vector $\vec{y} \in \{0, 1\}^{N_u}$, we have

$$\mathcal{R}(U^*, \vec{y}) \leq \|(I - \mathbf{P}_{L^b})U^b \vec{y}\|_2^2. \quad (\text{B.12})$$

The sufficient and necessary condition for $\mathcal{R}(U^*, \vec{y}) = 0$ is $\vec{\omega} \in \mathbb{R}^{N_l}$ such that

$$\forall i = k + 1, \dots, N, \langle \vec{y}^\top (\sigma_i I - A_{uu})^\dagger A_{ul}, l_i \rangle = \langle \vec{\omega}, l_i \rangle \quad (\text{B.13})$$

where σ_i is the i -th largest eigenvalue of A .

Proof. Define $\vec{y}' = [\vec{\zeta}^\top, \vec{y}^\top]^\top$ as an extended labeling vector, where $\vec{\zeta} \in \mathbb{R}^{N_l}$ can be a ‘‘placeholder’’ vector with any values. We have

$$\begin{aligned} \mathcal{R}(U^*, \vec{y}) &= \min_{\vec{\mu} \in \mathbb{R}^k} \|\vec{y} - U^* \vec{\mu}\|_2^2 \\ &= \min_{\vec{\mu} \in \mathbb{R}^k, \vec{\zeta} \in \mathbb{R}^{N_l}} \|\vec{y}' - V^* \vec{\mu}\|_2^2 \\ &= \min_{\vec{\zeta} \in \mathbb{R}^{N_l}} \|\vec{y}' - V^* V^{*\top} \vec{y}'\|_2^2 \\ &= \min_{\vec{\zeta} \in \mathbb{R}^{N_l}} \|V^{b\top} \vec{y}'\|_2^2 \\ &= \min_{\vec{\zeta} \in \mathbb{R}^{N_l}} \|L^{b\top} \vec{\zeta} + U^{b\top} \vec{y}\|_2^2 \\ &= \|(I - L^{b\top} (L^b L^{b\top})^\dagger L^b) U^{b\top} \vec{y}\|_2^2. \end{aligned}$$

The sufficient and necessary condition for $\mathcal{R}(U^*, \vec{y}) = 0$ is:

$$\exists \vec{\omega} \in \mathbb{R}^{N_l}, \forall i = k + 1, \dots, N, u_i^\top \vec{y} = l_i^\top \vec{\omega}.$$

We then look into the relationship between l_i and u_i . Since

$$\begin{bmatrix} A_{ll} & A_{ul}^\top \\ A_{ul} & A_{uu} \end{bmatrix} \begin{bmatrix} l_i \\ u_i \end{bmatrix} = \sigma_i \begin{bmatrix} l_i \\ u_i \end{bmatrix},$$

we have the following results:

$$u_i = (\sigma_i I - A_{uu})^\dagger A_{ul} l_i.$$

So the sufficient and necessary condition becomes: there exists $\vec{\omega} \in$

\mathbb{R}^{N_l} such that

$$\forall i = k + 1, \dots, N, \langle \vec{y}^\top (\sigma_i I - A_{uu})^\dagger A_{ul}, l_i \rangle = \langle \vec{\omega}, l_i \rangle, \quad (\text{B.14})$$

where σ_i is the i -th largest singular value of \dot{A} . \square

Interpretation of Theorem B.7. The bound of residual in Ineq. (6.10) composed of two projections: $U^{\flat\top}$ and $(I - P_{L^b})$. If we only consider $\|U^{\flat\top} \vec{y}\|_2^2$, it is equivalent to $\vec{y}^\top (I - U^* U^{*\top}) \vec{y}$ which indicates the information in \vec{y} that is not covered by the learned representation U^* . Then multiplying the second projection matrix $(I - P_{L^b})$ further reduces the residual by considering the information from labeled data, since P_{L^b} is a projection matrix that projects a vector to the linear span of L^b . In the extreme case, when $U^{\flat\top} \vec{y}$ fully lies in the linear span of L^b , the residual $\mathcal{R}(U^*, \vec{y})$ becomes 0. To provide further insights about Eq. (B.13), we analyze in a simplified setting by approximating \dot{A} in the next section.

B.1.3.2 Analysis with Approximation

In Theorem B.7, we put an analysis on how L^b can influence the residual function. However, L^b is a matrix with N_l rows, so it is hard to quantitatively understand the effect of N_l labeled samples individually. We resort to viewing the labeled samples as a whole. Our idea is motivated by the Stochastic Block Model (SBM) (Holland et al., 1983) model, which analyzes the probability between different communities instead of individual values. In our case, we aim to analyze the probability vector $\eta_u \in \mathbb{R}^{N_u}$ denoting the chance of each unlabeled data point having the same augmentation view as one of the samples from the known class. The relationship between η_u and A_{uu} is then of our interest. Specifically, we define \bar{A} with values at (i, j) be the following:

$$\bar{A}_{x_i x_j} = \begin{cases} \dot{A}_{x_i x_j} & \text{if } x_i \in \mathcal{X}_u, x_j \in \mathcal{X}_u, \\ \mathbb{E}_{x' \in \mathcal{X}_l} \dot{A}_{x_i x'} & \text{if } x_i \in \mathcal{X}_u, x_j \in \mathcal{X}_l, \\ \mathbb{E}_{x' \in \mathcal{X}_l} \dot{A}_{x' x_j} & \text{if } x_i \in \mathcal{X}_l, x_j \in \mathcal{X}_u, \\ \mathbb{E}_{x', x'' \in \mathcal{X}_l} \dot{A}_{x' x''} & \text{if } x_i \in \mathcal{X}_l, x_j \in \mathcal{X}_l. \end{cases} \quad (\text{B.15})$$

The probability is estimated by taking the average. It is equivalent to multiplying matrix P and P^\top on left and right side, where $P \in \mathbb{R}^{N \times N}$ is given by:

$$P = \begin{bmatrix} \frac{1}{N_l} \mathbf{1}_{N_l \times N_l} & \mathbf{0}_{N_l \times N_u} \\ \mathbf{0}_{N_u \times N_l} & I_{N_u} \end{bmatrix},$$

where $\mathbf{1}_{n \times m}$ and $\mathbf{0}_{n \times m}$ represent matrix filled with 1 and 0 respectively with shape $n \times m$. Then we can write $\bar{A} \in \mathbb{R}^{N \times N}$, the approximated version of A , as follows:

$$\bar{A} = PAP^\top = \begin{bmatrix} \eta_l \mathbf{1}_{N_l \times N_l} & \mathbf{1}_{N_l \times 1} \vec{\eta}_u^\top \\ \vec{\eta}_u \mathbf{1}_{1 \times N_l} & A_{uu} \end{bmatrix},$$

where $\eta_l \in \mathbb{R}$ and $\vec{\eta}_u \in \mathbb{R}^{N_u \times 1}$. Our analysis can then focus on how η_u influences the representation space learned by A_{uu} . Similar to Section B.1.3.1, we define the top- k and the remainder singular vectors with corresponding splits as :

$$\bar{V}^* = \begin{bmatrix} \bar{L}^* \\ \bar{U}^* \end{bmatrix} = \begin{bmatrix} \bar{l}_1 & \bar{l}_2 & \cdots & \bar{l}_k \\ \bar{u}_1 & \bar{u}_2 & \cdots & \bar{u}_k \end{bmatrix},$$

$$\bar{V}^b = \begin{bmatrix} \bar{L}^b \\ \bar{U}^b \end{bmatrix} = \begin{bmatrix} \bar{l}_{k+1} & \bar{l}_{k+2} & \cdots & \bar{l}_N \\ \bar{u}_{k+1} & \bar{u}_{k+2} & \cdots & \bar{u}_N \end{bmatrix}.$$

Note that due to the special structure of \bar{A} with N_l duplicated rows and

columns, the eigenvector \bar{V} has a special structure as we demonstrate in the next Lemma B.8. We defer the proof to Section B.1.3.3.

Lemma B.8. *Since A_{uu} is symmetric and has large diagonal values, we assume A_{uu} is a positive semi-definite matrix. \bar{L}^* is stacked by the same row such that $\bar{L}^* = \frac{\mathbf{1}_{N_l \times 1}}{N_l} \bar{V}^{*\top}$, where $\bar{V}^* \in \mathbb{R}^k$ and that \bar{L}^b has the following form:*

$$\bar{L}^b = \begin{bmatrix} \frac{\mathbf{1}_{N_l \times 1}}{N_l} \bar{V}^{*\top} & \bar{l}_{N-\Theta+1} & \dots & \bar{l}_N \end{bmatrix},$$

where Θ is the rank of the null space for $A_{uu} - \frac{\eta_u \eta_u^\top}{\eta}$, $\bar{V}^* \in \mathcal{R}^{N-k-\Theta}$ with non-zero values, and $\bar{l}_{N-\Theta+1}, \dots, \bar{l}_N$ are all perpendicular to $\mathbf{1}_{N_l}$.

By property in Lemma B.8, we define:

$$\bar{V}^p \triangleq \bar{L}^{b\top} \mathbf{1}_{N_l \times 1} = \begin{bmatrix} \bar{V}^{*\top} & 0 & \dots & 0 \end{bmatrix}^\top \in \mathbb{R}^{N-k}. \quad (\text{B.16})$$

Definition B.9. *To ease the notation, we let $\mathcal{I} \triangleq \{k+1, k+2, \dots, N-\Theta\}$ and we mainly discuss $i \in \mathcal{I}$.*

These definitions facilitate the presentation of the following Theorem B.10.

Theorem B.10. (With approximation) *Denote $\mathfrak{I}(\vec{y}) = \frac{\|\bar{U}^b \vec{y}\|_2}{\|\vec{y}\|_2}$ and $\kappa(\vec{y}) = \cos(\bar{U}^{b\top} \vec{y}, \bar{V}^p)$, where \cos measures the cosine distance between two vectors. Let σ_i as the i -th largest eigenvalue of \dot{A} and $\bar{\sigma}_i$ is for \bar{A} . For a labeling vector $\vec{y} \in \{0, 1\}^{N_u}$, we have*

$$\mathcal{R}(\bar{U}^*, \vec{y}) = \frac{N_u}{|\mathcal{Y}_u|} (1 - \kappa(\vec{y})^2) \mathfrak{I}(\vec{y})^2. \quad (\text{B.17})$$

If the ignorance degree $\mathfrak{I}(\vec{y})$ is non-zero, the sufficient and necessary condition for $\mathcal{R}(\bar{U}^, \vec{y}) = 0$: there exists $\omega \in \mathbb{R}$ such that*

$$\forall i \in \mathcal{I}, \vec{y}^\top (\bar{\sigma}_i I - A_{uu})^\dagger \vec{\eta}_u = \omega. \quad (\text{B.18})$$

Proof. Define $\bar{\mathbf{y}}' = [\zeta \mathbf{1}_{1 \times N_i}, \bar{\mathbf{y}}^\top]^\top$ as an extended labeling vector where ζ is any real number. We have

$$\begin{aligned}
\mathcal{R}(\bar{U}^*, \bar{\mathbf{y}}) &= \min_{\bar{\boldsymbol{\mu}} \in \mathbb{R}^k} \|\bar{\mathbf{y}} - \bar{U}^* \bar{\boldsymbol{\mu}}\|_2^2 \\
&= \min_{\bar{\boldsymbol{\mu}} \in \mathbb{R}^k, \zeta \in \mathbb{R}} \{ \|\bar{\mathbf{y}} - \bar{U}^* \bar{\boldsymbol{\mu}}\|_2^2 + \|(\zeta - \bar{\mathbf{v}}^{*\top} \bar{\boldsymbol{\mu}}) \mathbf{1}_{1 \times N_i}\|_2^2 \} \\
&= \min_{\bar{\boldsymbol{\mu}} \in \mathbb{R}^k, \zeta \in \mathbb{R}} \|\bar{\mathbf{y}}' - \bar{V}^* \bar{\boldsymbol{\mu}}\|_2^2 \\
&= \min_{\zeta \in \mathbb{R}} \|\bar{\mathbf{y}}' - \bar{V}^* \bar{V}^{*\top} \bar{\mathbf{y}}'\|_2^2 \\
&= \min_{\zeta \in \mathbb{R}} \|\bar{V}^{b\top} \bar{\mathbf{y}}'\|_2^2 \\
&= \min_{\zeta \in \mathbb{R}} \|\zeta \bar{L}^{b\top} \mathbf{1}_{N_i \times 1} + \bar{U}^{b\top} \bar{\mathbf{y}}\|_2^2 \\
&= \min_{\zeta \in \mathbb{R}} \|\zeta \bar{\mathbf{p}} + \bar{U}^{b\top} \bar{\mathbf{y}}\|_2^2 \\
&= \|(I - \frac{\bar{\mathbf{p}} \bar{\mathbf{p}}^\top}{\|\bar{\mathbf{p}}\|_2^2}) \bar{U}^{b\top} \bar{\mathbf{y}}\|_2^2 \\
&= (1 - \kappa(\bar{\mathbf{y}})^2) \|\bar{U}^{b\top} \bar{\mathbf{y}}\|_2^2 \\
&= \frac{N_u}{|\mathcal{Y}_u|} (1 - \kappa(\bar{\mathbf{y}})^2) \mathfrak{F}(\bar{\mathbf{y}})^2.
\end{aligned}$$

We then look into the components of $\bar{\mathbf{p}}$ and \bar{U}^b . According to Lemma B.8, when $i > N - \Theta$, we have:

$$\bar{\mathbf{p}} = \begin{bmatrix} \bar{\mathbf{v}}^\top & 0 & \dots & 0 \end{bmatrix}^\top = [(\bar{\mathbf{p}})_{k+1} \quad (\bar{\mathbf{p}})_{k+2} \quad \dots \quad (\bar{\mathbf{p}})_{N-\Theta} \quad 0 \dots 0]. \quad (\text{B.19})$$

And the sufficient and necessary condition for $\mathcal{R}(\bar{U}^*, \bar{\mathbf{y}})$ to be minimized by $\bar{\mathbf{p}}$ is:

$$\exists \omega \in \mathbb{R}, \forall i \in \mathcal{I}, \bar{u}_i^{b\top} \bar{\mathbf{y}} = \omega (\bar{\mathbf{p}})_i. \quad (\text{B.20})$$

Note that for $i \in \mathcal{I}$,

$$\begin{bmatrix} \eta_l \mathbf{1}_{N_l \times N_l} & \mathbf{1}_{N_l \times 1} \vec{\eta}_u^\top \\ \vec{\eta}_u \mathbf{1}_{1 \times N_l} & A_{uu} \end{bmatrix} \begin{bmatrix} \bar{l}_i \\ \bar{u}_i \end{bmatrix} = \bar{\sigma}_i \begin{bmatrix} \bar{l}_i \\ \bar{u}_i \end{bmatrix}.$$

Also since $(\bar{\mathcal{P}})_i = \mathbf{1}_{1 \times N_l} \bar{l}_i \in \mathbb{R}$, we have the following results:

$$\bar{u}_i = (\bar{\sigma}_i I - A_{uu})^\dagger \vec{\eta}_u (\bar{\mathcal{P}})_i.$$

Thus, the sufficient and necessary condition (B.20) becomes: there exists $\omega \in \mathbb{R}$ such that

$$\forall i \in \mathcal{I}, \vec{y}^\top (\bar{\sigma}_i I - A_{uu})^\dagger \vec{\eta}_u = \omega. \quad (\text{B.21})$$

□

B.1.3.3 Proof of Lemma B.8

Proof. To understand the structure of \bar{U} and \bar{L} , we consider the eigenvalue problem:

$$\begin{bmatrix} \eta_l \mathbf{1}_{N_l \times N_l} & \mathbf{1}_{N_l \times 1} \vec{\eta}_u^\top \\ \vec{\eta}_u \mathbf{1}_{1 \times N_l} & A_{uu} \end{bmatrix} \begin{bmatrix} \bar{l}_i \\ \bar{u}_i \end{bmatrix} = \bar{\sigma}_i \begin{bmatrix} \bar{l}_i \\ \bar{u}_i \end{bmatrix}.$$

In the non-trivial case, $\eta_l \neq 0, \vec{\eta}_u \neq \mathbf{0}_{N_l}$, we have the following two equations:

$$\begin{aligned} \eta_l \mathbf{1}_{N_l \times 1} \mathbf{1}_{1 \times N_l} \bar{l}_i + \mathbf{1}_{N_l \times 1} \vec{\eta}_u^\top \bar{u}_i &= \bar{\sigma}_i \bar{l}_i \\ (\bar{\sigma}_i I - A_{uu}) \bar{u}_i &= \vec{\eta}_u \mathbf{1}_{1 \times N_l} \bar{l}_i. \end{aligned}$$

(Case 1) When $\bar{\sigma}_i \neq 0$, then \bar{l}_i has N_l duplicated scalar values $\frac{\vec{\eta}_u^\top \bar{u}_i}{\bar{\sigma}_i - N_l \eta_l}$ for the first equation to satisfy.

(Case 2) When $\bar{\sigma}_i = 0$, then by combing the two equations, we have:

$$A_{uu}\bar{u}_i = \frac{\vec{\eta}_u\vec{\eta}_u^\top}{\eta_l}\bar{u}_i.$$

If $A_{uu} - \frac{\vec{\eta}_u\vec{\eta}_u^\top}{\eta_l}$ is a full rank matrix, then $\bar{u}_i = \mathbf{0}_{N_u}$, and by the first equation $\mathbf{1}_{1 \times N_i}\bar{l}_i = 0$. If $A_{uu} - \frac{\vec{\eta}_u\vec{\eta}_u^\top}{\eta_l}$ is a deficiency matrix and $\text{rank}(A_{uu} - \frac{\vec{\eta}_u\vec{\eta}_u^\top}{\eta_l}) \geq \text{rank}(A_{uu})$ ¹, then \bar{u}_i lies in the null space formed by $\vec{\eta}_u$ and A_{uu} jointly, then $\vec{\eta}_u^\top\bar{u}_i = 0$, we still have $\mathbf{1}_{1 \times N_i}\bar{l}_i = 0$.

Therefore when $i \in \{1, \dots, k\}$, $\bar{\sigma}$ is non-zero values, so that \bar{L}^* is stacked by the same row such that $\bar{L}^* = \frac{\mathbf{1}_{N_i \times 1}\bar{l}^{*\top}}{N_i}$, where $\bar{l}^* \in \mathbb{R}^k$. For $i \in \{k+1, \dots, N\}$, \bar{L}^b has the following form:

$$\bar{L}^b = \begin{bmatrix} \frac{\mathbf{1}_{N_i \times 1}\bar{l}^{\prime\top}}{N_i} & \bar{l}_{N-\Theta+1} & \dots & \bar{l}_N \end{bmatrix},$$

where Θ is the rank of the null space for $A_{uu} - \frac{\eta_u\eta_u^\top}{\eta_l}$, $\bar{l}' \in \mathcal{R}^{N-k-\Theta}$, and $\bar{l}_{N-\Theta+1}, \dots, \bar{l}_N$ are all perpendicular to $\mathbf{1}_{N_i}$. \square

B.1.3.4 Proof for the Main Theorem 6.7

In this section, we provide the main proof of Theorem 6.7. For reader's convenience, we provide the recap version in Theorem B.11 by omitting the definition claim, where the detailed definition of $A_{ul}, A_{ll}, q_i, \bar{U}^{b\top}, \bar{l}^b, \vec{\eta}_u$ is in Section B.1.3.2.

The proof of Theorem 6.7 consists of four steps. Firstly, $\mathcal{E}(f)$ is bounded by $\mathcal{R}(U^*)$ as we show in Lemma 6.2. Secondly, the residual $\mathcal{R}(U^*, \vec{y})$ of the original representation can be approximated by the residual $\mathcal{R}(\bar{U}^*, \vec{y})$ analyzed in Section B.1.3.2. Thirdly, the approximation error bound is in

¹When $\text{rank}(A_{uu} - \frac{\vec{\eta}_u\vec{\eta}_u^\top}{\eta_l}) < \text{rank}(A_{uu})$, it means that η_u happens to cancel out one of the direction in A_{uu} . Such an event has zero probability almost sure in reality. We do not consider this case in our proof.

the order of $\frac{\|\dot{A} - \bar{A}\|_2}{\sigma_k - \sigma_{k+1}}$ as shown in Section B.1.3.5. Finally, we show that the coverage measurement $\kappa(\vec{y})$ can be lower bounded in Section B.1.3.6.

Theorem B.11. (Recap of Theorem 6.7) *Based on the assumptions made in Lemma B.12, Lemma B.15 and Lemma B.16. The linear probing error is bounded by:*

$$\mathcal{E}(f) \lesssim \frac{2N_u}{|\mathcal{Y}_u|} \left(\sum_i^{|\mathcal{Y}_u|} \mathfrak{F}(\vec{y}_i) (1 - \kappa(\vec{y}_i)^2) + \frac{\|\dot{A} - \bar{A}\|_2}{\sigma_k - \sigma_{k+1}} \right), \quad (\text{B.22})$$

where for single labeling vector \vec{y} ,

$$\kappa(\vec{y}) = \cos(\bar{U}^{\text{b}\top} \vec{y}, \bar{\mathbf{p}}) \gtrsim \min_{i>k, j>k} \frac{2\sqrt{\frac{\vec{y}^\top q_i}{\bar{\eta}_u^\top q_i} \frac{\vec{y}^\top q_j}{\bar{\eta}_u^\top q_j}}}{\frac{\vec{y}^\top q_i}{\bar{\eta}_u^\top q_i} + \frac{\vec{y}^\top q_j}{\bar{\eta}_u^\top q_j}}.$$

Proof. According to Lemma 6.2, we have

$$\mathcal{E}(f) \leq 2\mathcal{R}(U^*) = 2 \sum_{i \in \mathcal{Y}_u} \mathcal{R}(U^*, \vec{y}_i),$$

where we can view each \vec{y}_i separately. For simplicity, we use \vec{y} in the following proof. As show in Section B.1.3.2, $\mathcal{R}(U^*, \vec{y})$ can be approximately estimated by $\mathcal{R}(\bar{U}^*, \vec{y}) = (1 - \kappa(\vec{y})^2) \|\bar{U}^{\text{b}\top} \vec{y}\|_2^2 = \mathfrak{F}(\vec{y}) (1 - \kappa(\vec{y})^2) \|\vec{y}\|_2^2$. Such approximation bound is given by

$$\mathcal{R}(U^*, \vec{y}) \lesssim \mathcal{R}(\bar{U}^*, \vec{y}) + \frac{2\|\dot{A} - \bar{A}\|_2}{\sigma_k - \sigma_{k+1}} \|\vec{y}\|_2^2,$$

as shown in Lemma B.12 in Section B.1.3.5. Putting things together, we have

$$\mathcal{E}(f) \lesssim 2 \sum_i^{|\mathcal{Y}_u|} \mathfrak{F}(\vec{y}_i) (1 - \kappa(\vec{y}_i)^2) \|\vec{y}_i\|_2^2 + \frac{2\|\dot{A} - \bar{A}\|_2}{\sigma_k - \sigma_{k+1}} \|\vec{y}\|_2^2.$$

If the sample size in the novel class is balanced, we have $\|\vec{y}\|_2^2 = \frac{N_u}{|\mathcal{Y}_u|}$, we

have:

$$\mathcal{E}(f) \lesssim \frac{2N_u}{|\mathcal{Y}_u|} \left(\sum_i^{|\mathcal{Y}_u|} \mathfrak{F}(\bar{y}_i)(1 - \kappa(\bar{y})^2) + \frac{\|\dot{A} - \bar{A}\|_2}{\sigma_k - \sigma_{k+1}} \right),$$

Finally, the lower bound of κ is given by Lemma B.16 and proved in Section B.1.3.6. \square

B.1.3.5 Error Bound by Approximation

We see in Section B.1.3.2 that we use the approximated version \bar{U}^* instead of the actual feature representation U^* , which creates a gap. In this section, we will present a formal analysis on the gap between the induced residuals $\mathcal{R}(U^*, \bar{y})$ and $\mathcal{R}(\bar{U}^*, \bar{y})$.

Lemma B.12. *When $\|\dot{A} - \bar{A}\|_2 < \frac{1}{2}(\sigma_k - \sigma_{k+1})$ and $|\mathcal{Y}_u| \triangleq \mathbb{E}_{i \in \mathcal{I}}(1 - \|\bar{u}_i\|_2^2)$ is a non-zero value², we have*

$$\mathcal{R}(U^*, \bar{y}) \lesssim \mathcal{R}(\bar{U}^*, \bar{y}) + 2 \frac{\|\dot{A} - \bar{A}\|_2}{\sigma_k - \sigma_{k+1}} \|\bar{y}\|_2^2.$$

Proof. Recall that $\bar{y}' = [\zeta \mathbf{1}_{1 \times N_i}, \bar{y}^{\top}]^{\top}$ is an extended labeling vector where ζ is any real number defined in the proof of Theorem B.10. We let $\zeta^* = \arg \min_{\zeta \in \mathbb{R}} \|\bar{V}^{\top} \bar{y}'\|_2^2$ so that $\bar{y}^* = [\zeta^* \mathbf{1}_{1 \times N_i}, \bar{y}^{\top}]$. We then define $\delta \triangleq \min\{\sigma_k -$

²Note that $|\mathcal{Y}_u| = 0$ happens in an extreme case that $\forall i \in \mathcal{I}, \|\bar{l}_i\|_2^2 = 0$ which means the extra knowledge is purely irrelevant to the feature representation. Specifically, this could happen when A_{ul} (defined in Section B.1.3.1) is a zero matrix.

$\bar{\sigma}_{k+1}, \bar{\sigma}_k - \sigma_{k+1}\}$,

$$\begin{aligned}
\mathcal{R}(U^*, \vec{y}) &= \min_{\zeta \in \mathbb{R}} \|V^{b\top} \vec{y}'\|_2^2 \\
&= \min_{\zeta \in \mathbb{R}} \vec{y}'^\top V^b V^{b\top} \vec{y}' \\
&= \min_{\zeta \in \mathbb{R}} (\vec{y}'^\top \bar{V}^b \bar{V}^{b\top} \vec{y}' + \vec{y}'^\top V^b V^{b\top} \vec{y}' - \vec{y}'^\top \bar{V}^b \bar{V}^{b\top} \vec{y}') \\
&\leq \mathcal{R}(\bar{U}^*, \vec{y}) + |\vec{y}^{*\top} (V^b V^{b\top} - \bar{V}^b \bar{V}^{b\top}) \vec{y}^*| \\
&\leq \mathcal{R}(\bar{U}^*, \vec{y}) + \|V^b V^{b\top} - \bar{V}^b \bar{V}^{b\top}\| \|\vec{y}^*\|_2^2 \\
&= \mathcal{R}(\bar{U}^*, \vec{y}) + \|V^{b\top} \bar{V}^*\| \|\vec{y}^*\|_2^2 \\
&\leq \mathcal{R}(\bar{U}^*, \vec{y}) + \frac{\|\dot{A} - \bar{A}\|_2}{\delta} \|\vec{y}^*\|_2^2 \\
&\leq \mathcal{R}(\bar{U}^*, \vec{y}) + \frac{2\|\dot{A} - \bar{A}\|_2}{\sigma_k - \sigma_{k+1}} \|\vec{y}^*\|_2^2,
\end{aligned}$$

where the second last inequality is from Davis-Kahan theorem on subspace distance $\|V^b V^{b\top} - \bar{V}^b \bar{V}^{b\top}\| = \|V^{b\top} \bar{V}^*\| = \|\bar{V}^{b\top} V^*\|$, and the last inequality is from Weyl's inequality so that $\delta \geq (\sigma_k - \sigma_{k+1}) - \|\dot{A} - \bar{A}\|_2 \geq \frac{1}{2}(\sigma_k - \sigma_{k+1})$.

We then investigate the magnitude order of $\|\vec{y}^*\|_2^2$. Note that $\|\vec{y}^*\|_2^2 = \|\vec{y}'\|_2^2 + N_l(\zeta^*)^2$ and $\zeta^* = \frac{\bar{\mathbf{p}}^\top \bar{U}^{b\top} \vec{y}}{\|\bar{\mathbf{p}}\|_2^2}$ according to the proof of Theorem B.10. Then,

$$\begin{aligned}
\|\vec{y}^*\|_2^2 &= \|\vec{y}'\|_2^2 + \frac{N_l(\bar{\mathbf{p}}^\top \bar{U}^{b\top} \vec{y})^2}{\|\bar{\mathbf{p}}\|_2^4} \\
&= \|\vec{y}'\|_2^2 + \frac{N_l \kappa(\vec{y})^2 \|\bar{U}^{b\top} \vec{y}\|_2^2}{\|\bar{\mathbf{p}}\|_2^2} \\
&= \|\vec{y}'\|_2^2 \left(1 + \frac{N_l \kappa(\vec{y})^2 \mathfrak{I}(\vec{y})^2}{\|\bar{\mathbf{p}}\|_2^2} \right) \\
&= \|\vec{y}'\|_2^2 \left(1 + \frac{\kappa(\vec{y})^2 \mathfrak{I}(\vec{y})^2}{\sum_{i=k+1}^{N-\Theta} (1 - \|\bar{u}_i\|_2^2)} \right),
\end{aligned}$$

where the last equation is given by Lemma B.8 when $i > N - \Theta$, $(\bar{\mathbf{p}})_i = 0$

and also by the fact that when $i \in \mathcal{I}$, $1 - \|\bar{u}_i\|_2^2 = \|\bar{l}_i\|_2^2 = N_l(\frac{(\bar{\mathbb{P}})_i}{N_l})^2 = (\bar{\mathbb{P}})_i^2/N_l$. Then by the assumption that $|\mathcal{Y}_u|$ is non-zero, we have

$$\|\bar{y}^*\|_2^2 = \|\bar{y}\|_2^2 \left(1 + \frac{\kappa(\bar{y})^2 \mathfrak{I}(\bar{y})^2}{(N - \Theta - k)|\mathcal{Y}_u|}\right) \lesssim \|\bar{y}\|_2^2 \left(1 + O\left(\frac{1}{N}\right)\right).$$

By plugging back $\|\bar{y}^*\|_2^2$, we have

$$\mathcal{R}(U^*, \bar{y}) \lesssim \mathcal{R}(\bar{U}^*, \bar{y}) + \frac{2\|\dot{A} - \bar{A}\|_2}{\sigma_k - \sigma_{k+1}} \|\bar{y}\|_2^2.$$

□

B.1.3.6 Analysis on the Coverage Measurement $\kappa(\bar{y})$

So far we have shown in Theorem B.10 that the sufficient and necessary condition for a zero residual is when the coverage measurement $\kappa(\bar{y}) = \cos(\bar{U}^{\text{b}\top} \bar{y}, \bar{\mathbb{P}})$ equals to one. In this section, we provide a deeper analysis on $\kappa(\bar{y})$ in a less restrictive case.

Recall that we have proved in Theorem B.10 that the sufficient and necessary condition for $\kappa(\bar{y}) = 1$ is:

$$\exists \omega \in \mathbb{R}, \forall i \in \mathcal{I}, \bar{y}^\top (\bar{\sigma}_i I - A_{uu})^\dagger \bar{\eta}_u = \omega. \quad (\text{B.23})$$

In a general case, we consider ω_i which is variant on i :

$$\omega_i \triangleq \bar{y}^\top (\bar{\sigma}_i I - A_{uu})^\dagger \bar{\eta}_u.$$

Our discussion on $\kappa(\bar{y})$ is based on the following definitions:

Definition B.13. Let q_j and d_j as the j -th eigenvector/eigenvalue of A_{uu} . Then we define $\tilde{\mathbf{y}}_j \triangleq \bar{y}^\top q_j$ and $\tilde{\boldsymbol{\eta}}_j \triangleq \bar{\eta}_u^\top q_j$.

Before showing the bound on $\kappa(\bar{y})$, we first show the following Lemma B.14 and Lemma B.15 which is the important ingredient needed to derive the

lower bound of $\kappa(\vec{y})$. We defer the proof to Section B.1.3.7 and Section B.1.3.8 respectively.

Lemma B.14. *Let $\Omega \in \mathbb{R}^{(N-\Theta-k) \times (N-\Theta-k)}$ be the diagonal matrix with $\Omega_{i'i'} = \omega_i$ ($i' = i - k$ to be aligned with the indexing of ω_i). For any vector $\mathfrak{l} \in \mathbb{R}^{N-\Theta-k}$, we have the following inequality:*

$$1 \geq \frac{\mathfrak{l}^\top \Omega \mathfrak{l}}{\|\Omega \mathfrak{l}\|_2 \|\mathfrak{l}\|_2} \geq \min_{i,j \in \mathcal{I}} \frac{2\sqrt{\omega_i \omega_j}}{\sqrt{\omega_j} + \sqrt{\omega_i}},$$

A sufficient and necessary condition for $\frac{\mathfrak{l}^\top \Omega \mathfrak{l}}{\|\Omega \mathfrak{l}\|_2 \|\mathfrak{l}\|_2}$ being 1 for all \mathfrak{l} is to let ω_i be the same for all $i \in \mathcal{I}$.

Lemma B.15. *Assume η_u is upper bounded by a small value $\frac{1}{M}$: $\max_{j=1 \dots N_u} (\vec{\eta}_u)_j = \frac{1}{M}$.³ For each indexing pair $i \in \mathcal{I}$ and $i' \in \mathcal{I}$ with order $\omega_i < \omega_{i'}$, we have*

$$\frac{\omega_i}{\omega_{i'}} \gtrsim \frac{\vec{y}^\top q_i}{\vec{\eta}_u^\top q_i} / \frac{\vec{y}^\top q_{i'}}{\vec{\eta}_u^\top q_{i'}}.$$

Putting the ingredients together, we can finally derive an analytical lower bound of $\kappa(\vec{y})$ in Lemma B.16 based on the angle of $\vec{y} / \vec{\eta}_u$ to each eigenvector of A_{uu} .

Lemma B.16. *W.o.l.g, we let $\omega > 0$ and assume that $\omega_i > 0, \forall i \in \mathcal{I}$ so that perturbation of ω_i to ω to be not significant enough to change the sign of ω . we have:*

$$\kappa(\vec{y}) = \cos(\vec{U}^{\text{b}\top} \vec{y}, \vec{\mathfrak{l}}^{\text{b}}) \gtrsim \min_{i > k, j > k} \frac{2\sqrt{\frac{\vec{y}^\top q_i}{\vec{\eta}_u^\top q_i} \frac{\vec{y}^\top q_j}{\vec{\eta}_u^\top q_j}}}{\frac{\vec{y}^\top q_i}{\vec{\eta}_u^\top q_i} + \frac{\vec{y}^\top q_j}{\vec{\eta}_u^\top q_j}},$$

³Such assumption is used to align the magnitude later in the proof between $\vec{y} \in [0, 1]$ and $\vec{\eta}_u \in [0, \frac{1}{M}]$ for the value range.

Proof. Recall that

$$\bar{u}_i = (\bar{\sigma}_i I - A_{uu})^\dagger \vec{\eta}_u(\bar{\mathbf{p}})_i,$$

we consider the specific form of $\kappa(\vec{y})$,

$$\begin{aligned} \kappa(\vec{y}) &= \cos(\bar{U}^b \vec{y}, \bar{\mathbf{p}}) \\ &= \frac{\sum_{i=k+1}^N \omega_i (\bar{\mathbf{p}})_i^2}{\sqrt{\sum_{i=k+1}^N \omega_i^2 (\bar{\mathbf{p}})_i^2} \sqrt{\sum_{i=k+1}^N (\bar{\mathbf{p}})_i^2}} \\ &= \frac{\sum_{i \in \mathcal{I}} \omega_i (\bar{\mathbf{p}})_i^2}{\sqrt{\sum_{i \in \mathcal{I}} \omega_i^2 (\bar{\mathbf{p}})_i^2} \sqrt{\sum_{i \in \mathcal{I}} (\bar{\mathbf{p}})_i^2}} \\ &= \frac{\bar{\mathbf{r}}^\top \Omega \bar{\mathbf{r}}}{\|\Omega \bar{\mathbf{r}}\|_2 \|\bar{\mathbf{r}}\|_2}, \end{aligned}$$

where $\Omega \in \mathbb{R}^{N_u - k - \Theta}$ is a diagonal matrix defined in Lemma B.14, and $\bar{\mathbf{r}}$ is defined in Eq. (B.19). According to Lemma B.14, we have

$$\begin{aligned} \kappa(\vec{y}) &= \frac{\bar{\mathbf{r}}^\top \Omega \bar{\mathbf{r}}}{\|\Omega \bar{\mathbf{r}}\|_2 \|\bar{\mathbf{r}}\|_2} \\ &\geq \min_{i,j \in \mathcal{I}} \frac{2\sqrt{\omega_i \omega_j}}{\sqrt{\omega_j} + \sqrt{\omega_i}} \\ &= \min_{i,j \in \mathcal{I}} \frac{2}{\sqrt{\frac{\omega_j}{\omega_i}} + \sqrt{\frac{\omega_i}{\omega_j}}}, \end{aligned}$$

Then by Lemma B.15 and by the fact that $\frac{2}{t+\frac{1}{t}}$ is a monotonically increasing

function when $t \in (0, 1)$:

$$\begin{aligned}
\kappa(\vec{y}) &\geq \min_{i,j \in \mathcal{I}} \frac{2}{\sqrt{\omega_j} + \sqrt{\omega_i}} \\
&\gtrsim \min_{i,j \in \mathcal{I}} \frac{2}{\sqrt{\frac{\vec{y}^\top q_i}{\bar{\eta}_u^\top q_i} / \frac{\vec{y}^\top q_j}{\bar{\eta}_u^\top q_j}} + \sqrt{\frac{\vec{y}^\top q_j}{\bar{\eta}_u^\top q_j} / \frac{\vec{y}^\top q_i}{\bar{\eta}_u^\top q_i}}} \\
&> \min_{i>k, j>k} \frac{2\sqrt{\frac{\vec{y}^\top q_i}{\bar{\eta}_u^\top q_i} \frac{\vec{y}^\top q_j}{\bar{\eta}_u^\top q_j}}}{\frac{\vec{y}^\top q_i}{\bar{\eta}_u^\top q_i} + \frac{\vec{y}^\top q_j}{\bar{\eta}_u^\top q_j}}.
\end{aligned}$$

□

B.1.3.7 Proof for Lemma B.14

Proof. Consider the function $g(\mathfrak{l}) = \frac{\mathfrak{l}^\top \Omega \mathfrak{l}}{\|\Omega \mathfrak{l}\|_2 \|\mathfrak{l}\|_2}$, the directional derivative $\partial g(\mathfrak{l}) / \partial \mathfrak{l}$ is given by:

$$\frac{\partial g(\mathfrak{l})}{\partial \mathfrak{l}} = \frac{2\Omega \mathfrak{l} \|\Omega \mathfrak{l}\|_2 \|\mathfrak{l}\|_2 - \Omega^2 \mathfrak{l} \frac{\|\mathfrak{l}\|_2}{\|\Omega \mathfrak{l}\|_2} \mathfrak{l}^\top \Omega \mathfrak{l} - \mathfrak{l} \frac{\|\Omega \mathfrak{l}\|_2}{\|\mathfrak{l}\|_2} \mathfrak{l}^\top \Omega \mathfrak{l}}{\|\Omega \mathfrak{l}\|_2^2 \|\mathfrak{l}\|_2^2}.$$

The condition for $\partial g(\mathfrak{l}) / \partial \mathfrak{l} = 0$ is

$$2\Omega \mathfrak{l} = \Omega^2 \mathfrak{l} \frac{\mathfrak{l}^\top \Omega \mathfrak{l}}{\|\Omega \mathfrak{l}\|_2^2} + \mathfrak{l} \frac{\mathfrak{l}^\top \Omega \mathfrak{l}}{\|\mathfrak{l}\|_2^2}.$$

Note that the first condition to satisfy this equation is to let \mathfrak{l} as the eigenvectors of $2\Omega - \Omega^2 \frac{\mathfrak{l}^\top \Omega \mathfrak{l}}{\|\Omega \mathfrak{l}\|_2^2}$ which is a diagonal matrix. Then one of the solutions sets is $\mathfrak{l} = c\mathbf{e}_j$ where c is any non-zero scalar value and \mathbf{e}_j is the unit vector with j -th value 1 and 0 elsewhere. Note that this solution set corresponds to the maximum value of $g(\mathfrak{l})$ which is 1. We are then looking into the local minimum value of $g(\mathfrak{l})$ by another solution set. We consider

another solution set by considering the following matrix as deficiency:

$$\Gamma \triangleq 2\Omega - \Omega^2 \frac{\Gamma^\top \Omega \Gamma}{\|\Omega \Gamma\|_2^2} - \frac{\Gamma^\top \Omega \Gamma}{\|\Gamma\|_2^2} I,$$

where Γ lies in the null space of this matrix. If we let $\varrho = \frac{\|\Gamma\|_2}{\|\Omega \Gamma\|_2}$, we have:

$$\Gamma = 2\Omega - \varrho g(\hat{\Gamma}) \Omega^2 - \varrho^{-1} g(\hat{\Gamma}) I$$

and

$$\Gamma_{i'i'} = 2\omega_i - \varrho g(\hat{\Gamma}) \omega_i^2 - \varrho^{-1} g(\hat{\Gamma}),$$

where i' is indexed starting from 1 and i is indexed starting from k . Note that $\Gamma_{i'i'}$ only has two zero roots. If we consider all $\omega_i(s)$ in Ω to be different, Γ can have at most two zero values in the diagonal. Let ω_a, ω_b as two roots of $2\omega - \varrho g(\hat{\Gamma}) \omega^2 - \varrho^{-1} g(\hat{\Gamma})$, we have:

$$\varrho \omega_a + (\varrho \omega_a)^{-1} = \varrho \omega_b + (\varrho \omega_b)^{-1} = \frac{2}{g(\hat{\Gamma})}$$

$$\varrho = \frac{\sqrt{\omega_b}}{\sqrt{\omega_a}}, g(\hat{\Gamma}) = \frac{2}{\sqrt{\frac{\omega_b}{\omega_a}} + \sqrt{\frac{\omega_a}{\omega_b}}},$$

which corresponds to one local minimal with the indexing pair (a, b) . By enumerating all the indexing pairs, we have the global minimum of $g(\Gamma)$:

$$g(\Gamma^*) = \min_{i,j \in \mathcal{I}} \frac{2\sqrt{\omega_i \omega_j}}{\sqrt{\omega_j} + \sqrt{\omega_i}}.$$

Note that when some ω_i, ω_j are identical, this is a special case where the local minimum is equal to the maximum 1. Therefore a sufficient and necessary condition for $g(\Gamma) = 1$ is to let ω_i be the same for all $i \in \mathcal{I}$.

□

B.1.3.8 Proof for Lemma B.15

Proof. We can write ω_i by $\tilde{\mathbf{y}}$ and $\tilde{\boldsymbol{\eta}}$ in Definition B.13:

$$\begin{aligned}
\omega_i &= \tilde{\mathbf{y}}^\top (\bar{\sigma}_i I - A_{uu})^\dagger \tilde{\boldsymbol{\eta}}_u \\
&= \sum_{j \in \mathcal{I}} \frac{(\tilde{\mathbf{y}}^\top \mathbf{q}_j)(\tilde{\boldsymbol{\eta}}_u^\top \mathbf{q}_j)}{\bar{\sigma}_i - d_j} + \sum_{j=N-\Theta+1}^{N_u} \frac{(\tilde{\mathbf{y}}^\top \mathbf{q}_j)(\tilde{\boldsymbol{\eta}}_u^\top \mathbf{q}_j)}{\bar{\sigma}_i} \\
&= \sum_{j \in \mathcal{I}} \frac{\tilde{\mathbf{y}}_j \tilde{\boldsymbol{\eta}}_j}{\bar{\sigma}_i - d_j} + \frac{1}{\bar{\sigma}_i} \sum_{j=N-\Theta+1}^{N_u} \tilde{\mathbf{y}}_j \tilde{\boldsymbol{\eta}}_j.
\end{aligned}$$

We then look into the value of $\bar{\sigma}_i$ by solving the eigenvalue problem:

$$\begin{aligned}
&\begin{bmatrix} \eta_l \mathbf{1}_{N_l \times N_l} & \mathbf{1}_{N_l \times 1} \tilde{\boldsymbol{\eta}}_u^\top \\ \tilde{\boldsymbol{\eta}}_u \mathbf{1}_{1 \times N_l} & A_{uu} \end{bmatrix} \begin{bmatrix} \bar{l}_i \\ \bar{u}_i \end{bmatrix} = \bar{\sigma}_i \begin{bmatrix} \bar{l}_i \\ \bar{u}_i \end{bmatrix} \\
&\iff \eta_l \mathbf{1}_{N_l \times N_l} \bar{l}_i + \mathbf{1}_{N_l \times 1} \tilde{\boldsymbol{\eta}}_u^\top \bar{u}_i = \bar{\sigma}_i \bar{l}_i \\
&\iff \mathbf{1}_{N_l \times 1} \eta_l (\bar{\mathbb{P}})_i + \mathbf{1}_{N_l \times 1} \tilde{\boldsymbol{\eta}}_u^\top \bar{u}_i = \mathbf{1}_{N_l \times 1} \bar{\sigma}_i \frac{1}{N_l} (\bar{\mathbb{P}})_i \\
&\iff \eta_l (\bar{\mathbb{P}})_i + \tilde{\boldsymbol{\eta}}_u^\top \bar{u}_i = \bar{\sigma}_i \frac{1}{N_l} (\bar{\mathbb{P}})_i \\
&\iff \eta_l (\bar{\mathbb{P}})_i + \tilde{\boldsymbol{\eta}}_u^\top (\bar{\sigma}_i I - A_{uu})^\dagger \tilde{\boldsymbol{\eta}}_u (\bar{\mathbb{P}})_i = \bar{\sigma}_i \frac{1}{N_l} (\bar{\mathbb{P}})_i \\
&\iff \eta_l + \tilde{\boldsymbol{\eta}}_u^\top (\bar{\sigma}_i I - A_{uu})^\dagger \tilde{\boldsymbol{\eta}}_u = \frac{\bar{\sigma}_i}{N_l} \\
&\iff \eta_l + \sum_{j \in \mathcal{I}} \frac{\tilde{\boldsymbol{\eta}}_j^2}{\bar{\sigma}_i - d_j} = \frac{\bar{\sigma}_i}{N_l}
\end{aligned}$$

Note that we get a $(|\mathcal{I}| + 1)$ -th degree polynomials of $\bar{\sigma}_i$ with $(|\mathcal{I}| + 1)$ roots. By observation, we see that there is one root significantly large ($\approx N_l \eta_l$) since N_l and other $|\mathcal{I}|$ roots are very close to each d_j . Based on this intuition, we approximately view it as a unary quadratic equation:

$$\eta_l + \phi_i + \frac{\tilde{\eta}_i^2}{\bar{\sigma}_i - d_i} = \frac{\bar{\sigma}_i}{N_l},$$

where we let $\phi_i \triangleq \sum_{j \in \mathcal{I}, j \neq i} \frac{\tilde{\eta}_j^2}{\bar{\sigma}_i - d_j}$. We then proceed by solving this unary quadratic equation by viewing ϕ_i as a variable.

$$\begin{aligned} \bar{\sigma}_i(\bar{\sigma}_i - d_i) &= N_l \eta_l (\bar{\sigma}_i - d_i) + N_l \phi_i (\bar{\sigma}_i - d_i) + N_l \tilde{\eta}_i^2 \\ \iff \bar{\sigma}_i^2 &= (d_i + N_l(\eta_l + \phi_i))\bar{\sigma}_i + N_l(\tilde{\eta}_i^2 - (\eta_l + \phi_i)d_i) \\ \iff \bar{\sigma}_i &= \frac{d_i + N_l(\eta_l + \phi_i)}{2} \pm \sqrt{\frac{(d_i + N_l(\eta_l + \phi_i))^2}{4} + N_l(\tilde{\eta}_i^2 - (\eta_l + \phi_i)d_i)} \\ \iff \bar{\sigma}_i &= \frac{d_i + N_l(\eta_l + \phi_i)}{2} \pm \sqrt{\frac{(N_l(\eta_l + \phi_i) - d_i)^2}{4} + N_l \tilde{\eta}_i^2} \\ \iff \bar{\sigma}_i &= \frac{d_i + N_l(\eta_l + \phi_i)}{2} \pm \left(\frac{N_l(\eta_l + \phi_i) - d_i}{2} + \frac{N_l \tilde{\eta}_i^2}{\frac{N_l(\eta_l + \phi_i) - d_i}{2} + \sqrt{\frac{(N_l(\eta_l + \phi_i) - d_i)^2}{4} + N_l \tilde{\eta}_i^2}} \right) \\ \iff \bar{\sigma}_i &= \frac{d_i + N_l(\eta_l + \phi_i)}{2} \pm \left(\frac{N_l(\eta_l + \phi_i) - d_i}{2} + \frac{1}{\frac{\eta_l + \phi_i - \frac{d_i}{N_l}}{2\tilde{\eta}_i^2} + \sqrt{\left(\frac{\eta_l + \phi_i - \frac{d_i}{N_l}}{2\tilde{\eta}_i^2}\right)^2 + 1}} \right) \\ \iff \bar{\sigma}_i &= \frac{d_i + N_l(\eta_l + \phi_i)}{2} \pm \left(\frac{N_l(\eta_l + \phi_i) - d_i}{2} + \frac{\tilde{\eta}_i^2}{\eta_l + \phi_i - \frac{d_i}{N_l}} - O\left(\left(\frac{\tilde{\eta}_i^2}{\eta_l + \phi_i}\right)^2\right) \right) \end{aligned}$$

Here we see that $\bar{\sigma}_i$ has two approximated solutions: in the first case, when \pm becomes $+$, $\bar{\sigma}_i \approx N_l \eta_l$ which is the unique very large solution as we mentioned. Another solution is by picking \pm as $-$, we then have $\bar{\sigma}_i \approx d_i - \frac{\tilde{\eta}_i^2}{\eta_l + \phi_i - \frac{d_i}{N_l}}$. The second case is what we are using in this proof since we are looking at the indexing of ω_i with $i \in \mathcal{I}$, which is beyond top- k .

For each indexing pair i and i' with order $\omega_i < \omega_{i'}$, we plug in the

solution of $\bar{\sigma}_i$ and $\bar{\sigma}'_i$ respectively:

$$\begin{aligned}
\frac{\omega_i}{\omega_{i'}} &= \frac{\sum_{j \in \mathcal{I}} \frac{\tilde{\mathbf{y}}_j \tilde{\boldsymbol{\eta}}_j}{d_j - \bar{\sigma}_i} + \frac{1}{\bar{\sigma}'_i} \sum_{j=N-\Theta+1}^{N_u} \tilde{\mathbf{y}}_j \tilde{\boldsymbol{\eta}}_j}{\sum_{j \in \mathcal{I}} \frac{\tilde{\mathbf{y}}_j \tilde{\boldsymbol{\eta}}_j}{d_j - \bar{\sigma}'_i} + \frac{1}{\bar{\sigma}'_i} \sum_{j=N-\Theta+1}^{N_u} \tilde{\mathbf{y}}_j \tilde{\boldsymbol{\eta}}_j} \\
&= \frac{\frac{\tilde{\mathbf{y}}_i \tilde{\boldsymbol{\eta}}_i}{d_i - \bar{\sigma}_i} + \sum_{j \in \mathcal{I}, j \neq i} \frac{\tilde{\mathbf{y}}_j \tilde{\boldsymbol{\eta}}_j}{d_j - \bar{\sigma}_i} + \frac{1}{\bar{\sigma}'_i} \sum_{j=N-\Theta+1}^{N_u} \tilde{\mathbf{y}}_j \tilde{\boldsymbol{\eta}}_j}{\frac{\tilde{\mathbf{y}}_{i'} \tilde{\boldsymbol{\eta}}_{i'}}{d_{i'} - \bar{\sigma}'_i} + \sum_{j \in \mathcal{I}, j \neq i'} \frac{\tilde{\mathbf{y}}_j \tilde{\boldsymbol{\eta}}_j}{d_j - \bar{\sigma}'_i} + \frac{1}{\bar{\sigma}'_i} \sum_{j=N-\Theta+1}^{N_u} \tilde{\mathbf{y}}_j \tilde{\boldsymbol{\eta}}_j} \\
&= \frac{\frac{\tilde{\mathbf{y}}_i \tilde{\boldsymbol{\eta}}_i}{\tilde{\boldsymbol{\eta}}_i} (\eta_i + \phi_i) + \tilde{\mathbf{y}}_i \tilde{\boldsymbol{\eta}}_i (O((\frac{\tilde{\boldsymbol{\eta}}_i^2}{\eta_i + \phi_i})^2) - O(\frac{1}{N_i})) + \sum_{j \in \mathcal{I}, j \neq i} \frac{\tilde{\mathbf{y}}_j \tilde{\boldsymbol{\eta}}_j}{d_j - \bar{\sigma}_i} + \frac{1}{\bar{\sigma}'_i} \sum_{j=N-\Theta+1}^{N_u} \tilde{\mathbf{y}}_j \tilde{\boldsymbol{\eta}}_j}{\frac{\tilde{\mathbf{y}}_{i'} \tilde{\boldsymbol{\eta}}_{i'}}{\tilde{\boldsymbol{\eta}}_{i'}} (\eta_{i'} + \phi_{i'}) + \tilde{\mathbf{y}}_{i'} \tilde{\boldsymbol{\eta}}_{i'} (O((\frac{\tilde{\boldsymbol{\eta}}_{i'}^2}{\eta_{i'} + \phi_{i'}})^2) - O(\frac{1}{N_{i'}})) + \sum_{j \in \mathcal{I}, j \neq i'} \frac{\tilde{\mathbf{y}}_j \tilde{\boldsymbol{\eta}}_j}{d_j - \bar{\sigma}'_i} + \frac{1}{\bar{\sigma}'_i} \sum_{j=N-\Theta+1}^{N_u} \tilde{\mathbf{y}}_j \tilde{\boldsymbol{\eta}}_j} \\
&= \frac{\frac{\tilde{\mathbf{y}}_i \tilde{\boldsymbol{\eta}}_i}{\tilde{\boldsymbol{\eta}}_i} \eta_i + \tilde{\mathbf{y}}_i \tilde{\boldsymbol{\eta}}_i (O((\frac{\tilde{\boldsymbol{\eta}}_i^2}{\eta_i + \phi_i})^2) - O(\frac{1}{N_i})) + \sum_{j \in \mathcal{I}, j \neq i} \frac{1}{d_j - \bar{\sigma}_i} \tilde{\boldsymbol{\eta}}_j (\tilde{\mathbf{y}}_j + \tilde{\mathbf{y}}_i \frac{\tilde{\boldsymbol{\eta}}_j}{\tilde{\boldsymbol{\eta}}_i}) + \frac{1}{\bar{\sigma}'_i} \sum_{j=N-\Theta+1}^{N_u} \tilde{\mathbf{y}}_j \tilde{\boldsymbol{\eta}}_j}{\frac{\tilde{\mathbf{y}}_{i'} \tilde{\boldsymbol{\eta}}_{i'}}{\tilde{\boldsymbol{\eta}}_{i'}} \eta_{i'} + \tilde{\mathbf{y}}_{i'} \tilde{\boldsymbol{\eta}}_{i'} (O((\frac{\tilde{\boldsymbol{\eta}}_{i'}^2}{\eta_{i'} + \phi_{i'}})^2) - O(\frac{1}{N_{i'}})) + \sum_{j \in \mathcal{I}, j \neq i'} \frac{1}{d_j - \bar{\sigma}'_i} \tilde{\boldsymbol{\eta}}_j (\tilde{\mathbf{y}}_j + \tilde{\mathbf{y}}_{i'} \frac{\tilde{\boldsymbol{\eta}}_j}{\tilde{\boldsymbol{\eta}}_{i'}}) + \frac{1}{\bar{\sigma}'_i} \sum_{j=N-\Theta+1}^{N_u} \tilde{\mathbf{y}}_j \tilde{\boldsymbol{\eta}}_j}.
\end{aligned}$$

According to assumption that η_u is bounded by $\frac{1}{M}$, we align the magnitude between \vec{y} and $\vec{\eta}_u$ by defining $\vec{\eta}'_u = M\vec{\eta}_u$ which is now also in the range of $[0, 1]$ like \vec{y} . Then we also scale the following terms: $\tilde{\boldsymbol{\eta}}' = M\tilde{\boldsymbol{\eta}}$. Therefore we can simplify the equation to be:

$$\begin{aligned}
\frac{\omega_i}{\omega_{i'}} &= \frac{M \frac{\tilde{\mathbf{y}}_i}{\tilde{\boldsymbol{\eta}}_i} \eta_i + \frac{1}{M} \tilde{\mathbf{y}}_i \tilde{\boldsymbol{\eta}}'_i (O(\frac{1}{M^4} (\frac{\tilde{\boldsymbol{\eta}}_i'^2}{\eta_i + \phi_i})^2) - O(\frac{1}{N_i})) + \frac{1}{M} \sum_{j \in \mathcal{I}, j \neq i} \frac{1}{d_j - \bar{\sigma}_i} \tilde{\boldsymbol{\eta}}'_j (\tilde{\mathbf{y}}_j + \tilde{\mathbf{y}}_i \frac{\tilde{\boldsymbol{\eta}}'_j}{\tilde{\boldsymbol{\eta}}_i}) + \frac{1}{M \bar{\sigma}'_i} \sum_{j=N-\Theta+1}^{N_u} \tilde{\mathbf{y}}_j \tilde{\boldsymbol{\eta}}'_j}{M \frac{\tilde{\mathbf{y}}_{i'}}{\tilde{\boldsymbol{\eta}}_{i'}} \eta_{i'} + \frac{1}{M} \tilde{\mathbf{y}}_{i'} \tilde{\boldsymbol{\eta}}'_{i'} (O(\frac{1}{M^4} (\frac{\tilde{\boldsymbol{\eta}}_{i'}'^2}{\eta_{i'} + \phi_{i'}})^2) - O(\frac{1}{N_{i'}})) + \frac{1}{M} \sum_{j \in \mathcal{I}, j \neq i'} \frac{1}{d_j - \bar{\sigma}'_i} \tilde{\boldsymbol{\eta}}'_j (\tilde{\mathbf{y}}_j + \tilde{\mathbf{y}}_{i'} \frac{\tilde{\boldsymbol{\eta}}'_j}{\tilde{\boldsymbol{\eta}}_{i'}}) + \frac{1}{M \bar{\sigma}'_i} \sum_{j=N-\Theta+1}^{N_u} \tilde{\mathbf{y}}_j \tilde{\boldsymbol{\eta}}'_j} \\
&= \frac{\frac{\tilde{\mathbf{y}}_i}{\tilde{\boldsymbol{\eta}}_i} \eta_i + \tilde{\mathbf{y}}_i \tilde{\boldsymbol{\eta}}'_i (O(\frac{1}{M^6}) - O(\frac{1}{M^2 N_i})) + \frac{1}{M^2} \sum_{j \in \mathcal{I}, j \neq i} \frac{1}{d_j - d_i + O(\frac{1}{M^2})} \tilde{\boldsymbol{\eta}}'_j (\tilde{\mathbf{y}}_j + \tilde{\mathbf{y}}_i \frac{\tilde{\boldsymbol{\eta}}'_j}{\tilde{\boldsymbol{\eta}}_i}) + \frac{1}{M^2 \bar{\sigma}'_i} \sum_{j=N-\Theta+1}^{N_u} \tilde{\mathbf{y}}_j \tilde{\boldsymbol{\eta}}'_j}{\frac{\tilde{\mathbf{y}}_{i'}}{\tilde{\boldsymbol{\eta}}_{i'}} \eta_{i'} + \tilde{\mathbf{y}}_{i'} \tilde{\boldsymbol{\eta}}'_{i'} (O(\frac{1}{M^6}) - O(\frac{1}{M^2 N_{i'}})) + \frac{1}{M^2} \sum_{j \in \mathcal{I}, j \neq i'} \frac{1}{d_j - d_{i'} + O(\frac{1}{M^2})} \tilde{\boldsymbol{\eta}}'_j (\tilde{\mathbf{y}}_j + \tilde{\mathbf{y}}_{i'} \frac{\tilde{\boldsymbol{\eta}}'_j}{\tilde{\boldsymbol{\eta}}_{i'}}) + \frac{1}{M^2 \bar{\sigma}'_i} \sum_{j=N-\Theta+1}^{N_u} \tilde{\mathbf{y}}_j \tilde{\boldsymbol{\eta}}'_j} \\
&= \frac{\frac{\tilde{\mathbf{y}}_i}{\tilde{\boldsymbol{\eta}}_i} \eta_i + O(\frac{1}{M^2})}{\frac{\tilde{\mathbf{y}}_{i'}}{\tilde{\boldsymbol{\eta}}_{i'}} \eta_{i'} + O(\frac{1}{M^2})},
\end{aligned}$$

where we simply regard the remaining term with a magnitude much smaller than M . Note that M can be viewed as the magnitude gap of $\frac{\max_i(\vec{y})_i}{\max_i(\vec{\eta}_u)_i}$. In our case, $\max_i(\vec{y})_i$ is set to 1. However, one can always multiply \vec{y} with a large constant to make M significantly large without changing

the residual analysis in the main theorem. In summary, we have

$$\frac{\omega_i}{\omega_{i'}} \approx \frac{\frac{\tilde{\mathbf{y}}_i \boldsymbol{\eta}_l}{\tilde{\boldsymbol{\eta}}_i}}{\frac{\tilde{\mathbf{y}}_{i'} \boldsymbol{\eta}_l}{\tilde{\boldsymbol{\eta}}_{i'}}} = \frac{\tilde{\mathbf{y}}_i / \tilde{\boldsymbol{\eta}}_i}{\tilde{\mathbf{y}}_{i'} / \tilde{\boldsymbol{\eta}}_{i'}} = \frac{\bar{\mathbf{y}}^\top \mathbf{q}_i / \bar{\boldsymbol{\eta}}_u^\top \mathbf{q}_i}{\bar{\mathbf{y}}^\top \mathbf{q}_{i'} / \bar{\boldsymbol{\eta}}_u^\top \mathbf{q}_{i'}}.$$

□

B.1.4 Experimental Details

B.1.4.1 Details of Training Configurations

For a fair comparison, we use ResNet-18 (He et al., 2016a) as the backbone for all methods. We add a trainable two-layer MLP projection head that projects the feature from the penultimate layer to an embedding space \mathbb{R}^k ($k = 1000$). We use the same data augmentation strategies as SimSiam (Chen and He, 2021; HaoChen et al., 2021). We train our model $f(\cdot)$ for 1200 epochs by NCD Spectral Contrastive Loss defined in Eq. (6.4). We set $\alpha = 0.0225$ and $\beta = 2$. We use SGD with momentum 0.95 as an optimizer with cosine annealing (lr=0.03), weight decay $5e-4$, and batch size 512. We also conduct a sensitivity analysis of the hyper-parameters in Figure B.1. The performance comparison for each hyper-parameter is reported by fixing other hyper-parameters. The results suggest that the novel class discovery performance of NSCL is stable when α, β in a reasonable range and with different learning rates.

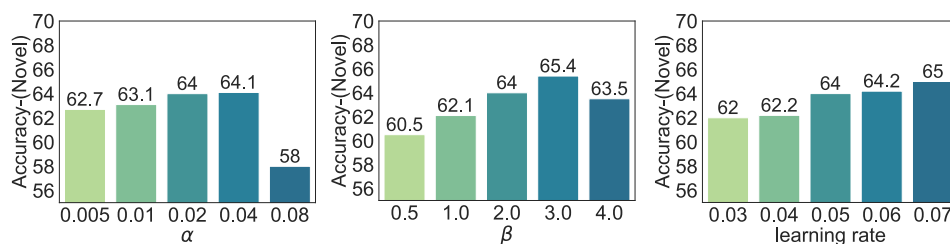


Figure B.1: Sensitivity analysis of hyper-parameters α , β , and learning rate. We use the training split of CIFAR-100-50/50, and report the novel class accuracy.

B.1.4.2 Experimental Details of Toy Example

Recap of set up. In Section 6.4.1 we consider a toy example that helps illustrate the core idea of our theoretical findings. Specifically, the example aims to cluster 3D objects of different colors and shapes, generated by a

3D rendering software (Johnson et al., 2017) with user-defined properties including colors, shape, size, position, etc.

In what follows, we define two data configurations and corresponding graphs, where the labeled data is correlated with the attribute of unlabeled data (**case 1**) vs. not (**case 2**). For both cases, we have an unlabeled dataset containing red/blue cubes/spheres as:

$$\mathcal{X}_u \triangleq \{X_{\color{red}\square, c_1}, X_{\color{red}\circ, c_1}, X_{\color{blue}\square, c_2}, X_{\color{blue}\circ, c_2}\}.$$

In the first case, we let the labeled data $\mathcal{X}_l^{\text{case 1}}$ be strongly correlated with the target class (red color) in unlabeled data:

$$\mathcal{X}_l^{\text{case 1}} \triangleq \{X_{\color{red}\Theta, c_1}\}(\text{red cylinder}).$$

In the second case, we use gray cylinders which have no overlap in either shape and color:

$$\mathcal{X}_l^{\text{case 2}} \triangleq \{X_{\Theta, c_3}\}(\text{gray cylinder}).$$

Putting it together, our entire training dataset is $\mathcal{X}^{\text{case 1}} = \mathcal{X}_l^{\text{case 1}} \cup \mathcal{X}_u$ or $\mathcal{X}^{\text{case 2}} = \mathcal{X}_l^{\text{case 2}} \cup \mathcal{X}_u$.

Experimental details for Figure 6.3. For training, we rendered 2500 samples for each type of data (4 types in \mathcal{X}_u and 1 type in \mathcal{X}_l). In total, we have 12500 samples for both $\mathcal{X}^{\text{case 1}}$ and $\mathcal{X}^{\text{case 2}}$. For training, we use the same data augmentation strategy as in SimSiam (Chen and He, 2021). We use ResNet18 and train the model for 40 epochs (sufficient for convergence) with a fixed learning rate of 0.005, using NSCL defined in Eq. (6.4). We set $\alpha = 0.04$ and $\beta = 1$, respectively. Our visualization is by PyTorch implementation of UMAP (McInnes et al., 2018), with parameters (n_neighbors=30, min_dist=1.5, spread=2, metric=euclidean).

B.2 A Graph-theoretic Framework for Understanding ORL

B.2.1 Technical Details of Spectral Open-world Representation Learning

Theorem B.17. (Recap of Theorem 7.1) We define $\mathbf{f}_x = \sqrt{w_x}f(x)$ for some function f . Recall η_u, η_l are two hyper-parameters defined in Eq. (7.1). Then minimizing the loss function $\mathcal{L}_{\text{mf}}(F, A)$ is equivalent to minimizing the following loss function for f , which we term **Spectral Open-world Representation Learning (SORL)**:

$$\begin{aligned} \mathcal{L}_{\text{SORL}}(f) \triangleq & -2\eta_u \mathcal{L}_1(f) - 2\eta_l \mathcal{L}_2(f) \\ & + \eta_u^2 \mathcal{L}_3(f) + 2\eta_u \eta_l \mathcal{L}_4(f) + \eta_l^2 \mathcal{L}_5(f), \end{aligned} \quad (\text{B.24})$$

where

$$\begin{aligned} \mathcal{L}_1(f) &= \sum_{i \in \mathcal{Y}_l} \mathbb{E}_{\substack{\bar{x}_l \sim \mathcal{P}_{l_i}, \bar{x}'_l \sim \mathcal{P}_{l_i}, \\ x \sim \mathcal{T}(\cdot | \bar{x}_l), x^+ \sim \mathcal{T}(\cdot | \bar{x}'_l)}} \left[f(x)^\top f(x^+) \right], \\ \mathcal{L}_2(f) &= \mathbb{E}_{\substack{\bar{x}_u \sim \mathcal{P}, \\ x \sim \mathcal{T}(\cdot | \bar{x}_u), x^+ \sim \mathcal{T}(\cdot | \bar{x}_u)}} \left[f(x)^\top f(x^+) \right], \\ \mathcal{L}_3(f) &= \sum_{i, j \in \mathcal{Y}_l} \mathbb{E}_{\substack{\bar{x}_l \sim \mathcal{P}_{l_i}, \bar{x}'_l \sim \mathcal{P}_{l_j}, \\ x \sim \mathcal{T}(\cdot | \bar{x}_l), x^- \sim \mathcal{T}(\cdot | \bar{x}'_l)}} \left[\left(f(x)^\top f(x^-) \right)^2 \right], \\ \mathcal{L}_4(f) &= \sum_{i \in \mathcal{Y}_l} \mathbb{E}_{\substack{\bar{x}_l \sim \mathcal{P}_{l_i}, \bar{x}_u \sim \mathcal{P}, \\ x \sim \mathcal{T}(\cdot | \bar{x}_l), x^- \sim \mathcal{T}(\cdot | \bar{x}_u)}} \left[\left(f(x)^\top f(x^-) \right)^2 \right], \\ \mathcal{L}_5(f) &= \mathbb{E}_{\substack{\bar{x}_u \sim \mathcal{P}, \bar{x}'_u \sim \mathcal{P}, \\ x \sim \mathcal{T}(\cdot | \bar{x}_u), x^- \sim \mathcal{T}(\cdot | \bar{x}'_u)}} \left[\left(f(x)^\top f(x^-) \right)^2 \right]. \end{aligned}$$

Proof. We can expand $\mathcal{L}_{\text{mf}}(F, A)$ and obtain

$$\begin{aligned}\mathcal{L}_{\text{mf}}(F, A) &= \sum_{x, x' \in \mathcal{X}} \left(\frac{w_{xx'}}{\sqrt{w_x w_{x'}}} - \mathbf{f}_x^\top \mathbf{f}_{x'} \right)^2 \\ &= \text{const} + \sum_{x, x' \in \mathcal{X}} \left(-2w_{xx'} f(x)^\top f(x') + w_x w_{x'} \left(f(x)^\top f(x') \right)^2 \right),\end{aligned}$$

where $\mathbf{f}_x = \sqrt{w_x} f(x)$ is a re-scaled version of $f(x)$. At a high level, we follow the proof in (HaoChen et al., 2021), while the specific form of loss varies with the different definitions of positive/negative pairs. The form of $\mathcal{L}_{\text{SORL}}(f)$ is derived from plugging $w_{xx'}$ and w_x .

Recall that $w_{xx'}$ is defined by

$$w_{xx'} = \eta_u \sum_{i \in \mathcal{Y}_l} \mathbb{E}_{\bar{x}_l \sim \mathcal{P}_{l_i}} \mathbb{E}_{\bar{x}'_l \sim \mathcal{P}_{l_i}} \mathcal{T}(x|\bar{x}_l) \mathcal{T}(x'|\bar{x}'_l) + \eta_l \mathbb{E}_{\bar{x}_u \sim \mathcal{P}} \mathcal{T}(x|\bar{x}_u) \mathcal{T}(x'|\bar{x}_u),$$

and w_x is given by

$$\begin{aligned}w_x &= \sum_{x'} w_{xx'} \\ &= \eta_u \sum_{i \in \mathcal{Y}_l} \mathbb{E}_{\bar{x}_l \sim \mathcal{P}_{l_i}} \mathbb{E}_{\bar{x}'_l \sim \mathcal{P}_{l_i}} \mathcal{T}(x|\bar{x}_l) \sum_{x'} \mathcal{T}(x'|\bar{x}'_l) + \eta_l \mathbb{E}_{\bar{x}_u \sim \mathcal{P}} \mathcal{T}(x|\bar{x}_u) \sum_{x'} \mathcal{T}(x'|\bar{x}_u) \\ &= \eta_u \sum_{i \in \mathcal{Y}_l} \mathbb{E}_{\bar{x}_l \sim \mathcal{P}_{l_i}} \mathcal{T}(x|\bar{x}_l) + \eta_l \mathbb{E}_{\bar{x}_u \sim \mathcal{P}} \mathcal{T}(x|\bar{x}_u).\end{aligned}$$

Plugging in $w_{xx'}$ we have,

$$\begin{aligned}
& -2 \sum_{x, x' \in \mathcal{X}} w_{xx'} f(x)^\top f(x') \\
&= -2 \sum_{x, x^+ \in \mathcal{X}} w_{xx^+} f(x)^\top f(x^+) \\
&= -2\eta_u \sum_{i \in \mathcal{Y}_l} \mathbb{E}_{\bar{x}_l \sim \mathcal{P}_{l_i}} \mathbb{E}_{\bar{x}'_l \sim \mathcal{P}_{l_i}} \sum_{x, x' \in \mathcal{X}} \mathcal{T}(x|\bar{x}_l) \mathcal{T}(x'|\bar{x}'_l) f(x)^\top f(x') \\
&\quad - 2\eta_l \mathbb{E}_{\bar{x}_u \sim \mathcal{P}} \sum_{x, x'} \mathcal{T}(x|\bar{x}_u) \mathcal{T}(x'|\bar{x}_u) f(x)^\top f(x') \\
&= -2\eta_u \sum_{i \in \mathcal{Y}_l} \mathbb{E}_{\substack{\bar{x}_l \sim \mathcal{P}_{l_i}, \bar{x}'_l \sim \mathcal{P}_{l_i}, \\ x \sim \mathcal{T}(\cdot|\bar{x}_l), x^+ \sim \mathcal{T}(\cdot|\bar{x}'_l)}} [f(x)^\top f(x^+)] \\
&\quad - 2\eta_l \mathbb{E}_{\substack{\bar{x}_u \sim \mathcal{P}, \\ x \sim \mathcal{T}(\cdot|\bar{x}_u), x^+ \sim \mathcal{T}(\cdot|\bar{x}_u)}} [f(x)^\top f(x^+)] \\
&= -2\eta_u \mathcal{L}_1(f) - 2\eta_l \mathcal{L}_2(f).
\end{aligned}$$

Plugging w_x and $w_{x'}$ we have,

$$\begin{aligned}
& \sum_{x, x' \in \mathcal{X}} w_x w_{x'} \left(f(x)^\top f(x') \right)^2 \\
= & \sum_{x, x^- \in \mathcal{X}} w_x w_{x^-} \left(f(x)^\top f(x^-) \right)^2 \\
= & \sum_{x, x' \in \mathcal{X}} \left(\eta_u \sum_{i \in \mathcal{Y}_l} \mathbb{E}_{\bar{x}_l \sim \mathcal{P}_{l_i}} \mathcal{T}(x | \bar{x}_l) + \eta_l \mathbb{E}_{\bar{x}_u \sim \mathcal{P}} \mathcal{T}(x | \bar{x}_u) \right) \\
& \cdot \left(\eta_u \sum_{j \in \mathcal{Y}_l} \mathbb{E}_{\bar{x}'_l \sim \mathcal{P}_{l_j}} \mathcal{T}(x^- | \bar{x}'_l) + \eta_l \mathbb{E}_{\bar{x}'_u \sim \mathcal{P}} \mathcal{T}(x^- | \bar{x}'_u) \right) \left(f(x)^\top f(x^-) \right)^2 \\
= & \eta_u^2 \sum_{x, x^- \in \mathcal{X}} \sum_{i \in \mathcal{Y}_l} \mathbb{E}_{\bar{x}_l \sim \mathcal{P}_{l_i}} \mathcal{T}(x | \bar{x}_l) \sum_{j \in \mathcal{Y}_l} \mathbb{E}_{\bar{x}'_l \sim \mathcal{P}_{l_j}} \mathcal{T}(x^- | \bar{x}'_l) \left(f(x)^\top f(x^-) \right)^2 \\
& + 2\eta_u \eta_l \sum_{x, x^- \in \mathcal{X}} \sum_{i \in \mathcal{Y}_l} \mathbb{E}_{\bar{x}_l \sim \mathcal{P}_{l_i}} \mathcal{T}(x | \bar{x}_l) \mathbb{E}_{\bar{x}_u \sim \mathcal{P}} \mathcal{T}(x^- | \bar{x}_u) \left(f(x)^\top f(x^-) \right)^2 \\
& + \eta_l^2 \sum_{x, x^- \in \mathcal{X}} \mathbb{E}_{\bar{x}_u \sim \mathcal{P}} \mathcal{T}(x | \bar{x}_u) \mathbb{E}_{\bar{x}'_u \sim \mathcal{P}} \mathcal{T}(x^- | \bar{x}'_u) \left(f(x)^\top f(x^-) \right)^2 \\
= & \eta_u^2 \sum_{i \in \mathcal{Y}_l} \sum_{j \in \mathcal{Y}_l} \mathbb{E}_{\substack{\bar{x}_l \sim \mathcal{P}_{l_i}, \bar{x}'_l \sim \mathcal{P}_{l_j}, \\ x \sim \mathcal{T}(\cdot | \bar{x}_l), x^- \sim \mathcal{T}(\cdot | \bar{x}'_l)}} \left[\left(f(x)^\top f(x^-) \right)^2 \right] \\
& + 2\eta_u \eta_l \sum_{i \in \mathcal{Y}_l} \mathbb{E}_{\substack{\bar{x}_l \sim \mathcal{P}_{l_i}, \bar{x}_u \sim \mathcal{P}, \\ x \sim \mathcal{T}(\cdot | \bar{x}_l), x^- \sim \mathcal{T}(\cdot | \bar{x}_u)}} \left[\left(f(x)^\top f(x^-) \right)^2 \right] \\
& + \eta_l^2 \mathbb{E}_{\substack{\bar{x}_u \sim \mathcal{P}, \bar{x}'_u \sim \mathcal{P}, \\ x \sim \mathcal{T}(\cdot | \bar{x}_u), x^- \sim \mathcal{T}(\cdot | \bar{x}'_u)}} \left[\left(f(x)^\top f(x^-) \right)^2 \right] \\
= & \eta_u^2 \mathcal{L}_3(f) + 2\eta_u \eta_l \mathcal{L}_4(f) + \eta_l^2 \mathcal{L}_5(f).
\end{aligned}$$

□

B.2.2 Technical Details for Toy Example

B.2.2.1 Calculation Details for Figure 7.2.

We first recap the toy example, which illustrates the core idea of our theoretical findings. Specifically, the example aims to distinguish 3D objects with different shapes, as shown in Figure 7.2. These images are generated by a 3D rendering software (Johnson et al., 2017) with user-defined properties including colors, shape, size, position, etc.

Data design. Suppose the training samples come from three types, \mathcal{X}_{\square} , \mathcal{X}_{\circ} , \mathcal{X}_{\ominus} . Let \mathcal{X}_{\square} be the sample space with **known** class, and \mathcal{X}_{\circ} , \mathcal{X}_{\ominus} be the sample space with **novel** classes. Further, the two novel classes are constructed to have different relationships with the known class. Specifically, we construct the toy dataset with 6 elements as shown in Figure B.2(a).

Augmentation graph. Based on the data design, we formally define the augmentation graph, which encodes the probability of augmenting a source image \bar{x} to the augmented view x :

$$\mathcal{T}(x | \bar{x}) = \begin{cases} \tau_1 & \text{if } \text{color}(x) = \text{color}(\bar{x}), \text{shape}(x) = \text{shape}(\bar{x}); \\ \tau_c & \text{if } \text{color}(x) = \text{color}(\bar{x}), \text{shape}(x) \neq \text{shape}(\bar{x}); \\ \tau_s & \text{if } \text{color}(x) \neq \text{color}(\bar{x}), \text{shape}(x) = \text{shape}(\bar{x}); \\ \tau_0 & \text{if } \text{color}(x) \neq \text{color}(\bar{x}), \text{shape}(x) \neq \text{shape}(\bar{x}). \end{cases} \quad (\text{B.25})$$

According to the definition above, the corresponding augmentation matrix T with each element formed by $\mathcal{T}(\cdot | \cdot)$ is given in Figure B.2(b). We proceed by showing the details to derive $A^{(u)}$ and A using T .

Derivation details for $A^{(u)}$ and A . Recall that each element of $A^{(u)}$ is formed by $w_{xx'}^{(u)} = \mathbb{E}_{\bar{x} \sim \mathcal{P}} \mathcal{T}(x|\bar{x})\mathcal{T}(x'|\bar{x})$. In this toy example, one can then see that $A^{(u)} = \frac{1}{6}TT^\top$ since augmentation matrix T is defined that each element $T_{x\bar{x}} = \mathcal{T}(x|\bar{x})$. Note that T is explicitly given in Figure B.2(b) and then if we let $\eta_u = 6$, we have the close-form:

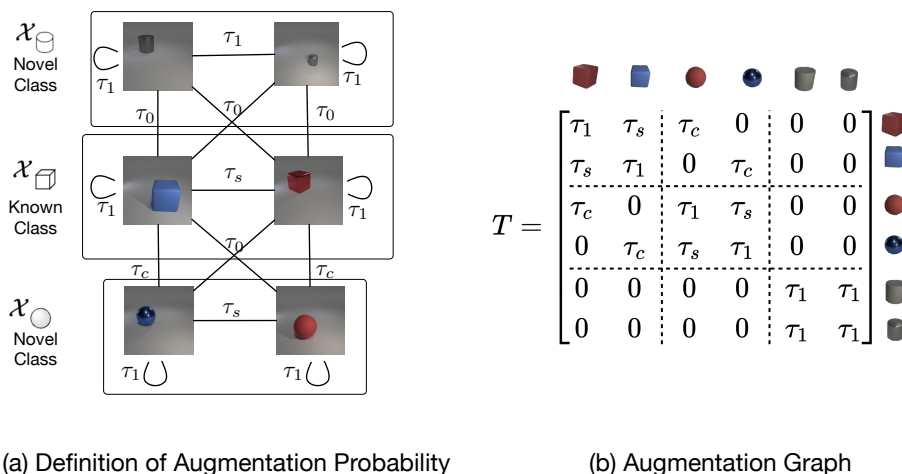


Figure B.2: An illustrative example for theoretical analysis. We consider a 6-node graph with one known class (cube) and two novel classes (sphere, cylinder). (a) The augmentation probabilities between nodes are defined by their color and shape in Eq. (B.25). (b) The augmentation matrices T derived by Eq. (B.25) where we let $\tau_0 = 0$.

$$\eta_u A^{(u)} = T^2 = \begin{bmatrix} \tau_1^2 + \tau_s^2 + \tau_c^2 & 2\tau_1\tau_s & 2\tau_1\tau_c & 2\tau_c\tau_s & 0 & 0 \\ 2\tau_1\tau_s & \tau_1^2 + \tau_s^2 + \tau_c^2 & 2\tau_c\tau_s & 2\tau_1\tau_c & 0 & 0 \\ 2\tau_1\tau_c & 2\tau_c\tau_s & \tau_1^2 + \tau_s^2 + \tau_c^2 & 2\tau_1\tau_s & 0 & 0 \\ 2\tau_c\tau_s & 2\tau_1\tau_c & 2\tau_1\tau_s & \tau_1^2 + \tau_s^2 + \tau_c^2 & 0 & 0 \\ 0 & 0 & 0 & 0 & 2\tau_1^2 & 2\tau_1^2 \\ 0 & 0 & 0 & 0 & 2\tau_1^2 & 2\tau_1^2 \end{bmatrix}.$$

We then derive the second part $A^{(l)}$ whose element is given by:

$$w_{xx'}^{(l)} \triangleq \sum_{i \in \mathcal{Y}_l} \mathbb{E}_{\bar{x}_l \sim \mathcal{P}_{l_i}} \mathbb{E}_{\bar{x}'_l \sim \mathcal{P}_{l_i}} \mathcal{T}(x|\bar{x}_l) \mathcal{T}(x'|\bar{x}'_l).$$

Such a form can be simplified in Section 7.4 by defining $\mathfrak{l} \in \mathbb{R}^N$, $(\mathfrak{l})_x =$

$\mathbb{E}_{\bar{x}_l \sim \mathcal{P}_{l_1}} \mathcal{T}(x|\bar{x}_l)$ and by letting $|\mathcal{Y}_l| = 1$. In this toy example, the known class only has two elements, so $\mathfrak{l} = \frac{1}{2}(T_{:,1} + T_{:,2})$ (average of T 's 1st & 2nd column), we then have:

$$A^{(\mathfrak{l})} = \mathfrak{U}^\top = \frac{1}{4} \begin{bmatrix} (\tau_1 + \tau_s)^2 & (\tau_1 + \tau_s)^2 & \tau_c(\tau_1 + \tau_s) & \tau_c(\tau_1 + \tau_s) & 0 & 0 \\ (\tau_1 + \tau_s)^2 & (\tau_1 + \tau_s)^2 & \tau_c(\tau_1 + \tau_s) & \tau_c(\tau_1 + \tau_s) & 0 & 0 \\ \tau_c(\tau_1 + \tau_s) & \tau_c(\tau_1 + \tau_s) & \tau_c^2 & \tau_c^2 & 0 & 0 \\ \tau_c(\tau_1 + \tau_s) & \tau_c(\tau_1 + \tau_s) & \tau_c^2 & \tau_c^2 & 0 & 0 \\ 0 & 0 & 0 & 0 & 0 & 0 \\ 0 & 0 & 0 & 0 & 0 & 0 \end{bmatrix}.$$

Finally, if we let $\eta_l = 4$ and $A = \eta_u A^{(u)} + \eta_l A^{(\mathfrak{l})}$, we have the full results in Figure 7.2.

B.2.2.2 Calculation Details for Figure 7.3.

In this section, we present the analysis of eigenvectors and their orders for toy examples shown in Figure 7.2. In Theorem B.18 we present the spectral analysis for the adjacency matrix with additional label information while in Theorem B.19, we show the spectral analysis for the unlabeled case.

Theorem B.18. *Let*

$$\eta_u A^{(u)} = \begin{bmatrix} \tau_1^2 + \tau_s^2 + \tau_c^2 & 2\tau_1\tau_s & 2\tau_1\tau_c & 2\tau_c\tau_s & 0 & 0 \\ 2\tau_1\tau_s & \tau_1^2 + \tau_s^2 + \tau_c^2 & 2\tau_c\tau_s & 2\tau_1\tau_c & 0 & 0 \\ 2\tau_1\tau_c & 2\tau_c\tau_s & \tau_1^2 + \tau_s^2 + \tau_c^2 & 2\tau_1\tau_s & 0 & 0 \\ 2\tau_c\tau_s & 2\tau_1\tau_c & 2\tau_1\tau_s & \tau_1^2 + \tau_s^2 + \tau_c^2 & 0 & 0 \\ 0 & 0 & 0 & 0 & 2\tau_1^2 & 2\tau_1^2 \\ 0 & 0 & 0 & 0 & 2\tau_1^2 & 2\tau_1^2 \end{bmatrix},$$

$$A = \eta_u A^{(u)} + \begin{bmatrix} (\tau_1 + \tau_s)^2 & (\tau_1 + \tau_s)^2 & \tau_c(\tau_1 + \tau_s) & \tau_c(\tau_1 + \tau_s) & 0 & 0 \\ (\tau_1 + \tau_s)^2 & (\tau_1 + \tau_s)^2 & \tau_c(\tau_1 + \tau_s) & \tau_c(\tau_1 + \tau_s) & 0 & 0 \\ \tau_c(\tau_1 + \tau_s) & \tau_c(\tau_1 + \tau_s) & \tau_c^2 & \tau_c^2 & 0 & 0 \\ \tau_c(\tau_1 + \tau_s) & \tau_c(\tau_1 + \tau_s) & \tau_c^2 & \tau_c^2 & 0 & 0 \\ 0 & 0 & 0 & 0 & 0 & 0 \\ 0 & 0 & 0 & 0 & 0 & 0 \end{bmatrix},$$

and we assume that $1 \gg \frac{\tau_c}{\tau_1} > \frac{\tau_s}{\tau_1} > 0$, $\frac{4}{9}\tau_c \leq \tau_s \leq \tau_c$ and $\tau_1 + \tau_c + \tau_s = 1$.

Let $\lambda_1, \lambda_2, \lambda_3$ and v_1, v_2, v_3 be the largest three eigenvalues and their corresponding eigenvectors of $D^{-\frac{1}{2}}AD^{-\frac{1}{2}}$, which is the normalized adjacency matrix of A . Then the concrete form of $\lambda_1, \lambda_2, \lambda_3$ and v_1, v_2, v_3 can be approximately given by:

$$\begin{aligned} \hat{\lambda}_1 &= 1, \quad \hat{\lambda}_2 = 1, \quad \hat{\lambda}_3 = 1 - \frac{16}{3} \frac{\tau_c}{\tau_1}, \\ \hat{v}_1 &= [0, 0, 0, 0, 1, 1], \\ \hat{v}_2 &= [\sqrt{3}, \sqrt{3}, 1, 1, 0, 0], \\ \hat{v}_3 &= [1, 1, -\sqrt{3}, -\sqrt{3}, 0, 0]. \end{aligned}$$

Note that the approximation gap can be tightly bounded. Specifically, for $i \in \{1, 2, 3\}$, we have $|\lambda_i - \hat{\lambda}_i| \leq O((\frac{\tau_c}{\tau_1})^2)$ and $\|\sin(U, \hat{U})\|_F \leq O(\frac{\tau_c}{\tau_1})$, where $U = [v_1, v_2, v_3]$, $\hat{U} = [\hat{v}_1, \hat{v}_2, \hat{v}_3]$.

Proof. By $\tau_1 + \tau_c + \tau_s = 1$ and $1 \gg \frac{\tau_c}{\tau_1} > \frac{\tau_s}{\tau_1} > 0$, we define the following equation which approximates the corresponding terms up to error

⁴The sin operation measures the distance of two matrices with orthonormal columns, which is usually used in the subspace distance. See more in <https://trungvietvu.github.io/notes/2020/DavisKahan>.

$O((\frac{\tau_c}{\tau_1})^2)$:

$$A \approx \hat{A} = \tau_1^2 \begin{bmatrix} 2 + 2\frac{\tau_s}{\tau_1} & 1 + 4\frac{\tau_s}{\tau_1} & 3\frac{\tau_c}{\tau_1} & \frac{\tau_c}{\tau_1} & 0 & 0 \\ 1 + 4\frac{\tau_s}{\tau_1} & 2 + 2\frac{\tau_s}{\tau_1} & \frac{\tau_c}{\tau_1} & 3\frac{\tau_c}{\tau_1} & 0 & 0 \\ 3\frac{\tau_c}{\tau_1} & \frac{\tau_c}{\tau_1} & 1 & 2\frac{\tau_s}{\tau_1} & 0 & 0 \\ \frac{\tau_c}{\tau_1} & 3\frac{\tau_c}{\tau_1} & 2\frac{\tau_s}{\tau_1} & 1 & 0 & 0 \\ 0 & 0 & 0 & 0 & 2 & 2 \\ 0 & 0 & 0 & 0 & 2 & 2 \end{bmatrix}.$$

$$D \approx \widehat{D} = \tau_1^2 \text{diag} \left(\left[3 \left(1 + 2\frac{\tau_s}{\tau_1} + \frac{4}{3}\frac{\tau_c}{\tau_1} \right), 3 \left(1 + 2\frac{\tau_s}{\tau_1} + \frac{4}{3}\frac{\tau_c}{\tau_1} \right), 1 + 2\frac{\tau_s}{\tau_1} + 4\frac{\tau_c}{\tau_1}, 1 + 2\frac{\tau_s}{\tau_1} + 4\frac{\tau_c}{\tau_1}, 4, 4 \right] \right).$$

$$D^{-\frac{1}{2}} \approx \widehat{D}^{-\frac{1}{2}} = \frac{1}{\tau_1} \text{diag} \left(\left[\sqrt{3} \left(1 - \frac{\tau_s}{\tau_1} - \frac{2}{3}\frac{\tau_c}{\tau_1} \right), \sqrt{3} \left(1 - \frac{\tau_s}{\tau_1} - \frac{2}{3}\frac{\tau_c}{\tau_1} \right), 1 - \frac{\tau_s}{\tau_1} - 2\frac{\tau_c}{\tau_1}, 1 - \frac{\tau_s}{\tau_1} - 2\frac{\tau_c}{\tau_1}, 2, 2 \right] \right).$$

$$D^{-\frac{1}{2}} A D^{-\frac{1}{2}} \approx \widehat{D}^{-\frac{1}{2}} \widehat{A} \widehat{D}^{-\frac{1}{2}}$$

$$= \begin{bmatrix} \frac{2}{3} \left(1 - \frac{\tau_s}{\tau_1} - \frac{4}{3}\frac{\tau_c}{\tau_1} \right) & \frac{1}{3} \left(1 + 2\frac{\tau_s}{\tau_1} - \frac{4}{3}\frac{\tau_c}{\tau_1} \right) & \sqrt{3}\frac{\tau_c}{\tau_1} & \frac{1}{\sqrt{3}}\frac{\tau_c}{\tau_1} & 0 & 0 \\ \frac{1}{3} \left(1 + 2\frac{\tau_s}{\tau_1} - \frac{4}{3}\frac{\tau_c}{\tau_1} \right) & \frac{2}{3} \left(1 - \frac{\tau_s}{\tau_1} - \frac{4}{3}\frac{\tau_c}{\tau_1} \right) & \frac{1}{\sqrt{3}}\frac{\tau_c}{\tau_1} & \sqrt{3}\frac{\tau_c}{\tau_1} & 0 & 0 \\ \sqrt{3}\frac{\tau_c}{\tau_1} & \frac{1}{\sqrt{3}}\frac{\tau_c}{\tau_1} & 1 - 2\frac{\tau_s}{\tau_1} - 4\frac{\tau_c}{\tau_1} & 2\frac{\tau_s}{\tau_1} & 0 & 0 \\ \frac{1}{\sqrt{3}}\frac{\tau_c}{\tau_1} & \sqrt{3}\frac{\tau_c}{\tau_1} & 2\frac{\tau_s}{\tau_1} & 1 - 2\frac{\tau_s}{\tau_1} - 4\frac{\tau_c}{\tau_1} & 0 & 0 \\ 0 & 0 & 0 & 0 & \frac{1}{2} & \frac{1}{2} \\ 0 & 0 & 0 & 0 & \frac{1}{2} & \frac{1}{2} \end{bmatrix}.$$

And we have

$$\begin{aligned} & \left\| D^{-\frac{1}{2}}AD^{-\frac{1}{2}} - \widehat{D}^{-\frac{1}{2}}\widehat{A}\widehat{D}^{-\frac{1}{2}} \right\|_2 \\ & \leq \left\| D^{-\frac{1}{2}}AD^{-\frac{1}{2}} - \widehat{D}^{-\frac{1}{2}}\widehat{A}\widehat{D}^{-\frac{1}{2}} \right\|_F \\ & \leq O\left(\left(\frac{\tau_c}{\tau_1}\right)^2\right). \end{aligned}$$

Let $\hat{\lambda}_a, \dots, \hat{\lambda}_f$ be six eigenvalues of $\widehat{D}^{-\frac{1}{2}}\widehat{A}\widehat{D}^{-\frac{1}{2}}$, and $\hat{v}_a, \dots, \hat{v}_f$ be corresponding eigenvectors. By direct calculation we have

$$\hat{\lambda}_a = 1, \quad \hat{\lambda}_b = 1, \quad \hat{\lambda}_c = 1 - \frac{16}{3} \frac{\tau_c}{\tau_1}, \quad \hat{\lambda}_d = 0$$

and corresponding eigenvectors as

$$\begin{aligned} \hat{v}_a &= [0, 0, 0, 0, 1, 1], \\ \hat{v}_b &= [\sqrt{3}, \sqrt{3}, 1, 1, 0, 0], \\ \hat{v}_c &= [1, 1, -\sqrt{3}, -\sqrt{3}, 0, 0], \\ \hat{v}_d &= [0, 0, 0, 0, 1, -1]. \end{aligned}$$

For the remaining two eigenvectors, by the symmetric property, they have the formula

$$\begin{aligned} \hat{v}_e &= \left[\alpha\left(\frac{\tau_s}{\tau_1}, \frac{\tau_c}{\tau_1}\right), -\alpha\left(\frac{\tau_s}{\tau_1}, \frac{\tau_c}{\tau_1}\right), \beta\left(\frac{\tau_s}{\tau_1}, \frac{\tau_c}{\tau_1}\right), -\beta\left(\frac{\tau_s}{\tau_1}, \frac{\tau_c}{\tau_1}\right), 0, 0 \right], \\ \hat{v}_f &= \left[\beta\left(\frac{\tau_s}{\tau_1}, \frac{\tau_c}{\tau_1}\right), -\beta\left(\frac{\tau_s}{\tau_1}, \frac{\tau_c}{\tau_1}\right), -\alpha\left(\frac{\tau_s}{\tau_1}, \frac{\tau_c}{\tau_1}\right), \alpha\left(\frac{\tau_s}{\tau_1}, \frac{\tau_c}{\tau_1}\right), 0, 0 \right], \end{aligned}$$

where α, β are some real functions. Then, by solving

$$\begin{aligned} \widehat{D}^{-\frac{1}{2}}\widehat{A}\widehat{D}^{-\frac{1}{2}}\hat{v}_e &= \hat{\lambda}_e\hat{v}_e \\ \widehat{D}^{-\frac{1}{2}}\widehat{A}\widehat{D}^{-\frac{1}{2}}\hat{v}_f &= \hat{\lambda}_f\hat{v}_f, \end{aligned}$$

we get

$$\begin{aligned}\hat{\lambda}_e &= \frac{1}{9} \left(\sqrt{(3 - 12\frac{\tau_s}{\tau_1} - 16\frac{\tau_c}{\tau_1})^2 + 108(\frac{\tau_c}{\tau_1})^2} - 24\frac{\tau_s}{\tau_1} - 20\frac{\tau_c}{\tau_1} + 6 \right) \\ \hat{\lambda}_f &= \frac{1}{9} \left(-\sqrt{(3 - 12\frac{\tau_s}{\tau_1} - 16\frac{\tau_c}{\tau_1})^2 + 108(\frac{\tau_c}{\tau_1})^2} - 24\frac{\tau_s}{\tau_1} - 20\frac{\tau_c}{\tau_1} + 6 \right).\end{aligned}$$

Now, we show that $\hat{\lambda}_c > \hat{\lambda}_e$. By $\frac{\tau_c}{\tau_1} \ll 1$ and $\frac{4}{9}\tau_c \leq \tau_s \leq \tau_c$

$$\begin{aligned}\hat{\lambda}_c \geq \hat{\lambda}_e &\Leftrightarrow 3 + 24\frac{\tau_s}{\tau_1} - 28\frac{\tau_c}{\tau_1} \geq \sqrt{(3 - 12\frac{\tau_s}{\tau_1} - 16\frac{\tau_c}{\tau_1})^2 + 108(\frac{\tau_c}{\tau_1})^2} \\ &\Leftrightarrow 36(\frac{\tau_s}{\tau_1})^2 + 35(\frac{\tau_c}{\tau_1})^2 - 144\frac{\tau_s}{\tau_1}\frac{\tau_c}{\tau_1} + 18\frac{\tau_s}{\tau_1} - 6\frac{\tau_c}{\tau_1} \geq 0.\end{aligned}$$

Thus, we have $1 = \hat{\lambda}_a = \hat{\lambda}_b > \hat{\lambda}_c > \hat{\lambda}_e > \hat{\lambda}_f > \hat{\lambda}_d = 0$. Moreover, we also have

$$\begin{aligned}\hat{\lambda}_c - \hat{\lambda}_e &= 1 - \frac{16}{3}\frac{\tau_c}{\tau_1} - \frac{1}{9} \left(\sqrt{(3 - 12\frac{\tau_s}{\tau_1} - 16\frac{\tau_c}{\tau_1})^2 + 108(\frac{\tau_c}{\tau_1})^2} - 24\frac{\tau_s}{\tau_1} - 20\frac{\tau_c}{\tau_1} + 6 \right) \\ &\geq \Omega\left(\frac{\tau_c}{\tau_1}\right).\end{aligned}$$

Let $\hat{\lambda}_1 = \hat{\lambda}_a, \hat{\lambda}_2 = \hat{\lambda}_b, \hat{\lambda}_3 = \hat{\lambda}_c$. Then, by Weyl's Theorem, for $i \in \{1, 2, 3\}$, we have

$$|\lambda_i - \hat{\lambda}_i| \leq \left\| D^{-\frac{1}{2}}AD^{-\frac{1}{2}} - \widehat{D}^{-\frac{1}{2}}\widehat{A}\widehat{D}^{-\frac{1}{2}} \right\|_2 \leq O\left(\left(\frac{\tau_c}{\tau_1}\right)^2\right).$$

By Davis-Kahan theorem, we have

$$\|\sin(U, \hat{U})\|_F \leq \frac{O\left(\left(\frac{\tau_c}{\tau_1}\right)^2\right)}{\Omega\left(\frac{\tau_c}{\tau_1}\right)} \leq O\left(\frac{\tau_c}{\tau_1}\right).$$

We finish the proof. \square

Theorem B.19. Recall $\eta_u A^{(u)}$ is defined in Theorem B.18. Assume $1 \gg \frac{\tau_c}{\tau_1} >$

$\frac{\tau_s}{\tau_1} > 0$ and $\tau_1 + \tau_c + \tau_s = 1$. Let $\lambda_1^{(u)}, \lambda_2^{(u)}, \lambda_3^{(u)}$ and $v_1^{(u)}, v_2^{(u)}, v_3^{(u)}$ be the largest three eigenvalues and their corresponding eigenvectors of $D^{(u)-\frac{1}{2}}(\eta_u A^{(u)})D^{(u)-\frac{1}{2}}$, which is the normalized adjacency matrix of $\eta_u A^{(u)}$. Let

$$\begin{aligned}\hat{\lambda}_1^{(u)} &= 1, \quad \hat{\lambda}_2^{(u)} = 1, \quad \hat{\lambda}_3^{(u)} = 1 - 4\frac{\tau_s}{\tau_1}, \\ \hat{v}_1^{(u)} &= [0, 0, 0, 0, 1, 1], \\ \hat{v}_2^{(u)} &= [1, 1, 1, 1, 0, 0], \\ \hat{v}_3^{(u)} &= [1, -1, 1, -1, 0, 0].\end{aligned}$$

Let $U^{(u)} = [v_1^{(u)}, v_2^{(u)}, v_3^{(u)}]$, $\hat{U}^{(u)} = [\hat{v}_1^{(u)}, \hat{v}_2^{(u)}, \hat{v}_3^{(u)}]$. Then, for $i \in \{1, 2, 3\}$, we have $|\lambda_i^{(u)} - \hat{\lambda}_i^{(u)}| \leq O((\frac{\tau_c}{\tau_1})^2)$ and $\|\sin(U^{(u)}, \hat{U}^{(u)})\|_F \leq O(\frac{\tau_c^2}{\tau_1(\tau_c - \tau_s)})$.

Proof. Similar to the proof of Theorem B.18, up to error $O((\frac{\tau_c}{\tau_1})^2)$, we have the following equation,

$$\widehat{\eta_u A^{(u)}} = \tau_1^2 \begin{bmatrix} 1 & 2\frac{\tau_s}{\tau_1} & 2\frac{\tau_c}{\tau_1} & 0 & 0 & 0 \\ 2\frac{\tau_s}{\tau_1} & 1 & 0 & 2\frac{\tau_c}{\tau_1} & 0 & 0 \\ 2\frac{\tau_c}{\tau_1} & 0 & 1 & 2\frac{\tau_s}{\tau_1} & 0 & 0 \\ 0 & 2\frac{\tau_c}{\tau_1} & 2\frac{\tau_s}{\tau_1} & 1 & 0 & 0 \\ 0 & 0 & 0 & 0 & 2 & 2 \\ 0 & 0 & 0 & 0 & 2 & 2 \end{bmatrix}.$$

$$\widehat{D^{(u)}} = \tau_1^2 \text{diag} \left(\left[1 + 2\frac{\tau_s}{\tau_1} + 2\frac{\tau_c}{\tau_1}, 1 + 2\frac{\tau_s}{\tau_1} + 2\frac{\tau_c}{\tau_1}, 1 + 2\frac{\tau_s}{\tau_1} + 2\frac{\tau_c}{\tau_1}, 1 + 2\frac{\tau_s}{\tau_1} + 2\frac{\tau_c}{\tau_1}, 4, 4 \right] \right).$$

$$\widehat{D^{(u)-\frac{1}{2}}} = \frac{1}{\tau_1} \text{diag} \left(\left[1 - \frac{\tau_s}{\tau_1} - \frac{\tau_c}{\tau_1}, 1 - \frac{\tau_s}{\tau_1} - \frac{\tau_c}{\tau_1}, 1 - \frac{\tau_s}{\tau_1} - \frac{\tau_c}{\tau_1}, 1 - \frac{\tau_s}{\tau_1} - \frac{\tau_c}{\tau_1}, 2, 2 \right] \right).$$

$$\widehat{D^{(u)-\frac{1}{2}}\eta_u A^{(u)}D^{(u)-\frac{1}{2}}} = \begin{bmatrix} 1 - 2\frac{\tau_s}{\tau_1} - 2\frac{\tau_c}{\tau_1} & 2\frac{\tau_s}{\tau_1} & 2\frac{\tau_c}{\tau_1} & 0 & 0 & 0 \\ 2\frac{\tau_s}{\tau_1} & 1 - 2\frac{\tau_s}{\tau_1} - 2\frac{\tau_c}{\tau_1} & 0 & 2\frac{\tau_c}{\tau_1} & 0 & 0 \\ 2\frac{\tau_c}{\tau_1} & 0 & 1 - 2\frac{\tau_s}{\tau_1} - 2\frac{\tau_c}{\tau_1} & 2\frac{\tau_s}{\tau_1} & 0 & 0 \\ 0 & 2\frac{\tau_c}{\tau_1} & 2\frac{\tau_s}{\tau_1} & 1 - 2\frac{\tau_s}{\tau_1} - 2\frac{\tau_c}{\tau_1} & 0 & 0 \\ 0 & 0 & 0 & 0 & \frac{1}{2} & \frac{1}{2} \\ 0 & 0 & 0 & 0 & \frac{1}{2} & \frac{1}{2} \end{bmatrix}.$$

Let $\hat{\lambda}_1^{(u)}, \dots, \hat{\lambda}_6^{(u)}$ be six eigenvalue of $\widehat{D^{(u)-\frac{1}{2}}\eta_u A^{(u)}D^{(u)-\frac{1}{2}}$, and $\hat{v}_1^{(u)}, \dots, \hat{v}_6^{(u)}$ be corresponding eigenvectors. By direct calculation we have

$$\hat{\lambda}_1^{(u)} = 1, \hat{\lambda}_2^{(u)} = 1, \hat{\lambda}_3^{(u)} = 1 - 4\frac{\tau_s}{\tau_1}, \hat{\lambda}_4^{(u)} = 1 - 4\frac{\tau_c}{\tau_1}, \hat{\lambda}_5^{(u)} = 1 - 4\frac{\tau_s}{\tau_1} - 4\frac{\tau_c}{\tau_1}, \hat{\lambda}_6^{(u)} = 0$$

and corresponding eigenvector as

$$\begin{aligned} \hat{v}_1^{(u)} &= [0, 0, 0, 0, 1, 1], \\ \hat{v}_2^{(u)} &= [1, 1, 1, 1, 0, 0], \\ \hat{v}_3^{(u)} &= [1, -1, 1, -1, 0, 0], \\ \hat{v}_4^{(u)} &= [1, 1, -1, -1, 0, 0], \\ \hat{v}_5^{(u)} &= [1, -1, -1, 1, 0, 0], \\ \hat{v}_6^{(u)} &= [0, 0, 0, 0, 1, -1]. \end{aligned}$$

Then, by Weyl's Theorem, for $i \in \{1, 2, 3\}$, we have

$$|\lambda_i^{(u)} - \hat{\lambda}_i^{(u)}| \leq \left\| \widehat{D^{(u)-\frac{1}{2}}\eta_u A^{(u)}D^{(u)-\frac{1}{2}} - \widehat{D^{(u)-\frac{1}{2}}\eta_u A^{(u)}D^{(u)-\frac{1}{2}}} \right\|_2 \leq O\left(\left(\frac{\tau_c}{\tau_1}\right)^2\right).$$

By Davis-Kahan theorem, we have

$$\|\sin(U^{(u)}, \hat{U}^{(u)})\|_F \leq \frac{O\left(\left(\frac{\tau_c}{\tau_1}\right)^2\right)}{4\left(\frac{\tau_c}{\tau_1} - \frac{\tau_s}{\tau_1}\right)} \leq O\left(\frac{\tau_c^2}{\tau_1(\tau_c - \tau_s)}\right).$$

We finish the proof. □

B.2.3 Technical Details for Main Theory

B.2.3.1 Matrix Form of K-means and the Derivative

Recall that we defined the K-means clustering measure of features in Sec. 7.4:

$$\mathcal{M}_{kms}(\Pi, Z) = \sum_{\pi \in \Pi} \sum_{i \in \pi} \|\mathbf{z}_i - \boldsymbol{\mu}_\pi\|^2 / \sum_{\pi \in \Pi} |\pi| \|\boldsymbol{\mu}_\pi - \boldsymbol{\mu}_\Pi\|^2, \quad (\text{B.26})$$

where the numerator measures the intra-class distance:

$$\mathcal{M}_{intra}(\Pi, Z) = \sum_{\pi \in \Pi} \sum_{i \in \pi} \|\mathbf{z}_i - \boldsymbol{\mu}_\pi\|^2, \quad (\text{B.27})$$

and the denominator measures the inter-class distance:

$$\mathcal{M}_{inter}(\Pi, Z) = \sum_{\pi \in \Pi} |\pi| \|\boldsymbol{\mu}_\pi - \boldsymbol{\mu}_\Pi\|^2. \quad (\text{B.28})$$

We will show next how to convert the intra-class and the inter-class measures into a matrix form, which is desirable for analysis.

Intra-class measure. Note that the K -means intra-class measure can be rewritten in a matrix form:

$$\mathcal{M}_{intra}(\Pi, Z) = \|Z - H_\Pi Z\|_F^2,$$

where H_Π is a matrix to convert Z to mean vectors w.r.t clusters defined by Π . Without losing the generality, we assume Z is ordered according to the partition in Π — first $|\pi_1|$ vectors are in π_1 , next $|\pi_2|$ vectors are in π_2 , etc. Then H_Π is given by:

$$H_{\Pi} = \begin{bmatrix} \frac{1}{|\pi_1|} \mathbf{1}_{|\pi_1| \times |\pi_1|} & \mathbf{0} & \dots & \mathbf{0} \\ \mathbf{0} & \frac{1}{|\pi_2|} \mathbf{1}_{|\pi_2| \times |\pi_2|} & \dots & \mathbf{0} \\ \dots & \dots & \dots & \dots \\ \mathbf{0} & \mathbf{0} & \dots & \frac{1}{|\pi_k|} \mathbf{1}_{|\pi_k| \times |\pi_k|} \end{bmatrix}.$$

Going further, we have:

$$\begin{aligned} \mathcal{M}_{intra}(\Pi, Z) &= \|Z - H_{\Pi}Z\|_F^2 \\ &= \text{Tr}((I - H_{\Pi})^2 Z Z^{\top}) \\ &= \text{Tr}((I - 2H_{\Pi} + H_{\Pi}^2) Z Z^{\top}) \\ &= \text{Tr}((I - H_{\Pi}) Z Z^{\top}). \end{aligned}$$

Inter-class measure. The inter-class measure can be equivalently given by:

$$\mathcal{M}_{inter}(\Pi, Z) = \|H_{\Pi}Z - \frac{1}{N} \mathbf{1}_{N \times N} Z\|_F^2,$$

where H_{Π} is defined as above. And we can also derive:

$$\begin{aligned} \mathcal{M}_{inter}(\Pi, Z) &= \|H_{\Pi}Z - \frac{1}{N} \mathbf{1}_{N \times N} Z\|_F^2 \\ &= \text{Tr}((H_{\Pi} - \frac{1}{N} \mathbf{1}_{N \times N})^2 Z Z^{\top}) \\ &= \text{Tr}((H_{\Pi}^2 - \frac{2}{N} H_{\Pi} \mathbf{1}_{N \times N} + \frac{1}{N^2} \mathbf{1}_{N \times N}^2) Z Z^{\top}) \\ &= \text{Tr}((H_{\Pi} - \frac{1}{N} \mathbf{1}_{N \times N}) Z Z^{\top}). \end{aligned}$$

B.2.3.2 K-means Measure Has the Same Order as K-means Error

Theorem B.20. We define the $\xi_{\pi \rightarrow \pi'}$ as the index of samples that is from class division π however is closer to $\boldsymbol{\mu}_{\pi'}$ than $\boldsymbol{\mu}_{\pi}$. In other word, $\xi_{\pi \rightarrow \pi'} = \{i : i \in \pi, \|\mathbf{z}_i - \boldsymbol{\mu}_{\pi}\|_2 \geq \|\mathbf{z}_i - \boldsymbol{\mu}_{\pi'}\|_2\}$. Assuming $|\xi_{\pi \rightarrow \pi'}| > 0$, we define below the clustering error ratio from π to π' as $\mathcal{E}_{\pi \rightarrow \pi'}$ and the overall cluster error ratio

$\mathcal{E}_{\Pi, Z}$ as the **Harmonic Mean** of $\mathcal{E}_{\pi \rightarrow \pi'}$ among all class pairs:

$$\mathcal{E}_{\Pi, Z} = C(C - 1) / \left(\sum_{\substack{\pi \neq \pi' \\ \pi, \pi' \in \Pi}} \frac{1}{\mathcal{E}_{\pi \rightarrow \pi'}} \right), \text{ where } \mathcal{E}_{\pi \rightarrow \pi'} = \frac{|\xi_{\pi \rightarrow \pi'}|}{|\pi'| + |\pi|}.$$

The K-means measure $\mathcal{M}_{kms}(\Pi, Z)$ has the same order as the Harmonic Mean of the cluster error ratio between all cluster pairs:

$$\mathcal{E}_{\Pi, Z} = O(\mathcal{M}_{kms}(\Pi, Z)).$$

Proof. We have the following inequality for $i \in \xi_{\pi \rightarrow \pi'}$:

$$4\|\mathbf{z}_i - \boldsymbol{\mu}_\pi\|_2^2 \geq 2\|\mathbf{z}_i - \boldsymbol{\mu}_\pi\|_2^2 + 2\|\mathbf{z}_i - \boldsymbol{\mu}_{\pi'}\|_2^2 \geq \|\boldsymbol{\mu}_\pi - \boldsymbol{\mu}_{\pi'}\|_2^2.$$

Then we have:

$$\begin{aligned} \mathcal{M}_{intra}(\Pi, Z) &= \sum_{\pi \in \Pi} \sum_{i \in \pi} \|\mathbf{z}_i - \boldsymbol{\mu}_\pi\|_2^2 \\ &\geq \sum_{i \in \pi} \|\mathbf{z}_i - \boldsymbol{\mu}_\pi\|_2^2 \\ &\geq \sum_{i \in \xi_{\pi \rightarrow \pi'}} \|\mathbf{z}_i - \boldsymbol{\mu}_\pi\|_2^2 \\ &\geq \frac{1}{4} \sum_{i \in \xi_{\pi \rightarrow \pi'}} \|\boldsymbol{\mu}_\pi - \boldsymbol{\mu}_{\pi'}\|_2^2 \\ &= \frac{1}{4} |\xi_{\pi \rightarrow \pi'}| \|\boldsymbol{\mu}_\pi - \boldsymbol{\mu}_{\pi'}\|_2^2. \end{aligned}$$

Note that the inter-class measure can be decomposed into the summa-

tion of cluster center distances:

$$\begin{aligned}
\mathcal{M}_{inter}(\Pi, Z) &= \sum_{\pi \in \Pi} |\pi| \|\boldsymbol{\mu}_\pi - \boldsymbol{\mu}_\Pi\|_2^2 \\
&= \sum_{\pi \in \Pi} \frac{|\pi|}{N^2} \left\| \left(\sum_{\pi' \in \Pi} |\pi'| \right) \boldsymbol{\mu}_\pi - \sum_{\pi' \in \Pi} |\pi'| \boldsymbol{\mu}_{\pi'} \right\|_2^2 \\
&\leq \frac{C}{N^2} \sum_{\pi \in \Pi} |\pi| \sum_{\pi' \in \Pi} |\pi'|^2 \|\boldsymbol{\mu}_\pi - \boldsymbol{\mu}_{\pi'}\|_2^2 \\
&= \frac{C}{N^2} \sum_{\pi \neq \pi'} |\pi| |\pi'| (|\pi'| + |\pi|) \|\boldsymbol{\mu}_\pi - \boldsymbol{\mu}_{\pi'}\|_2^2,
\end{aligned}$$

where $\sum_{\pi \neq \pi'}$ is enumerating over any two different class partitions in Π . Combining together, we have:

$$\begin{aligned}
C(C-1) / \left(\sum_{\pi \neq \pi'} \frac{(|\pi'| + |\pi|)}{|\xi_{\pi \rightarrow \pi'}|} \right) &= C(C-1) / \left(\sum_{\pi \neq \pi'} \frac{(|\pi'| + |\pi|) \|\boldsymbol{\mu}_\pi - \boldsymbol{\mu}_{\pi'}\|_2^2}{|\xi_{\pi \rightarrow \pi'}| \|\boldsymbol{\mu}_\pi - \boldsymbol{\mu}_{\pi'}\|_2^2} \right) \\
&\leq C(C-1) / \left(\sum_{\pi \neq \pi'} \frac{|\pi'| |\pi| (|\pi'| + |\pi|) \|\boldsymbol{\mu}_\pi - \boldsymbol{\mu}_{\pi'}\|_2^2}{N^2 |\xi_{\pi \rightarrow \pi'}| \|\boldsymbol{\mu}_\pi - \boldsymbol{\mu}_{\pi'}\|_2^2} \right) \\
&\leq C(C-1) / \left(\frac{\mathcal{M}_{inter}(\Pi, Z)}{4C \mathcal{M}_{intra}(\Pi, Z)} \right) \\
&= O(\mathcal{M}_{kms}(\Pi, Z)).
\end{aligned}$$

□

B.2.3.3 Proof of Theorem 7.2

We start by providing more details to supplement Sec. 7.4.2.1.

Matrix perturbation by adding labels. Recall that we define in Eq. 7.3 that the adjacency matrix is the unlabeled one $A^{(u)}$ plus the perturbation of the label information $A^{(l)}$:

$$A = \eta_u A^{(u)} + \eta_l A^{(l)}.$$

We study the perturbation from two aspects: (1) The direction of the perturbation which is given by $A^{(l)}$, (2) The perturbation magnitude η_l . We first consider the perturbation direction $A^{(l)}$ and recall that we defined the concrete form in Eq. 7.2:

$$A_{xx'}^{(l)} = w_{xx'}^{(l)} \triangleq \sum_{i \in \mathcal{Y}_l} \mathbb{E}_{\bar{x}_l \sim \mathcal{P}_{l_i}} \mathbb{E}_{\bar{x}'_l \sim \mathcal{P}_{l_i}} \mathcal{T}(x|\bar{x}_l) \mathcal{T}(x'|\bar{x}'_l).$$

For simplicity, we consider $|\mathcal{Y}_l| = 1$ in this theoretical analysis. Then we observe that $A_{xx'}^{(l)}$ is a rank-1 matrix can be written as

$$A_{xx'}^{(l)} = \mathfrak{l} \mathfrak{l}^\top,$$

where $\mathfrak{l} \in \mathbb{R}^{N \times 1}$ with $(\mathfrak{l})_x = \mathbb{E}_{\bar{x}_l \sim \mathcal{P}_{l_1}} \mathcal{T}(x|\bar{x}_l)$. And we define $D_l \triangleq \text{diag}(\mathfrak{l})$.

The perturbation function of representation. We then consider a more generalized form for the adjacency matrix:

$$A(\delta) \triangleq \eta_u A^{(u)} + \delta \mathfrak{l} \mathfrak{l}^\top.$$

where we treat the adjacency matrix as a function of the “labeling perturbation” degree δ . It is clear that $A(0) = \eta_u A^{(u)}$ which is the scaled adjacency matrix for the unlabeled case and that $A(\eta_l) = A$. When we let the adjacency matrix be a function of δ , the normalized form and the derived feature representation should also be the function of δ . We proceed by defining these terms.

Without losing the generality, we let $\text{diag}(\mathbf{1}_N^\top A(0)) = I_N$ which means the node in the unlabeled graph has equal degree. We then have:

$$D(\delta) \triangleq \text{diag}(\mathbf{1}_N^\top A(\delta)) = I_N + \delta D_l.$$

The normalized adjacency matrix is given by:

$$\dot{A}(\delta) \triangleq D(\delta)^{-\frac{1}{2}} A(\delta) D(\delta)^{-\frac{1}{2}}.$$

For feature representation $Z(\delta)$, it is derived from the top- k SVD components of $\dot{A}(\delta)$. Specifically, we have:

$$Z(\delta)Z(\delta)^\top = D(\delta)^{-\frac{1}{2}}\dot{A}_k(\delta)D(\delta)^{-\frac{1}{2}} = D(\delta)^{-\frac{1}{2}}\sum_{j=1}^k\lambda_j(\delta)\Phi_j(\delta)D(\delta)^{-\frac{1}{2}},$$

where we define $\dot{A}_k(\delta)$ as the top- k SVD components of $\dot{A}(\delta)$ and can be further written as $\dot{A}_k(\delta) = \sum_{j=1}^k\lambda_j(\delta)\Phi_j(\delta)$. Here the $\lambda_j(\delta)$ is the j -th singular value and $\Phi_j(\delta)$ is the j -th singular projector ($\Phi_j(\delta) = v_j(\delta)v_j(\delta)^\top$) defined by the j -th singular vector $v_j(\delta)$. **For brevity, when $\delta = 0$, we remove the suffix (0) since it is equivalent to the unperturbed version of notations. For example, we let**

$$\tilde{A}(0) = \tilde{A}^{(u)}, Z(0) = Z^{(u)}, \lambda_i(0) = \lambda_i^{(u)}, v_i(0) = v_i^{(u)}, \Phi_i(0) = \Phi_i^{(u)}.$$

Theorem B.21. (Recap of Theorem 7.2) Denote $V_\emptyset^{(u)} \in \mathbb{R}^{N \times (N-k)}$ as the null space of $V_k^{(u)}$ and $\tilde{A}_k^{(u)} = V_k^{(u)}\Sigma_k^{(u)}V_k^{(u)\top}$ as the rank- k approximation for $\tilde{A}^{(u)}$. Given $\delta, \eta_1 > 0$ and let \mathcal{G}_k as the spectral gap between k -th and $k+1$ -th singular values of $\tilde{A}^{(u)}$, we have:

$$\Delta_{kms}(\delta) = \delta\eta_1 \text{Tr} \left(\Upsilon \left(V_k^{(u)}V_k^{(u)\top} \mathbb{U}^\top (I + V_\emptyset^{(u)}V_\emptyset^{(u)\top}) - 2\tilde{A}_k^{(u)} \text{diag}(\mathbf{l}) \right) \right) + O\left(\frac{1}{\mathcal{G}_k} + \delta^2\right),$$

where $\text{diag}(\cdot)$ converts the vector to the corresponding diagonal matrix and $\Upsilon \in \mathbb{R}^{N \times N}$ is a matrix encoding the **ground-truth clustering structure** in the way that $\Upsilon_{xx'} > 0$ if x and x' has the same label and $\Upsilon_{xx'} < 0$ otherwise.

Proof. As we shown in Sec B.2.3.1, we can now also write the K-means measure as the function of perturbation:

$$\mathcal{M}_{kms}(\delta) = \frac{\text{Tr}((I - H_\Pi)Z(\delta)Z(\delta)^\top)}{\text{Tr}((H_\Pi - \frac{1}{N}\mathbf{1}_{N \times N})Z(\delta)Z(\delta)^\top)}.$$

The proof is directly given by the following Lemma B.22. □

Lemma B.22. Let η_1, η_2 be two real values and $\Upsilon = (1 + \eta_2)H_\Pi - I - \frac{\eta_2}{N}\mathbf{1}_N\mathbf{1}_N^\top$. Let the spectrum gap $\mathcal{G}_k = \frac{\lambda_k^{(u)}}{\lambda_{k+1}^{(u)}}$, we have the derivative of the K-means measure evaluated at $\delta = 0$:

$$[\mathcal{M}_{kms}(\delta)]' \Big|_{\delta=0} = -\eta_1 \operatorname{Tr} \left(\Upsilon \left(V_k^{(u)} V_k^{(u)\top} \mathbf{u}^\top - 2\tilde{A}_k^{(u)} D_l + V_k^{(u)} V_k^{(u)\top} \mathbf{u}^\top V_\emptyset^{(u)} V_\emptyset^{(u)\top} \right) \right) + O\left(\frac{1}{\mathcal{G}_k}\right).$$

The proof for Lemma B.22 is lengthy. We postpone it to Sec. B.2.3.5.

B.2.3.4 Proof of Theorem 7.3

We start by showing the justification of the assumptions made in Theorem 7.3.

Assumption B.23. We assume the spectral gap \mathcal{G}_k is large. Such an assumption is commonly used in theory works using spectral analysis (Shen et al., 2022; Joseph and Yu, 2016).

Assumption B.24. We assume \mathbf{l} lies in the linear span of $V_k^{(u)}$. i.e., $V_k^{(u)} V_k^{(u)\top} \mathbf{l} = \mathbf{l}$, $V_\emptyset^{(u)\top} \mathbf{l} = 0$. The goal of this assumption is to simplify $(V_k^{(u)} V_k^{(u)\top} \mathbf{u}^\top + V_k^{(u)} V_k^{(u)\top} \mathbf{u}^\top V_\emptyset^{(u)} V_\emptyset^{(u)\top})$ to \mathbf{u}^\top .

Assumption B.25. For any $\pi_c \in \Pi$, $\forall i, j \in \pi_c$, $\mathbf{l}_{(i)} = \mathbf{l}_{(j)} =: \mathbf{l}_{\pi_c}$. Recall that the $\mathbf{l}_{(i)}$ means the connection between the i -th sample to the labeled data. Here we can view \mathbf{l}_{π_c} as the connection between class c to the labeled data.

Theorem B.26. (Recap of Theorem 7.3.) With Assumption B.23, B.24 and B.25. Given $\delta, \eta_1, \eta_2 > 0$, we have:

$$\Delta_{kms}(\delta) \geq \delta \eta_1 \eta_2 \sum_{\pi_c \in \Pi} |\pi_c| \mathbf{l}_{\pi_c} \Delta_{\pi_c}(\delta),$$

where

$$\Delta_{\pi_c}(\delta) = (\mathfrak{l}_{\pi_c} - \frac{1}{N}) - 2(1 - \frac{|\pi_c|}{N})(\mathbb{E}_{i \in \pi_c} \mathbb{E}_{j \in \pi_c} \mathbf{z}_i^\top \mathbf{z}_j - \mathbb{E}_{i \in \pi_c} \mathbb{E}_{j \notin \pi_c} \mathbf{z}_i^\top \mathbf{z}_j).$$

Proof. The proof is directly given by Lemma B.27 and plugging the definition of $\Delta_{kms}(\delta)$. \square

Lemma B.27. *With Assumption B.23 B.24 and B.25, we have the derivative of K-means measure with the upper bound:*

$$[\mathcal{M}_{kms}(\delta)]' \Big|_{\delta=0} \leq -\eta_1 \eta_2 \sum_{\pi \in \Pi} |\pi| \mathfrak{l}_\pi \left((\mathfrak{l}_\pi - \frac{1}{N}) - 2(\boldsymbol{\mu}_\pi^\top \boldsymbol{\mu}_\pi - \boldsymbol{\mu}_\pi^\top \boldsymbol{\mu}_\Pi) \right).$$

Proof. By Assumption B.23 B.24 and B.25 and Theorem 7.2, we have

$$\begin{aligned} \frac{1}{\eta_1} [\mathcal{M}_{kms}(\delta)]' \Big|_{\delta=0} &= -\text{Tr} \left(\Upsilon \left(V_k^{(u)} V_k^{(u)\top} \mathfrak{U}^\top - 2\tilde{A}_k^{(u)} D_l \right) \right) \\ &= -\text{Tr} \left(\Upsilon \left(\mathfrak{U}^\top - 2\tilde{A}_k^{(u)} D_l \right) \right) \\ &= -\text{Tr} \left(\left((1 + \eta_2) H_\Pi - I - \frac{\eta_2}{N} \mathbf{1}_N \mathbf{1}_N^\top \right) \left(\mathfrak{U}^\top - 2\tilde{A}_k^{(u)} D_l \right) \right) \\ &= (1 + \eta_2) \mathcal{M}'_H + \mathcal{M}'_I + \eta_2 \mathcal{M}'_1, \end{aligned}$$

where

$$\begin{aligned} \mathcal{M}'_H &= -\text{Tr} \left(H_\Pi \left(\mathfrak{U}^\top - 2\tilde{A}_k^{(u)} D_l \right) \right) \\ &= -\sum_{\pi \in \Pi} \left(|\pi| (\mathbb{E}_{i \in \pi} \mathfrak{l}_{(i)})^2 - \frac{2}{|\pi|} \sum_{i \in \pi} \sum_{j \in \pi} \mathfrak{l}_{(i)} \tilde{A}_{k,(i,j)}^{(u)} \right) \\ &= -\sum_{\pi \in \Pi} \left(|\pi| \mathfrak{l}_\pi^2 - 2|\pi| \mathfrak{l}_\pi \mathbb{E}_{(i,j) \in \pi \times \pi} \mathbf{z}_i^\top \mathbf{z}_j \right) \\ &= -\sum_{\pi \in \Pi} |\pi| \mathfrak{l}_\pi (\mathfrak{l}_\pi - 2\boldsymbol{\mu}_\pi^\top \boldsymbol{\mu}_\pi), \end{aligned}$$

$$\begin{aligned}\mathcal{M}'_I &= \text{Tr} \left((\mathbf{U}^\top - 2\tilde{A}_k^{(u)} D_l) \right) \\ &= \sum_{\pi \in \Pi} |\pi| \mathfrak{l}_\pi (\mathfrak{l}_\pi - 2\mathbb{E}_{i \in \pi} \mathbf{z}_i^\top \mathbf{z}_i),\end{aligned}$$

and

$$\begin{aligned}\mathcal{M}'_1 &= \text{Tr} \left(\frac{1}{N} \mathbf{1}_N \mathbf{1}_N^\top (\mathbf{U}^\top - 2\tilde{A}_k^{(u)} D_l) \right) \\ &= \frac{1}{N} - 2 \sum_{\pi \in \Pi} \sum_{i \in \pi} \mathfrak{l}_{(i)} \mathbb{E}_{j \in [N]} \mathbf{z}_i^\top \mathbf{z}_j \\ &= \frac{1}{N} - 2 \sum_{\pi \in \Pi} |\pi| \mathfrak{l}_\pi \boldsymbol{\mu}_\pi^\top \boldsymbol{\mu}_\Pi.\end{aligned}$$

We observe that

$$\begin{aligned}\mathcal{M}'_I + \mathcal{M}'_H &= - \sum_{\pi \in \Pi} |\pi| \mathfrak{l}_\pi (\mathfrak{l}_\pi - 2\boldsymbol{\mu}_\pi^\top \boldsymbol{\mu}_\pi) + \sum_{\pi \in \Pi} |\pi| \mathfrak{l}_\pi (\mathfrak{l}_\pi - 2\mathbb{E}_{i \in \pi} \mathbf{z}_i^\top \mathbf{z}_i) \\ &= 2 \sum_{\pi \in \Pi} |\pi| \mathfrak{l}_\pi (\|\mathbb{E}_{i \in \pi} \mathbf{z}_i\|_2^2 - \mathbb{E}_{i \in \pi} \|\mathbf{z}_i\|_2^2) \\ &\leq 0,\end{aligned}$$

where the last inequality is by Jensen's Inequality. We then have

$$\begin{aligned}\frac{1}{\eta_1 \eta_2} [\mathcal{M}_{kms}(\delta)]' \Big|_{\delta=0} &\leq \mathcal{M}'_H + \mathcal{M}'_1 \\ &= - \sum_{\pi \in \Pi} |\pi| \mathfrak{l}_\pi (\mathfrak{l}_\pi - 2\boldsymbol{\mu}_\pi^\top \boldsymbol{\mu}_\pi) + \frac{1}{N} - 2 \sum_{\pi \in \Pi} |\pi| \mathfrak{l}_\pi \boldsymbol{\mu}_\pi^\top \boldsymbol{\mu}_\Pi \\ &= \frac{1}{N} - \sum_{\pi \in \Pi} |\pi| \mathfrak{l}_\pi (\mathfrak{l}_\pi - 2(\boldsymbol{\mu}_\pi^\top \boldsymbol{\mu}_\pi - \boldsymbol{\mu}_\pi^\top \boldsymbol{\mu}_\Pi)) \\ &= - \sum_{\pi \in \Pi} |\pi| \mathfrak{l}_\pi \left((\mathfrak{l}_\pi - \frac{1}{N}) - 2(\boldsymbol{\mu}_\pi^\top \boldsymbol{\mu}_\pi - \boldsymbol{\mu}_\pi^\top \boldsymbol{\mu}_\Pi) \right).\end{aligned}$$

□

B.2.3.5 Proof of Lemma B.22

Notation Recap: We define $\dot{A}_k(\delta)$ as the top- k SVD components of $\dot{A}(\delta)$ and can be further written as $\dot{A}_k(\delta) = \sum_{j=1}^k \lambda_j(\delta) \Phi_j(\delta)$. Here the $\lambda_j(\delta)$ is the j -th singular value and $\Phi_j(\delta)$ is the j -th singular projector ($\Phi_j(\delta) = v_j(\delta)v_j(\delta)^\top$) defined by the j -th singular vector $v_j(\delta)$. **For brevity, when $\delta = 0$, we remove the suffix (0) since it is equivalent to the unperturbed version of notations. For example, we let**

$$\tilde{A}(0) = \tilde{A}^{(u)}, Z(0) = Z^{(u)}, \lambda_i(0) = \lambda_i^{(u)}, v_i(0) = v_i^{(u)}, \Phi_i(0) = \Phi_i^{(u)}.$$

Proof. By the derivative rule, we have,

$$\begin{aligned} \mathcal{M}'_{kms}(\delta) &= \frac{1}{\mathcal{M}_{inter}(\Pi, Z)} \mathcal{M}'_{intra}(\delta) - \frac{\mathcal{M}_{intra}(\Pi, Z)}{\mathcal{M}_{inter}(\Pi, Z)^2} \mathcal{M}'_{inter}(\delta) \\ &= \eta_1 \mathcal{M}'_{intra}(\delta) - \eta_1 \eta_2 \mathcal{M}'_{inter}(\delta) \\ &= \eta_1 \left(\text{Tr}((I_\Pi - H_\Pi)[Z(\delta)Z(\delta)^\top]') - \eta_2 \text{Tr}((H_\Pi - \frac{1}{N} \mathbf{1}_{N \times N})[Z(\delta)Z(\delta)^\top]') \right) \\ &= \eta_1 \left(\text{Tr}((I_\Pi + \frac{\eta_2}{N} \mathbf{1}_{N \times N} - (\eta_2 + 1)H_\Pi)[Z(\delta)Z(\delta)^\top]') \right) \\ &= -\eta_1 \left(\text{Tr}(\Upsilon[Z(\delta)Z(\delta)^\top]') \right) \\ &= -\eta_1 \sum_{j=1}^k \text{Tr}(\Upsilon[D(\delta)^{-\frac{1}{2}} \lambda_j(\delta) \Phi_j(\delta) D(\delta)^{-\frac{1}{2}}]'), \end{aligned}$$

where we let $\eta_1 = \frac{1}{\mathcal{M}_{inter}(\Pi, Z)}$, $\eta_2 = \frac{\mathcal{M}_{intra}(\Pi, Z)}{\mathcal{M}_{inter}(\Pi, Z)}$ and $\Upsilon = (1 + \eta_2)H_\Pi - I_\Pi - \frac{\eta_2}{N} \mathbf{1}_N \mathbf{1}_N^\top$. We proceed by showing the calculation of $[D(\delta)^{-\frac{1}{2}}]'$, $[\lambda_j(\delta)]'$ and $[\Phi_j(\delta)]'$.

Since $D(\delta) = I + \delta D_l$, then $[D(\delta)^{-\frac{1}{2}}]'\Big|_{\delta=0} = -\frac{1}{2} D_l$. To calculate $[\lambda_j(\delta)]'$

and $[\Phi_j(\delta)]'$, we first need:

$$\begin{aligned} [\dot{A}(\delta)]' \Big|_{\delta=0} &= [D(\delta)^{-\frac{1}{2}} A(\delta) D(\delta)^{-\frac{1}{2}}]' \\ &= [D(\delta)^{-\frac{1}{2}}]' \tilde{A}^{(u)} + [A(\delta)]' + \tilde{A}^{(u)} [D(\delta)^{-\frac{1}{2}}]' \\ &= -\frac{1}{2} D_l \tilde{A}^{(u)} + \mathbb{U}^\top - \frac{1}{2} \tilde{A}^{(u)} D_l. \end{aligned}$$

Then, according to Equation (3) in [Greenbaum et al. \(2020\)](#), we have:

$$\begin{aligned} [\lambda_j(\delta)]' \Big|_{\delta=0} &= \text{Tr}(\Phi_j^{(u)} [\dot{A}(\delta)]') \\ &= \text{Tr}(\Phi_j^{(u)} (-\frac{1}{2} D_l \tilde{A}^{(u)} + \mathbb{U}^\top - \frac{1}{2} \tilde{A}^{(u)} D_l)) \\ &= \text{Tr}((-\frac{\lambda_j^{(u)}}{2} D_l \Phi_j^{(u)} + \Phi_j^{(u)} \mathbb{U}^\top - \frac{\lambda_j^{(u)}}{2} \Phi_j^{(u)} D_l)) \\ &= \text{Tr}(\Phi_j^{(u)} (\mathbb{U}^\top - \lambda_j^{(u)} D_l)). \end{aligned}$$

According to Equation (10) in [Greenbaum et al. \(2020\)](#), we have:

$$\begin{aligned} [\Phi_j(\delta)]' \Big|_{\delta=0} &= (\lambda_j^{(u)} I_N - \dot{A}^{(u)})^\dagger [\dot{A}(\delta)]' \Phi_j^{(u)} + \Phi_j^{(u)} [\dot{A}(\delta)]' (\lambda_j^{(u)} I_N - \dot{A}^{(u)})^\dagger \\ &= \sum_{i \neq j}^N \frac{1}{\lambda_j^{(u)} - \lambda_i^{(u)}} (\Phi_i^{(u)} [\dot{A}(\delta)]' \Phi_j^{(u)} + \Phi_j^{(u)} [\dot{A}(\delta)]' \Phi_i^{(u)}) \\ &= \sum_{i \neq j}^N \frac{1}{\lambda_j^{(u)} - \lambda_i^{(u)}} (\Phi_i^{(u)} (-\frac{1}{2} D_l \tilde{A}^{(u)} + \mathbb{U}^\top - \frac{1}{2} \tilde{A}^{(u)} D_l) \Phi_j^{(u)} + \Phi_j^{(u)} (\dots) \Phi_i^{(u)}) \\ &= \sum_{i \neq j}^N \frac{1}{\lambda_j^{(u)} - \lambda_i^{(u)}} (\Phi_i^{(u)} (\mathbb{U}^\top - \frac{\lambda_j^{(u)} + \lambda_i^{(u)}}{2} D_l) \Phi_j^{(u)} + \Phi_j^{(u)} (\mathbb{U}^\top - \frac{\lambda_j^{(u)} + \lambda_i^{(u)}}{2} D_l) \Phi_i^{(u)}). \end{aligned}$$

Now we calculate the derivative of the K -means loss:

$$\begin{aligned}
& \frac{1}{\eta_1} [\mathcal{M}_{kms}(\delta)]' \Big|_{\delta=0} \\
&= - \sum_{j=1}^k [\text{Tr}(\Upsilon D(\delta)^{-\frac{1}{2}} \lambda_j(\delta) \Phi_j(\delta) D(\delta)^{-\frac{1}{2}})]' \Big|_{\delta=0} \\
&= - \sum_{j=1}^k \text{Tr} \left(\Upsilon \left([D(\delta)^{-\frac{1}{2}}]' \lambda_j^{(u)} \Phi_j^{(u)} + \lambda_j^{(u)} \Phi_j^{(u)} [D(\delta)^{-\frac{1}{2}}]' + [\lambda_j(\delta)]' \Phi_j^{(u)} + \lambda_j^{(u)} [\Phi_j(\delta)]' \right) \right) \\
&= \sum_{j=1}^k \text{Tr} \left(\Upsilon \left(\frac{\lambda_j^{(u)}}{2} D_l \Phi_j^{(u)} + \frac{\lambda_j^{(u)}}{2} \Phi_j^{(u)} D_l - [\lambda_j(\delta)]' \Phi_j^{(u)} - \lambda_j^{(u)} [\Phi_j(\delta)]' \right) \right) \\
&= \mathcal{M}'_a + \mathcal{M}'_b + \mathcal{M}'_c,
\end{aligned}$$

where

$$\mathcal{M}'_a = \sum_{j=1}^k \frac{\lambda_j^{(u)}}{2} \text{Tr} \left(\Upsilon \left(D_l \Phi_j^{(u)} + \Phi_j^{(u)} D_l \right) \right),$$

$$\begin{aligned}
\mathcal{M}'_b &= - \sum_{j=1}^k \text{Tr} \left(\Upsilon [\lambda_j(\delta)]' \Phi_j^{(u)} \right) = - \sum_{j=1}^k \text{Tr} \left((\mathbb{I}^\top - \lambda_j^{(u)} D_l) \Phi_j^{(u)} \right) \text{Tr} \left(\Upsilon \Phi_j^{(u)} \right) \\
&= - \sum_{j=1}^k \text{Tr} \left((\mathbb{I}^\top - \lambda_j^{(u)} D_l) \Phi_j^{(u)} \Upsilon \Phi_j^{(u)} \right),
\end{aligned}$$

$$\begin{aligned}
& \mathcal{M}'_c \\
&= - \sum_{j=1}^k \text{Tr} \left(\Upsilon \lambda_j^{(u)} [\Phi_j(\delta)]' \right) \\
&= - \sum_{j=1}^k \text{Tr} \left(\sum_{i \neq j}^N \frac{\lambda_j^{(u)}}{\lambda_j^{(u)} - \lambda_i^{(u)}} \left(\Upsilon \Phi_i^{(u)} (\mathbb{U}^\top - \frac{\lambda_j^{(u)} + \lambda_i^{(u)}}{2} D_l) \Phi_j^{(u)} + \Upsilon \Phi_j^{(u)} (\mathbb{U}^\top - \frac{\lambda_j^{(u)} + \lambda_i^{(u)}}{2} D_l) \Phi_i^{(u)} \right) \right) \\
&= - \sum_{j=1}^k \text{Tr} \left(\sum_{i \neq j}^N \frac{\lambda_j^{(u)}}{\lambda_j^{(u)} - \lambda_i^{(u)}} \left((\Phi_j^{(u)} \Upsilon \Phi_i^{(u)} + \Phi_i^{(u)} \Upsilon \Phi_j^{(u)}) (\mathbb{U}^\top - \frac{\lambda_j^{(u)} + \lambda_i^{(u)}}{2} D_l) \right) \right) \\
&= - \sum_{j=1}^k \text{Tr} \left(\sum_{i \neq j, i \leq k} \frac{\lambda_j^{(u)}}{\lambda_j^{(u)} - \lambda_i^{(u)}} \left((\Phi_j^{(u)} \Upsilon \Phi_i^{(u)} + \Phi_i^{(u)} \Upsilon \Phi_j^{(u)}) (\mathbb{U}^\top - \frac{\lambda_j^{(u)} + \lambda_i^{(u)}}{2} D_l) \right) \right) \\
&\quad - \sum_{j=1}^k \text{Tr} \left(\sum_{i=k+1}^N \frac{\lambda_j^{(u)}}{\lambda_j^{(u)} - \lambda_i^{(u)}} \left((\Phi_j^{(u)} \Upsilon \Phi_i^{(u)} + \Phi_i^{(u)} \Upsilon \Phi_j^{(u)}) (\mathbb{U}^\top - \frac{\lambda_j^{(u)} + \lambda_i^{(u)}}{2} D_l) \right) \right) \\
&= - \sum_{j=1}^k \text{Tr} \left(\sum_{i < j} \left(\frac{\lambda_j^{(u)}}{\lambda_j^{(u)} - \lambda_i^{(u)}} + \frac{\lambda_i^{(u)}}{\lambda_i^{(u)} - \lambda_j^{(u)}} \right) \left((\Phi_j^{(u)} \Upsilon \Phi_i^{(u)} + \Phi_i^{(u)} \Upsilon \Phi_j^{(u)}) (\mathbb{U}^\top - \frac{\lambda_j^{(u)} + \lambda_i^{(u)}}{2} D_l) \right) \right) \\
&\quad - \sum_{j=1}^k \text{Tr} \left(\sum_{i=k+1}^N \frac{\lambda_j^{(u)}}{\lambda_j^{(u)} - \lambda_i^{(u)}} \left((\Phi_j^{(u)} \Upsilon \Phi_i^{(u)} + \Phi_i^{(u)} \Upsilon \Phi_j^{(u)}) (\mathbb{U}^\top - \frac{\lambda_j^{(u)} + \lambda_i^{(u)}}{2} D_l) \right) \right) \\
&= - \sum_{j=1}^k \text{Tr} \left(\sum_{i < j} \left((\Phi_j^{(u)} \Upsilon \Phi_i^{(u)} + \Phi_i^{(u)} \Upsilon \Phi_j^{(u)}) (\mathbb{U}^\top - \frac{\lambda_j^{(u)} + \lambda_i^{(u)}}{2} D_l) \right) \right) \\
&\quad - \sum_{j=1}^k \text{Tr} \left(\sum_{i=k+1}^N \frac{\lambda_j^{(u)}}{\lambda_j^{(u)} - \lambda_i^{(u)}} \left((\Phi_j^{(u)} \Upsilon \Phi_i^{(u)} + \Phi_i^{(u)} \Upsilon \Phi_j^{(u)}) (\mathbb{U}^\top - \frac{\lambda_j^{(u)} + \lambda_i^{(u)}}{2} D_l) \right) \right) \\
&= - \sum_{j=1}^k \text{Tr} \left(\sum_{i \neq j, i \leq k} \frac{1}{2} \left((\Phi_j^{(u)} \Upsilon \Phi_i^{(u)} + \Phi_i^{(u)} \Upsilon \Phi_j^{(u)}) (\mathbb{U}^\top - \frac{\lambda_j^{(u)} + \lambda_i^{(u)}}{2} D_l) \right) \right) \\
&\quad - \sum_{j=1}^k \text{Tr} \left(\sum_{i=k+1}^N \frac{\lambda_j^{(u)}}{\lambda_j^{(u)} - \lambda_i^{(u)}} \left((\Phi_j^{(u)} \Upsilon \Phi_i^{(u)} + \Phi_i^{(u)} \Upsilon \Phi_j^{(u)}) (\mathbb{U}^\top - \frac{\lambda_j^{(u)} + \lambda_i^{(u)}}{2} D_l) \right) \right).
\end{aligned}$$

Thus, we have:

$$\begin{aligned}
& \mathcal{M}'_b + \mathcal{M}'_c \\
&= - \sum_{j=1}^k \text{Tr} \left(\sum_{i=1}^k \frac{1}{2} \left((\Phi_j^{(u)} \Upsilon \Phi_i^{(u)} + \Phi_i^{(u)} \Upsilon \Phi_j^{(u)}) (\mathbb{I}^\top - \frac{\lambda_j^{(u)} + \lambda_i^{(u)}}{2} D_l) \right) \right) \\
& \quad - \sum_{j=1}^k \text{Tr} \left(\sum_{i=k+1}^N \frac{\lambda_j^{(u)}}{\lambda_j^{(u)} - \lambda_i^{(u)}} \left((\Phi_j^{(u)} \Upsilon \Phi_i^{(u)} + \Phi_i^{(u)} \Upsilon \Phi_j^{(u)}) (\mathbb{I}^\top - \frac{\lambda_j^{(u)} + \lambda_i^{(u)}}{2} D_l) \right) \right),
\end{aligned}$$

$$\begin{aligned}
\mathcal{M}'_a &= \sum_{j=1}^k \frac{\lambda_j^{(u)}}{2} \text{Tr} \left(\Upsilon (D_l \Phi_j^{(u)} + \Phi_j^{(u)} D_l) \right) \\
&= \sum_{j=1}^k \frac{\lambda_j^{(u)}}{2} \text{Tr} \left((\Phi_j^{(u)} \Upsilon + \Upsilon \Phi_j^{(u)}) D_l \right) \\
&= \sum_{j=1}^k \frac{\lambda_j^{(u)}}{2} \text{Tr} \left(\left(\Phi_j^{(u)} \Upsilon \sum_{i=1}^N \Phi_i^{(u)} + \sum_{i=1}^N \Phi_i^{(u)} \Upsilon \Phi_j^{(u)} \right) D_l \right) \\
&= \sum_{j=1}^k \text{Tr} \left(\sum_{i=1}^N \frac{\lambda_j^{(u)}}{2} (\Phi_j^{(u)} \Upsilon \Phi_i^{(u)} + \Phi_i^{(u)} \Upsilon \Phi_j^{(u)}) D_l \right).
\end{aligned}$$

Then $[\mathcal{M}_{kms-all}(\delta)]' \Big|_{\delta=0} / \eta_1$ is given by:

$$\begin{aligned}
& \mathcal{M}'_a + \mathcal{M}'_b + \mathcal{M}'_c \\
&= - \sum_{j=1}^k \text{Tr} \left(\sum_{i=1}^k \frac{1}{2} \left((\Phi_j^{(u)} \Upsilon \Phi_i^{(u)} + \Phi_i^{(u)} \Upsilon \Phi_j^{(u)}) (\mathbb{U}^\top - \frac{3\lambda_j^{(u)} + \lambda_i^{(u)}}{2} D_l) \right) \right) \\
&\quad - \sum_{j=1}^k \text{Tr} \left(\sum_{i=k+1}^N \frac{\lambda_j^{(u)}}{\lambda_j^{(u)} - \lambda_i^{(u)}} \left((\Phi_j^{(u)} \Upsilon \Phi_i^{(u)} + \Phi_i^{(u)} \Upsilon \Phi_j^{(u)}) (\mathbb{U}^\top - \lambda_j^{(u)} D_l) \right) \right) \\
&= - \sum_{j=1}^k \text{Tr} \left(\sum_{i=1}^k \frac{1}{2} \left((\Phi_j^{(u)} \Upsilon \Phi_i^{(u)} + \Phi_i^{(u)} \Upsilon \Phi_j^{(u)}) (\mathbb{U}^\top - 2\lambda_j^{(u)} D_l) \right) \right) \\
&\quad - \sum_{j=1}^k \text{Tr} \left(\sum_{i=k+1}^N \frac{\lambda_j^{(u)}}{\lambda_j^{(u)} - \lambda_i^{(u)}} \left((\Phi_j^{(u)} \Upsilon \Phi_i^{(u)} + \Phi_i^{(u)} \Upsilon \Phi_j^{(u)}) (\mathbb{U}^\top - \lambda_j^{(u)} D_l) \right) \right) \\
&= - \sum_{j=1}^k \sum_{i=1}^k v_i^{(u)\top} \Upsilon v_j^{(u)} \cdot v_i^{(u)\top} (\mathbb{U}^\top - 2\lambda_j^{(u)} D_l) v_j^{(u)} \\
&\quad - \sum_{j=1}^k \sum_{i=k+1}^N \frac{2\lambda_j^{(u)}}{\lambda_j^{(u)} - \lambda_i^{(u)}} v_i^{(u)\top} \Upsilon v_j^{(u)} \cdot v_i^{(u)\top} (\mathbb{U}^\top - \lambda_j^{(u)} D_l) v_j^{(u)}.
\end{aligned}$$

We can represent $\frac{\lambda_j^{(u)}}{\lambda_j^{(u)} - \lambda_i^{(u)}} = 1 + \sum_{p=1}^{\infty} \left(\frac{\lambda_i^{(u)}}{\lambda_j^{(u)}}\right)^p$. Denote the residual term as :

$$\mathcal{M}'_e = - \sum_{j=1}^k \sum_{i=k+1}^N \sum_{p=1}^{\infty} 2 \left(\frac{\lambda_i^{(u)}}{\lambda_j^{(u)}}\right)^p v_i^{(u)\top} \Upsilon v_j^{(u)} \cdot v_i^{(u)\top} (\mathbb{U}^\top - \lambda_j^{(u)} D_l) v_j^{(u)} = O\left(\frac{1}{\mathcal{G}_k}\right).$$

We then have:

$$\begin{aligned}
& \frac{1}{\eta_1} [\mathcal{M}_{kms-all}(\delta)]' \Big|_{\delta=0} \\
&= -\text{Tr}(V_k^{(u)\top} \Upsilon V_k^{(u)} \cdot V_k^{(u)\top} \mathfrak{U}^\top V_k^{(u)}) + 2\text{Tr}(V_k^{(u)\top} \Upsilon V_k^{(u)} \cdot \Sigma_k^{(u)} V_k^{(u)\top} D_l V_k^{(u)}) \\
&\quad - 2\text{Tr}(V_\emptyset^{(u)\top} \Upsilon V_k^{(u)} \cdot V_k^{(u)\top} \mathfrak{U}^\top V_\emptyset^{(u)}) + 2\text{Tr}(V_\emptyset^{(u)\top} \Upsilon V_k^{(u)} \cdot \Sigma_k^{(u)} V_k^{(u)\top} D_l V_\emptyset^{(u)}) + \mathcal{M}'_e \\
&= -\text{Tr}(\Upsilon V_k^{(u)} V_k^{(u)\top} \mathfrak{U}^\top V_k^{(u)} V_k^{(u)\top}) + 2\text{Tr}(\Upsilon \tilde{A}_k^{(u)} D_l V_k^{(u)} V_k^{(u)\top}) \\
&\quad - 2\text{Tr}(\Upsilon V_k^{(u)} V_k^{(u)\top} \mathfrak{U}^\top (I_N - V_k^{(u)} V_k^{(u)\top})) + 2\text{Tr}(\Upsilon \tilde{A}_k^{(u)} D_l (I_N - V_k^{(u)} V_k^{(u)\top})) + \mathcal{M}'_e \\
&= -2\text{Tr}(\Upsilon V_k^{(u)} V_k^{(u)\top} \mathfrak{U}^\top) + 2\text{Tr}(\Upsilon \tilde{A}_k^{(u)} D_l) + \text{Tr}(\Upsilon V_k^{(u)} V_k^{(u)\top} \mathfrak{U}^\top V_k^{(u)} V_k^{(u)\top}) + \mathcal{M}'_e \\
&= -2\text{Tr} \left(\Upsilon \left(V_k^{(u)} V_k^{(u)\top} \mathfrak{U}^\top - \tilde{A}_k^{(u)} D_l - \frac{1}{2} V_k^{(u)} V_k^{(u)\top} \mathfrak{U}^\top V_k^{(u)} V_k^{(u)\top} \right) \right) + \mathcal{M}'_e \\
&= -\text{Tr} \left(\Upsilon \left(V_k^{(u)} V_k^{(u)\top} \mathfrak{U}^\top - 2\tilde{A}_k^{(u)} D_l + V_k^{(u)} V_k^{(u)\top} \mathfrak{U}^\top V_\emptyset V_\emptyset^\top \right) \right) + O\left(\frac{1}{\mathcal{G}_k}\right).
\end{aligned}$$

□

B.2.4 Analysis on Other Contrastive Losses

In this section, we discuss the extension of our graphic-theoretic analysis to one of the most common contrastive loss functions – SimCLR (Chen et al., 2020a). SimCLR loss is an extended version of InfoNCE loss (Van den Oord et al., 2018) that achieves great empirical success and inspires a proliferation of follow-up works (Khosla et al., 2020; Vaze et al., 2022; Caron et al., 2020; He et al., 2020; Zbontar et al., 2021; Bardes et al., 2022; Chen and He, 2021). Specifically, SupCon (Khosla et al., 2020) extends SimCLR to the supervised setting. GCD (Vaze et al., 2022) and OpenCon (Sun and Li, 2023) further leverage the SupCon and SimCLR losses, and are tailored to the open-world representation learning setting considering both labeled and unlabeled data.

At a high level, we consider a general form of the SimCLR and its extensions (including SupCon, GCD, OpenCon) as:

$$\mathcal{L}_{\text{gnl}}(f; \mathcal{P}_+) = -\frac{1}{\tau} \mathbb{E}_{(x, x^+) \sim \mathcal{P}_+} [f(x)^\top f(x^+)] + \mathbb{E}_{x \sim \mathcal{P}} \left[\log \left(\mathbb{E}_{\substack{x' \sim \mathcal{P} \\ x' \neq x}} e^{f(x')^\top f(x)/\tau} \right) \right], \quad (\text{B.29})$$

where we let the \mathcal{P}_+ as the distribution of **positive pairs** defined in Section 7.3.1. In SimCLR (Chen et al., 2020a), the positive pairs are purely sampled in the *unlabeled case* (u) while SupCon (Khosla et al., 2020) considers the *labeled case* (l). With both labeled and unlabeled data, GCD (Vaze et al., 2022) and OpenCon (Sun and Li, 2023) sample positive pairs in both cases.

In this section, we investigate an alternative form that eases the theo-

retical analysis (also applied in (Wang and Isola, 2020)):

$$\widehat{\mathcal{L}}_{\text{gnl}}(f; \mathcal{P}_+) = -\frac{1}{\tau} \mathbb{E}_{(x, x^+) \sim \mathcal{P}_+} [f(x)^\top f(x^+)] + \log \left(\mathbb{E}_{\substack{x, x' \sim \mathcal{P} \\ x \neq x'}} e^{f(x')^\top f(x)/\tau} \right) \quad (\text{B.30})$$

$$\geq \mathcal{L}_{\text{gnl}}(f; \mathcal{P}_+), \quad (\text{B.31})$$

which serves an upper bound of $\mathcal{L}_{\text{gnl}}(f)$ according to Jensen's Inequality.

A graph-theoretic view. Recall in Section 7.3.1, we define the graph $G(\mathcal{X}, w)$ with vertex set \mathcal{X} and edge weights w . Each entry of adjacency matrix A is given by $w_{xx'}$, which denotes the marginal probability of generating the pair for any two augmented data $x, x' \in \mathcal{X}$:

$$w_{xx'} = \eta_u w_{xx'}^{(u)} + \eta_l w_{xx'}^{(l)},$$

and w_x measures the degree of node x :

$$w_x = \sum_{x'} w_{xx'}.$$

One can view the difference between SimCLR and its variants in the following way: (1) SimCLR (Chen et al., 2020a) corresponds to $\eta_l = 0$ when there is no labeled case; (2) SupCon (Khosla et al., 2020) corresponds to $\eta_u = 0$ when only labeled case is considered. (3) GCD (Vaze et al., 2022) and OpenCon (Sun and Li, 2023) correspond to the cases when η_u, η_l are both non-zero due to the availability of both labeled and unlabeled data.

With the define marginal probability of sampling positive pairs $w_{xx'}$ and the marginal probability of sampling a single sample w_x , we have:

$$\begin{aligned}\widehat{\mathcal{L}}_{\text{gnl}}(Z; G(\mathcal{X}, w)) &= -\frac{1}{\tau} \sum_{x, x' \in \mathcal{X}} w_{xx'} f(x)^\top f(x') + \log \left(\sum_{\substack{x, x' \in \mathcal{X} \\ x \neq x'}} w_x w_{x'} e^{f(x')^\top f(x)/\tau} \right) \\ &= -\frac{1}{\tau} \text{Tr}(Z^\top AZ) + \log \text{Tr} \left((D\mathbf{1}_N \mathbf{1}_N^\top D - D^2) \exp\left(\frac{1}{\tau} ZZ^\top\right) \right).\end{aligned}$$

When τ is large:

$$\begin{aligned}\widehat{\mathcal{L}}_{\text{simclr}}(Z; G(\mathcal{X}, w)) &\approx -\frac{1}{\tau} \text{Tr}(Z^\top AZ) + \log \text{Tr} \left((D\mathbf{1}_N \mathbf{1}_N^\top D - D^2) (\mathbf{1}_N \mathbf{1}_N^\top + \frac{1}{\tau} ZZ^\top) \right) \\ &= -\frac{1}{\tau} \text{Tr}(Z^\top AZ) + \log \left(1 + \frac{\frac{1}{\tau} \text{Tr}(Z^\top (D\mathbf{1}_N \mathbf{1}_N^\top D - D^2) Z)}{\text{Tr}(D)^2 - \text{Tr}(D^2)} \right) + \text{const} \\ &\approx -\frac{1}{\tau} \text{Tr}(Z^\top AZ) + \frac{\frac{1}{\tau} \text{Tr}(Z^\top (D\mathbf{1}_N \mathbf{1}_N^\top D - D^2) Z)}{\text{Tr}(D)^2 - \text{Tr}(D^2)} + \text{const} \\ &= -\frac{1}{\tau} \text{Tr} \left(Z^\top \left(A - \frac{D\mathbf{1}_N \mathbf{1}_N^\top D - D^2}{\text{Tr}(D)^2 - \text{Tr}(D^2)} \right) Z \right) + \text{const}.\end{aligned}$$

If we further consider the constraint that the $Z^\top Z = I$, minimizing $\widehat{\mathcal{L}}_{\text{simclr}}(Z; G(\mathcal{X}, w))$ boils down to the eigenvalue problem such that Z is formed by the top- k eigenvectors of matrix $(A - \frac{D\mathbf{1}_N \mathbf{1}_N^\top D - D^2}{\text{Tr}(D)^2 - \text{Tr}(D^2)})$. Recall that our main analysis for Theorem 7.2 and Theorem 7.3 is based on the insight that the feature space is formed by the top- k eigenvectors of the normalized adjacency matrix $D^{-\frac{1}{2}}AD^{-\frac{1}{2}}$. Viewed in this light, the same analysis could be applied to the SimCLR loss as well, which only differs in the concrete matrix form. We do not include the details in this thesis but leave it as future work.

B.2.5 Additional Experiments Details

B.2.5.1 Experimental Details of Toy Example

Recap of set up. In Section 7.4.1 we consider a toy example that helps illustrate the core idea of our theoretical findings. Specifically, the example aims to cluster 3D objects of different colors and shapes, generated by a 3D rendering software (Johnson et al., 2017) with user-defined properties including colors, shape, size, position, etc. Suppose the training samples come from three shapes, \mathcal{X}_{\square} , \mathcal{X}_{\circ} , \mathcal{X}_{\ominus} . Let \mathcal{X}_{\square} be the sample space with **known** class, and $\mathcal{X}_{\circ}, \mathcal{X}_{\ominus}$ be the sample space with **novel** classes. Further, the two novel classes are constructed to have different relationships with the known class. Specifically, the toy dataset contains elements with 5 unique types:

$$\mathcal{X} = \mathcal{X}_{\square} \cup \mathcal{X}_{\circ} \cup \mathcal{X}_{\ominus},$$

where

$$\mathcal{X}_{\square} = \{x_{\square}, x_{\square}\},$$

$$\mathcal{X}_{\circ} = \{x_{\circ}, x_{\circ}\},$$

$$\mathcal{X}_{\ominus} = \{x_{\ominus}\}.$$

Experimental details for Figure 7.3(b). We rendered 2500 samples for each type of data. In total, we have 12500 samples. For known class \mathcal{X}_{\square} , we randomly select 50% as labeled data and treat the rest as unlabeled. For training, we use the same data augmentation strategy as in SimSiam (Chen and He, 2021). We use ResNet18 and train the model for 40 epochs (sufficient for convergence) with a fixed learning rate of 0.005, using SORL defined in Eq. (7.6). We set $\eta_l = 0.2$ and $\eta_u = 1$, respectively. Our visualization is by PyTorch implementation of UMAP (McInnes et al., 2018), with parameters (n_neighbors=30, min_dist=1.5, spread=2, metric=euclidean).

B.2.5.2 Experimental Details for Benchmarks

Training settings. For a fair comparison, we use ResNet-18 (He et al., 2016a) as the backbone for all methods. Similar to (Cao et al., 2022), we pre-train the backbone using the unsupervised Spectral Contrastive Learning (HaoChen et al., 2021) for 1200 epochs. The configuration for the pre-training stage is consistent with (HaoChen et al., 2021). Note that the pre-training stage does not incorporate any label information. At the training stage, we follow the same practice in (Sun and Li, 2023; Cao et al., 2022), and train our model $f(\cdot)$ by only updating the parameters of the last block of ResNet. In addition, we add a trainable two-layer MLP projection head that projects the feature from the penultimate layer to an embedding space \mathbb{R}^k ($k = 1000$). We use the same data augmentation strategies as SimSiam (Chen and He, 2021; HaoChen et al., 2021). We train for 400 epochs by SORL defined in Eq. (7.6). For CIFAR-10, we set $\eta_l = 0.5, \eta_u = 1$ while for CIFAR-100, we set $\eta_l = 0.15, \eta_u = 3$. We use SGD with momentum 0.9 as an optimizer with cosine annealing ($\text{lr}=0.05$), weight decay $5e-4$, and batch size 512.

Evaluation settings. At the inference stage, we evaluate the performance in a transductive manner (evaluate on \mathcal{D}_u). We run a semi-supervised K-means algorithm as proposed in (Vaze et al., 2022). We follow the evaluation strategy in (Cao et al., 2022) and report the following metrics: (1) classification accuracy on known classes, (2) clustering accuracy on the novel data, and (3) overall accuracy on all classes. The accuracy of the novel classes is measured by solving an optimal assignment problem using the Hungarian algorithm (Kuhn, 1955). When reporting accuracy on all classes, we solve optimal assignments using both known and novel classes.

B.3 OpenCon: Open-world Contrastive Learning

B.3.1 Preliminaries of Contrastive Losses

Recall in the main context of this chapter, we provide a general form of the per-sample contrastive loss:

$$\mathcal{L}_\phi(\mathbf{x}; \tau, \mathcal{P}(\mathbf{x}), \mathcal{N}(\mathbf{x})) = -\frac{1}{|\mathcal{P}(\mathbf{x})|} \sum_{\mathbf{z}^+ \in \mathcal{P}(\mathbf{x})} \log \frac{\exp(\mathbf{z}^+ \cdot \mathbf{z}^+ / \tau)}{\sum_{\mathbf{z}^- \in \mathcal{N}(\mathbf{x})} \exp(\mathbf{z}^+ \cdot \mathbf{z}^- / \tau)},$$

where τ is the temperature parameter, \mathbf{z} is the L_2 normalized embedding of \mathbf{x} , $\mathcal{P}(\mathbf{x})$ is the positive set of embeddings *w.r.t.* \mathbf{z} , and $\mathcal{N}(\mathbf{x})$ is the negative set of embeddings.

In this section, we provide a detailed definition of Supervised Contrastive Loss (SupCon) (Khosla et al., 2020) and Self-supervised Contrastive Loss (SimCLR) (Chen et al., 2020a).

Supervised Contrastive Loss. For a mini-batch \mathcal{B}_l with samples drawn from \mathcal{D}_l , we apply two random augmentations for each sample and generate a multi-viewed batch $\tilde{\mathcal{B}}_l$. We denote the embeddings of the multi-viewed batch as \mathcal{A}_l , where the cardinality $|\mathcal{A}_l| = 2|\mathcal{B}_l|$. For any sample \mathbf{x} in the mini-batch $\tilde{\mathcal{B}}_l$, the positive and negative set of embeddings are as follows:

$$\begin{aligned} \mathcal{P}_l(\mathbf{x}) &= \{\mathbf{z}' \mid \mathbf{z}' \in \{\mathcal{A}_l \setminus \mathbf{z}\}, y' = y\} \\ \mathcal{N}_l(\mathbf{x}) &= \mathcal{A}_l \setminus \mathbf{z}, \end{aligned}$$

where y is the ground-truth label of \mathbf{x} , and y' is the predicted label for the corresponding sample of \mathbf{z}' . Formally, the supervised contrastive loss

is defined as:

$$\mathcal{L}_l = \mathcal{L}_\phi(\mathbf{x}; \tau_l, \mathcal{P}_l(\mathbf{x}), \mathcal{N}_l(\mathbf{x})),$$

where τ_l is the temperature.

Self-Supervised Contrastive Loss. For a mini-batch \mathcal{B}_u with samples drawn from unlabeled dataset \mathcal{D}_u , we apply two random augmentations for each sample and generate a multi-viewed batch $\tilde{\mathcal{B}}_u$. We denote the embeddings of the multi-viewed batch as \mathcal{A}_u , where the cardinality $|\mathcal{A}_u| = 2|\mathcal{B}_u|$. For any sample \mathbf{x} in the mini-batch $\tilde{\mathcal{B}}_u$, the positive and negative set of embeddings is as follows:

$$\begin{aligned} \mathcal{P}_u(\mathbf{x}) &= \{\mathbf{z}' \mid \mathbf{z}' = \phi(\mathbf{x}'), \mathbf{x}' \text{ is augmented from the same sample as } \mathbf{x}\} \\ \mathcal{N}_u(\mathbf{x}) &= \mathcal{A}_u \setminus \mathbf{z} \end{aligned}$$

The self-supervised contrastive loss is then defined as:

$$\mathcal{L}_u = \mathcal{L}_\phi(\mathbf{x}; \tau_u, \mathcal{P}_u(\mathbf{x}), \mathcal{N}_u(\mathbf{x})),$$

where τ_u is the temperature.

B.3.2 Algorithm

Below we summarize the full algorithm of open-world contrastive learning. The notation of $\mathcal{B}_u, \mathcal{B}_l, \mathcal{A}_u, \mathcal{A}_l$ is defined in Appendix B.3.1.

Algorithm 2 Open-world Contrastive Learning

Input: Labeled set $\mathcal{D}_l = \{\mathbf{x}_i, y_i\}_{i=1}^n$ and unlabeled set $\mathcal{D}_u = \{\mathbf{x}_i\}_{i=1}^m$, neural network encoder ϕ , randomly initialized prototypes \mathbf{M} .

Training Stage:

repeat

Data Preparation:

Sample a mini-batch of labeled data $\mathcal{B}_l = \{\mathbf{x}_i, y_i\}_{i=1}^{b_l}$ and unlabeled data $\mathcal{B}_u = \{\mathbf{x}_i\}_{i=1}^{b_u}$

Generate augmented batch and extract normalized embedding set $\mathcal{A}_l, \mathcal{A}_u$

OOD detection:

Calculate OOD detection threshold λ by \mathcal{A}_l

Separate \mathcal{A}_n from \mathcal{A}_u

Positive/Negative Set Selection:

Assign pseudo-labels \hat{y}_i by prototypes for each sample in \mathcal{A}_n

Obtain $\mathcal{P}_n, \mathcal{N}_n$ from \mathcal{A}_n

Back-propagation:

Calculate loss $\mathcal{L}_{\text{OpenCon}}$

Update network ϕ using the gradients.

Prototype Update:

Update prototype vectors with Equation 8.6

until Convergence

B.3.3 Additional Theoretical Details

B.3.3.1 Theoretical Justification of OOD Detection for OpenCon

In this section, we theoretically show that OOD detection helps open-world representation learning by reducing the lower bound of loss $\mathbb{E}_{\mathbf{x} \in \mathcal{D}_n} \mathcal{L}_n(\mathbf{x})$.

We start with the definition of the supervised loss of the Mean Classifier, which provides the lower bound in Lemma B.29.

Definition B.28. (*Mean Classifier*) the mean classifier is a linear layer with weight matrix \mathbf{M}^* whose c -th row is the mean $\tilde{\boldsymbol{\mu}}_c$ of representations of inputs with class c : $\tilde{\boldsymbol{\mu}}_c = \mathbb{E}_{\mathbf{x} \in \mathcal{S}(c)} [\phi(\mathbf{x})]$, where $\mathcal{S}(c)$ defined in Appendix 8.3 is the set of samples with predicted label c . The average supervised loss of its mean classifier is:

$$\mathcal{L}_{sup}^* := - \mathbb{E}_{c^+, c^- \in \mathcal{Y}_{all}^2} \left[\mathbb{E}_{\mathbf{x} \in \mathcal{S}(c^+)} \phi(\mathbf{x}) (\tilde{\boldsymbol{\mu}}_{c^+} - \tilde{\boldsymbol{\mu}}_{c^-}) \mid c^+ \neq c^- \right] \quad (\text{B.32})$$

Lemma B.29. Let $\gamma = p(c^+ = c^-)$, $c^+, c^- \in \mathcal{Y}_{all}^2$, it holds that

$$\mathbb{E}_{\mathbf{x} \in \mathcal{D}_n} \mathcal{L}_n(\mathbf{x}) \geq \frac{1 - \gamma}{\tau} \mathcal{L}_{sup}^*$$

Proof.

$$\begin{aligned}
& \mathbb{E}_{\mathbf{x} \in \mathcal{D}_n} \mathcal{L}_n(\mathbf{x}) \\
&= \mathbb{E}_{\mathbf{x} \in \mathcal{D}_n} \left[-\frac{1}{|\mathcal{P}(\mathbf{x})|} \sum_{\mathbf{z}^+ \in \mathcal{P}(\mathbf{x})} \log \frac{\exp(\mathbf{z}^\top \cdot \mathbf{z}^+ / \tau)}{\sum_{\mathbf{z}^- \in \mathcal{N}(\mathbf{x})} \exp(\mathbf{z} \cdot \mathbf{z}^- / \tau)} \right] \\
&= \mathbb{E}_{\mathbf{x} \in \mathcal{D}_n} \left[-\frac{1}{|\mathcal{P}(\mathbf{x})|} \sum_{\mathbf{z}^+ \in \mathcal{P}(\mathbf{x})} (\mathbf{z}^\top \cdot \mathbf{z}^+ / \tau) + \frac{1}{|\mathcal{P}(\mathbf{x})|} \sum_{\mathbf{z}^+ \in \mathcal{P}(\mathbf{x})} \log \sum_{\mathbf{z}^- \in \mathcal{N}(\mathbf{x})} \exp(\mathbf{z}^\top \cdot \mathbf{z}^- / \tau) \right] \\
&\stackrel{(a)}{\approx} - \mathbb{E}_{c^+ \in \mathcal{Y}_{\text{all}}} \mathbb{E}_{\mathbf{x}, \mathbf{x}^+ \in \mathcal{S}^2(c^+)} \left[\phi(\mathbf{x})^\top \cdot \phi(\mathbf{x}^+) / \tau - \log \mathbb{E}_{c^- \in \mathcal{Y}_{\text{all}}, \mathbf{x} \in \mathcal{S}(c^-)} \exp(\phi(\mathbf{x})^\top \cdot \phi(\mathbf{x}^-) / \tau) \right] \\
&\stackrel{(b)}{\geq} - \mathbb{E}_{c^+ \in \mathcal{Y}_{\text{all}}} \mathbb{E}_{\mathbf{x}, \mathbf{x}^+ \in \mathcal{S}^2(c^+)} \left[\phi(\mathbf{x})^\top \cdot \phi(\mathbf{x}^+) / \tau - \mathbb{E}_{c^- \in \mathcal{Y}_{\text{all}}, \mathbf{x} \in \mathcal{S}(c^-)} \phi(\mathbf{x})^\top \cdot \phi(\mathbf{x}^-) / \tau \right] \\
&= - \mathbb{E}_{c^+, c^- \in \mathcal{Y}_{\text{all}}} \mathbb{E}_{\mathbf{x} \in \mathcal{S}(c^+)} \phi(\mathbf{x}) (\tilde{\boldsymbol{\mu}}_{c^+} - \tilde{\boldsymbol{\mu}}_{c^-}) / \tau \\
&= p(c^+ \neq c^-) \cdot \mathbb{E}_{c^+, c^- \in \mathcal{Y}_{\text{all}}^2} \left[- \mathbb{E}_{\mathbf{x} \in \mathcal{S}(c^+)} \phi(\mathbf{x}) (\tilde{\boldsymbol{\mu}}_{c^+} - \tilde{\boldsymbol{\mu}}_{c^-}) / \tau \mid c^+ \neq c^- \right] + p(c^+ = c^-) \cdot 0 \\
&= \frac{1-\gamma}{\tau} \mathcal{L}_{sup}^*,
\end{aligned}$$

where in (a) we approximate the summation over the positive/negative set by taking the expectation over the positive/negative sample in set $\mathcal{S}(c)$ (defined in Appendix 8.3) and in (b) we apply the Jensen Inequality since the log is a concave function. \square

In the first step, we show in Lemma B.29 that $\mathbb{E}_{\mathbf{x} \in \mathcal{D}_n} \mathcal{L}_n(\mathbf{x})$ is lower-bounded by a constant $\frac{1-\gamma}{\tau}$ times supervised loss \mathcal{L}_{sup}^* defined in Definition B.28. Note that \mathcal{L}_{sup}^* is non-positive and close to -1 in practice. Then the lower bound of $\mathbb{E}_{\mathbf{x} \in \mathcal{D}_n} \mathcal{L}_n(\mathbf{x})$ has a positive correlation with $\gamma = p(c^+ = c^-)$. Note that γ can be reduced by OOD detection. To explain this:

When we separate novelty samples and form \mathcal{D}_n , it has fewer hidden classes than \mathcal{D}_u . With fewer hidden classes, the probability of c^+ being equal to c^- in random sampling is decreased, and thus reduces the lower bound of the $\mathbb{E}_{\mathbf{x} \in \mathcal{D}_n} \mathcal{L}_n(\mathbf{x})$.

In summary, OOD detection facilitates open-world contrastive learning by having fewer candidate classes.

B.3.3.2 Proof Details

Proof of Lemma 8.2.

Proof.

$$\begin{aligned}
\operatorname{argmax}_{\phi, \mathbf{M}} \sum_{i=1}^{|\mathcal{D}_n|} \sum_{c \in \mathcal{Y}_{\text{all}}} q_i(c) \log \frac{p(\mathbf{x}_i, c | \phi, \mathbf{M})}{q_i(c)} &\stackrel{(a)}{=} \operatorname{argmax}_{\phi, \mathbf{M}} \sum_{i=1}^{|\mathcal{D}_n|} \sum_{c \in \mathcal{Y}_{\text{all}}} q_i(c) \log p(\mathbf{x}_i | c, \phi, \mathbf{M}) \\
&\stackrel{(b)}{=} \operatorname{argmax}_{\phi, \mathbf{M}} \sum_{i=1}^{|\mathcal{D}_n|} \sum_{c \in \mathcal{Y}_{\text{all}}} \mathbf{1}\{\hat{y}_i = c\} \log p(\mathbf{x}_i | c, \phi, \mathbf{M}) \\
&\stackrel{(d)}{=} \operatorname{argmax}_{\phi, \mathbf{M}} \sum_{c \in \mathcal{Y}_{\text{all}}} \sum_{\mathbf{x} \in \mathcal{S}(c)} \log p(\mathbf{x} | c, \phi, \mathbf{M}) \\
&\stackrel{(e)}{=} \operatorname{argmax}_{\phi, \mathbf{M}} \sum_{c \in \mathcal{Y}_{\text{all}}} \sum_{\mathbf{x} \in \mathcal{S}(c)} \phi(\mathbf{x})^\top \cdot \boldsymbol{\mu}_c,
\end{aligned}$$

where equation (a) is given by removing the constant term $q_i(c) \log \frac{p(c)}{q_i(c)}$ in argmax , (b) is by plugging $q_i(c)$, (d) is by reorganizing the index, and (e) is by plugging the vMF density function and removing the constant. \square

Proof of Lemma 8.3.

Proof.

$$\begin{aligned}
\operatorname{argmin}_{\phi} \sum_{\mathbf{x} \in \mathcal{D}_n} \mathcal{L}_a(\mathbf{x}) &= \operatorname{argmin}_{\phi} - \sum_{\mathbf{x} \in \mathcal{D}_n} \frac{1}{|\mathcal{P}(\mathbf{x})|} \sum_{\mathbf{z}^+ \in \mathcal{P}(\mathbf{x})} \phi(\mathbf{x})^\top \cdot \mathbf{z}^+ \\
&= \operatorname{argmin}_{\phi} - \sum_{c \in \mathcal{Y}_{\text{all}}} \sum_{\mathbf{x} \in \mathcal{S}(c)} \frac{1}{|\mathcal{S}_c| - 1} \sum_{\mathbf{x}^+ \in \mathcal{S}(c) \setminus \mathbf{x}} \phi(\mathbf{x})^\top \cdot \phi(\mathbf{x}^+) \\
&= \operatorname{argmin}_{\phi} - \sum_{c \in \mathcal{Y}_{\text{all}}} \sum_{\mathbf{x} \in \mathcal{S}(c)} \frac{1}{|\mathcal{S}_c| - 1} \left(\left(\sum_{\mathbf{x}^+ \in \mathcal{S}(c)} \phi(\mathbf{x})^\top \cdot \phi(\mathbf{x}^+) \right) - 1 \right) \\
&\stackrel{(a)}{=} \operatorname{argmin}_{\phi} - \sum_{c \in \mathcal{Y}_{\text{all}}} \sum_{\mathbf{x} \in \mathcal{S}(c)} \eta_{\mathcal{S}_c} \phi(\mathbf{x})^\top \cdot \boldsymbol{\mu}_c^* \\
&\stackrel{(b)}{\approx} \operatorname{argmax}_{\phi} \sum_{c \in \mathcal{Y}_{\text{all}}} \sum_{\mathbf{x} \in \mathcal{S}(c)} \phi(\mathbf{x})^\top \cdot \boldsymbol{\mu}_c^*,
\end{aligned}$$

where in (a) $\eta_{\mathcal{S}_c} = \frac{|\mathcal{S}_c|}{|\mathcal{S}_c| - 1} \|\mathbb{E}_{\mathbf{x} \in \mathcal{S}(c)}[\phi(\mathbf{x})]\|_2$ is a constant value close to 1, and in (b) we show the approximation to the optimization target in Equation 8.8 with the fixed prototypes. The proof is done by using the equation in Lemma 8.2. \square

B.3.4 Additional Experiments

B.3.4.1 Discussion on Using Samples in $\mathcal{D}_u \setminus \mathcal{D}_n$

We discussed in Section 8.2.2 that samples from $\mathcal{D}_u \setminus \mathcal{D}_n$ contain indistinguishable data from known and novel classes. In this section, we show that using these samples for prototype-based learning may be undesirable.

We first show that the overlapping between the novel and known classes in $\mathcal{D}_u \setminus \mathcal{D}_n$ can be non-trivial. In Figure B.3, we show the distribution plot of the scores $\max_{j \in \mathcal{Y}_i} \boldsymbol{\mu}_j^\top \cdot \phi(\mathbf{x}_i)$. It is notable that there exists a large overlapping area when $\max_{j \in \mathcal{Y}_i} \boldsymbol{\mu}_j^\top \cdot \phi(\mathbf{x}_i) > \lambda$. For visualization clarity, we color the known classes in blue and the novel classes in gray.

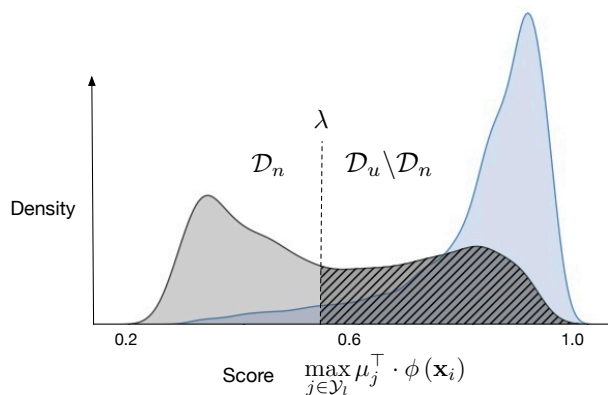


Figure B.3: Distribution of OOD score $\max_{j \in \mathcal{Y}_l} \boldsymbol{\mu}_j^\top \cdot \phi(\mathbf{x}_i)$ for unlabeled data \mathcal{D}_u on CIFAR-100. For visual clarity, gray indicates samples from novel classes and blue indicates samples from known classes. The shaded area highlights samples from novel classes but misidentified as known classes.

We next show that using this part of data will be harmful to representation learning. Specifically, we replace \mathcal{L}_l to be the following loss:

$$\mathcal{L}_{known} = \sum_{\mathbf{x} \in \tilde{\mathcal{B}}_k} \mathcal{L}_\phi(\mathbf{x}; \tau_k, \mathcal{P}_k(\mathbf{x}), \mathcal{N}_k(\mathbf{x})),$$

where we define \mathcal{B}_k to be a minibatch with samples drawn from $\mathcal{D}_l \cup (\mathcal{D}_u \setminus \mathcal{D}_n)$ —labeled data with known classes, along with the unlabeled data *predicted as known classes*. And we apply two random augmentations for each sample and generate a multi-viewed batch $\tilde{\mathcal{B}}_k$. We denote the embeddings of the multi-viewed batch as \mathcal{A}_k . The positive set of embeddings is as follows:

$$\begin{aligned} \mathcal{P}_k(\mathbf{x}) &= \{\mathbf{z}' \mid \mathbf{z}' \in \{\mathcal{A}_k \setminus \mathbf{z}\}, \tilde{y}' = \tilde{y}\} \\ \mathcal{N}_k(\mathbf{x}) &= \mathcal{A}_k \setminus \mathbf{z}, \end{aligned}$$

where

$$\tilde{y}_i = \begin{cases} \hat{y}_i \text{ (pseudo-label)} & \text{if } \mathbf{x}_i \in \mathcal{D}_u \\ y_i \text{ (ground-truth label),} & \text{if } \mathbf{x}_i \in \mathcal{D}_l \end{cases}$$

Intuitively, \mathcal{L}_{known} is an extension of \mathcal{L}_l , where we utilize both labeled and unlabeled data from known classes for representation learning. The final loss now becomes:

$$\mathcal{L}_{\text{Modified}} = \lambda_n \mathcal{L}_n + \lambda_k \mathcal{L}_{\text{known}} + \lambda_u \mathcal{L}_u, \quad (\text{B.33})$$

We show results in Table B.1. Compared to the original loss, the seen accuracy drops by 6.6%. This finding suggests that using $\mathcal{D}_u \setminus \mathcal{D}_n$ for prototype-based learning is suboptimal.

Table B.1: Comparison with loss $\mathcal{L}_{\text{Modified}}$ on CIFAR-100.

Method	CIFAR-100		
	All	Novel	Seen
$\mathcal{L}_{\text{Modified}}$	47.7	46.4	62.4
$\mathcal{L}_{\text{OpenCon}}$	53.7	48.7	69.0

B.3.4.2 Results on CIFAR-10

We show results for CIFAR-10 in Table B.2, where OpenCon consistently outperforms strong baselines, particularly ORCA and GCD. Classes are divided into 50% known and 50% novel classes. We then select 50% of known classes as the labeled dataset and the rest as the unlabeled set. The division is consistent with (Cao et al., 2022), which allows us to compare the performance in a fair setting.

Table B.2: Results on CIFAR-10. Asterisk (*) denotes that the original method can not recognize seen classes. Dagger (†) denotes the original method can not detect novel classes (and we had to extend it). Results on GCD, ORCA, and OpenCon (mean and standard deviation) are averaged over five different runs. The ORCA results are reported by running the official repo (Cao, 2022).

Method	CIFAR-10		
	All	Novel	Seen
†FixMatch (Kurakin et al., 2020)	49.5	50.4	71.5
†DS ³ L (Guo et al., 2020)	40.2	45.3	77.6
†CGDL (Sun et al., 2020a)	39.7	44.6	72.3
*DTC (Han et al., 2019)	38.3	39.5	53.9
*RankStats (Zhao and Han, 2021)	82.9	81.0	86.6
*SimCLR (Chen et al., 2020a)	51.7	63.4	58.3
ORCA (Cao et al., 2022)	88.3 \pm 0.3	87.5 \pm 0.2	89.9 \pm 0.4
GCD (Vaze et al., 2022)	87.5 \pm 0.5	86.7 \pm 0.4	90.1 \pm 0.3
OpenCon (Ours)	90.4 \pm 0.6	91.1 \pm 0.1	89.3 \pm 0.2

B.3.4.3 More Qualitative Comparisons of Embeddings

In Figure B.4, we visualize the feature embeddings for a subset of 20 classes using UMAP (McInnes et al., 2018). This covers more classes than what has been shown in the main context of the chapter (Figure 8.2). The model is trained on ImageNet-100. OpenCon produces a more compact and distinguishable embedding space than GCD and ORCA.

B.3.4.4 Hyperparameters and Sensitivity Analysis

In this section, we introduce the hyper-parameter settings for OpenCon. We also show a validation strategy to determine important hyper-parameters (weight and temperature) in loss $\mathcal{L}_{OpenCon}$ and conduct a sensitivity analysis to show that the validation strategy can select near-optimal hyper-

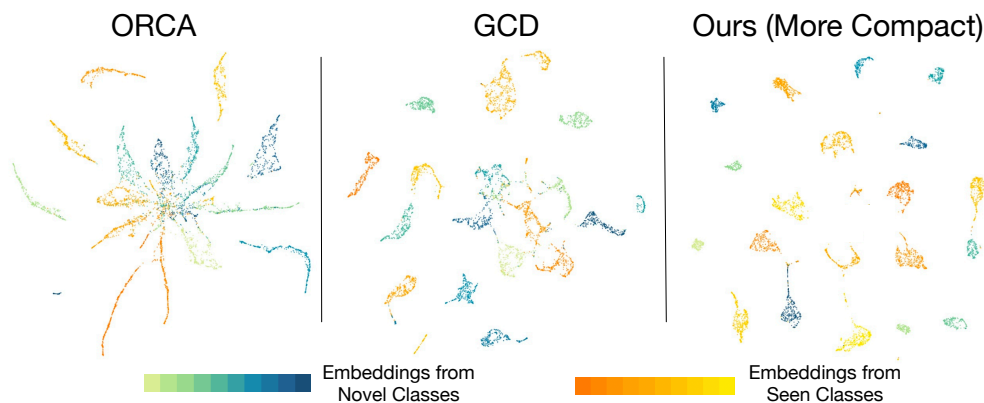


Figure B.4: UMAP (McInnes et al., 2018) visualization of the feature embedding from 20 classes (10 for seen, 10 for novel). The model is trained on ImageNet-100 with ORCA (Cao et al., 2022), GCD (Vaze et al., 2022), and OpenCon (ours).

parameters. We start by introducing the basic training setting.

For CIFAR-100/ImageNet-100, the model is trained for 200/120 epochs with batch-size 512 using stochastic gradient descent with momentum 0.9, and weight decay 10^{-4} . The learning rate starts at 0.02 and decays by a factor of 10 at the 50% and the 75% training stage. The momentum for prototype updating γ is fixed at 0.9. The percentile p for OOD detection is 70%. We fix the weight for the KL-divergence regularizer to be 0.05.

Since the label for \mathcal{D}_u is not available, we propose a validation strategy by using labeled data \mathcal{D}_l . Specifically, we split the classes in \mathcal{Y}_l equally into two parts: known classes and “novel” classes (for which we know the labels). Moreover, 50% samples of the selected known classes are labeled. We further use the new validation dataset to select the best hyper-parameters by grid searching. The selected hyper-parameter groups are summarized in Table B.3. Note that the only difference between CIFAR-100 and ImageNet-100 settings is the temperature of the self-supervised loss \mathcal{L}_u .

We show the sensitivity of hyper-parameters in Figure B.5. The per-

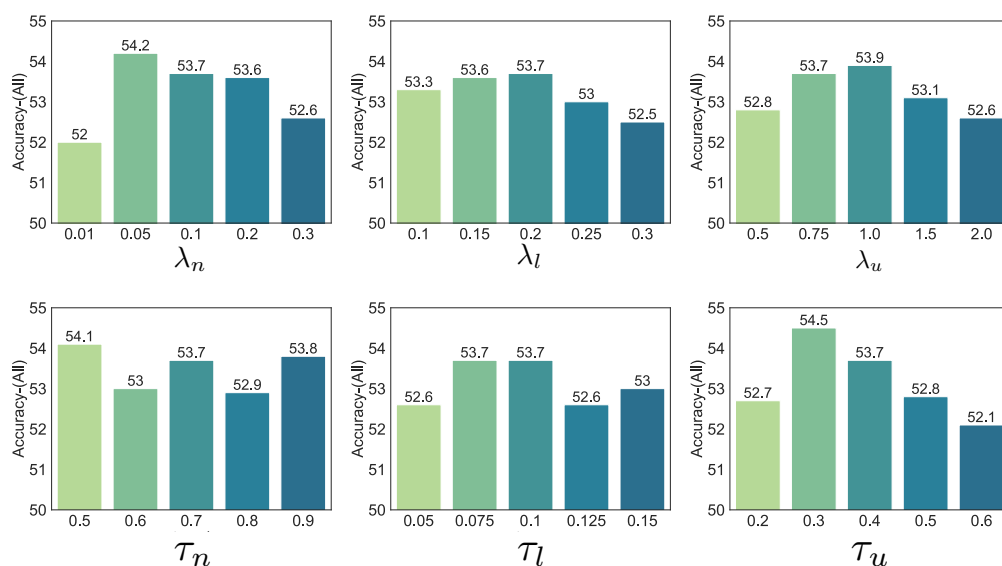


Figure B.5: Sensitivity analysis of hyper-parameters on CIFAR-100. The overall accuracy is reported on three (weight, temperature) pairs: (λ_n, τ_n) for loss \mathcal{L}_n , (λ_l, τ_l) for loss \mathcal{L}_l , and the (λ_u, τ_u) for loss \mathcal{L}_u . The middle bar in each plot corresponds to the hyperparameter value used in our main experiments.

formance comparison in the bar plot for each hyper-parameter is reported by fixing other hyper-parameters. We see that our validation strategy successfully selects λ_l , λ_u , and τ_l with the optimal one, and the other three λ_n , τ_u and τ_n are close to the optimal (with $<1\%$ gap in overall accuracy).

Table B.3: Hyperparameters in OpenCon.

	λ_n	τ_n	λ_l	τ_l	λ_u	τ_u
ImageNet-100	0.1	0.7	0.2	0.1	1	0.6
CIFAR-100	0.1	0.7	0.2	0.1	1	0.4

B.3.4.5 OOD Detection Comparison

We compare different OOD detection methods in Table B.4. Results show that several popular OOD detection methods produce similar OOD detection performance. Note that Mahalanobis (Lee et al., 2018) require heavier computation which causes an unbearable burden in the training stage. Our method incurs minimal computational overhead.

Table B.4: Comparison of OOD detection performance with popular methods. Results are reported on CIFAR-100. Samples from 50 known classes are treated as in-distribution (ID) data and samples from the remaining 50 classes are used as out-of-distribution (OOD) data. The OOD detection threshold is estimated on the labeled known classes \mathcal{D}_l .

Method	FPR95	AUROC
MSP (Hendrycks and Gimpel, 2017)	58.9	86.0
Energy (Liu et al., 2020)	57.1	87.4
Mahalanobis (Lee et al., 2018)	54.6	88.7
Ours	57.1	87.4

references

Alexandari, Amr, Anshul Kundaje, and Avanti Shrikumar. 2020. Maximum likelihood with bias-corrected calibration is hard-to-beat at label shift adaptation. In *International conference on machine learning*, 222–232. PMLR.

Argyriou, Andreas, Mark Herbster, and Massimiliano Pontil. 2005. Combining graph laplacians for semi-supervised learning. *Advances in Neural Information Processing Systems* 18.

Arora, Sanjeev, Hrishikesh Khandeparkar, Mikhail Khodak, Orestis Plevrakis, and Nikunj Saunshi. 2019. A theoretical analysis of contrastive unsupervised representation learning. *International Conference on Machine Learning*.

Azizzadenesheli, Kamyar, Anqi Liu, Fanny Yang, and Animashree Anandkumar. 2019. Regularized learning for domain adaptation under label shifts. In *International conference on learning representations*.

Ba, Jimmy, and Brendan Frey. 2013. Adaptive dropout for training deep neural networks. In *Advances in neural information processing systems*, vol. 26.

Babaeizadeh, Mohammad, Paris Smaragdis, and Roy H. Campbell. 2016. Noiseout: A simple way to prune neural networks. *arXiv preprint arxiv:1611.06211*.

- Bai, Haoyue, Gregory Canal, Xuefeng Du, Jeongyeol Kwon, Robert D Nowak, and Yixuan Li. 2023. Feed two birds with one scone: Exploiting wild data for both out-of-distribution generalization and detection. In *International conference on machine learning*, 1454–1471. PMLR.
- Balcan, Maria-Florina, and Avrim Blum. 2005. A pac-style model for learning from labeled and unlabeled data. In *Colt*, 111–126. Springer.
- Balestrieri, Randall, and Yann LeCun. 2022. Contrastive and non-contrastive self-supervised learning recover global and local spectral embedding methods. *Advances in Neural Information Processing Systems*.
- Bardes, Adrien, Jean Ponce, and Yann Lecun. 2022. Vicreg: Variance-invariance-covariance regularization for self-supervised learning. In *Iclr 2022-10th international conference on learning representations*.
- Bendale, Abhijit, and Terrance Boult. 2015. Towards open world recognition. In *Proceedings of the ieee conference on computer vision and pattern recognition*, 1893–1902.
- Bergman, Liron, Niv Cohen, and Yedid Hoshen. 2020. Deep nearest neighbor anomaly detection. *Proceedings of the IEEE Conference on Computer Vision and Pattern Recognition*.
- Bevandić, Petra, Ivan Krešo, Marin Oršić, and Siniša Šegvić. 2018. Discriminative out-of-distribution detection for semantic segmentation. *arXiv preprint arXiv:1808.07703*.
- Bigcommerce. 2023. Ecommerce machine learning brings the future to the present of online shopping. <https://www.bigcommerce.com/articles/ecommerce/machine-learning/>.
- Blum, A. 2001. Learning from labeled and unlabeled data using graph mincuts. In *18th international conference on machine learning*.

Boulkenafet, Zinelabidine, Jukka Komulainen, and Abdenour Hadid. 2015. Face anti-spoofing based on color texture analysis. In *2015 IEEE International Conference on Image Processing (ICIP)*, 2636–2640. IEEE.

Breunig, Markus M, Hans-Peter Kriegel, Raymond T Ng, and Jörg Sander. 2000. Lof: identifying density-based local outliers. In *Proceedings of the 2000 ACM SIGMOD International Conference on Management of Data*, 93–104.

Cao, Kaidi. 2022. Open-world semi-supervised learning. <https://github.com/snap-stanford/orca>.

Cao, Kaidi, Maria Brbic, and Jure Leskovec. 2022. Open-world semi-supervised learning. In *Proceedings of the International Conference on Learning Representations*.

Caron, Mathilde, Ishan Misra, Julien Mairal, Priya Goyal, Piotr Bojanowski, and Armand Joulin. 2020. Unsupervised learning of visual features by contrasting cluster assignments. *Proceedings of Advances in Neural Information Processing Systems*.

Caron, Mathilde, Hugo Touvron, Ishan Misra, Hervé Jégou, Julien Mairal, Piotr Bojanowski, and Armand Joulin. 2021. Emerging properties in self-supervised vision transformers. In *Proceedings of the International Conference on Computer Vision (ICCV)*.

Cha, Hyuntak, Jaeho Lee, and Jinwoo Shin. 2021. Co2l: Contrastive continual learning. In *Proceedings of the IEEE/CVF International Conference on Computer Vision*, 9516–9525.

Chapelle, Olivier, Bernhard Schölkopf, and Alexander Zien, eds. 2006. *Semi-supervised learning*. The MIT Press.

Cheeger, Jeff. 2015. A lower bound for the smallest eigenvalue of the laplacian. In *Problems in analysis*, 195–200. Princeton University Press.

Chen, Jiefeng, Yixuan Li, Xi Wu, Yingyu Liang, and Somesh Jha. 2021. Atom: Robustifying out-of-distribution detection using outlier mining. *Proceedings of European Conference on Machine Learning and Principles and Practice of Knowledge Discovery in Databases*.

Chen, Liang-Chieh, George Papandreou, Iasonas Kokkinos, Kevin Murphy, and Alan L Yuille. 2017. Deeplab: Semantic image segmentation with deep convolutional nets, atrous convolution, and fully connected crfs. *IEEE Transactions on Pattern Analysis and Machine Intelligence* 40(4): 834–848.

Chen, Ting, Simon Kornblith, Mohammad Norouzi, and Geoffrey Hinton. 2020a. A simple framework for contrastive learning of visual representations. In *Proceedings of the international conference on machine learning*, 1597–1607. PMLR.

Chen, Ting, Simon Kornblith, Kevin Swersky, Mohammad Norouzi, and Geoffrey E Hinton. 2020b. Big self-supervised models are strong semi-supervised learners. *Proceedings of Advances in Neural Information Processing Systems* 33:22243–22255.

Chen, Xinlei, and Kaiming He. 2021. Exploring simple siamese representation learning. In *Proceedings of the IEEE/CVF conference on computer vision and pattern recognition*, 15750–15758.

Chen, Yanbei, Xiatian Zhu, Wei Li, and Shaogang Gong. 2020c. Semi-supervised learning under class distribution mismatch. In *Proceedings of the AAAI conference on artificial intelligence*, 3569–3576.

Chi, Haoang, Feng Liu, Wenjing Yang, Long Lan, Tongliang Liu, Bo Han, Gang Niu, Mingyuan Zhou, and Masashi Sugiyama. 2021. Meta discovery: Learning to discover novel classes given very limited data. In *International conference on learning representations*.

Chung, Fan RK. 1997. *Spectral graph theory*, vol. 92. American Mathematical Soc.

Cimpoi, Mircea, Subhansu Maji, Iasonas Kokkinos, Sammy Mohamed, and Andrea Vedaldi. 2014. Describing textures in the wild. In *Proceedings of the IEEE conference on computer vision and pattern recognition*, 3606–3613.

Cui, Jiequan, Zhisheng Zhong, Shu Liu, Bei Yu, and Jiaya Jia. 2021. Parametric contrastive learning. In *Proceedings of the IEEE/CVF international conference on computer vision*, 715–724.

Dang, Taurus T, Henry YT Ngan, and Wei Liu. 2015. Distance-based k-nearest neighbors outlier detection method in large-scale traffic data. In *2015 IEEE international conference on digital signal processing (DSP)*, 507–510. IEEE.

Deng, Jia, Wei Dong, Richard Socher, Li-Jia Li, Kai Li, and Li Fei-Fei. 2009. Imagenet: A large-scale hierarchical image database. In *IEEE conference on computer vision and pattern recognition*, 248–255.

Dosovitskiy, Alexey, Lucas Beyer, Alexander Kolesnikov, Dirk Weissenborn, Xiaohua Zhai, Thomas Unterthiner, Mostafa Dehghani, Matthias Minderer, Georg Heigold, Sylvain Gelly, Jakob Uszkoreit, and Neil Houlsby. 2021. An image is worth 16x16 words: Transformers for image recognition at scale. In *Proceedings of the international conference on learning representations*.

Dosovitskiy, Alexey, Lucas Beyer, Alexander Kolesnikov, Dirk Weissenborn, Xiaohua Zhai, Thomas Unterthiner, Mostafa Dehghani, Matthias Minderer, Georg Heigold, Sylvain Gelly, et al. 2020. An image is worth 16x16 words: Transformers for image recognition at scale. In *International conference on learning representations*.

- Du, Xuefeng, Gabriel Gozum, Yifei Ming, and Yixuan Li. 2022a. Siren: Shaping representations for detecting out-of-distribution objects. *Advances in Neural Information Processing Systems* 35:20434–20449.
- Du, Xuefeng, Xin Wang, Gabriel Gozum, and Yixuan Li. 2022b. Unknown-aware object detection: Learning what you don't know from videos in the wild. In *Proceedings of the IEEE/CVF conference on computer vision and pattern recognition*.
- Du, Xuefeng, Zhaoning Wang, Mu Cai, and Sharon Li. 2022c. Towards unknown-aware learning with virtual outlier synthesis. In *Proceedings of the international conference on learning representations*.
- Dwibedi, Debidatta, Yusuf Aytar, Jonathan Tompson, Pierre Sermanet, and Andrew Zisserman. 2021. With a little help from my friends: Nearest-neighbor contrastive learning of visual representations. In *Proceedings of the IEEE/CVF international conference on computer vision*, 9588–9597.
- Eckart, Carl, and Gale Young. 1936. The approximation of one matrix by another of lower rank. *Psychometrika* 1(3):211–218.
- Fang, Zhen, Yixuan Li, Jie Lu, Jiahua Dong, Bo Han, and Feng Liu. 2022. Is out-of-distribution detection learnable? *Advances in Neural Information Processing Systems* 35:37199–37213.
- Fergus, Rob, Yair Weiss, and Antonio Torralba. 2009. Semi-supervised learning in gigantic image collections. *Advances in neural information processing systems* 22.
- Filos, Angelos, Panagiotis Tigkas, Rowan McAllister, Nicholas Rhinehart, Sergey Levine, and Yarin Gal. 2020. Can autonomous vehicles identify, recover from, and adapt to distribution shifts? In *International conference on machine learning*, 3145–3153. PMLR.

Fini, Enrico, Enver Sangineto, Stéphane Lathuilière, Zhun Zhong, Moin Nabi, and Elisa Ricci. 2021. A unified objective for novel class discovery. In *Proceedings of the IEEE/CVF International Conference on Computer Vision*, 9284–9292.

Fisher, Ronald Aylmer. 1953. Dispersion on a sphere. *Proceedings of the Royal Society of London. Series A. Mathematical and Physical Sciences* 217(1130):295–305.

Gao, Yizhao, Nanyi Fei, Guangzhen Liu, Zhiwu Lu, and Tao Xiang. 2021. Contrastive prototype learning with augmented embeddings for few-shot learning. In *Proceedings of the thirty-seventh conference on uncertainty in artificial intelligence*, 140–150.

Geifman, Yonatan, and Ran El-Yaniv. 2019. Selectivenet: A deep neural network with an integrated reject option. *arXiv preprint arXiv:1901.09192*.

Girshick, Ross. 2015. Fast r-cnn. In *Proceedings of the IEEE International Conference on Computer Vision*, 1440–1448.

Gomez, Aidan N., Ivan Zhang, Kevin Swersky, Yarin Gal, and Geoffrey E. Hinton. 2019. Learning sparse networks using targeted dropout. *arXiv preprint arXiv:1905.13678*.

Goyal, Priya, Mathilde Caron, Benjamin Lefaudeaux, Min Xu, Pengchao Wang, Vivek Pai, Mannat Singh, Vitaliy Liptchinsky, Ishan Misra, Armand Joulin, et al. 2021. Self-supervised pretraining of visual features in the wild. *arXiv preprint arXiv:2103.01988*.

Greenbaum, Anne, Ren-cang Li, and Michael L Overton. 2020. First-order perturbation theory for eigenvalues and eigenvectors. *SIAM review* 62(2):463–482.

Gu, Xiaoyi, Leman Akoglu, and Alessandro Rinaldo. 2019. Statistical analysis of nearest neighbor methods for anomaly detection. In *Proceedings of the advances in neural information processing systems*, vol. 32.

Guo, Lan-Zhe, Zhen-Yu Zhang, Yuan Jiang, Yu-Feng Li, and Zhi-Hua Zhou. 2020. Safe deep semi-supervised learning for unseen-class unlabeled data. In *Proceedings of the international conference on machine learning*, vol. 119 of *Proceedings of Machine Learning Research*, 3897–3906. PMLR.

Han, K, SA Rebuffi, S Ehrhardt, A Vedaldi, and A Zisserman. 2020a. Automatically discovering and learning new visual categories with ranking statistics. In *Proceedings of the 8th international conference on learning representations*. Schloss Dagstuhl-Leibniz-Zentrum für Informatik.

Han, Kai, Sylvestre-Alvise Rebuffi, Sebastien Ehrhardt, Andrea Vedaldi, and Andrew Zisserman. 2020b. Automatically discovering and learning new visual categories with ranking statistics. *International Conference on Learning Representations*.

Han, Kai, Andrea Vedaldi, and Andrew Zisserman. 2019. Learning to discover novel visual categories via deep transfer clustering. In *Proceedings of the IEEE/CVF International Conference on Computer Vision*.

Han, Song, Huizi Mao, and William J. Dally. 2016. Deep compression: Compressing deep neural network with pruning, trained quantization and Huffman coding. In *4th international conference on learning representations, ICLR*.

Han, Song, Jeff Pool, John Tran, and William Dally. 2015. Learning both weights and connections for efficient neural network. In *Advances in neural information processing systems*, vol. 28, 1135–1143.

HaoChen, Jeff Z, Colin Wei, Adrien Gaidon, and Tengyu Ma. 2021. Provable guarantees for self-supervised deep learning with spectral con-

trastive loss. *Advances in Neural Information Processing Systems* 34:5000–5011.

HaoChen, Jeff Z, Colin Wei, Ananya Kumar, and Tengyu Ma. 2022. Beyond separability: Analyzing the linear transferability of contrastive representations to related subpopulations. *Advances in neural information processing systems*.

He, Kaiming, Haoqi Fan, Yuxin Wu, Saining Xie, and Ross Girshick. 2020. Momentum contrast for unsupervised visual representation learning. In *Proceedings of the IEEE conference on computer vision and pattern recognition*, 9729–9738.

He, Kaiming, Xiangyu Zhang, Shaoqing Ren, and Jian Sun. 2016a. Deep residual learning for image recognition. In *Proceedings of the IEEE conference on computer vision and pattern recognition*, 770–778.

———. 2016b. Identity mappings in deep residual networks. In *European conference on computer vision*, 630–645. Springer.

Hein, Matthias, Maksym Andriushchenko, and Julian Bitterwolf. 2019. Why relu networks yield high-confidence predictions far away from the training data and how to mitigate the problem. In *Proceedings of the IEEE conference on computer vision and pattern recognition*, 41–50.

Hendrycks, Dan, and Thomas Dietterich. 2019. Benchmarking neural network robustness to common corruptions and perturbations. *arXiv preprint arXiv:1903.12261*.

Hendrycks, Dan, and Kevin Gimpel. 2017. A baseline for detecting misclassified and out-of-distribution examples in neural networks. *Proceedings of International Conference on Learning Representations*.

- Hendrycks, Dan, Mantas Mazeika, and Thomas Dietterich. 2018. Deep anomaly detection with outlier exposure. *arXiv preprint arXiv:1812.04606*.
- Henze, N, and B Zirkler. 1990. A class of invariant consistent tests for multivariate normality. *Communications in statistics-Theory and Methods* 19(10):3595–3617.
- Holland, Paul W, Kathryn Blackmond Laskey, and Samuel Leinhardt. 1983. Stochastic blockmodels: First steps. *Social networks* 5(2):109–137.
- Horn, Grant, Oisín Aodha, Yang Song, Yin Cui, Chen Sun, Alex Shepard, Hartwig Adam, Pietro Perona, and Serge Belongie. 2018. The inaturalist species classification and detection dataset.
- Hsu, Yen-Chang, Zhaoyang Lv, and Zsolt Kira. 2018. Learning to cluster in order to transfer across domains and tasks. *Proceedings of the International Conference on Learning Representations*.
- Hsu, Yen-Chang, Zhaoyang Lv, Joel Schlosser, Phillip Odom, and Zsolt Kira. 2019. Multi-class classification without multi-class labels. *Proceedings of the International Conference on Learning Representations*.
- Hsu, Yen-Chang, Yilin Shen, Hongxia Jin, and Zsolt Kira. 2020. Generalized odin: Detecting out-of-distribution image without learning from out-of-distribution data. In *Proceedings of the IEEE/CVF conference on computer vision and pattern recognition*.
- Huang, Gao, Zhuang Liu, Laurens Van Der Maaten, and Kilian Q Weinberger. 2017. Densely connected convolutional networks. In *Proceedings of the IEEE conference on computer vision and pattern recognition*, 4700–4708.
- Huang, Junkai, Chaowei Fang, Weikai Chen, Zhenhua Chai, Xiaolin Wei, Pengxu Wei, Liang Lin, and Guanbin Li. 2021a. Trash to trea-

sure: Harvesting ood data with cross-modal matching for open-set semi-supervised learning. In *Proceedings of the IEEE/CVF International Conference on Computer Vision*, 8310–8319.

Huang, Rui, Andrew Geng, and Yixuan Li. 2021b. On the importance of gradients for detecting distributional shifts in the wild. In *Advances in Neural Information Processing Systems*.

Huang, Rui, and Yixuan Li. 2021. Mos: Towards scaling out-of-distribution detection for large semantic space. In *Proceedings of the IEEE/CVF Conference on Computer Vision and Pattern Recognition (CVPR)*, 8710–8719.

Huber, Peter J. 1964. Robust estimation of a location parameter. *Annals of Mathematical Statistics* 35:73–101.

Ioffe, Sergey, and Christian Szegedy. 2015. Batch normalization: Accelerating deep network training by reducing internal covariate shift. In *Proceedings of the 32nd International Conference on Machine Learning*, ed. Francis Bach and David Blei, vol. 37 of *Proceedings of Machine Learning Research*, 448–456. Lille, France: PMLR.

Jebara, Tony, Jun Wang, and Shih-Fu Chang. 2009. Graph construction and b-matching for semi-supervised learning. In *Proceedings of the 26th Annual International Conference on Machine Learning*, 441–448.

Jeong, Taewon, and Heeyoung Kim. 2020. Ood-maml: Meta-learning for few-shot out-of-distribution detection and classification. *Proceedings of the Advances in Neural Information Processing Systems* 33:3907–3916.

Jia, Xuhui, Kai Han, Yukun Zhu, and Bradley Green. 2021. Joint representation learning and novel category discovery on single- and multi-modal data. In *Proceedings of the IEEE/CVF International Conference on Computer Vision*, 610–619.

- Jiang, Ziyu, Tianlong Chen, Ting Chen, and Zhangyang Wang. 2021. Improving contrastive learning on imbalanced data via open-world sampling. *Proceedings of Advances in Neural Information Processing Systems* 34.
- Jing, Tian, Azarian Michael, and Michael Pech. 2014. Anomaly detection using self-organizing maps-based k-nearest neighbor algorithm. In *Phm society european conference*, 2(1).
- Johnson, Jeff, Matthijs Douze, and Hervé Jégou. 2019. Billion-scale similarity search with gpus. *IEEE Transactions on Big Data* 7(3):535–547.
- Johnson, Justin, Bharath Hariharan, Laurens van der Maaten, Li Fei-Fei, C Lawrence Zitnick, and Ross Girshick. 2017. Clevr: A diagnostic dataset for compositional language and elementary visual reasoning. In *Cvpr*.
- Joseph, Antony, and Bin Yu. 2016. Impact of regularization on spectral clustering. *The Annals of Statistics* 44(4):1765–1791.
- Kahou, Samira Ebrahimi, Xavier Bouthillier, Pascal Lamblin, Caglar Gulcehre, Vincent Michalski, Kishore Konda, Sébastien Jean, Pierre Froumenty, Yann Dauphin, Nicolas Boulanger-Lewandowski, et al. 2016. Emonets: Multimodal deep learning approaches for emotion recognition in video. *Journal on Multimodal User Interfaces* 10:99–111.
- Kannan, Ravi, Santosh Vempala, and Adrian Vetta. 2004. On clusterings: Good, bad and spectral. *Journal of the ACM (JACM)* 51(3):497–515.
- Karim, Nazmul, Mamshad Nayeem Rizve, Nazanin Rahnavard, Ajmal Mian, and Mubarak Shah. 2022. Unicon: Combating label noise through uniform selection and contrastive learning. In *Proceedings of the IEEE conference on computer vision and pattern recognition*.
- Katz-Samuels, Julian, Julia Nakhleh, Robert Nowak, and Yixuan Li. 2022. Training ood detectors in their natural habitats. In *International conference on machine learning (icml)*. PMLR.

Khosla, Prannay, Piotr Teterwak, Chen Wang, Aaron Sarna, Yonglong Tian, Phillip Isola, Aaron Maschinot, Ce Liu, and Dilip Krishnan. 2020. Supervised contrastive learning. *Proceedings of Advances in Neural Information Processing Systems* 33:18661–18673.

Koh, Pang Wei, Shiori Sagawa, Sang Michael Xie, Marvin Zhang, Akshay Balsubramani, Weihua Hu, Michihiro Yasunaga, Richard Lanus Phillips, Irena Gao, Tony Lee, et al. 2021. Wilds: A benchmark of in-the-wild distribution shifts. In *International conference on machine learning*, 5637–5664. PMLR.

Krizhevsky, Alex. 2010. Convolutional deep belief networks on cifar-10.

Krizhevsky, Alex, Geoffrey Hinton, et al. 2009. Learning multiple layers of features from tiny images.

Kuhn, H. W., and Bryn Yaw. 1955. The hungarian method for the assignment problem. *Naval Res. Logist. Quart* 83–97.

Kuhn, Harold W. 1955. The hungarian method for the assignment problem. *Naval research logistics quarterly* 2(1-2):83–97.

Kurakin, Alex, Chun-Liang Li, Colin Raffel, David Berthelot, Ekin Dogus Cubuk, Han Zhang, Kihyuk Sohn, Nicholas Carlini, and Zizhao Zhang. 2020. Fixmatch: Simplifying semi-supervised learning with consistency and confidence. In *Proceedings of advances in neural information processing systems*.

Laine, Samuli, and Timo Aila. 2017. Temporal ensembling for semi-supervised learning. *Proceedings of the International Conference on Learning Representations*.

Lakshminarayanan, Balaji, Alexander Pritzel, and Charles Blundell. 2017. Simple and scalable predictive uncertainty estimation using deep

- ensembles. In *Advances in neural information processing systems*, 6402–6413.
- Lee, Dong-Hyun, et al. 2013. Pseudo-label: The simple and efficient semi-supervised learning method for deep neural networks. In *Workshop on challenges in representation learning, icml*, 896.
- Lee, James R, Shayan Oveis Gharan, and Luca Trevisan. 2014. Multiway spectral partitioning and higher-order cheeger inequalities. *Journal of the ACM (JACM)* 61(6):1–30.
- Lee, Jason D, Qi Lei, Nikunj Saunshi, and Jiacheng Zhuo. 2021. Predicting what you already know helps: Provable self-supervised learning. *Advances in Neural Information Processing Systems* 34:309–323.
- Lee, Kimin, Honglak Lee, Kibok Lee, and Jinwoo Shin. 2017. Training confidence-calibrated classifiers for detecting out-of-distribution samples. *arXiv preprint arXiv:1711.09325*.
- Lee, Kimin, Kibok Lee, Honglak Lee, and Jinwoo Shin. 2018. A simple unified framework for detecting out-of-distribution samples and adversarial attacks. In *Advances in neural information processing systems*, 7167–7177.
- Li, Hao, Asim Kadav, Igor Durdanovic, Hanan Samet, and Hans Peter Graf. 2017. Pruning filters for efficient convnets. *ICLR*.
- Li, Junnan, Caiming Xiong, and Steven Hoi. 2020. Mopro: Webly supervised learning with momentum prototypes. In *International conference on learning representations*.
- Li, Junnan, Caiming Xiong, and Steven C.H. Hoi. 2021a. Semi-supervised learning with contrastive graph regularization. In *Proceedings of the international conference on learning representations*.

Li, Junnan, Pan Zhou, Caiming Xiong, and Steven CH Hoi. 2021b. Prototypical contrastive learning of unsupervised representations. *Proceedings of the International Conference on Learning Representations*.

Li, Lei, Xiaoyi Feng, Zinelabidine Boulkenafet, Zhaoqiang Xia, Mingming Li, and Abdenour Hadid. 2016a. An original face anti-spoofing approach using partial convolutional neural network. In *2016 sixth international conference on image processing theory, tools and applications (ipta)*, 1–6. IEEE.

Li, Shikun, Xiaobo Xia, Shiming Ge, and Tongliang Liu. 2022a. Selective-supervised contrastive learning with noisy labels. In *Proceedings of the IEEE conference on computer vision and pattern recognition*.

Li, Tianhong, Peng Cao, Yuan Yuan, Lijie Fan, Yuzhe Yang, Rogério Feris, Piotr Indyk, and Dina Katabi. 2022b. Targeted supervised contrastive learning for long-tailed recognition. In *Proceedings of the IEEE conference on computer vision and pattern recognition*.

Li, Yixuan, Jason Yosinski, Jeff Clune, Hod Lipson, and John E Hopcroft. 2016b. Convergent learning: Do different neural networks learn the same representations? In *International conference on learning representations (iclr)*.

Li, Ziyun, Jona Otholt, Ben Dai, Christoph Meinel, Haojin Yang, et al. 2022c. A closer look at novel class discovery from the labeled set. *arXiv preprint arXiv:2209.09120*.

Liang, Shiyu, Yixuan Li, and Rayadurgam Srikant. 2018. Enhancing the reliability of out-of-distribution image detection in neural networks. In *6th international conference on learning representations, iclr 2018*.

Lin, Ziqian, Sreya Dutta Roy, and Yixuan Li. 2021. Mood: Multi-level out-of-distribution detection. In *Proceedings of the IEEE/CVF conference on computer vision and pattern recognition (CVPR)*, 15313–15323.

Lipton, Zachary, Yu-Xiang Wang, and Alexander Smola. 2018. Detecting and correcting for label shift with black box predictors. In *International conference on machine learning*, 3122–3130. PMLR.

Liu, Fei Tony, Kai Ming Ting, and Zhi-Hua Zhou. 2008. Isolation forest. In *2008 eighth IEEE international conference on data mining*, 413–422.

Liu, Wei, Junfeng He, and Shih-Fu Chang. 2010. Large graph construction for scalable semi-supervised learning. In *Proceedings of the 27th international conference on machine learning (ICML-10)*, 679–686. Citeseer.

Liu, Weitang, Xiaoyun Wang, John Owens, and Yixuan Li. 2020. Energy-based out-of-distribution detection. *Advances in Neural Information Processing Systems (NeurIPS)*.

Loshchilov, Ilya, and Frank Hutter. 2017. Sgdr: Stochastic gradient descent with warm restarts. In *International conference on learning representations*.

Louizos, Christos, Max Welling, and Diederik P. Kingma. 2018. Learning sparse neural networks through l_0 regularization. In *International conference on learning representations*.

MacQueen, J. 1967. Classification and analysis of multivariate observations. In *5th Berkeley symp. math. statist. probability*, 281–297.

Mahalanobis, Prasanta Chandra. 1936. On the generalized distance in statistics.

Malinin, Andrey, and Mark Gales. 2018. Predictive uncertainty estimation via prior networks. In *Advances in neural information processing systems*, 7047–7058.

McInnes, Leland, John Healy, Nathaniel Saul, and Lukas Grossberger. 2018. Umap: Uniform manifold approximation and projection. *The Journal of Open Source Software* 3(29):861.

McSherry, Frank. 2001. Spectral partitioning of random graphs. In *Proceedings 42nd ieee symposium on foundations of computer science*, 529–537. IEEE.

Meinke, Alexander, and Matthias Hein. 2020. Towards neural networks that provably know when they don't know. In *International conference on learning representations*.

Ming, Yifei, Ziyang Cai, Jiuxiang Gu, Yiyu Sun, Wei Li, and Yixuan Li. 2022a. Delving into out-of-distribution detection with vision-language representations. *Proceedings of the Advances in Neural Information Processing Systems*.

Ming, Yifei, Ying Fan, and Yixuan Li. 2022b. Poem: Out-of-distribution detection with posterior sampling. In *Proceedings of the international conference on machine learning*. PMLR.

Ming, Yifei, Yiyu Sun, Ousmane Dia, and Yixuan Li. 2023. How to exploit hyperspherical embeddings for out-of-distribution detection? In *The eleventh international conference on learning representations*.

Mohseni, Sina, Mandar Pitale, JBS Yadawa, and Zhangyang Wang. 2020. Self-supervised learning for generalizable out-of-distribution detection. In *Proceedings of the aaai conference on artificial intelligence*, vol. 34, 5216–5223.

Morcos, Ari S., David G.T. Barrett, Neil C. Rabinowitz, and Matthew Botvinick. 2018. On the importance of single directions for generalization. In *International conference on learning representations*.

Morteza, Peyman, and Yixuan Li. 2022. Provable guarantees for understanding out-of-distribution detection. *Proceedings of the AAAI Conference on Artificial Intelligence*.

Mudholkar, Govind S, and Alan D Hutson. 2000. The epsilon-skew-normal distribution for analyzing near-normal data. *Journal of statistical planning and inference* 83(2):291–309.

Netzer, Yuval, Tao Wang, Adam Coates, Alessandro Bissacco, Bo Wu, and Andrew Y Ng. 2011. Reading digits in natural images with unsupervised feature learning.

Ng, Andrew, Michael Jordan, and Yair Weiss. 2001. On spectral clustering: Analysis and an algorithm. *Advances in neural information processing systems* 14.

Nguyen, Anh, Jason Yosinski, and Jeff Clune. 2015. Deep neural networks are easily fooled: High confidence predictions for unrecognizable images. In *Proceedings of the IEEE conference on computer vision and pattern recognition*, 427–436.

Niyogi, Partha. 2013. Manifold regularization and semi-supervised learning: Some theoretical analyses. *Journal of Machine Learning Research* 14(5).

Oliver, Avital, Augustus Odena, Colin A Raffel, Ekin Dogus Cubuk, and Ian Goodfellow. 2018. Realistic evaluation of deep semi-supervised learning algorithms. *Proceedings of Advances in Neural Information Processing Systems* 31.

Van den Oord, Aaron, Yazhe Li, and Oriol Vinyals. 2018. Representation learning with contrastive predictive coding. *arXiv e-prints* arXiv-1807.

Ovadia, Yaniv, Emily Fertig, Jie Ren, Zachary Nado, D Sculley, Sebastian Nowozin, Joshua Dillon, Balaji Lakshminarayanan, and Jasper Snoek. 2019. Can you trust your model's uncertainty? evaluating predictive uncertainty under dataset shift. *Advances in Neural Information Processing Systems* 32:13991–14002.

Oymak, Samet, and Talha Cihad Gulcu. 2021. A theoretical characterization of semi-supervised learning with self-training for gaussian mixture models. In *International conference on artificial intelligence and statistics*, 3601–3609. PMLR.

Park, Jongjin, Sukmin Yun, Jongheon Jeong, and Jinwoo Shin. 2023. Opencos: Contrastive semi-supervised learning for handling open-set unlabeled data. In *Computer vision—eccv 2022 workshops: Tel aviv, israel, october 23–27, 2022, proceedings, part ii*, 134–149. Springer.

Paszke, Adam, Sam Gross, Francisco Massa, Adam Lerer, James Bradbury, Gregory Chanan, Trevor Killeen, Zeming Lin, Natalia Gimelshein, Luca Antiga, Alban Desmaison, Andreas Kopf, Edward Yang, Zachary DeVito, Martin Raison, Alykhan Tejani, Sasank Chilamkurthy, Benoit Steiner, Lu Fang, Junjie Bai, and Soumith Chintala. 2019. Pytorch: An imperative style, high-performance deep learning library. In *Proceedings of the advances in neural information processing systems 32*, 8024–8035.

Pevny, Tomavs. 2016. Loda: Lightweight on-line detector of anomalies. *Mach. Learn.* 102(2):275–304.

Pires, Catarina, Marília Barandas, Letícia Fernandes, Duarte Folgado, and Hugo Gamboa. 2020. Towards knowledge uncertainty estimation for open set recognition. *Machine Learning Knowledge* 2:505–532.

- Pu, Nan, Zhun Zhong, and Nicu Sebe. 2023. Dynamic conceptional contrastive learning for generalized category discovery.
- Purwins, Hendrik, Bo Li, Tuomas Virtanen, Jan Schlüter, Shuo-Yiin Chang, and Tara Sainath. 2019. Deep learning for audio signal processing. *IEEE Journal of Selected Topics in Signal Processing* 13(2):206–219.
- Radford, Alec, Jong Wook Kim, Chris Hallacy, Aditya Ramesh, Gabriel Goh, Sandhini Agarwal, Girish Sastry, Amanda Askell, Pamela Mishkin, Jack Clark, et al. 2021. Learning transferable visual models from natural language supervision. In *International conference on machine learning*, 8748–8763. PMLR.
- Rebuffi, Sylvestre-Alvise, Sebastien Ehrhardt, Kai Han, Andrea Vedaldi, and Andrew Zisserman. 2020. Semi-supervised learning with scarce annotations. In *Proceedings of the IEEE/CVF conference on computer vision and pattern recognition workshops*, 762–763.
- Rigollet, Philippe. 2007. Generalization error bounds in semi-supervised classification under the cluster assumption. *Journal of Machine Learning Research* 8(7).
- Rizve, Mamshad Nayeem, Navid Kardan, Salman Khan, Fahad Shahbaz Khan, and Mubarak Shah. 2022. Openldn: Learning to discover novel classes for open-world semi-supervised learning. *Proceedings of the European Conference on Computer Vision*.
- Roy, Abhijit Guha, Jie Ren, Shekoofeh Azizi, Aaron Loh, Vivek Nataraajan, Basil Mustafa, Nick Pawlowski, Jan Freyberg, Yuan Liu, Zach Beaver, et al. 2021. Does your dermatology classifier know what it doesn't know? detecting the long-tail of unseen conditions. *arXiv preprint arXiv:2104.03829*.

Saerens, Marco, Patrice Latinne, and Christine Decaestecker. 2002. Adjusting the outputs of a classifier to new a priori probabilities: a simple procedure. *Neural Computation* 14(1):21–41.

Saito, Kuniaki, Donghyun Kim, and Kate Saenko. 2021. Openmatch: Open-set consistency regularization for semi-supervised learning with outliers. *Proceedings of Advances in Neural Information Processing Systems*.

Sajjadi, Mehdi, Mehran Javanmardi, and Tolga Tasdizen. 2016. Regularization with stochastic transformations and perturbations for deep semi-supervised learning. *Proceedings of Advances in Neural Information Processing Systems* 29.

Salimans, Tim, and Diederik P Kingma. 2016. Weight normalization: a simple reparameterization to accelerate training of deep neural networks. In *Proceedings of the 30th international conference on neural information processing systems*, 901–909.

Sandler, Mark, Andrew Howard, Menglong Zhu, Andrey Zhmoginov, and Liang-Chieh Chen. 2018. Mobilenetv2: Inverted residuals and linear bottlenecks. In *Proceedings of the IEEE conference on computer vision and pattern recognition (cvpr)*.

Schölkopf, Bernhard, John C. Platt, John Shawe-Taylor, Alex J. Smola, and Robert C. Williamson. 2001. Estimating the Support of a High-Dimensional Distribution. *Neural Computation* 13(7):1443–1471.

Sehwag, Vikash, Mung Chiang, and Prateek Mittal. 2021. Ssd: A unified framework for self-supervised outlier detection. In *International conference on learning representations*.

Shaham, Uri, Kelly Stanton, Henry Li, Boaz Nadler, Ronen Basri, and Yuval Kluger. 2018. Spectralnet: Spectral clustering using deep neural networks. *International Conference on Learning Representations*.

Shen, Kendrick, Robbie M Jones, Ananya Kumar, Sang Michael Xie, Jeff Z HaoChen, Tengyu Ma, and Percy Liang. 2022. Connect, not collapse: Explaining contrastive learning for unsupervised domain adaptation. In *International conference on machine learning*, 19847–19878. PMLR.

Shi, Jianbo, and Jitendra Malik. 2000. Normalized cuts and image segmentation. *IEEE Transactions on pattern analysis and machine intelligence* 22(8):888–905.

Shi, Zhenmei, Jiefeng Chen, Kunyang Li, Jayaram Raghuram, Xi Wu, Yingyu Liang, and Somesh Jha. 2023. The trade-off between universality and label efficiency of representations from contrastive learning. In *International conference on learning representations*.

Shrikumar, Avanti, and Anshul Kundaje. 2019. Calibration with bias-corrected temperature scaling improves domain adaptation under label shift in modern neural networks. *Preprint at <https://arxiv.org/abs/1901.06852> v1*.

Shyu, Mei-Ling, Shu-Ching Chen, Kanoksri Sarinnapakorn, and Liwu Chang. 2003. A novel anomaly detection scheme based on principal component classifier. Tech. Rep.

Singh, Aarti, Robert Nowak, and Jerry Zhu. 2008. Unlabeled data: Now it helps, now it doesn't. *Advances in neural information processing systems* 21.

Sokolovska, Nataliya, Olivier Cappé, and François Yvon. 2008. The asymptotics of semi-supervised learning in discriminative probabilistic models. In *Proceedings of the 25th international conference on machine learning*, 984–991.

Song, Yang, Jascha Sohl-Dickstein, Diederik P Kingma, Abhishek Kumar, Stefano Ermon, and Ben Poole. 2020. Score-based generative mod-

eling through stochastic differential equations. In *International conference on learning representations*.

Srivastava, Nitish, Geoffrey Hinton, Alex Krizhevsky, Ilya Sutskever, and Ruslan Salakhutdinov. 2014. Dropout: A simple way to prevent neural networks from overfitting. *Journal of Machine Learning Research* 15(56): 1929–1958.

Sun, Xin, Zhenning Yang, Chi Zhang, Keck-Voon Ling, and Guohao Peng. 2020a. Conditional gaussian distribution learning for open set recognition. In *Proceedings of the IEEE conference on computer vision and pattern recognition*, 13480–13489.

Sun, Yiyou, Chuan Guo, and Yixuan Li. 2021a. React: Out-of-distribution detection with rectified activations. In *Proceedings of the advances in neural information processing systems*.

Sun, Yiyou, Bastin Joseph, Alison Deatsch, Robert Jeraj, and Sharon Yixuan Li. 2021b. Localization-based uncertainty estimation for safe medical imaging diagnosis. *Proceedings of the International Conference on Machine Learning (Workshop)*.

Sun, Yiyou, and Yixuan Li. 2022. Dice: Leveraging sparsification for out-of-distribution detection. In *Computer vision—eccv 2022: 17th european conference, tel aviv, israel, october 23–27, 2022, proceedings, part xxiv*, 691–708. Springer.

———. 2023. Opencon: Open-world contrastive learning. *Transactions of Machine Learning Research*.

Sun, Yiyou, Yifei Ming, Xiaojin Zhu, and Yixuan Li. 2022. Out-of-distribution detection with deep nearest neighbors. In *International conference on machine learning*, 20827–20840. PMLR.

Sun, Yiyou, Sathya N Ravi, and Vikas Singh. 2019. Adaptive activation thresholding: Dynamic routing type behavior for interpretability in convolutional neural networks. In *Proceedings of the IEEE/CVF International Conference on Computer Vision*, 4938–4947.

Sun, Yiyou, Zhenmei Shi, and Yixuan Li. 2023a. A graph-theoretic framework for understanding open-world representation learning. In *Advances in neural information processing systems*.

Sun, Yiyou, Zhenmei Shi, Yingyu Liang, and Yixuan Li. 2023b. When and how does known class help discover unknown ones? provable understanding through spectral analysis. In *Proceedings of the International Conference on Machine Learning*. PMLR.

Sun, Yiyou, Tonghua Su, and Zhiying Tu. 2017. Faster r-cnn based autonomous navigation for vehicles in warehouse. In *2017 IEEE International Conference on Advanced Intelligent Mechatronics (AIM)*, 1639–1644. IEEE.

Sun, Yu, Xiaolong Wang, Zhuang Liu, John Miller, Alexei Efros, and Moritz Hardt. 2020b. Test-time training with self-supervision for generalization under distribution shifts. In *International Conference on Machine Learning*, 9229–9248. PMLR.

Tack, Jihoon, Sangwoo Mo, Jongheon Jeong, and Jinwoo Shin. 2020. Csi: Novelty detection via contrastive learning on distributionally shifted instances. In *Advances in neural information processing systems*.

Tao, Leitian, Xuefeng Du, Xiaojin Zhu, and Yixuan Li. 2023. Non-parametric outlier synthesis. *International Conference on Learning Representations*.

Templeton, Brad. 2020. Tesla in taiwan crashes directly into overturned truck, ignores pedestrian, with autopilot on. <https://www.forbes.com/sites/bradtempleton/2020/06/02/>

[tesla-in-taiwan-crashes-directly-into-overtuned-truck-ignores-\pedestrian-with-autopilot-on/](#).

Tian, Yonglong, Olivier J Henaff, and Aäron van den Oord. 2021. Divide and contrast: Self-supervised learning from uncurated data. In *Proceedings of the IEEE/CVF International Conference on Computer Vision*, 10063–10074.

Tosh, Christopher, Akshay Krishnamurthy, and Daniel Hsu. 2021a. Contrastive estimation reveals topic posterior information to linear models. *J. Mach. Learn. Res.* 22:281–1.

———. 2021b. Contrastive learning, multi-view redundancy, and linear models. In *Algorithmic learning theory*, 1179–1206. PMLR.

Tsai, Yao-Hung Hubert, Tianqin Li, Weixin Liu, Peiyuan Liao, Ruslan Salakhutdinov, and Louis-Philippe Morency. 2022. Learning weakly-supervised contrastive representations. In *International conference on learning representations*.

Uppaal, Rheeeya, Junjie Hu, and Yixuan Li. 2023. Is fine-tuning needed? pre-trained language models are near perfect for out-of-domain detection. *Annual Meeting of the Association for Computational Linguistics*.

Van Amersfoort, Joost, Lewis Smith, Yee Whye Teh, and Yarin Gal. 2020. Uncertainty estimation using a single deep deterministic neural network. In *Proceedings of the international conference on machine learning*.

Vaze, Sagar, Kai Han, Andrea Vedaldi, and Andrew Zisserman. 2022. Generalized category discovery. In *Proceedings of the IEEE conference on computer vision and pattern recognition*.

Von Luxburg, Ulrike. 2007. A tutorial on spectral clustering. *Statistics and computing* 17(4):395–416.

Wan, Li, Matthew D. Zeiler, Sixin Zhang, Yann LeCun, and Rob Fergus. 2013. Regularization of neural networks using dropconnect. In *Icml*, vol. 28, 1058–1066.

Wang, Fei, and Changshui Zhang. 2006. Label propagation through linear neighborhoods. In *Proceedings of the 23rd international conference on machine learning*, 985–992.

Wang, Haobo, Ruixuan Xiao, Yixuan Li, Lei Feng, Gang Niu, Gang Chen, and Junbo Zhao. 2022a. Pico: Contrastive label disambiguation for partial label learning. *Proceedings of the International Conference on Learning Representations*.

Wang, Haoqi, Zhizhong Li, Litong Feng, and Wayne Zhang. 2022b. Vim: Out-of-distribution with virtual-logit matching. *Proceedings of the IEEE Conference on Computer Vision and Pattern Recognition*.

Wang, Haoran, Weitang Liu, Alex Bocchieri, and Yixuan Li. 2021. Can multi-label classification networks know what they don't know? *Advances in Neural Information Processing Systems*.

Wang, Tongzhou, and Phillip Isola. 2020. Understanding contrastive representation learning through alignment and uniformity on the hypersphere. In *International conference on machine learning*, 9929–9939. PMLR.

Wang, Xiaosong, Yifan Peng, Le Lu, Zhiyong Lu, Mohammadhadi Bagheri, and Ronald M Summers. 2017. Chestx-ray8: Hospital-scale chest x-ray database and benchmarks on weakly-supervised classification and localization of common thorax diseases. In *Proceedings of the IEEE conference on computer vision and pattern recognition*, 2097–2106.

Wasserman, Larry, and John Lafferty. 2007. Statistical analysis of semi-supervised regression. *Advances in Neural Information Processing Systems* 20.

- Wei, Hongxin, Renchunzi Xie, Hao Cheng, Lei Feng, Bo An, and Yixuan Li. 2022. Mitigating neural network overconfidence with logit normalization. *Proceedings of the International Conference on Machine Learning*.
- Winkens, Jim, Rudy Bunel, Abhijit Guha Roy, Robert Stanforth, Vivek Natarajan, Joseph R Ledsam, Patricia MacWilliams, Pushmeet Kohli, Alan Karthikesalingam, Simon Kohl, et al. 2020. Contrastive training for improved out-of-distribution detection. *arXiv preprint arXiv:2007.05566*.
- Wong, Eric, Shibani Santurkar, and Aleksander Madry. 2021. Leveraging sparse linear layers for debuggable deep networks. In *Proceedings of the international conference on machine learning*, 11205–11216. PMLR.
- Wu, Ruihan, Chuan Guo, Yi Su, and Kilian Q Weinberger. 2021a. Online adaptation to label distribution shift. *arXiv preprint arXiv:2107.04520*.
- Wu, Yuxin, and Kaiming He. 2018. Group normalization. In *Proceedings of the european conference on computer vision (eccv)*, 3–19.
- Wu, Zhi-Fan, Tong Wei, Jianwen Jiang, Chaojie Mao, Mingqian Tang, and Yu-Feng Li. 2021b. Ngc: A unified framework for learning with open-world noisy data. In *Proceedings of the IEEE/CVF International Conference on Computer Vision*, 62–71.
- Xiao, Jianxiong, James Hays, Krista A. Ehinger, Aude Oliva, and Antonio Torralba. 2010. Sun database: Large-scale scene recognition from abbey to zoo. In *Cvpr*, 3485–3492. IEEE Computer Society.
- Xu, Pingmei, Krista A Ehinger, Yinda Zhang, Adam Finkelstein, Sanjeev R Kulkarni, and Jianxiong Xiao. 2015. Turkergaze: Crowdsourcing saliency with webcam based eye tracking. *arXiv preprint arXiv:1504.06755*.

Yang, Fan, Kai Wu, Shuyi Zhang, Guannan Jiang, Yong Liu, Feng Zheng, Wei Zhang, Chengjie Wang, and Long Zeng. 2022a. Class-aware contrastive semi-supervised learning. In *Proceedings of the IEEE conference on computer vision and pattern recognition*.

Yang, Jingkan, Haoqi Wang, Litong Feng, Xiaopeng Yan, Huabin Zheng, Wayne Zhang, and Ziwei Liu. 2021. Semantically coherent out-of-distribution detection. In *Proceedings of the IEEE international conference on computer vision*, 8301–8309.

Yang, Jingkan, Pengyun Wang, Dejian Zou, Zitang Zhou, Kunyuan Ding, Wenxuan Peng, Haoqi Wang, Guangyao Chen, Bo Li, Yiyu Sun, et al. 2022b. Openood: Benchmarking generalized out-of-distribution detection. *Advances in Neural Information Processing Systems* 35:32598–32611.

Yang, Muli, Yuehua Zhu, Jiaping Yu, Aming Wu, and Cheng Deng. 2022c. Divide and conquer: Compositional experts for generalized novel class discovery. In *Proceedings of the IEEE/CVF conference on computer vision and pattern recognition*, 14268–14277.

Yosinski, Jason, Jeff Clune, Yoshua Bengio, and Hod Lipson. 2014. How transferable are features in deep neural networks? In *Advances in neural information processing systems*, vol. 27.

Yu, Fisher, Ari Seff, Yinda Zhang, Shuran Song, Thomas Funkhouser, and Jianxiong Xiao. 2015. Lsun: Construction of a large-scale image dataset using deep learning with humans in the loop. *arXiv preprint arXiv:1506.03365*.

Yu, Qing, Daiki Ikami, Go Irie, and Kiyoharu Aizawa. 2020. Multi-task curriculum framework for open-set semi-supervised learning. In *Proceedings of the European conference on computer vision*, 438–454. Springer.

Zbontar, Jure, Li Jing, Ishan Misra, Yann LeCun, and Stéphane Deny. 2021. Barlow twins: Self-supervised learning via redundancy reduction. In *International conference on machine learning*, 12310–12320. PMLR.

Zeiler, Matthew D, and Rob Fergus. 2014. Visualizing and understanding convolutional networks. In *European conference on computer vision*, 818–833. Springer.

Zha, Hongyuan, Xiaofeng He, Chris Ding, Ming Gu, and Horst Simon. 2001. Spectral relaxation for k-means clustering. *Advances in neural information processing systems* 14.

Zhai, Xiaohua, Avital Oliver, Alexander Kolesnikov, and Lucas Beyer. 2019. S4l: Self-supervised semi-supervised learning. In *Proceedings of the IEEE/CVF International Conference on Computer Vision*, 1476–1485.

Zhang, Chiyuan, Samy Bengio, Moritz Hardt, Benjamin Recht, and Oriol Vinyals. 2016. Understanding deep learning requires rethinking generalization. *ICLR*.

Zhang, Dejiao, Feng Nan, Xiaokai Wei, Shangwen Li, Henghui Zhu, Kathleen McKeown, Ramesh Nallapati, Andrew Arnold, and Bing Xiang. 2021. Supporting clustering with contrastive learning. *Proceedings of the North American Chapter of the Association for Computational Linguistics*.

Zhang, Kai, James T Kwok, and Bahram Parvin. 2009. Prototype vector machine for large scale semi-supervised learning. In *Proceedings of the 26th annual international conference on machine learning*, 1233–1240.

Zhang, Sheng, Salman Khan, Zhiqiang Shen, Muzammal Naseer, Guangyi Chen, and Fahad Khan. 2022a. Promptcal: Contrastive affinity learning via auxiliary prompts for generalized novel category discovery.

Zhang, Shu, Ran Xu, Caiming Xiong, and Chetan Ramaiah. 2022b. Use all the labels: A hierarchical multi-label contrastive learning framework. In *Proceedings of the IEEE conference on computer vision and pattern recognition*.

Zhang, Yuhang, Xiaopeng Zhang, Jie Li, Robert Qiu, Haohang Xu, and Qi Tian. 2022c. Semi-supervised contrastive learning with similarity calibration. *IEEE Transactions on Multimedia*.

Zhao, Bingchen, and Kai Han. 2021. Novel visual category discovery with dual ranking statistics and mutual knowledge distillation. *Proceedings of Advances in Neural Information Processing Systems* 34.

Zhao, Puning, and Lifeng Lai. 2020. Analysis of knn density estimation. *arXiv preprint arXiv:2010.00438*.

Zheng, Mingkai, Fei Wang, Shan You, Chen Qian, Changshui Zhang, Xiaogang Wang, and Chang Xu. 2021. Weakly supervised contrastive learning. *Proceedings of the IEEE/CVF International Conference on Computer Vision*.

Zhong, Zhun, Enrico Fini, Subhankar Roy, Zhiming Luo, Elisa Ricci, and Nicu Sebe. 2021a. Neighborhood contrastive learning for novel class discovery. In *Proceedings of the IEEE conference on computer vision and pattern recognition*, 10867–10875.

Zhong, Zhun, Linchao Zhu, Zhiming Luo, Shaozi Li, Yi Yang, and Nicu Sebe. 2021b. Openmix: Reviving known knowledge for discovering novel visual categories in an open world. In *Proceedings of the IEEE/CVF conference on computer vision and pattern recognition*, 9462–9470.

Zhou, Bolei, Agata Lapedriza, Aditya Khosla, Aude Oliva, and Antonio Torralba. 2017. Places: A 10 million image database for scene recogni-

tion. *IEEE transactions on pattern analysis and machine intelligence* 40(6): 1452–1464.

Zhou, Bolei, Yiyou Sun, David Bau, and Antonio Torralba. 2018. Revisiting the importance of individual units in cnns via ablation. *arXiv preprint arXiv:1806.02891*.

Zhou, Dengyong, Thomas Hofmann, and Bernhard Schölkopf. 2004. Semi-supervised learning on directed graphs. *Advances in neural information processing systems* 17.

Zhu, Xiaojin. 2002. Learning from labeled and unlabeled data with label propagation. *Tech. Report*.

Zhu, Xiaojin, Zoubin Ghahramani, and John D Lafferty. 2003. Semi-supervised learning using gaussian fields and harmonic functions. In *Proceedings of the 20th international conference on machine learning (icml-03)*, 912–919.